The Dissertation Committee for Carl Jackson Stolle Certifies that this is the approved version of the following dissertation:

Low Cost Processing of $CuInSe_2$ Nanocrystals for Photovoltaic Devices

Committee:

Brian A. Korgel, Supervisor

C. Buddie Mullins

Arumugam Manthiram

David A. Vanden Bout

John T. Markert

Low Cost Processing of $CuInSe_2$ Nanocrystals for Photovoltaic Devices

by

Carl Jackson Stolle, B.S.Phy.; M.S.E.

Dissertation

Presented to the Faculty of the Graduate School of

The University of Texas at Austin

in Partial Fulfillment

of the Requirements

for the Degree of

Doctor of Philosophy

The University of Texas at Austin

May 2015

Dedication

For Andrea

Acknowledgements

I have been surrounded by many bright and talented individuals throughout my graduate career and I owe a tremendous amount of my success to them. Graduate school has been a transformative time for me. I have grown as a scientist, as a leader, as a teammate, and as a human being due to my interactions with all of these people. I am extremely grateful.

First, I would like to thank my adviser Brian Korgel for all of his guidance and support. To say that my graduate research would not have been possible without him is stating the obvious, but he provided much more than funding and equipment for my research. He provided motivation and guidance when I felt lost, fresh ideas when mine had run dry, and space to grow and work through challenges on my own. Brian is an amazing scientists, communicator, and creative thinker. I sincerely hope that those good qualities have rubbed off on my over the past four plus years. I am also extremely grateful to Jon Peck, who has made all of the administrative hurdles of being a graduate student and conducting research very easy to navigate.

The group of people that I have had the pleasure to work with during my graduate career is truly exceptional. I owe a lot to the students who mentored me through my early years in graduate school. Aaron Chockla, Chet Steinhagen, Kate Collier, Kate Shipman, Vince Holmberg, Justin Harris, Colin Hessel, Bran Goodfellow, Matt Panthani, and Vahid Akhavan. They taught me what it means to be a scientist through their example. I would like to especially thank Matt and Vahid for teaching me everything they know about photovoltaics and for guiding my research not only during our shared time at UT,

but through my entire graduate career. It is no coincidence that over half of my total publications have one of these two as an author as well.

I have had a wonderful four plus years with Taylor Harvey, Tim Bogart, Yixuan Yu, and Chris Bosoy, who all started the chemical engineering program at the same time as me. Taylor and I have worked closely together the entire time and it has been invaluable sharing ideas and working on projects together. Our research projects feed off one another and the results that the two of us have produced during graduate school is greater than the sum of our individual parts. I am also extremely thankful for all of the knowledge and help provided to me by the rest of the PV team: Doug Pernik, Jiang Du, Vikas Reddy, Cherrelle Thomas, Chen Ming, and Cao Meng.

All of the other students, have had a great influence on me as well. Xiaotang Lu, Philip Liu, Adrien Guillaussier, Dorothy Silbaugh, and Emily Adkins have all taught me new things and have had an impact on my research and development as a scientist. Even the first year students, Taizhi Jiang, Gang Fan, Hyun Gyung Kim, Dan Houck, and Tim Siegler, have had an influence on me. It is good to know that I am leaving the group in the hands of many bright and capable people. I am very grateful for all of the undergraduates and visiting students who have worked with me over the past four years: Andrey Aseev, Jarett Hibbert, Dong Joon Rhee, Jamir Thompson, Ty Updegrave, Aditya Shetkar, Soa-Jin Sher, Jing Li, Arunkumar Akkineni, Saatviki Gupta, Ailey Lim, and Omar Ali. All of the people in the Korgel group have made my time in graduate school very fun an enjoyable as well. I have had countless great conversations, many fun lunches, and some challenging racquetball matches as well. Finally, I hope that I have had a positive impact on each and every student’s scientific development just as each of you have had a large impact on me.

I would like to thank all of the people who I have collaborated with or who have supported my research by helping with equipment and characterization. First, I would like to thank Rich Schaller for a very successful collaboration doing transient absorption spectroscopy. I would also like to thank Damon Smith, Josh Bolinger, and Mark Andrews for their help with all of the device fabrication and solar testing equipment, Hugo Celio for help with the TGA, FTIR, and XPS/UPS, Sayan Saha for help with the Banerjee group IPCE tester, Vanessa Pool for help with in-situ XRD at SLAC, and Dwight Romanovicz for help with the SEM and TEM.

I would like to thank Kyle Klavetter and Diane Forbes for help with studying for qualifying exams and for being great friends during my time in graduate school. Learning course material is so much easier when you have friends to help you. Kyle and Diane made the transition from physics to chemical engineering manageable.

I would like to thank all of my family for their love and support. I am extremely fortunate to have all of my family in town so I can spend time with them frequently. I have the best in-laws that anyone could possibly hope for. I also am fortunate to get to have lunch with my sister-in-law every week at UT. My parents have been extremely supportive of me through my entire education. Finally, I thank my new son Colin for providing me with extra motivation to succeed not just in science, but as a father and person as well. He has been such a joy to me. Most importantly, I thank my wife, Andrea, for the immense amount of caring, wisdom, guidance, laughter, fun, support, and love that she has given me. I could not have done it without her.

Low Cost Processing of $CuInSe_2$ Nanocrystals for Photovoltaic Devices

Carl Jackson Stolle, Ph.D.

The University of Texas at Austin, 2015

Supervisor: Brian Korgel

Semiconductor nanocrystal-based photovoltaics are an interesting new technology with the potential to achieve high efficiencies at low cost. $CuInSe_2$ nanocrystals have been synthesized in solution using arrested precipitation and dispersed in solvent to form a "solar ink". The inks have been deposited under ambient conditions to fabricate photovoltaic devices with efficiency up to 3%. Despite the low cost spray coating deposition technique, device efficiencies remain too low for commercialization. Higher efficiencies up to 7% have been achieved using a high temperature selenization process, but this process is too expensive. New nanocrystal film treatment processes are necessary which can improve the device efficiency at low cost.

To this end, $CuInSe_2$ nanocrystals were synthesized using a diphenyl phosphine:Se precursor which allows for precise control over the nanocrystal size. The size is controlled by changing the temperature of the reaction. The smallest size nanocrystals demonstrated extremely high device open circuit voltage. Ligand exchange procedures were used to replace the insulating oleylamine capping ligand used during synthesis with more conductive halide ions or inorganic chalcogenidometallate cluster (ChaM) ligands. These ligands led to improved charge transport in the nanocrystal films.

A high-intensity pulsed light processing technique known as photonic curing was used which allows for high temperature sintering of nanocrystal films on temperature-

sensitive substrates. High energy pulses cause the nanocrystals to sinter into large grains, primarily through melting and resolidification. The choice of metal back contact has a dramatic effect on the final film morphology, with Au and $MoSe_2$ back contacts providing much better adhesion with the $CuInSe_2$ than Mo back contacts. Nanocrystal sintering without melting can be achieved by replacing the oleylamine ligands with ChaM ligands prior to photonic curing.

Low energy photonic curing pulses vaporize the oleylamine ligands without inducing sintering or grain growth. This greatly improved nanocrystal coupling and interparticle charge transport. Multiexcitons were successfully extracted from these nanocrystal films and external quantum efficiencies over 100% were observed. Transient absorption spectroscopy was used to study the multiexciton generation process in $CuInSe_2$ nanocrystal films and colloidal suspensions. The multiexciton generation efficiency, threshold, and Auger lifetimes for $CuInSe_2$ compare well with other nanocrystal materials.

Table of Contents

List of Tables xv

List of Figures xvii

Chapter 1: Introduction 1

1.1 Introduction to Photovoltaics 1

1.2 Solar Cell Technologies 3

1.2.1 Silicon Solar Cells 3

1.2.2 Multijunction Solar Cells 4

1.2.3 Thin Film Solar Cells 5

1.2 4 Organic and Dye Sensitized Solar Cells 6

1.2.5 Perovskite Solar Cells 6

1.2.6 Nanocrystal Solar Cells 7

1.3 Device Physics 8

1.4 Overview of Nanocrystal Photovoltaics 9

1.5 Multiexciton Generation 15

1.7 $CuInSe_2$ Nanocrystal Photovoltaics 19

1.8 Conclusions and Dissertation Overview 20

1.9 References 21

Chapter 2: Synthesis and Device Performance of Size-Controlled $CuInSe_2$ Nanocrystal Quantum Dots 28

2.1 Introduction 28

2.2 Experimental Methods 30

2.2.1 Materials 30

2.2.2 $CuInSe_2$ Quantum Dot Synthesis 30

2.2.3 Device Fabrication 31

2.2.4 Characterization Techniques 32

2.3 Results and Discussion 33

2.3.1 Nanocrystal Characterization 33

2.3.2 Photovoltaic Device Analysis 36

2.3.3 Comparison of Electronic and Optical Band Gaps 38
2.4 Conclusions 41
2.5 References 42

Chapter 3: Inorganic Ligand-Capped $CuInSe_2$ Nanocrystal Photovoltaics 45
3.1 Introduction 45
3.2 Experimental Methods 47
3.2.1 Chemicals 47
3.2.2 $CuInSe_2$ Nanocrystal Synthesis 47
3.2.3 Metal Chalcogenide Complex Preparation 48
3.2.4 Oleylamine/MCC Ligand Exchange 48
3.2.5 Materials Characterization 49
3.2.6 CIS Nanocrystal PV Device Fabrication 50
3.3 Results and Discussion 51
3.3.1 $CuInSe_2$ (CIS) Nanocrystals Before and After Inorganic Ligand Exchange 51
3.3.2 CIS Nanocrystal Film Deposition 53
3.3.3 PV Device Performance 55
3.4 Conclusions 58
3.5 References 59

Chapter 4: $CuInSe_2$ Nanocrystal Sintering Using Photonic Curing 62
4.1 Introduction 62
4.2 Experimental Methods 64
4.2.1 Chemicals 64
4.2.2 Nanocrystal Synthesis 64
4.2.3 Nanocrystal Film Preparation 65
4.2.4 Photonic Curing 65
4.2.5 Materials Characterization 66
4.2.6 PV Device Fabrication 66
4.3 Results and Discussion 67
4.3.1 Photonic Curing of Nanocrystal Films on Mo Back Contacts 67

4.3.2 Photonic Curing on $MoSe_2$/Mo Bilayer Contacts 70
4.3.3 Optimization of Photonic Curing Pulse Length 75
4.3.4 Photonic Curing on Au and Other Metal Contacts 78
4.3.5 Photovoltaic Device Performance 82
4.4 Conclusions 84
4.5 References 85

Chapter 5: Photonic Curing of Nanocrystals Capped with Inorganic ChaM Ligands 87
5.1 Introduction 87
5.2 Experimental Methods 88
5.2.1 Nanocrystal Synthesis 88
5.2.2 Ligand Exchange 89
5.2.3 Film Deposition and Treatment 89
5.2.4 Characterization Techniques 90
5.3 Results and Discussion 90
5.3.1 Film Morphology and Photonic Curing Temperature 90
5.3.2 XRD Peak Narrowing and Phase Transformations 95
5.3.3 Device Performance 97
5.4 Conclusions 98
5.5 References 99

Chapter 6: Ligand Removal with Photonic Curing: Enhanced Nanocrystal Coupling and Multiexciton Extraction 101
6.1 Introduction 101
6.2 Experimental Methods 103
6.2.1 Materials 103
6.2.2 $CuInSe_2$ nanocrystal synthesis 103
6.2.3 Film Deposition 104
6.2.4 PV Device Fabrication 104
6.2.5 Characterization 105
6.2.6 PV Device Testing 106

6.3 Results and Discussion 107
6.3.1 Ligand Removal 107
6.3.2 Film Morphology and Device Results 112
6.3.3 Quantum Efficiency Analysis 114
6.3.4 Possible Anomalous Effects 117
6.3.5 Transient Absorption Spectroscopy 121
6.3.6 Surface Trap States 126
6.3.7 Photonic Curing of Multi-Layer Films 128
6.3.8 Surface Repassivation 131
6.4 Conclusions 133
6.5 References 134

Chapter 7: Multiexciton Generation in Colloidal $CuInSe_2$ Nanocrystals 138
7.1 Introduction 138
7.2 Experimental Methods 139
7.2.1 Nanocrystal Synthesis 139
7.2.2 Characterization Techniques 140
7.3 Results and Discussion 140
7.3.1 Materials Characterization 140
7.3.2 TA Spectra, Carrier Cooling, and Absorption Cross Sections 143
7.3.3 TA Kinetics, Auger Lifetimes, and Multiexciton generation 148
7.3.4 Comparison of MEG Efficiency, MEG Threshold, and Auger Lifetimes 153
7.4 Conclusions 156
7.5 References 157

Chapter 8: Conclusions and Future Directions 160
8.1 Conclusions 160
8.1.1 Nanocrystal Synthesis and Ligand Exchanges 160
8.1.2 Photonic Curing 162
8.1.3 Transient Absorption Spectroscopy 163
8.2 Future Directions 164

8.3 References....166

Appendix A: Nanocrystal Synthesis Recipes....167

A.1 $Cu(In,Ga)Se_2$ and Related Nanocrystal Synthesis Recipes....167

A.1.1 Elemental:Se Reaction....167

A.1.2 TBP:Se and DPP:Se Reactions....169

A.1.3 Hydrated Precursors Recipe....171

A.1.4 $Cu(In,Ga)S_2$ Recipe....172

A.1.5 In_2Se_3 recipe....174

A.1.6 $Cu_{2-x}Se$ /Recipe....176

A.2 Other Nanocrystal Synthesis Recipes....178

A.2.1 PbS Recipe....178

A.2.2 CdTe Recipe....180

A.3 References....181

References....182

Vita….....195

List of Tables

Table 1.1 PV performance for all-inorganic nanocrystal photovoltaics. The device structures are shown including the contact layers and the absorber layer in bold. Power conversion efficiency (η), short circuit current density (J_{sc}), open circuit voltage (V_{oc}) and fill factor (FF) were determined under AM1.5G (100 mW/cm^2) illumination. Record efficiencies of PVs made using conventional processes are shown for comparison and taken from the Solar Cell Efficiency Tables (version 44).[3] 14

Table 2.1 Absorption onsets of CISe QDs determined by absorbance spectroscopy of dispersions in toluene and from EQE measurements of PVs. The nanocrystal diameter was determined by TEM. 40

Table 3.1 Characteristics of PV devices fabricated with CIS nanocrystals capped with various ligands. 57

Table 4.1 Device Characteristics of Pulsed Films deposited on $MoSe_2$-coated Mo and Au back contacts. 82

Table 6.1 Table showing peak EQE and calculated Jsc for each probe beam intensity from Figure 6.11.....120

Table 6.2 Table showing the PV device PCE, V_{oc}, J_{sc}, and fill factor for devices corresponding to the films shown in Figure 6.18. 130

Table 6.3 Table showing the PV device PCE, V_{oc}, J_{sc}, fill factor, and peak quantum efficiency for the devices shown in Figure 6.19. 133

Table 7.1 A table showing the MEG threshold, MEG efficiency, and Bulk band gap values for a variety of semiconductor nanocrystals. Nanocrystals marked with an * were measured without sample stirring to eliminate effects from photocharging and may not be accurate. 154

List of Figures

Figure 1.1 Department of Energy SunShot models of the amount of installed solar power depending on the average installed price of solar by the year 2020. The SunShot reference line is for power generated at $\$1/W_p$. Source: DOE SunShot Vision Study.[1] 2

Figure 1.2 Department of Energy SunShot Vision Study analysis of the total cost of installed solar energy in the United States in 2012. Source: DOE SunShot Vision Study.[1].....2

Figure 1.3 Chart of record solar cell efficiencies categorized by technology and tracked over time. Source: NREL National Center for Photovoltaics.3

Figure 1.4 (A) An illustration of a nanocrystal solar cell with an opaque metal contact, a p-n junction made with semiconductor nanocrystals, and a transparent contact. (B) A band diagram illustration of photogenerated carriers in a p-n junction solar cell.....9

Figure 1.5 (A) Photograph of a dispersion of $CuInSe_2$ nanocrystals in toluene forming a "solar ink." (B) TEM image of $CuInSe_2$ nanocrystals. (C) Photograph of ambient spray deposition of semiconductor nanocrystals into thin film photovoltaic absorber layers. (D) Photograph of a $CuInSe_2$ nanocrystal photovoltaic device fabricated on a flexible polyimide substrate. 10

Figure 1.6 An illustration showing the change in band gap and energy level splitting from a bulk semiconductor to a quantum confined nanocrystal based on nanocrystal size.....11

Figure 1.7 (A) An illustration and SEM images demonstrating high-temperature nanocrystal sintering. (B) An illustration of a ligand exchange procedure. The procedure can be done either through a solution-based method or a solid-state method. 13

Figure 1.8 (A) A schematic illustration of the thermalization process. High energy photons are absorbed and produce a hot electron and a hot hole. These hot carriers rapidly cool to the band edge in bulk semiconductors where they can then recombine. (B) A schematic illustration of the MEG process in nanocrystals. High energy photons are absorbed and produce a hot electron and a hot hole. These hot carriers can then cool by transferring their energy to promote a second electron hole pair. This creates a multiexciton, which decays very rapidly through Auger processes. 16

Figure 1.9 The maximum theoretical efficiency of a single junction solar cell utilizing MEG (red) and without MEG (black) as a function of the band gap energy. Adapted from ref. [64], copyright 2008 Wiley-VCH....16

Figure 1.10 (A) Schematic illustration of a typical pump-probe transient absorption spectroscopy setup. (B) Schematic illustrating the sample measurement. First, the sample is probed and the absorbance is measured. Then, after a long time delay (1ms), the sample is pumped with a laser and then probed after a short time delay (<5000 ps). (C) The difference in absorption is measured and then plotted as a function of delay time. Figure adapted from Ref. [64], copyright 2008 Wiley-VCH.....18

Figure 2.1 TEM images of CISe QDs synthesized at (A) 130°C, (B) 160°C, (C) 180°C, and (D) 240°C. The average QD diameters are 2.2, 3.3, 4.7, and 6.6 nm, respectively. (E) Absorbance spectra and (F) XRD (λ=1.54 Å) of nanocrystals synthesized at temperatures between 100°C and 240°C (<1 nm to 6.6 nm diameter). Inset in (E) shows Tauc plots used to determine the absorption edge reported in Table 1. The reference XRD pattern in (F) (green bars) for chalcopyrite $CuInSe_2$ is from JCPDS #97-006-8917. 34

Figure 2.2 Absorbance and photoluminescence spectra of CIS QDs synthesized at 100°C (< 1 nm diameter) and 115°C (1.1 nm diameter). The PL maxima (< 1 nm:1.68, 1.1 nm: 1.55 eV) match well with that determined by Tauc analysis (1.65 and 1.54 eV, respectively). 35

Figure 2.3 (A) Illustration of the cross section and top-view of a CISe QD solar cell. (B) *J-V* characteristics and (C) summary of device parameters (PCE, J_{sc}, FF, and V_{oc}) of solar cells versus the optical gap of the CISe QDs under AM1.5 illumination (100 mW/cm^2). 37

Figure 2.4 Fraction of maximum theoretical open circuit voltage (top) and reported open circuit voltages (bottom) in this work and other works demonstrating high open circuit voltages.[5,22,37] Theoretical maximum open circuit voltage is determined by formula described by C.H. Henry.[38] 38

Figure 2.5 (a) EQE measurements of solar cells of solar cell made from CISe QDs. The average QD diameter in each device is shown in the inset. (b) Comparison of the absorbance spectra of dispersed nanocrystals in toluene (dashed) and the PV EQE (solid) of 3.0 (top) nm and 1.1 nm (bottom) CISe QDs. 39

Figure 3.1 TEM images of CIS nanocrystals: (a,b) as-synthesized with oleylamine capping ligands and after ligand exchange with (c,d) Na_2S and (e,f) CIS-MCC. (g) High-resolution TEM image and (h) corresponding FFT of a CIS nanocrystal after oleylamine ligand exchange with CIS-MCC. The nanocrystal is imaged down the [110] crystallographic zone axis and the FFT is indexed to chalcopyrite CIS. The measured d-spacing is d_{112} = 3.3 Å.....52

Figure 3.2 XRD patterns from CIS nanocrystals synthesized with oleylamine capping ligands before and after exchange with Cu_2S-MCC and In_2Se_4-MCC ligands. The red reference lines correspond to chalcopyrite CIS (PDF #97-006-892). The absence of the (112) peak indicates that there may be Cu and In positional disorder. 53

Figure 3.3 SEM images of (a) the surface of a spin-coated CIS nanocrystal film and (b) a cross-sectioned PV device with a layer of CIS-MCC ligand-capped CIS nanocrystals. The Au, CIS-MCC nanocrystal, ZnO and ITO layers are 70 nm, 75 nm, 40 nm and 200 nm thick, respectively. 55

Figure 3.4 Dark and light I-V characteristics for the highest performance devices fabricated using oleylamine-capped CIS nanocrystals (blue), CIS-MCC ligand-capped CIS nanocrystals (red), and Na_2S-capped CIS nanocrystals (green). The dashed lines are the dark I-V characteristics and the solid lines are the light I-V characteristics. IPCE measurements for each device are shown in the inset. 57

Figure 4.1 A schematic illustration of the photonic curing process. 68

Figure 4.2 SEM images of $CuInSe_2$ nanocrystal films on Mo-coated soda lime glass a) before and after photonic curing with a 300 μs pulse with b) 1.0 J/cm^2, c) 1.3 J/cm^2, d) 1.8 J/cm^2, and e) 2.2 J/cm^2 energy. Cross sectional SEM images f) before and g) after a 2.2 J/cm^2 pulse are also shown. 69

Figure 4.3 XRD of CIS deposited on Mo. XRD is shown for $CuInSe_2$ nanocrystals on Mo-coated soda-lime glass (solid lines) before and after photonic curing. Reference patterns are for chalcopyrite $CuInSe_2$ (PDF # 97-006-8928) and Mo (PDF# 97-064-3959). 70

Figure 4.4 SEM images of $CuInSe_2$ nanocrystals films a) before and after b) 2 J/cm^2, c) 2.2 J/cm^2, d) 2.5 J/cm^2, e) 3 J/cm^2 and f) 3.5 J/cm^2 on $MoSe_2$-coated Mo back contacts. Minimal change is observed with lower energy pulses from the as-deposited nanocrystal film. With increasing pulse energy, more sintering is observed. Some localized $CuInSe_2$ sintering is observed; however, the formation of large melt balls is significantly reduced compared to the treatment of nanocrystal films on Mo back contacts. 72

Figure 4.5 XRD data of nanocrystal films before and after 2, 2.2, 2.5, 3 and 3.5 J/cm^2 pulses on $MoSe_2$/Mo bilayer back contacts (from top to bottom). Indexed XRD references for chalcopyrite $CuInSe_2$, Mo, and $MoSe_2$ (pdf# 97-004-9800) are also shown. As is typical of $MoSe_2$ synthesized via selenization of Mo, the (103) peak intensity is significantly reduced due to the preferential orientation of the $MoSe_2$ to the underlying Mo.[19,20] 73

Figure 4.6 Higher magnification SEM images of $CuInSe_2$ on $MoSe_2$. (a) Spatial and (b) cross sectional SEM of films with no photonic treatment. (c) Spatial SEM of film after 3 J/cm^2 treatment showing some agglomeration of sintered CIS layer as well as areas of local sintering seen in more detail in (d)cross sectional SEM image. (e) SEM of film after 3.5 J/cm^2 pulse showing increased sintering leading to large grain CIS seen in (F)cross sectional SEM image. 74

Figure 4.7 A patterned CuO nanoparticle slurry before and after photonic curing with a 380 V, 2000 µs pulse. During photonic curing, the CuO reacts with a reducing agent to form conductive copper.....76

Figure 4.8 SEM images of a spray-cast CuO nanoparticle slurry (A) before photonic curing and after photonic curing pulses with durations of (B) 300 µs, (C) 1200 µs, and (D) 2000 µs. 77

Figure 4.9 SEM images of a $CuInSe_2$ nanocrystal film spray cast on a $MoSe_2$/Mo bilayer substrate after photonic curing with varying pulse conditions of (A) 600 V, 300 µs, (B) 550 V, 600 µs, (C) 520 V, 900 µs, (D) 500 V, 1200 µs, (E) 470 V, 1500 µs, and (F) 450 V, 2000 µs. The pulse voltage was varied inversely to the pulse duration in order to maintain a similar lamp output power (based on the NovaCentrix pulse modeling software). 78

Figure 4.10 (a) XRD of CIS (112) peak before and after photonic curing with 3 and 3.5 J/cm^2 pulses of nanocrystal films deposited on Au back contacts. Cross sectional SEM images (b)before, (c) after 3 J/cm2 and (d) 3.5 J/cm^2 treatment. (e) Spatial SEM and (f-g) Spatial EDS maps of film after 3.5 J/cm^2 pulse. (f) Composite EDS response for Cu (red), In (green), Se (dark blue), Au (light blue) and Si(violet). (g) Au EDS response showing Au agglomeration scattered across the substrate.80

Figure 4.11 SEM images of $CuInSe_2$ nanocrystal films deposited on Mo, $MoSe_2$/Mo, Au, Ni, and ITO back contacts before photonic curing and after photonic curing at 1.6 J/cm^2 and 3.1 J/cm^2.....81

Figure 4.12 Current/Voltage characteristics of photonic cured nanocrystal films on Au (left) and $MoSe_2$-coated Mo (right) back contacts.....83

Figure 4.13 EDS maps and IV curves of sintered CIS film on $MoSe_2$/Mo back contacts with pulse energies of 3 J/cm^2. a) Cu (red), In (green), Se (dark blue), and Mo (light blue) composite response, b) green In EDS response showing absorber layer location, and d) light blue Mo EDS response showing exposed back contact. d) IV response for device after 3 J/cm^2 pulse. 84

Figure 5.1 SEM images of a 1 μm thick oleylamine-capped $CuInSe_2$ nanocrystal film (A) before photonic curing and after photonic curing pulses of (B) 1.6 J/cm^2, (C) 2.1 J/cm^2, (D) 2.6 J/cm^2, (E) 3.1 J/cm^2, and (F) 3.5 J/cm^2. (G) SimPulse modeling of the nanocrystal film temperature during photonic curing pulses of 1.6, 2.1, 2.6, 3.1, and 3.5 J/cm^2, each 300 μs in duration. For the model a layered structure was used with a 1 μm thick $CuInSe_2$ film on a 60 nm thick Au metal film deposited on a 1.1 mm thick soda-lime glass substrate.....92

Figure 5.2 SEM images of a 1 μm thick ChaM-capped $CuInSe_2$ nanocrystal film (A) before photonic curing and after photonic curing pulses of (B) 1.0 J/cm^2, (C) 1.4 J/cm^2, (D) 1.8 J/cm^2, (E) 2.3 J/cm^2, and (F) 2.8 J/cm^2. Higher magnification is shown for each image in the insets, with the scale bars 500 nm long. (G) SimPulse modeling of the nanocrystal film temperature during photonic curing pulses of 1.0, 1.4, 1.8, 2.3, and 2.8 J/cm^2, each 300 μs in duration. For the model a layered structure was used with a 1 μm thick $CuInSe_2$ film on a 60 nm thick Au metal film deposited on a 1.1 mm thick soda-lime glass substrate. 93

Figure 5.3 Cross-sectional SEM of ChaM-capped nanocrystals (A) before photonic curing and after photonic curing pulses of (B) 1.8 J/cm^2, (C) 2.3 J/cm^2, and (D) 2.8 J/cm^2. 94

Figure 5.4 (A) XRD of both oleylamine-capped and ChaM-capped nanocrystals with and without photonic curing. The diffraction peaks for chalcopyrite $CuInSe_2$ (red lines, PDF #01-073-6321) and Au (blue lines, PDF #01-075-6560) are shown for reference. (B) XRD highlighting the (112) diffraction peak of $CuInSe_2$ for oleylamine-capped nanocrystals before photonic curing (black), and after photonic curing pulses of 1.6 J/cm^2 (red), 2.1 J/cm^2 (blue), 2.6 J/cm^2 (green), 3.1 J/cm^2 (purple), and 3.5 J/cm^2 (gold). (C) XRD highlighting the (112) diffraction peak of $CuInSe_2$ for ChaM-capped nanocrystals before photonic curing (black) and after photonic curing pulses of 1.0 J/cm^2 (red), 1.4 J/cm^2 (blue), 1.8 J/cm^2 (green), 2.3 J/cm^2 (purple), and 2.8 J/cm^2 (gold).....96

Figure 5.5 Current-voltage plots showing the dark (black curves) and light (red curves) photovoltaic response of ChaM-capped nanocrystals (A) before photonic curing and after photonic curing with pulse energies of (B) 1.0 J/cm^2, (C) 1.4 J/cm^2, (D) 1.8 J/cm^2, (E) 2.3 J/cm^2, and (F) 2.8 J/cm^2.98

Figure 6.1 Photonic curing of nanocrystal films on Au-coated glass substrates. (a) Photonic curing can be used to remove oleylamine capping ligands from the CuInSe2 nanocrystal film without inducing grain growth. (b) When the capping ligands are present, they inhibit the collection of multiexcitons from the film, leading to electron-hole recombination by Auger recombination. (c) Without the ligand barrier between nanocrystals, multiexciton transport becomes much more probable.108

Figure 6.2 Thermogravimetric analysis (TGA) of $CuInSe_2$ nanocrystals processed by photonic curing using various pulse conditions.....109

Figure 6.3 FTIR analysis of $CuInSe_2$ nanocrystals without photonic curing (black) and treated with a 2.5 J/cm^2 pulse.....109

Figure 6.4 Temperature of a 500 nm thick $CuInSe_2$ (CIS) nanocrystal layer on 60 nm thick Au on soda lime glass (1.1 mm thick) induced by a single (160 μs) photonic curing pulse (calculated using SimPulse software from NovaCentrix).....110

Figure 6.5 (A) X-ray diffraction (XRD) data highlighting the (112) diffraction peak of chalcopyrite $CuInSe_2$. The crystal sizes for each pulse condition were calculated using Scherrer analysis. Prior to photonic curing, the nanocrystals are 8.3 nm in diameter, which matches well with the size measured in TEM. After curing at 2.2 J/cm^2 and 2.5 J/cm^2, the nanocrystal size is 9.2 and 23.1 nm respectively. After curing at 3 J/cm^2 and 3.5 J/cm^2, the nanocrystals have sintered and the size is too large to calculate using Scherrer analysis. (B) XRD data showing a nanocrystal film before and after curing at 3.9 J/cm^2. The red reference lines are for chalcopyrite $CuInSe_2$ (PDF #01-073-6321) and the blue lines are for Au (the back contact material) (PDF #01-075-6560). 111

Figure 6.6 TEM image of $CuInSe_2$ nanocrystals with average particle diameter of 8.1±2.1 nm based on the histogram shown in the inset generated from the TEM image. 112

Figure 6.7 $CuInSe_2$ nanocrystal layers before and after photonic curing and their PV device performance. Top-down and cross-section SEM images of oleylamine-capped $CuInSe_2$ (CIS) nanocrystal film on Au-coated glass (a, d) before and after photonic curing with (b, e) 2.2 J/cm^2 and (c, f) and 3 J/cm^2 pulse fluence. (g, h, i) Corresponding current-voltage measurements (black curve is dark current; red curve is measured under AM1.5G illumination (100 mW/cm^2)) of devices made with the nanocrystal films are provided below the SEM images.....113

Figure 6.8 External quantum efficiency (EQE) enhancements resulting from photonic curing of the $CuInSe_2$ nanocrystal layer used in PV devices. (a) EQE measurements taken under white light bias for $CuInSe_2$ nanocrystal devices without photonic curing (black curve) compared to the device made with cured (2.2 J/cm^2 pulse fluence) nanocrystals (red curve). The short circuit currents determined from these data, of 4.95 mA/cm^2 and 14.29 mA/cm^2, are consistent with the short circuit currents measured under AM1.5 illumination (100 mW/cm^2). (b) EQE measured under varying white light bias intensity (100%, 50%, 25%, 10%, and 0% of the 50 mW/cm^2 bias light) with the same intensity of monochromated probe light. There is no change in EQE for the device made with as-deposited nanocrystals (inset), but the EQE decreases significantly for the cured device when the white light bias intensity was reduced to the amounts indicated. 115

Figure 6.9 External quantum efficiency (blue), internal quantum efficiency (red), and absorptance (black) for a PV device made with $CuInSe_2$ nanocrystals and cured with a 2.2 J/cm^2 pulse.....116

Figure 6.10 External quantum efficiency of a PV device made with $CuInSe_2$ nanocrystals cured at 2.2 J/cm^2 taken with two separate testing setups. The setup using the Newport monochrometer had a probe beam chopped at 213 Hz and the commercial setup from PV Measurements, Inc. had a probe beam chopped at 100 Hz.....119

Figure 6.11 External quantum efficiency of a PV device made with $CuInSe_2$ nanocrystals cured at 2.2 J/cm2. Neutral density filters are used to cut the monochromated probe beam to 100% (no filter, black), 80% (red), 50% (blue), 25% (green), and 10% (pink) of its original intensity. The white light bias intensity (~50 mW/cm2) was the same for all measurements.....120

Figure 6.12 Transient absorption (TA) spectra showing the spectral peak in the bleach signal for a nanocrystal film without photonic curing (black) and a film cured with a 2.5 J/cm^2 pulse (red). 122

Figure 6.13 Transient absorption (TA) spectroscopy of $CuInSe_2$ nanocrystal films after photonic curing. (a) TA kinetics normalized to $-\Delta\alpha=1$ at 1000 ps with an 800 nm pump wavelength and pump fluences of 300 $\mu J/cm^2$ (dark blue), 90 $\mu J/cm^2$ (green), 60 $\mu J/cm^2$ (pink), 30 $\mu J/cm^2$ (teal), 15 $\mu J/cm^2$ (blue), 6 $\mu J/cm^2$ (red) and 3 $\mu J/cm^2$ (black). (b) TA kinetics normalized to $-\Delta\alpha=1$ at 1000 ps with a 400 nm pump wavelength and pump fluences of 18 $\mu J/cm^2$ (red) and 9 $\mu J/cm^2$ (blue). The average low fluence background (average of 3, 6, 15 and 30 $\mu J/cm^2$ signals) at 800 nm pump wavelength is also shown for comparison (black). (c) TA kinetics showing the Auger recombination rate. The single exciton TA kinetics background (average 800 nm wavelength low fluence pump) is subtracted from the high fluence TA kinetics at 800 nm, 300 $\mu J/cm^2$ pump, which shows the creation of multiexcitons due to the absorption of multiple photons per nanocrystal. The kinetics are plotted on a log scale and can be fitted to a single exponential with a time constant of 92 ps. (d) TA kinetics showing Auger recombination at 400 nm pump and low fluence. The single exciton TA kinetics background (average 800 nm wavelength low fluence pump) is subtracted from the TA kinetics at 400 nm, 9 $\mu J/cm^2$ pump, which should only show Auger recombination if MEG is present. The kinetics are plotted on a log scale and can be fitted to a single exponential with a time constant of 74 ps.....123

Figure 6.14 Transient absorption kinetics measured with and without sample translation and normalized to $-\Delta\alpha=1$ at 1 ns for a film photonically cured at 2.5 J/cm^2. Sample translation helps ensure that sample charging does not affect the TA signal. 124

Figure 6.15 The ratio of exciton population (R_{pop}) at early-time compared to late-time TA signal for high energy (circles, $3.1E_g$) and low energy (squares, $1.6E_g$) pump energy with varying exciton occupancy ($<N_0>$). The exciton population is normalized so that the exciton population at low energy pump is one in the limit of low pump fluence, since only a single exciton can be generated per nanocrystal. The data is fitted to the expected Poisson statistics for high energy (dashed line) and low energy (solid line) pump energy. 125

Figure 6.16 Transient absorption kinetics normalized to $-\Delta\alpha=1$ at 1 ns for a nanocrystal film cured at 2.5 J/cm^2. The kinetics were taken using 9 and 18 μJ /cm^2 pump fluences at 400 nm pump wavelength. 127

Figure 6.17 Absorptance measurements of a $CuInSe_2$ nanocrystal film before (black) and after photonic curing (red, 2.5 J/cm^2). Inset: Absorptance measured near the band edge; the dashed lines indicate the optical gap of each film: 0.91 and 0.79 eV for the nanocrystals before and after curing.127

Figure 6.18 SEM images of nanocrystal films pulsed at 2.5 J/cm^2 and with some additional spray deposition steps. (A) A nanocrystal film pulsed one time. (B) After the photonic curing pulse, a new layer of nanocrystals is spray deposited. (C) The second nanocrystal layer is treated with a photonic curing pulse. (D) Finally, a third nanocrystal layer is deposited on top of the twice-pulsed film. 129

Figure 6.19 Current-voltage measurements for photovoltaic devices fabricated from nanocrystal films before photonic curing (black), after photonic curing with no further repassivation treatments (red), and after photonic curing with repassivation treatments using oleylamine (blue), pyridine (green), Br- ions (magenta), and InSe-ChaM ligands (gold).....132

Figure 7.1 $CuInSe_2$ nanocrystals studied by TAS. (A) optical absorbance spectra and (B-D) TEM images**.** (A) Absorbance spectra were measured at room temperature for nanocrystals dispersed in toluene. Spectra are offset by 0.2 O.D. for clarity. The temperatures noted in (A) correspond to the synthesis temperatures used to make the samples with corresponding TEM images in (B) 180^{o}C, (C) 200^{o}C, and (D) 240^{o}C. The insets of (B-D) are size histograms obtained from the TEM images average diameters of (B) 4.5 ± 0.8 nm, (C) 6.2 ± 1.5 nm and (D) 9.2 ± 3.2 nm. The absorption edges determined in the inset of (A) are 0.98 eV (240 °C), 1.05 eV (200 °C), and 1.14 eV (180 °C). 141

Figure 7.2 Optical absorbance spectra of $CuInSe_2$ nanocrystals dispersed in toluene synthesized at the reaction temperatures indicated. Higher reaction temperatures yielded larger nanocrystals, consistent with the observed shift of the exciton peak and absorption edge to longer wavelength. Absorbance spectra are normalized to 1 at 400 nm and offset for clarity. 142

Figure 7.3 X-ray diffraction data for $CuInSe_2$ nanocrystals synthesized at 200°C. The reference pattern corresponds to chalcopyrite $CuInSe_2$ (PDF #01-073-6321). The ordered chalcopyrite phase is distinguished from the disordered sphalerite phase by the presence of the (211) diffraction peak at 35.6°. 142

Figure 7.4 $CuInSe_2$ nanocrystal transient absorption spectra (TAS) acquired with 800 nm pump wavelength. Samples with three different average diameters were measured: (A,B) 4.5 ± 0.8 nm, (C,D) 6.2 ± 1.5 nm, and (E,F) 9.2 ± 3.2 nm. (A,C,E) show the evolution of the TA bleach spectra as function of delay time (spectra with 0.1 ps delay time are shown in black) and (B,D,F) show TA spectra of each sample after 2.5 ps delay time with varying average number of photons absorbed per nanocrystal, N. N was varied by changing the pump fluence, j_p (# of photons/cm^2): $N = \sigma \cdot jp$, where σ is the absorption cross section of each nanocrystal sample (cm^2).....144

Figure 7.5 Carrier cooling rates. A) Early–time (<5 ps) TA kinetics for each nanocrystal sample at 800 nm pump wavelength (black squares, 4.5 nm nanocrystals; red circles, 6.2 nm nanocrystals; blue triangles, 9.2 nm nanocrystals). The TA kinetics are examined at the location of the absorption bleach maximum for each sample (910 nm for the 4.5 nm diameter nanocrystals, 1050 nm for the 6.2 nm nanocrystals, and 1170 nm for the 9.2 nm nanocrystals). The maximum bleach signals are normalized to one. To calculate the carrier cooling rate, the characteristic cooling times were taken as the delay time when the normalized TA bleach reached 1-1e (dashed line).[23] B) Carrier cooling rates versus nanocrystal volume measured using 800 nm pump wavelength. Carrier cooling rates were calculated from the difference in energy between the 800 nm pump energy and the nanocrystal optical gap (taken as the peak of the TA bleach) divided by the carrier cooling time. The nanocrystal volume was determined from the average diameter assuming spherical shape. The error bars shown for the carrier cooling rate represent the standard deviation obtained from four measurements using different pump fluence. The error bars for nanocrystal volume correspond to the standard deviation of particle size distribution. .145

Figure 7.6 Absorption Cross Section. Transient absorption signal at long delay time (1000 ps) for each nanocrystal sample (4.5 nm, black squares; 6.2 nm, red circles; 9.2 nm, blue triangles) as a function of pump fluence for (A) 800 nm pump wavelength and (B) 400 nm pump wavelength. C) Absorption cross section plotted against particle volume for both (blue) 400 nm pump wavelength and (red) 800 nm pump wavelength. The absorption cross section is calculated by fitting the data in A and B to Eq. (7.1). The error bars for absorption cross section correspond to error in the fit of the data. 147

Figure 7.7 Transient absorption kinetics of (A,B) 4.5 ± 0.8 nm nanocrystals, (C,D) 6.2 ± 1.5 nm nanocrystals, and (E,F) 9.2 ± 3.2 nm diameter $CuInSe_2$ nanocrystals measured using two different pump wavelengths of 400 nm and 800 nm. All curves are normalized at long delay times (1 ns) where only single excitons are present in the nanocrystals. TA kinetics taken with a low pump fluence at 400 nm and 800 nm pump wavelength for (B) 4.5 nm nanocrystals, (D) 6.2 nm nanocrystals, and (F) 9.2 nm nanocrystals, where the kinetics measured at 400 nm are shown in blue and kinetic measured at 800 nm are shown in red. The kinetics are taken at the peak in the absorption bleach for each sample (910 nm for the 4.5 nm particles, 1050 nm for the 6.2 nm particles, and 1170 nm for the 9.2 nm particles).....149

Figure 7.8 Transient absorption kinetics at 800 nm pump wavelength used to determine the biexciton lifetime for $CuInSe_2$ nanocrystals with varying diameter (9.2 nm nanocrystals, black squares; 6.2 nm nanocrystals, red circles; 4.5 nm nanocrystals, blue triangles). The low-fluence (single photon per nanocrystal) background is subtracted from high-fluence (multiple photons per nanocrystal) and fitted to a single exponential. The error in the calculated Auger lifetimes comes from error in the exponential fit of the data (See Fig. 7.9A).....150

Figure 7.9 Auger lifetimes and MEG quantum yield. A) Biexciton lifetimes plotted against particle volume for the 4.5 ± 0.8 nm, 6.2 ± 1.5 nm, and 9.2 ± 3.2 nm diameter $CuInSe_2$ nanocrystals. The error bars for nanocrystal volume correspond to the standard deviation of nanocrystal sizes within each sample. The error bars for biexciton lifetime correspond to error in the single exponential fit in Fig. S3. B) MEG quantum yield plotted as a function of pump energy (relative to the nanocrystal band gap energy). Data were collected for 4.5 nm, 6.2 nm, and 9.2 nm diameter nanocrystals using pump wavelengths of 400 nm, 340 nm, and 320 nm. The data are fit to a straight line, excluding the data point at 2.28E_g, which is below the MEG threshold. The intersection of the lines QY=0 and the fit line is defined as the MEG threshold ((2.4 ± 0.2)E_g) and the slope of the fit line times 100% is defined as the MEG efficiency (36 ± 6%). The open red box corresponds to the MEG quantum yield measured for the $CuInSe_2$ nanocrystal film from Chapter 6. Error bars for the measured MEG quantum yield correspond to the standard deviation of quantum yields measured for a range of pump fluences (See Fig. S4).....151

Figure 7.10 The ratio of the transient absorption signal at short time delay (5 ps) and long time delay (1000 ps) as a function of pump fluence for low pump fluences. The ratio is shown for (black) 800 nm, (red) 400nm, (teal) 340 nm, and (blue) 320 nm pump wavelengths. The ratio for each nanocrystal samples is represented by squares (4.5 nm), circles (6.2 nm), and triangles (9.2 nm). The MEG quantum yield is calculated by dividing the average ratio at each high-energy pump wavelength by the average ratio at 800 nm pump wavelength (See Fig. 7). The error in the MEG quantum yield is derived from the standard deviations of the measured ratios. 153

Figure 7.11 Auger lifetimes as a function of nanocrytstal volume and band gap energy for $CuInSe_2$, PbSe[19], PbS[24], InAs[25], Ag_2S[12], and Si[8] nanocrystals. The green box shows the optimal band gap range for an MEG solar cell. 156

Figure A.1 TEM image of $CuInSe_2$ nanocrystals synthesized using recipe A.1.1.169

Figure A.2 (left) TEM image of $CuInSe_2$ nanocrystals synthesized using recipe A.1.2 (TBP method). (right) TEM image of $CuInSe_2$ nanocrystals synthesized using recipe A.1.2 (DPP method).....171

Figure A.3 TEM image of $CuInSe_2$ nanocrystals synthesized using recipe A.1.3.172

Figure A.4 TEM image of $CuInS_2$ nanocrystals synthesized using recipe A.1.4.174

Figure A.5 TEM image of In_2Se_3 nanocrystals synthesized using recipe A.1.5.176

Figure A.6 TEM image of In_2Se_3 nanocrystals synthesized using recipe A.1.6.178

Figure A.7 TEM image of PbS nanocrystals synthesized using recipe A.2.1...179

Figure A.8 TEM image of CdTe nanocrystals synthesized using recipe A.2.2.181

Chapter 1: Introduction*

1.1 INTRODUCTION TO PHOTOVOLTAICS

Photovoltaic devices (PVs), also known as solar cells, convert sunlight directly to electricity. Since solar energy is plentiful and freely available, PV electricity has obvious economic, environmental and social benefits. Nonetheless, the high cost compared to fossil fuels currently limits its use. The DOE estimates that solar energy needs to reach a total installed cost of about $1 per peak Watt ($1/W_p) to become achieve significant adoption and become a large part of our energy generation in the future.[1] In general, approximately 50% of the total cost for solar energy comes from the cost of the module itself and the rest comes from installation, permitting, and other balance of systems costs.[1] Thus, a significant reduction in the module cost (either through the use of less expensive materials or the reduction of processing costs) could have a large impact on the photovoltaics market.

At the moment, PV technologies exhibit a tradeoff between cost and efficiency: the highest efficiency devices cost too much to produce while the devices that are inexpensive in terms of materials and manufacturing have efficiencies that are too low. Low efficiency leads to higher installation and operation cost, significantly increasing the overall cost of the "cheaper" technologies. Therefore, PV research has sought to develop a new generation of PV devices that uses low cost materials and manufacturing processes combined with high efficiency.

---

* Reproduced in part with permission from: Stolle, C. Jackson; Harvey, Taylor B.; Korgel, Brian A., Nanocrystal Photovoltaics: A Review of Recent Progress, *Current Opinion in Chemical Engineering* (2013), **2**, 160-167. Copyright 2013 Elsevier. CJS wrote the manuscript with assistance from TBH and BAK.

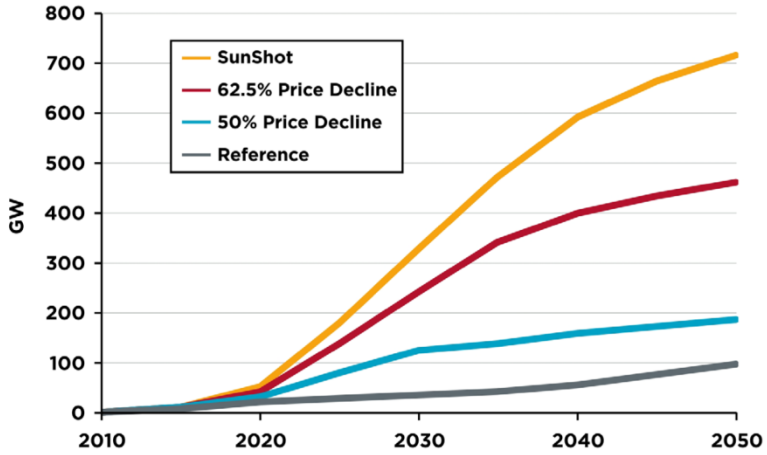

Figure 1.1 Department of Energy SunShot models of the amount of installed solar power depending on the average installed price of solar by the year 2020. The SunShot reference line is for power generated at $\$1/W_p$. Source: DOE SunShot Vision Study.[1]

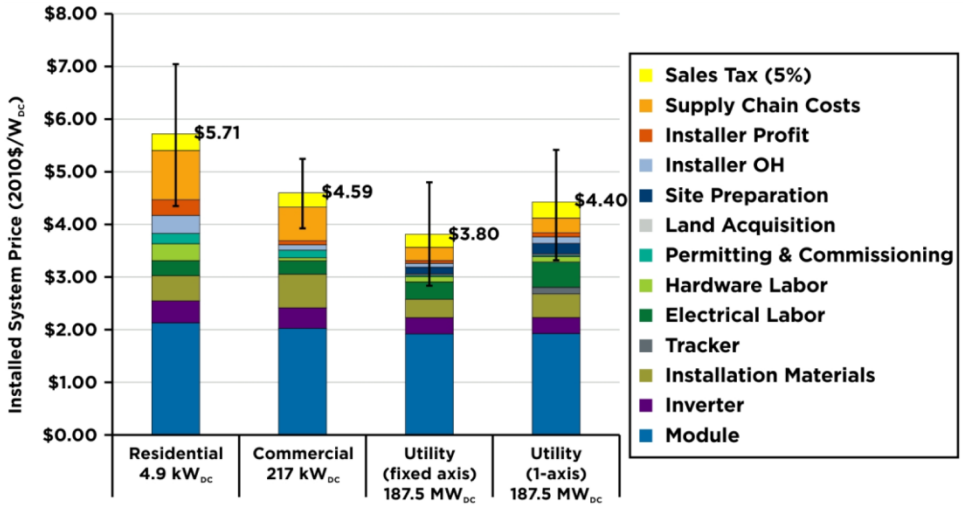

Figure 1.2 Department of Energy SunShot Vision Study analysis of the total cost of installed solar energy in the United States in 2012. Source: DOE SunShot Vision Study.[1]

1.2 SOLAR CELL TECHNOLOGIES

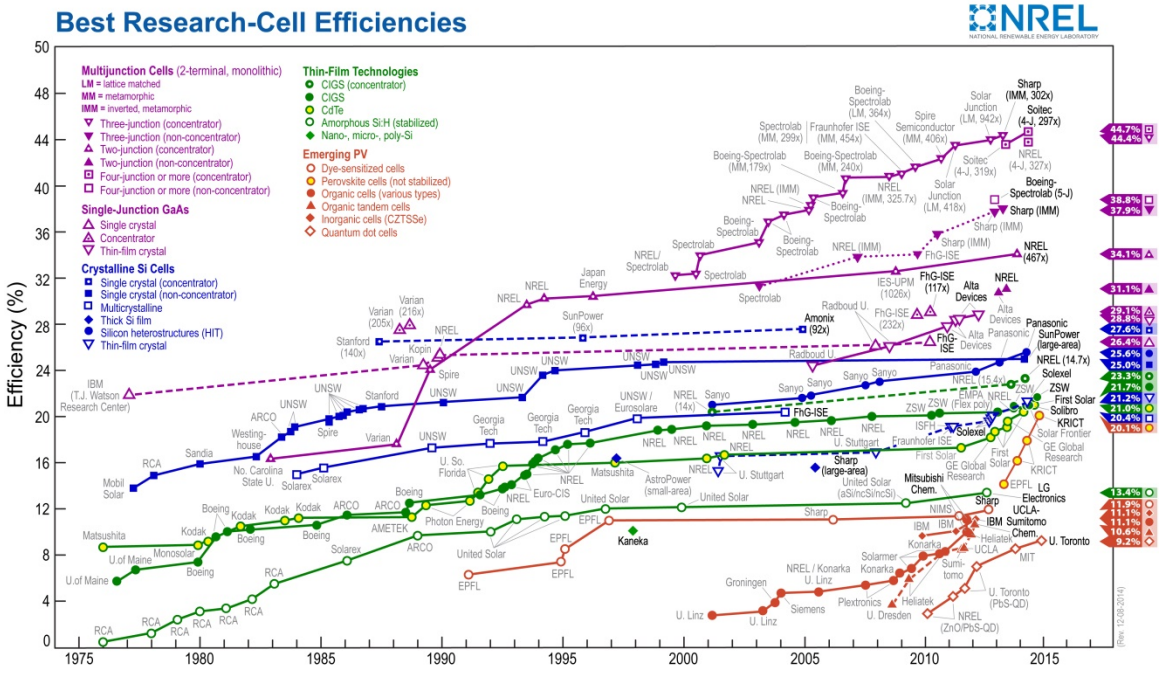

Figure 1.3 Chart of record solar cell efficiencies categorized by technology and tracked over time. Source: NREL National Center for Photovoltaics.

1.2.1 Silicon Solar Cells

The first modern solar cell was developed by Bell Labs in 1954 using a p-n junction in silicon.[2] Sixty years later, silicon is still the dominant technology in the photovoltaics market. Silicon solar cells have not only benefited from their long history, but also from extensive research in the microelectronics industry into silicon material quality, manufacturing processes, and basic device physics. The current record efficiency for a single-junction silicon solar cell without concentration is 25.6% and module efficiencies are also quite high, with a record efficiency of 22.9%.[3,4] Not only are silicon solar cells highly efficient, but they are rapidly becoming less expensive as well. The cost

of producing silicon modules has recently dropped below $\$1/W_p$, a substantial improvement over the mark of ~$\$2/W_p$ only a few years ago.[1]

Silicon solar cells currently make up 85-90% of the photovoltaics market.[5] Because the technology is so dominant, much of the balance of systems (such as power electronics and installation hardware) has been optimized for silicon solar cell technology. Thus, in order for new technologies to make a large impact in the market, they must either provide substantially lower module costs on a per Watt basis or allow for greatly reduced balance of systems costs. The only segment of the market where silicon is not dominant is in flexible photovoltaics. Crystalline silicon solar cells are ridged, typically requiring a glass substrate and, due to the poor light absorption in silicon, a thick silicon layer as well.

1.2.2 Multijunction Solar Cells

Multijunction solar cells have the highest record efficiencies of up to 44.7%; however, the cost of manufacturing these solar cells is extremely expensive.[6] Currently, these solar cells are used primarily for extraterrestrial applications, where the cost per Watt is much less important than the power generated per unit area. Terrestrial multijunction solar cells almost always make use of solar concentrators, where a glass lens is used to collect light over a large area and concentrate it down to a very small device area. Traditional single junction solar cells use the relatively expensive semiconducting material to both harvest light and generate electricity. Concentrating solar cells, on the other hand, use relatively inexpensive glass lenses to collect the light and a very expensive, but also very small, semiconductor to generate electricity. Although this technology has the potential compete with traditional silicon solar cells on

a cost/Watt basis, there are many drawbacks to this technology as well. In particular, concentrating sunlight makes the semiconducting materials very hot, which tends to hurt performance. Furthermore, because a lens is used to harvest the sunlight, excellent solar tracking is required and diffuse sunlight (such as on a cloudy day) is very difficult to collect.

1.2.3 Thin Film Solar Cells

Thin film solar cells, most notably Cu(In,Ga)Se2 (CIGS), CdTe, and amorphous silicon (a-Si), make use of materials with very strong light absorption to make solar cells with a fraction of the thickness of silicon solar cells (~2 μm compared to ~250μm for silicon). By substantially reducing the thickness of the absorber layer, thin film solar cells use much less material and are far less ridged, allowing for the fabrication of flexible solar cells.[7–9] Thin film solar cells can achieve relatively high efficiencies, with record CIGS and CdTe efficiencies just over 20%.[10,11] Despite achieving relatively high efficiencies and the large reduction in materials costs compared to crystalline silicon, processing costs for CdTe and CIGS (especially) remain too high. Altogether, thin film solar cells make up about 10% of the solar energy market, with at least half of that coming from CdTe.[5]

Thin absorber layers are particularly important for the most successful thin film solar cells (CIGS and CdTe) since indium and tellurium are rare and expensive elements. Amorphous silicon does not use any rare elements, but also suffers from low efficiency and stability, particularly under high light intensities.[12] $Cu_2(Zn,Sn)S_4$ (CZTS) is being explored as an alternative to CIGS, since it shares many of the advantages of CIGS without using any rare or expensive elements. However, the efficiency of CZTS solar

cells is still very low and there are many fundamental challenges which must be overcome before CZTS is commercially viable.[13]

1.2 4 Organic and Dye Sensitized Solar Cells

Organic photovoltaics (OPVs) and dye sensitized solar cells (DSSCs) are interesting primarily due to their extremely low processing costs. OPVs typically utilize a light absorbing polymer combined with a fullerene-based electron acceptor in a bulk heterojunction.[14] OPVs can be easily fabricated on flexible substrates, however the electron accepting fullerens are very expensive. DSSCs use an organic light absorbing dye adsorbed on the surface of porous TiO_2 with a liquid electrolyte for hole transport.[15] All of the materials used in DSSCs are very inexpensive, although the TiO_2 layer and liquid electrolyte make fabrication on flexible substrate more challenging. Both OPVs and DSSCs have achieved record efficiencies near 11%.[3] Despite the relatively high efficiency and very low cost associated with these devices, low stability of the organics in OPVs and the electrolyte solution in DSSCs make them difficult to commercialize.

1.2.5 Perovskite Solar Cells

Research into perovskite solar cells has exploded in the past few years, with record efficiencies increasing from under 4% in 2009[16] to over 20% in 2014[17]. Initially, perovskite solar cells utilized a similar structure to DSSCs, with a thin layer of $CH_3NH_3PbI_3$ perovskite deposited onto a porous TiO_2 network and a liquid electrolyte for hole transport. The first major advance came with the replacement of the liquid electrolyte with the solid electrolyte Sprio-OMeTAD. The current best perovskite solar cells no longer resemble DSSCs, as they do not use a porous TiO_2 network or any

electrolyte material at all. Perovskite solar cells are also very low cost both in materials and processing. The primary challenge to commercialization of perovskite solar cells is their stability. $CH_3NH_3PbI_3$ is highly soluble in water, and any exposure to moisture degrades the device performance. Thus, despite their promise for high efficiencies at low cost, perovskite solar cells still have a long way to go before reaching large scale commercialization.

1.2.6 Nanocrystal Solar Cells

Nanocrystal solar cells share many similarities with thin film solar cells, but use semiconductors with nanocrystalline grains instead of bulk. Semiconductor nanocrystals can be synthesized in solution and dispersed in solvent to form a nanocrystal ink.[18–20] The inks can be formulated with a wide range of chemical composition and tunable optical properties, and spread onto large substrate areas using high throughput printing processes.[21–24] Nanocrystal inks share with organic PV materials the characteristics of solution-processability and large-scale synthesis, but also exhibit broadband light absorption, better air and thermal stability, and higher carrier mobilities.[20,25] Inorganic nanocrystals can also be made from an assortment of materials, targeting those with highest availability, lowest toxicity, and lowest raw materials cost. Many different nanocrystals have now been tested, including CdTe,[26–28] CIGS,[29–31] CZTS,[32,33] Cu_2S,[34] PbSe,[35,36] and PbS,[22,37–39] and device efficiencies are approaching values needed to become commercially viable. Further improvements in device efficiency predominantly require better charge transport and extraction from the nanocrystal layers and new processing strategies are being developed to address this issue.

1.3 DEVICE PHYSICS

A PV device consists of a light-absorbing semiconductor layer sandwiched between two electrical contacts, one of which is optically transparent—usually a transparent conducting oxide (TCO) (See Figure 1.4A). The semiconductor layer is either doped to create a p-n junction or interfaced with another semiconductor layer to form a heterojunction. This leads to a built-in electric field that forces apart photoexcited electrons and holes to generate a photocurrent (Figure 1.4B). The power conversion efficiency (PCE, η) of the device is a measure of how much incident solar radiation P_{in}, is converted to electrical power. PCE depends on the illumination conditions, so the maximum power output P_{max}, of devices intended for terrestrial PV applications is usually measured under simulated Air Mass 1.5 Global (AM1.5) full-sun illumination with 1 sun intensity (P_{in} =100 mW/cm^2):[40]

$$\eta = \frac{P_{max}}{P_{in}} = \frac{J_{sc} * V_{oc} * FF}{100\ mW/cm^2} \qquad (1.1)$$

Other important solar cell parameters are the short circuit current (J_{sc}), open circuit voltage (V_{oc}) and fill factor (FF) (Figure 1.4C). In contrast to PCE, external quantum efficiency (EQE) (or incident photon conversion efficiency (IPCE)) and internal quantum efficiency (IQE) are measures of how many electrons and holes are extracted from the devices as electrical current relative to the total incident photon flux in the case of EQE, and the amount of light absorbed by the semiconductor layer in the case of IQE, *at specific wavelengths*. Device can have EQE and IQE values near 100% at certain wavelengths, whereas PCE is fundamentally limited to a maximum value of 34% for a single junction device with a semiconductor having an optimal band gap of around 1.3-1.4 eV—this is the so-called Shockley-Quiesser limit.[41] If it were possible using nanocrystal quantum dots to extract hot electrons and holes, or if more than one

electron/hole pair could be generated per absorbed photon (i.e., multiple exciton generation), the Shockley-Queisser limit could be exceeded.[42]

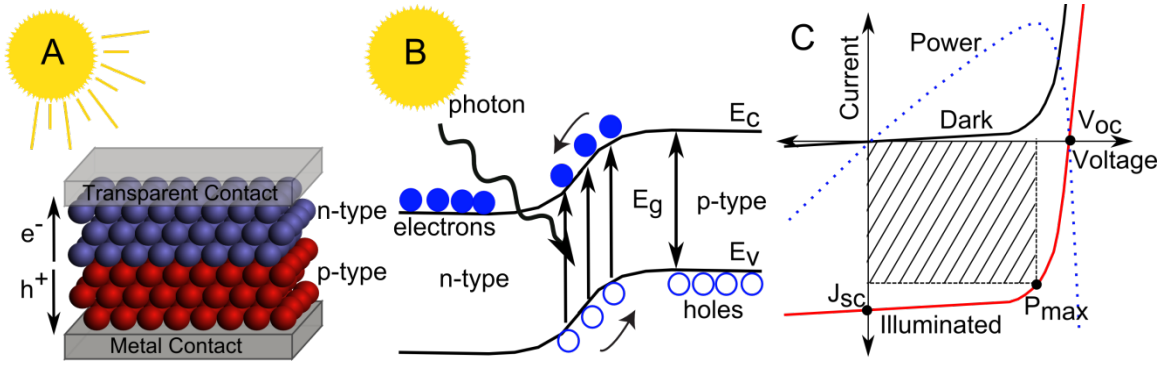

Figure 1.4 (A) An illustration of a nanocrystal solar cell with an opaque metal contact, a p-n junction made with semiconductor nanocrystals, and a transparent contact. (B) A band diagram illustration of photogenerated carriers in a p-n junction solar cell.

1.4 Overview of Nanocrystal Photovoltaics

Nanocrystals offer a flexible materials platform to fabricate PVs of different semiconductors using essentially the same device fabrication and processing approaches, equipment and methods. Nanocrystal inks (Figure 1.5A,B) are simply synthesized with a desired chemical composition and then inserted into a standard PV process flow. Nanocrystals also enable device fabrication on light-weight mechanically flexible substrates with low thermal tolerance (Figure 1.5C,D).[21] Plastic PVs with high efficiency could lead to new market opportunities in building-integrated PV applications and portable power applications in which weight and other architectural characteristics are just as important as power conversion efficiency. Nanocrystal inks that can be deposited near room temperature under ambient conditions to create relatively high efficiency

devices could ultimately enable a wide range of new PV application opportunities currently unavailable with conventional materials and processing approaches.

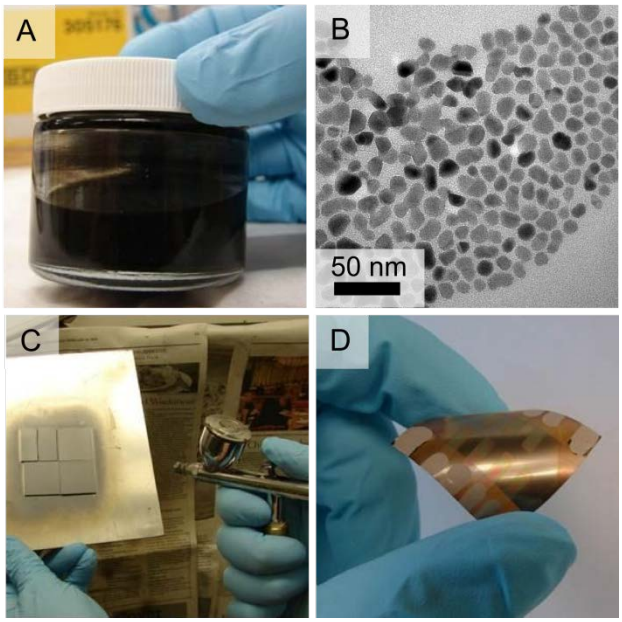

Figure 1.5 (A) Photograph of a dispersion of $CuInSe_2$ nanocrystals in toluene forming a "solar ink." (B) TEM image of $CuInSe_2$ nanocrystals. (C) Photograph of ambient spray deposition of semiconductor nanocrystals into thin film photovoltaic absorber layers. (D) Photograph of a $CuInSe_2$ nanocrystal photovoltaic device fabricated on a flexible polyimide substrate.

For single junction PVs, the optimal band gap is 1.3-1.4 eV, which is one reason why Si (1.1 eV), CdTe (1.4 eV) and CIGS (1.0-1.6 eV) are commonly used.[41] PbS and PbSe have band gaps that are too low, but can be used by increasing the band gap through quantum confinement in nanocrystals (Figure 1.6). The ability to tune the optical properties of nanocrystals by varying size is especially useful in device constructions requiring semiconductors with a range of band gaps, as in tandem or multijunction PVs.[24,43,44] Quantum dots (nanocrystals in the quantum size regime) with band gaps

much lower than 1.3-1.4 eV might also be useful for multiple exciton generation at visible photon energies since MEG occurs at photon energies two to three times higher than the band gap energy.[45–47]

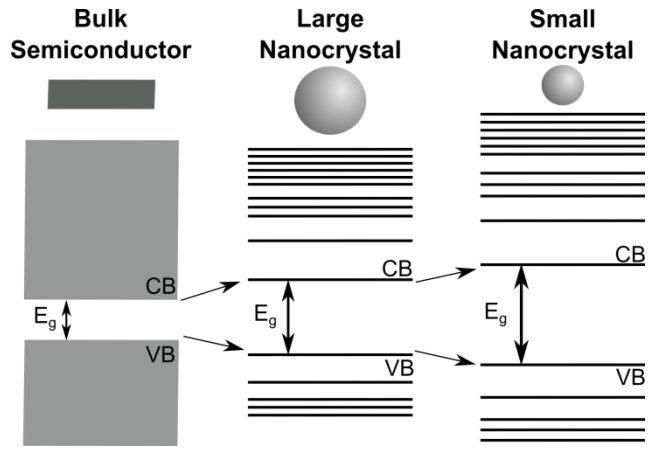

Figure 1.6 An illustration showing the change in band gap and energy level splitting from a bulk semiconductor to a quantum confined nanocrystal based on nanocrystal size.

Despite their many advantages, nanocrystal photovoltaics have not yet made an impact on the solar energy market primarily due to their limited efficiency. Nanocrystals are typically synthesized with large insulating organic capping ligands, which allow the nanocrystals to be stabilized in solution for low cost processing, but greatly hinders charge transport through the nanocrystal film. Without any further processing to remedy this problem, device efficiencies have been limited to a record 5% for PbS nanocrystals.[37] Higher device efficiencies can be achieved by removing or altering this capping ligand either through high temperature nanocrystal sintering or a ligand exchange process (Figure 1.7). A list of record nanocrystal device efficiencies are shown in Table 1.1.

High temperature sintering is used to burn away the organic capping ligand and cause the nanocrystals to grow into large grains similar to traditional thin film solar cells (Figure 1.7A). This method allows nanocrystal photovoltaics to reach record efficiencies of 12.6% for CdTe.[48] However, because this method requires high temperatures, much of the cost benefit of using nanocrystal inks (namely ambient processing conditions) is lost and it becomes challenging to make devices on flexible substrates.

Ligand exchange procedures are used to replace the long organic ligands used during synthesis with much smaller organic, inorganic, or ionic capping ligands (Figure 1.7B).[26,38,39,49–54] These short ligands can passivate the nanocrystal surfaces to a greater extent than the long capping ligands and also cause the nanocrystals to come into closer contact, thereby improving interparticle charge transport.[39,55,56] Ligand exchanges can be performed on nanocrystals in solution or in the solid state directly on a nanocrystal film. Using these methods, a record device efficiency of 8.6% has been achieved for PbS.[38] Although these methods have not yet reached the efficiencies attainable with nanocrystal sintering, ligand exchange processes do not require high temperatures and can be done on flexible substrates.

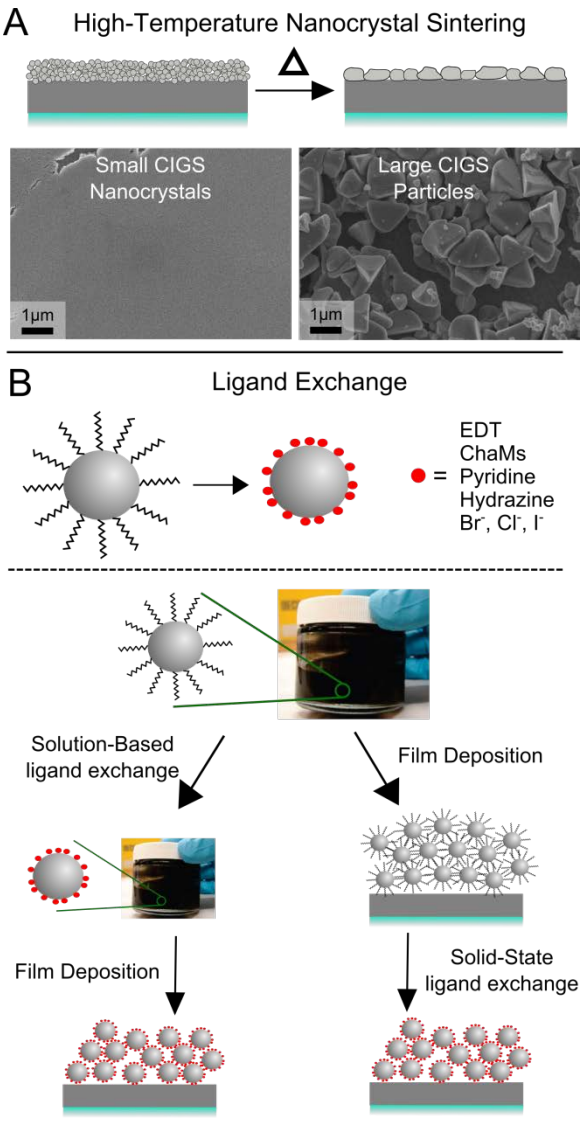

Figure 1.7 (A) An illustration and SEM images demonstrating high-temperature nanocrystal sintering. (B) An illustration of a ligand exchange procedure. The procedure can be done either through a solution-based method or a solid-state method.

Nanocrystal Material	Design	η (%)	J_{sc} (mA/cm^2)	V_{oc} (mV)	FF	Ref.
$CuInSe_2$	Au/**$CuInSe_2$**/CdS/ZnO/ITO	3.1	16.3	410	0.46	[30]
$CuInS_2$	ITO/**$CuInS_2$**/CdS/Al	4.0	12.4	590	0.55	[57]
$CuInSe_xS_{1-x}$	FTO/TiO_2/**$CuInSe_xS_{1-x}$**/S^{2-}/Cu_xS/Cu	5.5	16.8	560	0.59	[58]
Cu_2ZnSnS_4	Au/**CZTS**/CdS/ZnO/ITO	0.2	1.95	320	0.37	[32]
CdSe/CdTe	Ca/**CdTe**/**CdSe**/ITO	2.9	13.2	450	0.49	[28]
PbS	ITO/ZnO/**PbS**/MoO_3/Au	8.6	24.2	555	0.64	[38]
PbSe	ITO/TiO_2/**PbSe**/MoO_3/Al	6.2	23.4	517	0.52	[59]
PbS/PbS tandem	ITO/TiO_2/**PbS(1.6eV)**/GRL/**PbS(1eV)**/Au	4.2	8.3	1060	0.48	[44]
Cu_2S-CdS	Al/**CdS**/**Cu_2S**/ITO	1.6	5.63	600	0.47	[34]
CdS-P3HT NWs	ITO/PEDOT/**CdS-P3HT**/BCP/Mg:Ag	1.6	10.9	1100	0.35	[60]
High-Temperature Nanocrystal Sintering						
$Cu(In,Ga)Se_2$	Mo/**CIGS**/CdS/ZnO/ITO	7.1	25.9	480	0.58	[61]
$Cu(In,Ga)(S,Se)_2$	Mo/**CIGSSe**/CdS/ZnO/ITO	12.0	28.8	630	0.66	[62]
$Cu_2ZnSn(S,Se)_4$	Mo/**CZTSSe**/CdS/ZnO/ITO	9.8	38.1	404	0.64	[63]
CdTe	ITO/CdTe/ZnO/Al	12.3	25.8	684	0.71	[48]
Selected Record Efficiencies for Comparison (from Solar Cell Efficiency Tables[3])						
$Cu(In,Ga)Se_2$		20.5	35.30	752	0.77	
$Cu_2ZnSn(S,Se)_4$		12.6	35.21	513	0.70	
CdTe		21.0	30.25	876	0.79	
Si (crystalline)		25.6	41.80	740	0.83	
Si (amorphous)		10.2	16.36	896	0.70	
DSSC		11.9	22.47	744	0.71	
Organic PV		11.0	19.40	793	0.71	
Perovskite		20.1	24.65	1059	0.77	

Table 1.1 PV performance for all-inorganic nanocrystal photovoltaics. The device structures are shown including the contact layers and the absorber layer in bold. Power conversion efficiency (η), short circuit current density (J_{sc}), open circuit voltage (V_{oc}) and fill factor (FF) were determined under AM1.5G (100 mW/cm^2) illumination. Record efficiencies of PVs made using conventional processes are shown for comparison and taken from the Solar Cell Efficiency Tables (version 44).[3]

1.5 MULTIEXCITON GENERATION

Traditional single-junction photovoltaics are limited to a maximum theoretical efficiency of 34%, known as the Shockley-Queisser limit.[41] This is primarily due to the fact that photons with energy greater than the band gap of the semiconductor loose that excess energy as heat and photons with energy less than the band gap are not absorbed at all. When a high energy photon is absorbed in a semiconductor, it produces a hot electron and hot hole which quickly relax down to the band edge via thermalization processes (heat loss) (Figure 1.8A). There are a variety of ways in the Shockley-Queisser limit can be exceeded, most notably by using multijunction solar cells. Another interesting way to surpass this limit is by harnessing some of the excess energy from high-energy photons through multiexciton generation. Multiexciton generation (MEG), also referred to as multiple exciton generation or carrier multiplication (CM), is a process in which a single high-energy photon (with at least twice the semiconductor band gap energy) excites more than one electron-hole pair (Figure 1.8B). In bulk semiconductors, MEG is an inefficient process; however, MEG is much more efficient in nanocrystals due to the special confinement of the electron and hole.[45] By utilizing efficient MEG in nanocrystals, the maximum theoretical efficiency can be increased up to 43% (Figure 1.9).

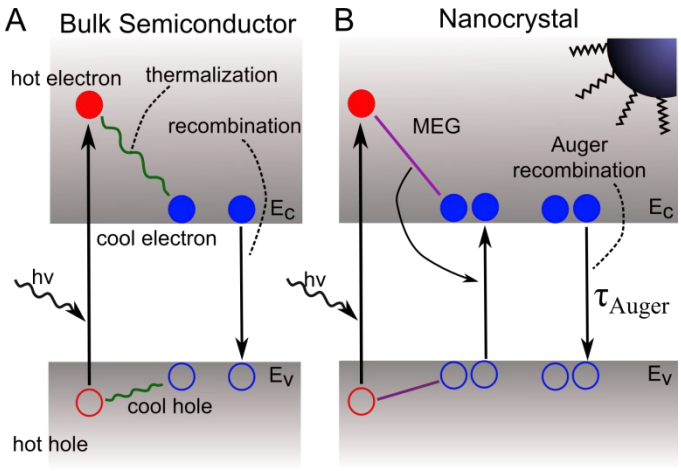

Figure 1.8 (A) A schematic illustration of the thermalization process. High energy photons are absorbed and produce a hot electron and a hot hole. These hot carriers rapidly cool to the band edge in bulk semiconductors where they can then recombine. (B) A schematic illustration of the MEG process in nanocrystals. High energy photons are absorbed and produce a hot electron and a hot hole. These hot carriers can then cool by transferring their energy to promote a second electron hole pair. This creates a multiexciton, which decays very rapidly through Auger processes.

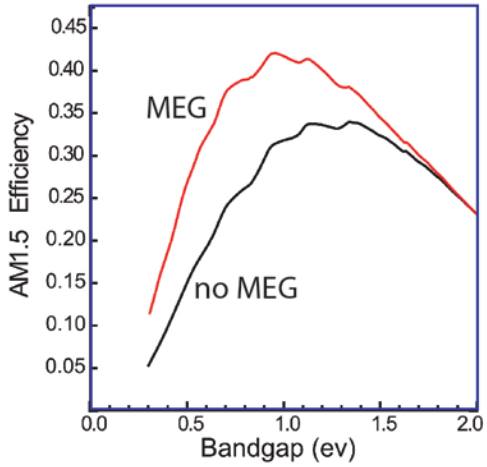

Figure 1.9 The maximum theoretical efficiency of a single junction solar cell utilizing MEG (red) and without MEG (black) as a function of the band gap energy. Adapted from ref. [64], copyright 2008 Wiley-VCH.

Multiexciton generation has been observed in colloidal suspensions of numerous semiconductor nanocrystals including PbSe, PbS, PbTe, CdSe, InAs, InP, Ag_2S, and Si.[65–72] Typically, multiexciton generation is studied by observing the inverse process, Auger recombination, with transient absorption spectroscopy (TAS). TAS is a pump-probe technique wherein a low-intensity pulsed laser (pump) is used to excite carriers in the nanocrystals and the absorbance is measured after a set time delay using a white light pulse (probe). The absorbance is measured before and after the laser pulse and the change in absorbance is proportional to the average number of excited electrons in the conduction band of each nanocrystal. The kinetics of these excited electrons is observed by varying the time delay between the pump and probe from less than 1 ps up to 5 ns. A schematic illustration of a typical TAS setup is show in Figure 1.10.

Multiexciton generation in colloidal nanocrystals is typically characterized using three key parameters, the MEG threshold, MEG efficiency, and Auger lifetime. The MEG threshold is the minimum photon energy required excite multiexcitons. This parameter depends on the band structure of the material. The MEG efficiency is the number of extra electrons produced per absorbed photon for each band gap multiple of energy that the photon has in excess of the MEG threshold energy. The Auger lifetime is the lifetime of multiexcitons within a single nanocrystal. The ideal multiexciton solar cell would use a material with an MEG threshold close to 2, an MEG efficiency near 100%, and would have a long Auger lifetime so that the multiexcitons can be easily extracted.

Even though multiexciton generation is relatively efficient in a variety of colloidal nanocrystals, extracting multiexcitons in a working solar cell has proven much more difficult. The primary challenge is separating multiexcitons before they recombine so they can be extracted from the device. Multiexcitons recombine extremely rapidly

through Auger processes, with lifetimes typically on the order of 10-100 ps, compared to single excitons, which typically have lifetimes greater than a few nanoseconds up to a hundreds of microseconds.[73–78] Thus, nanocrystal films must have excellent interparticle charge transport in order for the multiexcitons to separate before they recombine. Thus far there is only one report of external quantum efficiencies over 100% due to multiexciton generation and extraction.[35] In this study, PbSe nanocrystals were electronically coupled by treated in film with hydrazine. Still, this process has not been successfully applied to other materials to achieve multiexciton extraction.

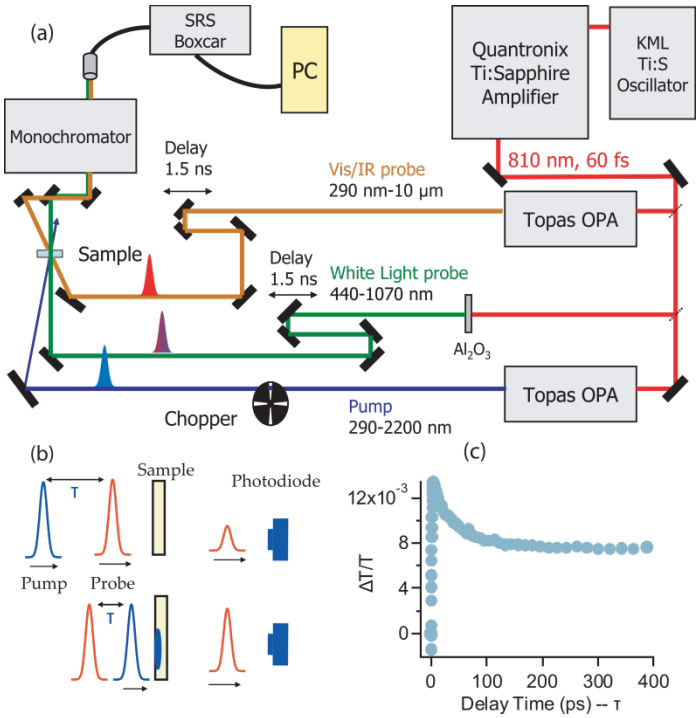

Figure 1.10 (A) Schematic illustration of a typical pump-probe transient absorption spectroscopy setup. (B) Schematic illustrating the sample measurement. First, the sample is probed and the absorbance is measured. Then, after a long time delay (1ms), the sample is pumped with a laser and then probed after a short time delay (<5000 ps). (C) The difference in absorption is measured and then plotted as a function of delay time. Figure adapted from Ref. [64], copyright 2008 Wiley-VCH.

1.7 $CuInSe_2$ Nanocrystal Photovoltaics

$CuInSe_2$ (CIS) and $Cu(In,Ga)Se_2$ (CIGS) are some of the most promising thin film PV materials. CIGS has a band gap in the appropriate range (1.0-1.7 eV depending on Ga content), it is a strong light absorber, and has the second highest record efficiency of all thin film PV materials of just over 20% (See Table 1.1 for a list of record device efficiencies). However, CIGS commercialization has been hindered by expensive vapor-deposition and high temperature processing (~525°C) under Se vapor that is challenging to control on large area substrates. CIGS nanocrystals can be synthesized with targeted composition and chalcopyrite crystal phase by arrested precipitation in oleylamine ($C_{18}H_{37}N$):[29]

$$CuCl + (1-x)InCl_3 + xGaCl_3 + 2Se \xrightarrow[240\ ^oC]{\text{oleylamine}} Cu(In_{1-x}Ga_x)Se_2\ nanocrystals + byproducts \quad (1.2)$$

The In:Ga composition can be tuned by changing the In:Ga reactant ratio.[29] CIS and CIGS nanocrystals disperse in various organic solvents and can be deposited into PV device structures under ambient conditions. CIS PV devices have been made with spray-deposited nanocrystals with efficiencies up to 3.1%,[30] and similar devices on plastic substrates processed under ambient conditions have had efficiencies of up to 2%.[21] The efficiency of these as-deposited nanocrystal devices has been limited by relatively poor electron and hole transport due to the bulky organic oleylamine capping ligands.[79]

Higher device efficiencies can be obtained from CIGS nanocrystals by sintering into polycrystalline films to improve electron/hole transport and extraction. Sintering CIGS nanocrystals requires high temperature selenization—i.e., heating at temperatures exceeding 500°C under Se vapor. Se vapor is required as CIGS nanocrystals do not sinter without it, even at temperatures exceeding 500°C, due to selenium outgassing from the nanocrystal film.[80] Selenized CIGS nanocrystal films have exhibited device efficiencies

of up to 7%.[61,81] Higher efficiencies of up to 12% have been achieved by selenizing sulfur-containing $Cu(In,Ga)S_2$ nanocrystals.[62,82] Hillhouse and Agrawal have explained that selenizing $Cu(In,Ga)S_2$ nanocrystals instead of $Cu(In,Ga)Se_2$ expands the film as the larger Se atoms replace S atoms. This expansion is necessary to fill the significant void space in films. The expansion can be significant with up to 14.5% expansion for complete replacement of S with Se. Although selenization allows for higher device efficiencies, the process adds significant cost and does not allow for device fabrication on flexible substrates such as plastic.

1.8 Conclusions and Dissertation Overview

Since the first demonstration of an all-inorganic nanocrystal PV by Alivisatos in 2005 of devices with almost 2% efficiency,[28] nanocrystal PV efficiency has improved to 8.6% for as-deposited nanocrystals[38] and 12% with high-temperature nanocrystal sintering.[48,62] Efficiencies continue to improve with better understanding of nanocrystal synthesis, processing and device fabrication and a large library of different nanocrystal materials is now available due to advances in synthetic chemistry. To become commercially viable, however, nanocrystal PVs must achieve higher device efficiency without adding significant processing costs or reducing process flexibility. The major limitation to higher efficiency remains the need for improved charge transport in nanocrystal layers and more efficient charge extraction. Either the nanocrystals must be sintered—preferably at relatively low temperature under mild processing conditions—or the interfacial chemistry, i.e., the capping ligand layer, needs to be modified to passivate electronic trap states while enabling efficient interparticle transport.

Chapter 2 discusses the synthesis and device properties of size-controlled $CuInSe_2$ nanocrystals. Chapter 3 explores solution-based ligand exchanges using inorganic chalcogenidometallate cluster (ChaM) ligands to improve charge transport in nanocrystal films. Chapters 4, 5, and 6 are based on photonic curing. Photonic curing is a high-intensity pulsed light technique which allows for high temperature nanocrystal film processing on temperature-sensitive substrates. Chapter 4 discusses the sintering of $CuInSe_2$ nanocrystals using photonic curing. In particular, Chapter 4 covers the effects of substrate choice and photonic curing pulse parameters on the film morphology and device performance. Chapter 5 focuses on uniform film sintering of ChaM-capped nanocrystals with photonic curing. Chapter 6 discusses the use of low-intensity photonic curing to vaporize organic ligands without nanocrystal sintering. This includes discussion of nanocrystal electronic coupling and multiexciton generation and extraction. Chapter 7 covers multiexciton generation in colloidal $CuInSe_2$ nanocrystals and provides comparison to other materials exhibiting MEG. Finally, Chapter 8 provides overall conclusions and future directions for this research.

1.9 REFERENCES

1. U.S.Department of Energy. SunShot Vision Study. (2012).
2. Chapin, D. M., Fuller, C. S. & Pearson, G. L. A New Silicon p-n Junction Photocell for Converting Solar Radiation into Electrical Power. *J. Appl. Phys.* **25,** 676–677 (1954).
3. Green, M. A., Emery, K., Hishikawa, Y., Warta, W. & Dunlop, E. D. Solar cell efficiency tables (version 44). *Prog. Photovolt. Res. Appl.* **22,** 701–710 (2014).
4. Zhao, J. *et al.* 20 000 PERL silicon cells for the '1996 World Solar Challenge' solar car race. *Prog. Photovolt. Res. Appl.* **5,** 269–276 (1997).
5. Fraunhofer Institute for Solar Energy Systems. *Photovoltaics Report*. (2014). at <http://www.ise.fraunhofer.de/en/downloads-englisch/pdf-files-englisch/photovoltaics-report-slides.pdf>

6. Sharp Develops Concentrator Solar Cell with World's Highest Conversion Efficiency of 43.5% | Press Releases | Sharp Global. at <http://sharp-world.com/corporate/news/120531.html>

7. Chirilă, A. *et al.* Highly efficient Cu(In,Ga)Se2 solar cells grown on flexible polymer films. *Nat. Mater.* **10,** 857–861 (2011).

8. Kessler, F., Herrmann, D. & Powalla, M. Approaches to flexible CIGS thin-film solar cells. *Thin Solid Films* **480–481,** 491–498 (2005).

9. Romeo, A. *et al.* High-efficiency flexible CdTe solar cells on polymer substrates. *Sol. Energy Mater. Sol. Cells* **90,** 3407–3415 (2006).

10. Jackson, P. *et al.* New world record efficiency for Cu(In,Ga)Se2 thin-film solar cells beyond 20%. *Prog. Photovolt. Res. Appl.* **19,** 894–897 (2011).

11. *First Solar Sets World Record for CdTe Solar PV Efficiency*. (First Solar, Inc., 2011). at <http://investor.firstsolar.com/releasedetail.cfm?ReleaseID=593,994>

12. Zhu, J. *et al.* Optical Absorption Enhancement in Amorphous Silicon Nanowire and Nanocone Arrays. *Nano Lett.* **9,** 279–282 (2008).

13. Mitzi, D. B., Gunawan, O., Todorov, T. K., Wang, K. & Guha, S. The path towards a high-performance solution-processed kesterite solar cell. *Sol. Energy Mater. Sol. Cells* **95,** 1421–1436 (2011).

14. Kippelen, B. & Brédas, J.-L. Organic photovoltaics. *Energy Environ. Sci.* **2,** 251–261 (2009).

15. Hagfeldt, A., Boschloo, G., Sun, L., Kloo, L. & Pettersson, H. Dye-Sensitized Solar Cells. *Chem. Rev.* **110,** 6595–6663 (2010).

16. Kojima, A., Teshima, K., Shirai, Y. & Miyasaka, T. Organometal Halide Perovskites as Visible-Light Sensitizers for Photovoltaic Cells. *J. Am. Chem. Soc.* **131,** 6050–6051 (2009).

17. Kamat, P. V. Emergence of New Materials for Light–Energy Conversion: Perovskites, Metal Clusters, and 2-D Hybrids. *J. Phys. Chem. Lett.* **5,** 4167–4168 (2014).

18. Stolle, C. J., Harvey, T. B. & Korgel, B. A. Nanocrystal photovoltaics: a review of recent progress. *Curr. Opin. Chem. Eng.* **2,** 160–167 (2013).

19. Kramer, I. J. & Sargent, E. H. Colloidal Quantum Dot Photovoltaics: A Path Forward. *ACS Nano* **5,** 8506–8514 (2011).

20. Hillhouse, H. W. & Beard, M. C. Solar cells from colloidal nanocrystals: Fundamentals, materials, devices, and economics. *Curr. Opin. Colloid Interface Sci.* **14,** 245–259 (2009).

21. Akhavan, V. A. *et al.* Spray-deposited CuInSe2 nanocrystal photovoltaics. *Energy Environ. Sci.* **3,** 1600 (2010).

22. Kramer, I. J. *et al.* Efficient Spray-Coated Colloidal Quantum Dot Solar Cells. *Adv. Mater.* **27,** 116–121 (2015).

23. MacDonald, B. I. *et al.* Layer-by-Layer Assembly of Sintered CdSexTe1–x Nanocrystal Solar Cells. *ACS Nano* **6,** 5995–6004 (2012).

24. Choi, J. J. *et al.* Solution-Processed Nanocrystal Quantum Dot Tandem Solar Cells. *Adv. Mater.* **23,** 3144–3148 (2011).

25. Janssen, R. A. J. & Nelson, J. Factors Limiting Device Efficiency in Organic Photovoltaics. *Adv. Mater.* **25,** 1847–1858 (2013).

26. Jasieniak, J., MacDonald, B. I., Watkins, S. E. & Mulvaney, P. Solution-Processed Sintered Nanocrystal Solar Cells via Layer-by-Layer Assembly. *Nano Lett.* **11,** 2856–2864 (2011).

27. Olson, J. D., Rodriguez, Y. W., Yang, L. D., Alers, G. B. & Carter, S. A. CdTe Schottky diodes from colloidal nanocrystals. *Appl. Phys. Lett.* **96,** 242103 (2010).

28. Gur, I., Fromer, N. A., Geier, M. L. & Alivisatos, A. P. Air-Stable All-Inorganic Nanocrystal Solar Cells Processed from Solution. *Science* **310,** 462–465 (2005).

29. Panthani, M. G. *et al.* Synthesis of CuInS2, CuInSe2, and Cu(InxGa1-x)Se2 (CIGS) Nanocrystal 'Inks' for Printable Photovoltaics. *J. Am. Chem. Soc.* **130,** 16770–16777 (2008).

30. Akhavan, V. A., Panthani, M. G., Goodfellow, B. W., Reid, D. K. & Korgel, B. A. Thickness-limited performance of CuInSe2 nanocrystal photovoltaic devices. *Opt. Express* **18,** A411–A420 (2010).

31. Guo, Q. *et al.* Development of CuInSe2 Nanocrystal and Nanoring Inks for Low-Cost Solar Cells. *Nano Lett.* **8,** 2982–2987 (2008).

32. Steinhagen, C. *et al.* Synthesis of Cu2ZnSnS4 Nanocrystals for Use in Low-Cost Photovoltaics. *J. Am. Chem. Soc.* **131,** 12554–12555 (2009).

33. Guo, Q., Hillhouse, H. W. & Agrawal, R. Synthesis of Cu2ZnSnS4 Nanocrystal Ink and Its Use for Solar Cells. *J. Am. Chem. Soc.* **131,** 11672–11673 (2009).

34. Wu, Y., Wadia, C., Ma, W., Sadtler, B. & Alivisatos, A. P. Synthesis and Photovoltaic Application of Copper(I) Sulfide Nanocrystals. *Nano Lett.* **8,** 2551–2555 (2008).

35. Semonin, O. E. *et al.* Peak External Photocurrent Quantum Efficiency Exceeding 100% via MEG in a Quantum Dot Solar Cell. *Science* **334,** 1530–1533 (2011).

36. Choi, J. J. *et al.* PbSe Nanocrystal Excitonic Solar Cells. *Nano Lett.* **9,** 3749–3755 (2009).

37. Pattantyus-Abraham, A. G. *et al.* Depleted-Heterojunction Colloidal Quantum Dot Solar Cells. *ACS Nano* **4,** 3374–3380 (2010).

38. Chuang, C.-H. M., Brown, P. R., Bulović, V. & Bawendi, M. G. Improved performance and stability in quantum dot solar cells through band alignment engineering. *Nat. Mater.* **13,** 796–801 (2014).

39. Ip, A. H. *et al.* Hybrid passivated colloidal quantum dot solids. *Nat. Nanotechnol.* **7,** 577–582 (2012).

40. Nelson, J. *The Physics of Solar Cells: Photons In, Electrons Out.* (Imperial College Press, 2003).

41. Henry, C. H. Limiting efficiencies of ideal single and multiple energy gap terrestrial solar cells. *J. Appl. Phys.* **51,** 4494–4500 (1980).

42. Hanna, M. C. & Nozik, A. J. Solar conversion efficiency of photovoltaic and photoelectrolysis cells with carrier multiplication absorbers. *J. Appl. Phys.* **100,** 074510 (2006).

43. Koleilat, G. I., Wang, X. & Sargent, E. H. Graded Recombination Layers for Multijunction Photovoltaics. *Nano Lett.* **12,** 3043–3049 (2012).

44. Wang, X. *et al.* Tandem colloidal quantum dot solar cells employing a graded recombination layer. *Nat. Photonics* **5,** 480–484 (2011).

45. Beard, M. C. *et al.* Comparing Multiple Exciton Generation in Quantum Dots To Impact Ionization in Bulk Semiconductors: Implications for Enhancement of Solar Energy Conversion. *Nano Lett.* **10,** 3019–3027 (2010).

46. Binks, D. J. Multiple exciton generation in nanocrystal quantum dots – controversy, current status and future prospects. *Phys. Chem. Chem. Phys.* **13,** 12693–12704 (2011).

47. Klimov, V. I. Detailed-balance power conversion limits of nanocrystal-quantum-dot solar cells in the presence of carrier multiplication. *Appl. Phys. Lett.* **89,** 123118 (2006).

48. Panthani, M. G. *et al.* High Efficiency Solution Processed Sintered CdTe Nanocrystal Solar Cells: The Role of Interfaces. *Nano Lett.* (2013). doi:10.1021/nl403912w

49. Stolle, C. J., Panthani, M. G., Harvey, T. B., Akhavan, V. A. & Korgel, B. A. Comparison of the Photovoltaic Response of Oleylamine and Inorganic Ligand-Capped CuInSe2 Nanocrystals. *ACS Appl. Mater. Interfaces* **4,** 2757–2761 (2012).

50. Tang, J. *et al.* Colloidal-quantum-dot photovoltaics using atomic-ligand passivation. *Nat. Mater.* **10,** 765–771 (2011).

51. Brown, P. R. *et al.* Energy Level Modification in Lead Sulfide Quantum Dot Thin Films through Ligand Exchange. *ACS Nano* **8,** 5863–5872 (2014).

52. Kovalenko, M. V., Scheele, M. & Talapin, D. V. Colloidal Nanocrystals with Molecular Metal Chalcogenide Surface Ligands. *Science* **324,** 1417–1420 (2009).

53. Lee, J.-S., Kovalenko, M. V., Huang, J., Chung, D. S. & Talapin, D. V. Band-like transport, high electron mobility and high photoconductivity in all-inorganic nanocrystal arrays. *Nat. Nanotechnol.* **6,** 348–352 (2011).

54. Nag, A. *et al.* Metal-free Inorganic Ligands for Colloidal Nanocrystals: S2–, HS–, Se2–, HSe–, Te2–, HTe–, TeS32–, OH–, and NH2– as Surface Ligands. *J. Am. Chem. Soc.* **133,** 10612–10620 (2011).

55. Baumgardner, W. J., Whitham, K. & Hanrath, T. Confined-but-Connected Quantum Solids via Controlled Ligand Displacement. *Nano Lett.* **13,** 3225–3231 (2013).

56. Green, M. The nature of quantum dot capping ligands. *J. Mater. Chem.* **20,** 5797–5809 (2010).

57. Li, L., Coates, N. & Moses, D. Solution-Processed Inorganic Solar Cell Based on in Situ Synthesis and Film Deposition of CuInS2 Nanocrystals. *J. Am. Chem. Soc.* **132,** 22–23 (2010).

58. McDaniel, H., Fuke, N., Makarov, N. S., Pietryga, J. M. & Klimov, V. I. An integrated approach to realizing high-performance liquid-junction quantum dot sensitized solar cells. *Nat. Commun.* **4,** (2013).

59. Zhang, J. *et al.* PbSe Quantum Dot Solar Cells with More than 6% Efficiency Fabricated in Ambient Atmosphere. *Nano Lett.* **14,** 6010–6015 (2014).

60. Ren, S. *et al.* Inorganic–Organic Hybrid Solar Cell: Bridging Quantum Dots to Conjugated Polymer Nanowires. *Nano Lett.* **11,** 3998–4002 (2011).

61. Harvey, T. B. *et al.* Copper Indium Gallium Selenide (CIGS) Photovoltaic Devices Made Using Multistep Selenization of Nanocrystal Films. *ACS Appl. Mater. Interfaces* **5,** 9134–9140 (2013).

62. Guo, Q., Ford, G. M., Agrawal, R. & Hillhouse, H. W. Ink formulation and low-temperature incorporation of sodium to yield 12% efficient Cu(In,Ga)(S,Se)2 solar cells from sulfide nanocrystal inks. *Prog. Photovolt. Res. Appl.* **21,** 64–71 (2013).

63. Miskin, C. K. *et al.* 9.0% efficient Cu2ZnSn(S,Se)4 solar cells from selenized nanoparticle inks. *Prog. Photovolt. Res. Appl.* n/a–n/a (2014). doi:10.1002/pip.2472

64. Beard, M. c. & Ellingson, R. j. Multiple exciton generation in semiconductor nanocrystals: Toward efficient solar energy conversion. *Laser Photonics Rev.* **2,** 377–399 (2008).

65. Schaller, R. D. & Klimov, V. I. High Efficiency Carrier Multiplication in PbSe Nanocrystals: Implications for Solar Energy Conversion. *Phys. Rev. Lett.* **92,** 186601 (2004).

66. Ellingson, R. J. *et al.* Highly Efficient Multiple Exciton Generation in Colloidal PbSe and PbS Quantum Dots. *Nano Lett.* **5,** 865–871 (2005).

67. Lin, Z., Franceschetti, A. & Lusk, M. T. Size Dependence of the Multiple Exciton Generation Rate in CdSe Quantum Dots. *ACS Nano* **5,** 2503–2511 (2011).

68. Sun, J. *et al.* Generation of Multiple Excitons in Ag2S Quantum Dots: Single High-Energy versus Multiple-Photon Excitation. *J. Phys. Chem. Lett.* **5,** 659–665 (2014).

69. Stubbs, S. K. *et al.* Efficient carrier multiplication in InP nanoparticles. *Phys. Rev. B* **81,** 081303 (2010).

70. Califano, M. Direct and Inverse Auger Processes in InAs Nanocrystals: Can the Decay Signature of a Trion Be Mistaken for Carrier Multiplication? *ACS Nano* **3,** 2706–2714 (2009).

71. Luther, J. M. *et al.* Multiple Exciton Generation in Films of Electronically Coupled PbSe Quantum Dots. *Nano Lett.* **7,** 1779–1784 (2007).

72. Beard, M. C. *et al.* Multiple Exciton Generation in Colloidal Silicon Nanocrystals. *Nano Lett.* **7,** 2506–2512 (2007).

73. Padilha, L. A. *et al.* Aspect Ratio Dependence of Auger Recombination and Carrier Multiplication in PbSe Nanorods. *Nano Lett.* **13,** 1092–1099 (2013).

74. Wang, F., Wu, Y., Hybertsen, M. S. & Heinz, T. F. Auger recombination of excitons in one-dimensional systems. *Phys. Rev. B* **73,** 245424 (2006).

75. Wang, L.-W., Califano, M., Zunger, A. & Franceschetti, A. Pseudopotential Theory of Auger Processes in CdSe Quantum Dots. *Phys. Rev. Lett.* **91,** 056404 (2003).

76. Kobayashi, Y., Nishimura, T., Yamaguchi, H. & Tamai, N. Effect of Surface Defects on Auger Recombination in Colloidal CdS Quantum Dots. *J. Phys. Chem. Lett.* **2,** 1051–1055 (2011).

77. An, J. M., Franceschetti, A. & Zunger, A. The Excitonic Exchange Splitting and Radiative Lifetime in PbSe Quantum Dots. *Nano Lett.* **7,** 2129–2135 (2007).

78. Dovrat, M., Goshen, Y., Jedrzejewski, J., Balberg, I. & Sa'ar, A. Radiative versus nonradiative decay processes in silicon nanocrystals probed by time-resolved photoluminescence spectroscopy. *Phys. Rev. B* **69,** 155311 (2004).

79. Akhavan, V. A. *et al.* Colloidal CIGS and CZTS nanocrystals: A precursor route to printed photovoltaics. *J. Solid State Chem.* **189,** 2–12 (2012).

80. Repins, I. *et al.* 19·9%-efficient ZnO/CdS/CuInGaSe2 solar cell with 81·2% fill factor. *Prog. Photovolt. Res. Appl.* **16,** 235–239 (2008).

81. Akhavan, V. A. *et al.* Influence of Composition on the Performance of Sintered Cu(In,Ga)Se2 Nanocrystal Thin-Film Photovoltaic Devices. *ChemSusChem* **6,** 481–486 (2013).

82. Guo, Q., Ford, G. M., Hillhouse, H. W. & Agrawal, R. Sulfide Nanocrystal Inks for Dense Cu(In1−xGax)(S1−ySey)2 Absorber Films and Their Photovoltaic Performance. *Nano Lett.* **9,** 3060–3065 (2009).

Chapter 2: Synthesis and Device Performance of Size-Controlled $CuInSe_2$ Nanocrystal Quantum Dots†

2.1 INTRODUCTION

Colloidal quantum dots (QDs) are interesting materials for photovoltaic devices (PVs) due to their unique properties, like size-tunable optical gap, enhanced absorption cross-section, extended carrier lifetimes, and solution processability.[1–3] PbS and PbSe QD PVs have been made with relatively high power conversion efficiencies (PCE) of over 8%,[4–6] and high external quantum efficiency (EQE) of over 100% EQE due to multiple exciton generation, which appears to occur commonly in QDs, including Si.[7–13] A major limitation of Pb-chalcogenide QD-based PVs, however, appears to be midgap carrier trapping that severely limits the open circuit voltage.[14,15]

Higher device PCEs have been achieved by sintering nanocrystals of CdTe, $Cu(In,Ga)S_2$, $Cu(In,Ga)Se_2$, and Cu_2ZnSnS_4.[16–21] Sintering, however, requires significant energy input, especially in the case of CIGS-related nanocrystals that require selenization at temperatures in excess of 500^{o}C, which leads to significant increase in processing cost and complexity. Unsintered films of colloidal nanocrystals have also been explored including PbSe,[4] PbS,[6] CdSe,[22] and I-III-VI_2 materials such as $Cu(In_xGa_{1-x})Se_2$ (CIGS),[23] $CuIn(S,Se)_2$,[24] and Cu_2ZnSnS_4 (CZTS).[25]

† Reproduced in part with permission from: Panthani, Matthew G.; Stolle, C. Jackson; Reid, Dariya K.; Rhee, DongJoon; Harvey, Taylor B.; Akhavan, Vahid A.; Yu, Yixuan; Korgel, Brian A., $CuInSe_2$ Quantum Dot Solar Cells with High Open-Circuit Voltage, *J. Phys. Chem. Lett.* (2013), **4**, 2030-2034. Copyright 2013 American Chemical Society. MGP designed the initial experiments, developed the synthesis procedure, analyzed the results, and wrote the manuscript. CJS synthesized and characterized the range of nanocrystals sizes reported, fabricated and tested photovoltaic devices, assisted with data analysis, and assisted in writing the manuscript. DKR and DR assisted with nanocrystal synthesis. TBH and VAA assisted with materials characterization. BAK provided funding, guidance, and assisted with writing the manuscript.

A number of approaches have been developed to synthesize I-III-VI_2 nanocrystals, such as $CuInSe_2$.[20,23,26–28] One method involves reacting metal salts or complexes (such as halides, acetates, or acetylacetonates) with chalcogen powder or tertiary phosphine chalcogenides and oleylamine as a capping ligand. Depending on the precursors or reaction conditions, this approach can yield sphalerite, chalcopyrite, or ordered-vacancy Cu-In-Se nanocrystals.[29] Wurtzite phase nanocrystals have also been made.[30] In general, this approach yields larger non-quantum confined nanocrystals with band gap of the bulk semiconductor.

An approach to I-III-VI_2 nanocrystals that provides more size control has been the use of alkanethiols as a sulfur source and capping ligand. For example, Cu and In precursors are heated in the presence of an alkanethiol like dodecanethiol, which begin to react when heated to over 180°C. Se can be added as a tertiary phosphine selenide. Using this approach, quantum-size $CuInS_2$ and $CuInSe_xS_{2-x}$ nanocrystals have been synthesized with size-tunable absorbance and photoluminescence and have been used for *in vivo* bioimaging and as sensitizers in QD-sensitized solar cells.[24,31–33]

Here, we report a new synthesis for oleylamine-capped $CuInSe_2$ (CISe) QDs. Diphenylphosphine selenide (DPP:Se) was found to be much more reactive than Se sources of tertiary phosphine selenides, trioctylphosphine selenide and tributylphosphine selenide. The use of DPP:Se in turn leads to significantly higher conversion of precursor to nanocrystals and the ability to more accurately control nanocrystal size by carrying out reactions at lower temperatures than possible using tertiary phosphine selenides. This enables the synthesis of CISe QDs without the use of thiol or S incorporation to limit the size. PV devices were then made without heat or chemical treatment of the nanocrystal layer in a glass/Au/CISe QD/CdS/ZnO/ITO configuration.

2.2 EXPERIMENTAL METHODS

2.2.1 Materials

Oleylamine (OLA) was purchased from TCI America or Corsitech; copper (I) chloride (CuCl; 99.99+%), gallium (III) chloride ($GaCl_3$; 99.999+%), selenium powder (Se; 99.99%), diphenylphosphine (DPP, 98%), and cadmium sulfate ($CdSO_4$; 99.999%) from Aldrich Chemical Co.; indium (III) chloride ($InCl_3$; 99.999%) from Strem Chemicals; ammonium hydroxide (18M NH_3; ACS certified), toluene (99.99%), ethanol (absolute), and nitric acid (trace metal grade).) from Fischer Scientific; and thiourea (> 99.0%) from Sigma-Aldrich. Prior to use, oleylamine was degassed overnight under vacuum at 110°C. All other chemicals were used as received without further purification. Copper (I) chloride, indium (III) chloride, diphenylphosphine, and degassed oleylamine were stored in a N_2-filled glovebox.

2.2.2 $CuInSe_2$ Quantum Dot Synthesis

In a N_2-filled glove box, 1 mmol of CuCl, 1 mmol of $InCl_3$, and 10 mL degassed OLA were loaded into a 3 neck flask. DPP:Se solution was made by mixing 2 mmol each of Se powder and DPP and diluting with 5mL OLA. The flask was sealed with septa, removed from the glovebox, and attached to a Schlenk line equipped with a stir plate and a heating mantle. The reaction mixture was stirred and heated to 110°C under vacuum for a 30 minute period, forming a yellow solution. It was then blanketed with nitrogen and heated to a desired injection temperature (between 100 and 180°C). When the solution stabilized at the injection temperature, the DPP:Se solution was injected and the reaction proceeded for one hour. To make larger nanocrystals, an injection temperature of 180°C was used, and then the flask was heated to higher temperature.

Injection temperatures of over 180°C were not used because the Cu and In precursors decomposed, forming a cloudy brown solution. After one hour, the nanocrystals were precipitated with excess ethanol and centrifuged at 4000 rpm for 2 min. The supernatant was discarded and the precipitate was redispersed with a minimal amount of toluene, usually about 5 mL. The dispersion was centrifuged at 4000 rpm for 1 min to precipitate poorly-capped nanocrystals. The supernatant was transferred to a centrifuge tube. Ethanol was added dropwise until the mixture became slightly turbid. After centrifugation at 4000 rpm for 1 min, the supernatant was discarded and the precipitate was dispersed in toluene. The nanocrystal dispersion was stored in a N_2-filled glovebox.

2.2.3 Device Fabrication

A layer of CISe QDs approximately 200 nm thick was spray cast from a 20 mg mL^{-1} dispersion in toluene onto a patterned Au electrode on a glass substrate. A ~10 nm layer of CdS was then deposited using a chemical surface deposition technique developed by McCandless and Shafarman.[34] After depositing the CISe QD layer, the substrates were placed on a hotplate set to 90°C and covered with a glass petri dish. The substrates were allowed to heat for 10 minutes. Aqueous stock solutions of 0.015M $CdSO_4$, 1.5M thiourea, and ~18M NH_4OH were used. To prepare the solution for chemical surface deposition, 0.22 ml $CdSO_4$ solution, 0.22 mL thiourea solution, 0.28 mL NH_4OH, and 1.5 mL H_2O were combined and chilled in an ice bath if storing for more than 10 minutes to prevent homogenous nucleation of CdS particles. The dish was removed and 700 µL of the solution was dispensed on each of the substrates (25 mm x 25mm). The petri dish was reapplied and the deposition was allowed to proceed for 2 min at which the substrates were removed from the hotplate, thoroughly rinsed with DI water, and blown

dry with a stream of clean air. Top window layers of 50 nm of ZnO and 600 nm of indium tin oxide (ITO) were deposited by sputtering (sputtered ZnO: 99.9 % Lesker, 5 ppm O_2 in Ar; sputtered ITO:99.99 % Lesker, ultrahigh purity Ar) through shadow masks so that the active area of the device (defined by the electrode overlap) was 8 mm^2 (a 4×2 mm rectangle), which was confirmed by optical microscopy.

2.2.4 Characterization Techniques

Current-voltage (IV) characteristics were collected using a Keithley 2400 general purpose source meter and a Xenon lamp solar simulator (Newport) equipped with an AM1.5G filter. The light source intensity was calibrated using a Si photodiode (Hamamatsu, S1787-08) with certification traceable to NIST. External quantum efficiency (EQE) was measured using monochromatic light generated using a commercial monochromator (Newport Cornerstone 260 1/4M) chopped at 213 Hz and focused to a spot size of 1 mm diameter on the active region. EQE measurements were made with the device at zero bias at wavelengths ranging from 300 and 1300 nm in 10 nm increments using a lock-in-amplifier (Stanford Research Systems, model SR830). Light intensity was calibrated using calibrated photodiodes of silicon (Hamamatsu) and germanium (Judson).

Inductive coupled plasma mass spectroscopy (ICP-MS) data was acquired with an Agilent 7500ce Quadrupole ICP-MS. A known fraction of CIS nanocrystal solution in toluene was dried and were digested in 70 wt% nitric acid. The resulting solution was diluted with 2 wt% nitric acid such that the concentration of Cu and In atoms would be between 1 and 100 ppm.

XRD was collected on a Rigaku R-Axis Spider diffractometer equipped with a Bruker Sol-X Si(Li) solid state detector and 1.54 Å radiation (Cu K_α). Data were

collected at 0.01 increments of 2θ at a scan rate of 6°/min. Transmission electron microscope (TEM) images were collected with a FEI Tecnai G2 Spirit BioTwin microscope operating at 80 kV.

2.3 RESULTS AND DISCUSSION

2.3.1 Nanocrystal Characterization

Figure 2.1 shows TEM images of CISe QDs produced by arrested precipitation using DPP:Se reactant. The nanocrystal size depended on the reaction temperature, with 100°C producing the smallest nanocrystals of diameter near 1 nm and 240°C yielding the largest nanocrystals studied here of 6.6 nm diameter. As shown in Figure 2.1f, X-ray diffraction (XRD) of all of the nanocrystals matched chalcopyrite $CuInSe_2$, with the expected peak broadening with decreasing nanocrystal size.

The secondary phosphine selenide reactant, DPP:Se, was found to yield significantly higher amounts of nanocrystals than the tertiary phosphine selenide, TBP:Se. Under similar reaction conditions, DPP:Se gives typical conversions of metal precursor to nanocrystals of 85% compared to only 15% when TBP:Se is used. The increase in reactant conversion using secondary phosphine selenide is similar to what has been found for PbSe nanocrystals. Evans, et al.[35] for example first showed that secondary phosphine impurities in trioctylphosphine are actually the predominant reactive species in the synthesis. When they used pure DPP:Se as the Se precursor, the reaction yield was significantly higher and the synthesis could be carried out at lower temperature than when the tertiary phosphine selenide was used. In the case of CISe QDs, the lower synthesis temperature enabled by DPP:Se enabled nanocrystals in the quantum size range to be synthesized.

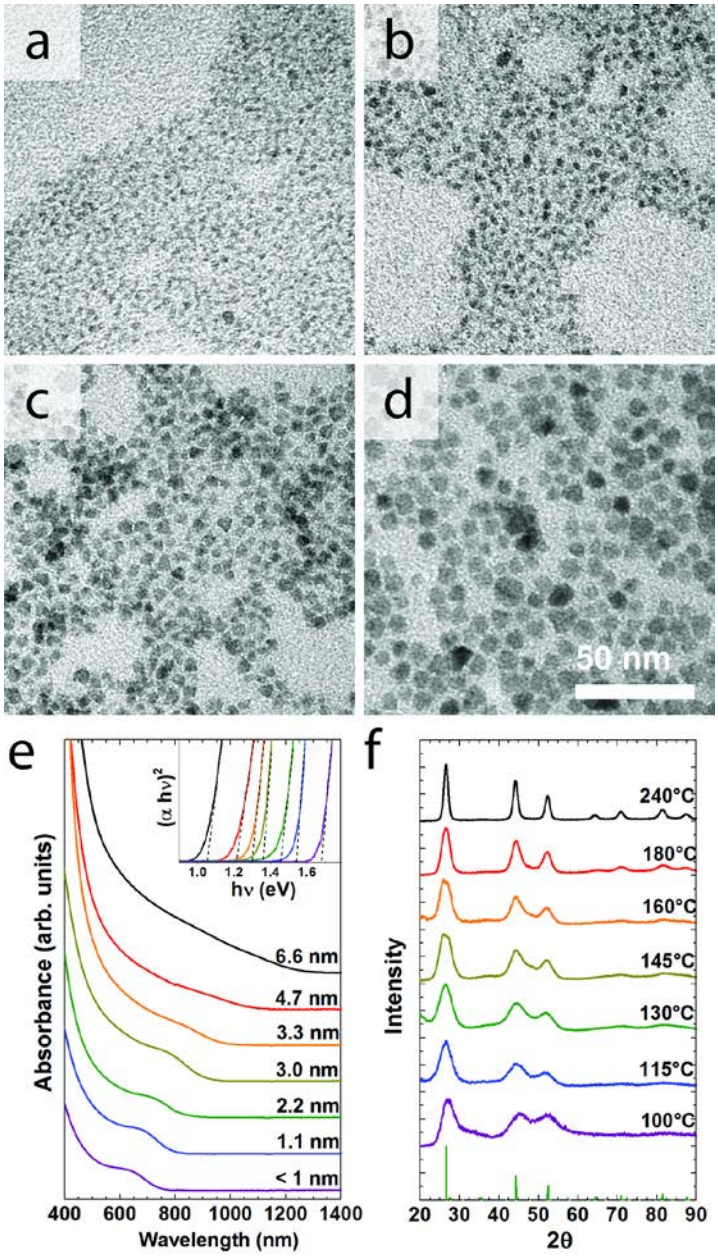

Figure 2.1 TEM images of CISe QDs synthesized at (A) 130°C, (B) 160°C, (C) 180°C, and (D) 240°C. The average QD diameters are 2.2, 3.3, 4.7, and 6.6 nm, respectively. (E) Absorbance spectra and (F) XRD (λ=1.54 Å) of nanocrystals synthesized at temperatures between 100°C and 240°C (<1 nm to 6.6 nm diameter). Inset in (E) shows Tauc plots used to determine the absorption edge reported in Table 1. The reference XRD pattern in (F) (green bars) for chalcopyrite $CuInSe_2$ is from JCPDS #97-006-8917.

The optical gap determined from absorbance spectra (Figure 2.1E) decreased in wavelength with decreasing size due to quantum confinement. Furthermore, nanocrystals smaller than 5 nm diameter exhibited exciton peaks, similar to QDs of other I-III-VI_2 materials and CZTS.[24,32,33,36] The optical absorption edges of the QDs determined by extrapolation of Tauc plots (Figure 2.1E, inset) varied over a wide range, from 1.65 eV (100°C) to 1.05 eV (240°C)—the optical gap of the largest nanocrystals was close to the bulk bandgap of $CuInSe_2$ (0.95-1.05 eV).

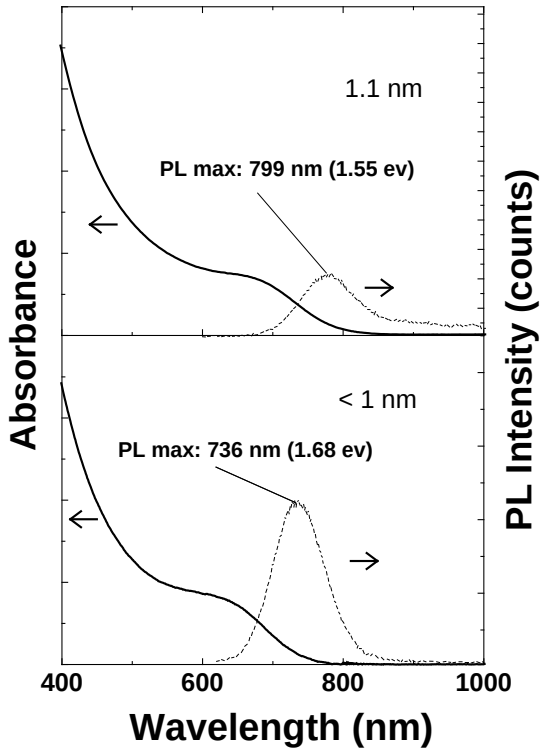

Figure 2.2 Absorbance and photoluminescence spectra of CIS QDs synthesized at 100°C (< 1 nm diameter) and 115°C (1.1 nm diameter). The PL maxima (< 1 nm:1.68, 1.1 nm: 1.55 eV) match well with that determined by Tauc analysis (1.65 and 1.54 eV, respectively).

The CISe QDs also exhibited size-dependent photoluminescence (PL) (Figure 2.2). The smallest nanocrystals exhibited PL maxima at ~735 nm (1.68 eV) and 800 nm (1.55 eV), matching the absorption edge energies determined from the Tauc analysis (1.65 and 1.54 eV, respectively). Slightly larger QDs with diameters of 2 to 3.3 nm showed weak PL with broadened PL peaks due to the presence of some smaller diameter QDs. QDs with diameter larger than 3.3 nm showed no detectable PL between 600 and 1200 nm.

2.3.2 Photovoltaic Device Analysis

Solar cells of CISe QDs were fabricated by spray-coating under ambient conditions into a glass/Au/CISe QD/CdS/ZnO/ITO structure illustrated in Figure 2.3A. Figure 2.3B shows the current-voltage characteristics of CISe QD devices illuminated under AM1.5 (100 mW/cm^2) solar simulation. There is a trend of increasing open circuit voltage (V_{oc}) and decreasing short circuit current (J_{sc}) with decreasing QD diameter. Device PCEs range from 0.3% to 1.2%. Figure 2.3C plots J_{sc}, V_{oc}, fill factor (FF) and power conversion efficiency (PCE) of devices compared to the optical gap of the CISe QDs. Relatively low J_{sc} values likely result from poor charge transport between nanocrystals due to the oleylamine capping ligands. Both FF and J_{sc} decrease with decreasing QD diameter, most likely due to the increasing volume fraction of oleylamine in the QD films inhibiting charge transport. V_{oc}, however, increases substantially with decreasing QD size, consistent with the larger optical gap of the nanocrystals. The highest V_{oc} observed was 849 mV, which to our knowledge is the highest reported V_{oc} obtained to date in any QD solar cell. The ratios of V_{oc} to optical gap ($E_{g,opt}$) are higher than PbS and CdSe-based QD solar cells reported in literature,[22,37] reaching as high as

76% of the theoretical maximum V_{oc} for the CISe QDs with 1.45 eV optical gap. Figure 2.4 shows the ratio of the maximum theoretical open circuit voltage to the measured open circuit voltage of CISe QD PVs compared to other studies of nanocrystal PVs with high open circuit voltage.

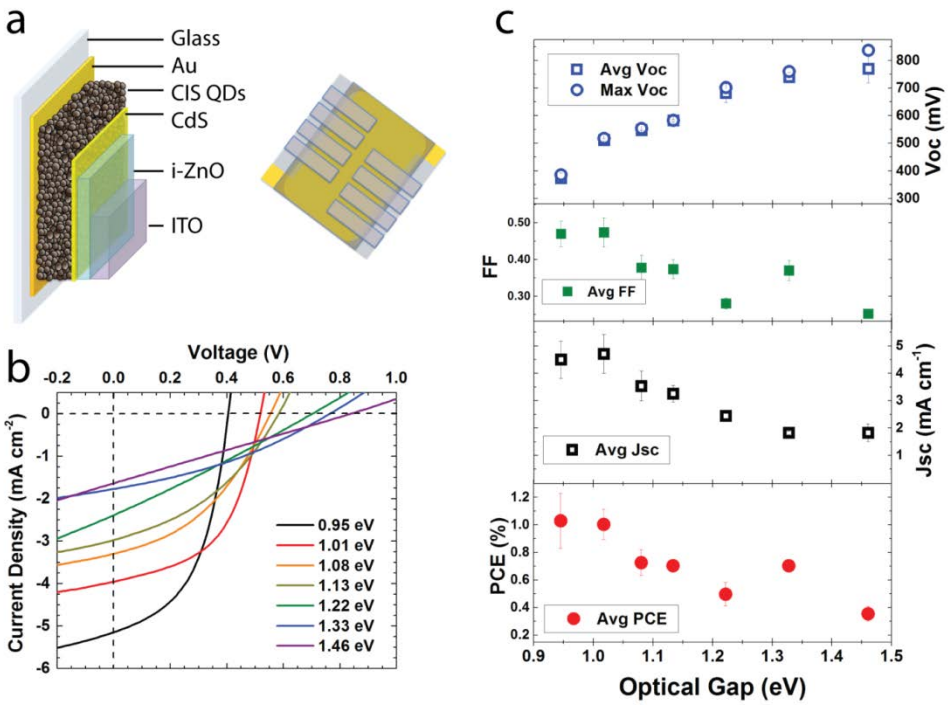

Figure 2.3 (A) Illustration of the cross section and top-view of a CISe QD solar cell. (B) *J-V* characteristics and (C) summary of device parameters (PCE, J_{sc}, FF, and V_{oc}) of solar cells versus the optical gap of the CISe QDs under AM1.5 illumination (100 mW/cm^2).

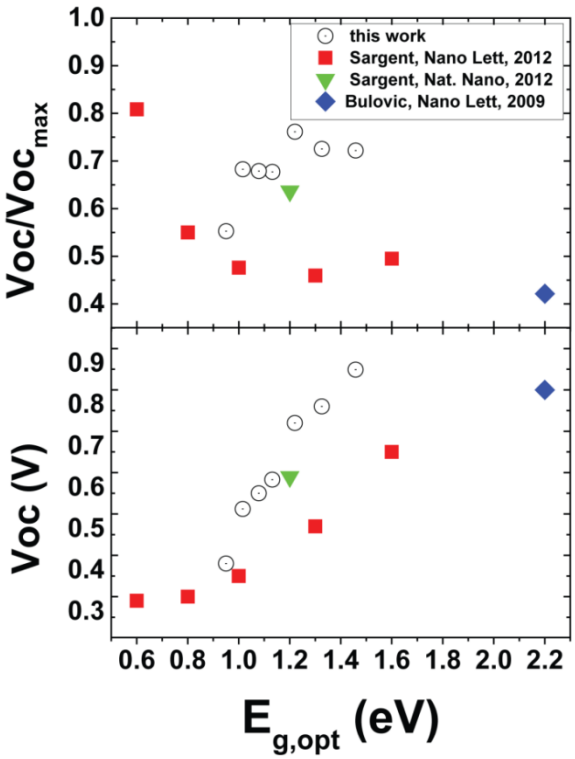

Figure 2.4 Fraction of maximum theoretical open circuit voltage (top) and reported open circuit voltages (bottom) in this work and other works demonstrating high open circuit voltages.[5,22,37] Theoretical maximum open circuit voltage is determined by formula described by C.H. Henry.[38]

2.3.3 Comparison of Electronic and Optical Band Gaps

The external quantum efficiency (EQE), or incident photon-to-current conversion efficiency (IPCE), was also measured for PVs made with CISe QDs of varying size. The absorption edge observed in the EQE measurements shifts systematically to lower wavelength with decreasing size, consistent with quantum confinement and the absorbance spectroscopy measurements. Also, the EQE generally decreased as the QD size decreased (Figure 2.5A), most likely from a combination of decreased absorbance with smaller size (i.e., because of the shift in absorption edge and the relatively low

density of states near the band edge) and the poorer charge transport between smaller QDs. A relatively large (~200 meV) redshift of the absorption edge was also observed in the EQE measurements compared to the optical gap measured from the absorbance spectra of the dispersions (Figure 2.5B). Table 2.1 compares the absorption edges of the CISe QDs determined by absorbance spectroscopy of toluene dispersions and observed from the EQE measurements.

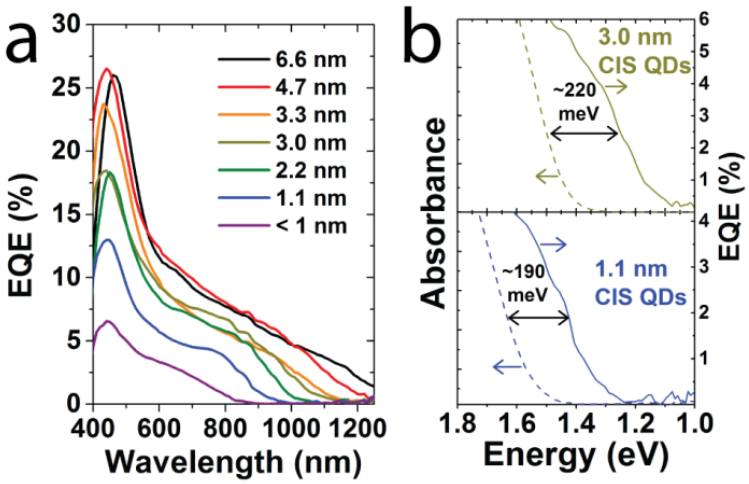

Figure 2.5 (a) EQE measurements of solar cells of solar cell made from CISe QDs. The average QD diameter in each device is shown in the inset. (b) Comparison of the absorbance spectra of dispersed nanocrystals in toluene (dashed) and the PV EQE (solid) of 3.0 (top) nm and 1.1 nm (bottom) CISe QDs.

Synthesis Temperature	100°C	115°C	130°C	145°C	160°C	180°C	240°C
QD diameter (nm)	< 1	1.1±0.4	2.2±.0.5	3.0±0.5	3.3±0.6	4.7±0.8	6.6±1.5
Dispersion absorption edge (eV)	1.65	1.54	1.45	1.34	1.30	1.21	1.05
EQE absorption edge (eV)	1.46	1.33	1.22	1.13	1.08	1.01	0.95

Table 2.1 Absorption onsets of CISe QDs determined by absorbance spectroscopy of dispersions in toluene and from EQE measurements of PVs. The nanocrystal diameter was determined by TEM.

PbS and PbSe QD solar cells have had much smaller (~10-20 meV) differences between their solvent dispersion absorbance spectra and EQE absorption edge measured from PVs,[39] which have been attributed to slight differences in dielectric environment. In the case of these CISe QD solar cells, the difference in absorption edge is too large to be simply due to differences in the dielectric environment. The difference in absorption edge appears to be related to relatively poor capping of the CISe QDs. Although oleylamine ligands are not intentionally removed during device fabrication, dispersions stored under ambient conditions lose colloidal stability within only a few hours of storage in air indicating that the capping is not very robust. The relatively poor passivation could allow QDs to approach close enough for interparticle coupling to occur. The observed size-dependence of the EQE absorption edge indicates that there is not a significant change in particle size, which would occur if the QDs were sintering. Redshifts of up to 120 meV have been reported in thiocyanate-capped PbSe nanocrystals annealed at 250°C;[40] however, the CISe QD films are not thermally treated and remain mostly coated with oleylamine, so a ~200 meV redshift simply due to coupling between QDs is

unlikely. One possibility is that neighboring CISe QDs develop shallow defect levels upon close approach when passivating ligands are removed. These states could create such a redshift in the absorption edge.

2.4 CONCLUSIONS

In summary, we show that for CISe QD synthesis, secondary phosphine selenide precursor (DPP:Se) shows much higher reactivity compared to tertiary phosphine selenides, leading to a significant increase in product yield and the ability to react at relatively low (100-180°C) temperatures enabling the synthesis of nanocrystals small enough for quantum confinement and enabling the tuning of CISe QD optical gap from 1.65 eV to about 1.0 eV. In solar cells, these QDs exhibit exceptionally high open circuit voltages without any additional surface modification. We observe that EQE of solar cells show a large (~200 meV) shift in bandgap compared to the nanocrystals in toluene solution. This could arise from the formation of shallow defect levels due to poor ligand passivation. For CISe QD solar cells that were tested, the V_{oc} reached 60-75% of the theoretical maximum V_{oc}. This compares favorably to PbS QD solar cells, which to date have achieved 50-65% of the theoretical maximum V_{oc}. The high V_{oc} indicates that if poor passivation leads to defect levels, these levels are shallow—i.e., midgap trapping does not occur. The devices exhibit low short circuit currents, partially due to the fact that they are too thin to absorb all light, but also likely due to poor charge transport within the film. Because these nanocrystals show high V_{oc} with low diffusion length, these QDs might be ideal for infiltration into mesoporous scaffolds, as in a QD-sensitized solar cell architecture.

2.5 REFERENCES

1. Murray, C. B., Norris, D. J. & Bawendi, M. G. Synthesis and characterization of nearly monodisperse CdE (E = sulfur, selenium, tellurium) semiconductor nanocrystallites. *J. Am. Chem. Soc.* **115**, 8706–8715 (1993).

2. Panthani, M. G. & Korgel, B. A. Nanocrystals for Electronics. *Annu. Rev. Chem. Biomol. Eng.* **3**, 287–311 (2012).

3. Stolle, C. J., Harvey, T. B. & Korgel, B. A. Nanocrystal photovoltaics: a review of recent progress. *Curr. Opin. Chem. Eng.* **2**, 160–167 (2013).

4. Luther, J. M. *et al.* Schottky Solar Cells Based on Colloidal Nanocrystal Films. *Nano Lett.* **8**, 3488–3492 (2008).

5. Ip, A. H. *et al.* Hybrid passivated colloidal quantum dot solids. *Nat. Nanotechnol.* **7**, 577–582 (2012).

6. Chuang, C.-H. M., Brown, P. R., Bulović, V. & Bawendi, M. G. Improved performance and stability in quantum dot solar cells through band alignment engineering. *Nat. Mater.* **13**, 796–801 (2014).

7. Semonin, O. E. *et al.* Peak External Photocurrent Quantum Efficiency Exceeding 100% via MEG in a Quantum Dot Solar Cell. *Science* **334**, 1530–1533 (2011).

8. Ellingson, R. J. *et al.* Highly Efficient Multiple Exciton Generation in Colloidal PbSe and PbS Quantum Dots. *Nano Lett.* **5**, 865–871 (2005).

9. Murphy, J. E. *et al.* PbTe Colloidal Nanocrystals: Synthesis, Characterization, and Multiple Exciton Generation. *J. Am. Chem. Soc.* **128**, 3241–3247 (2006).

10. Luther, J. M. *et al.* Multiple Exciton Generation in Films of Electronically Coupled PbSe Quantum Dots. *Nano Lett.* **7**, 1779–1784 (2007).

11. Beard, M. C. *et al.* Multiple Exciton Generation in Colloidal Silicon Nanocrystals. *Nano Lett.* **7**, 2506–2512 (2007).

12. Stolle, C. J. *et al.* Multiexciton Solar Cells of CuInSe2 Nanocrystals. *J. Phys. Chem. Lett.* **5**, 304–309 (2014).

13. Stolle, C. J., Schaller, R. D. & Korgel, B. A. Efficient Carrier Multiplication in Colloidal CuInSe2 Nanocrystals. *J. Phys. Chem. Lett.* 3169–3174 (2014). doi:10.1021/jz501640f

14. Tang, J. *et al.* Quantum Dot Photovoltaics in the Extreme Quantum Confinement Regime: The Surface-Chemical Origins of Exceptional Air- and Light-Stability. *ACS Nano* **4**, 869–878 (2010).

15. Nagpal, P. & Klimov, V. I. Role of mid-gap states in charge transport and photoconductivity in semiconductor nanocrystal films. *Nat. Commun.* **2**, 486 (2011).

16. Jasieniak, J., MacDonald, B. I., Watkins, S. E. & Mulvaney, P. Solution-Processed Sintered Nanocrystal Solar Cells via Layer-by-Layer Assembly. *Nano Lett.* **11**, 2856–2864 (2011).

17. Guo, Q. *et al.* Fabrication of 7.2% Efficient CZTSSe Solar Cells Using CZTS Nanocrystals. *J. Am. Chem. Soc.* **132**, 17384–17386 (2010).

18. Guo, Q., Ford, G. M., Hillhouse, H. W. & Agrawal, R. Sulfide Nanocrystal Inks for Dense Cu(In1−xGax)(S1−ySey)2 Absorber Films and Their Photovoltaic Performance. *Nano Lett.* **9**, 3060–3065 (2009).

19. Guo, Q., Hillhouse, H. W. & Agrawal, R. Synthesis of Cu2ZnSnS4 Nanocrystal Ink and Its Use for Solar Cells. *J. Am. Chem. Soc.* **131**, 11672–11673 (2009).

20. Guo, Q. *et al.* Development of CuInSe2 Nanocrystal and Nanoring Inks for Low-Cost Solar Cells. *Nano Lett.* **8**, 2982–2987 (2008).

21. Akhavan, V. A. *et al.* Influence of Composition on the Performance of Sintered Cu(In,Ga)Se2 Nanocrystal Thin-Film Photovoltaic Devices. *ChemSusChem* **6**, 481–486 (2013).

22. Arango, A. C., Oertel, D. C., Xu, Y., Bawendi, M. G. & Bulović, V. Heterojunction Photovoltaics Using Printed Colloidal Quantum Dots as a Photosensitive Layer. *Nano Lett.* **9**, 860–863 (2009).

23. Panthani, M. G. *et al.* Synthesis of CuInS2, CuInSe2, and Cu(InxGa1-x)Se2 (CIGS) Nanocrystal 'Inks' for Printable Photovoltaics. *J. Am. Chem. Soc.* **130**, 16770–16777 (2008).

24. McDaniel, H., Fuke, N., Pietryga, J. M. & Klimov, V. I. Engineered CuInSexS2–x Quantum Dots for Sensitized Solar Cells. *J. Phys. Chem. Lett.* 355–361 (2013). doi:10.1021/jz302067r

25. Steinhagen, C. *et al.* Synthesis of Cu2ZnSnS4 Nanocrystals for Use in Low-Cost Photovoltaics. J. Am. Chem. Soc. 131, 12554–12555 (2009).

26. Akhavan, V. A. *et al.* Spray-deposited CuInSe2 nanocrystal photovoltaics. *Energy Environ. Sci.* **3**, 1600 (2010).

27. Koo, B., Patel, R. N. & Korgel, B. A. Synthesis of CuInSe2 Nanocrystals with Trigonal Pyramidal Shape. *J. Am. Chem. Soc.* **131**, 3134–3135 (2009).

28. Zhong, H. *et al.* Colloidal CuInSe2 Nanocrystals in the Quantum Confinement Regime: Synthesis, Optical Properties, and Electroluminescence. *J. Phys. Chem. C* **115**, 12396–12402 (2011).

29. Allen, P. M. & Bawendi, M. G. Ternary I−III−VI Quantum Dots Luminescent in the Red to Near-Infrared. *J. Am. Chem. Soc.* **130**, 9240–9241 (2008).

30. Koo, B., Patel, R. N. & Korgel, B. A. Wurtzite−Chalcopyrite Polytypism in CuInS2 Nanodisks. *Chem. Mater.* **21**, 1962–1966 (2009).

31. Li, L. *et al.* Efficient Synthesis of Highly Luminescent Copper Indium Sulfide-Based Core/Shell Nanocrystals with Surprisingly Long-Lived Emission. *J. Am. Chem. Soc.* **133**, 1176–1179 (2011).

32. Cassette, E. *et al.* Synthesis and Characterization of Near-Infrared Cu−In−Se/ZnS Core/Shell Quantum Dots for In vivo Imaging. *Chem. Mater.* **22**, 6117–6124 (2010).

33. Pons, T. *et al.* Cadmium-Free CuInS2/ZnS Quantum Dots for Sentinel Lymph Node Imaging with Reduced Toxicity. *ACS Nano* **4**, 2531–2538 (2010).

34. McCandless, B. E. & Shafarman, W. N. Chemical surface deposition of ultra-thin semiconductors. (2003). at <http://www.google.com/patents/US6537845>

35. Evans, C. M., Evans, M. E. & Krauss, T. D. Mysteries of TOPSe Revealed: Insights into Quantum Dot Nucleation. *J. Am. Chem. Soc.* **132**, 10973–10975 (2010).

36. Khare, A., Wills, A. W., Ammerman, L. M., Norris, D. J. & Aydil, E. S. Size control and quantum confinement in Cu2ZnSnS4 nanocrystals. *Chem. Commun.* **47**, 11721–11723 (2011).

37. Tang, J. *et al.* Quantum Junction Solar Cells. *Nano Lett.* **12**, 4889–4894 (2012).

38. Henry, C. H. Limiting efficiencies of ideal single and multiple energy gap terrestrial solar cells. *J. Appl. Phys.* **51**, 4494–4500 (1980).

39. Law, M. *et al.* Determining the Internal Quantum Efficiency of PbSe Nanocrystal Solar Cells with the Aid of an Optical Model. *Nano Lett.* **8**, 3904–3910 (2008).

40. Choi, J.-H. *et al.* Bandlike Transport in Strongly Coupled and Doped Quantum Dot Solids: A Route to High-Performance Thin-Film Electronics. *Nano Lett.* **12**, 2631–2638 (2012).

Chapter 3: Inorganic Ligand-Capped $CuInSe_2$ Nanocrystal Photovoltaics‡

3.1 INTRODUCTION

There is an active search to identify semiconductor nanocrystals that can be deposited under ambient conditions to create light absorber layers in low cost, high efficiency photovoltaic devices (PVs). Semiconductor nanocrystals can be dispersed in solvents and represent an alternative to organic PV materials that may have better air- and photostability and higher performance. To date, the highest efficiency from a nanocrystal-based PV without high temperature processing is just over 8% power conversion efficiency (PCE) under AM 1.5 illumination, achieved using PbS nanocrystals.[1] PVs using nanocrystals of PbSe,[2] Cu_2S,[3] CdTe,[4,5] Cu_2ZnSnS_4,[6,7] and $Cu(In_{1-x}Ga_x)Se_2$ (CIGS)[8,9] have achieved efficiencies in the range of 1-5%. Higher device efficiencies, even exceeding 10%, have been achieved by sintering films of CdTe,[10,11] $Cu(In_{1-x}Ga_x)Se_2$,[12–14] $Cu(In_{1-x}Ga_x)S_2$,[15,16] and Cu_2ZnSnS_4[17] nanocrystals at high temperature to improve electrical transport and charge extraction from the nanocrystal layer. This high temperature processing step, however, adds significant cost and eliminates the possibility of using plastic substrates. The ideal case would be to achieve high efficiency (>10% PCE) without resorting to high temperature. One thought is that

‡ Reproduced in part with permission from: Stolle, C. Jackson; Panthani, Matthey G.; Harvey, Taylor B.; Akhavan, Vahid A.; Korgel, Brian A., Comparison of the Photovoltaics Response of Oleylamine and Inorganic Ligand-Capped $CuInSe_2$ Nanocrystals, *ACS Appl. Mater. Interface* (2012), **4**(5), 2757-2761. Copyright 2012 American Chemical Society. CJS designed the experiments, fabricated and characterized the photovoltaic devices, analyzed the results, and wrote the manuscript. MGP assisted with the experimental design, data analysis, and manuscript writing. TBH and VAA assisted with characterization and data analysis. BAK provided funding, guidance, and assistance with writing the manuscript.

the capping ligands on the nanocrystals might be engineered and optimized for efficient performance.

Nanocrystals are typically synthesized using organic capping ligands to stabilize their size and prevent aggregation, but these ligands create an insulating barrier that retards the passage of charge between particles.[18] This limits device performance in PVs with nanocrystal absorber layers.[19] Significantly enhanced carrier mobility has been reported in a few cases in nanocrystal films with the organic ligands exchanged with hydrazine[20] or pyridine[8]. Even higher carrier mobilities have been achieved by capping the nanocrystals with inorganic species;[1,20,21] for example, mobilities of more than 10 cm^2/Vs were observed in films of CdSe nanocrystals capped with metal chalcogenide complexes (MCCs), also known as chalcogenidometallate clusters (ChaMs).[22–24] Although this would appear to be promising for PVs, there have been no reports of PVs made with inorganic ligand-capped nanocrystals. If the high carrier mobilities of the inorganic ligand-capped nanocrystals are trap-related it may not be possible to use them in PVs. Therefore, we sought to determine the viability of using inorganic ligands for improving nanocrystal-based PV device efficiency.

As a benchmark, we compare the performance of oleylamine-capped $CuInSe_2$ (CIS) nanocrystal PVs with devices fabricated using CIS nanocrystals capped with inorganic MCC ligands. With oleylamine-capped CIS nanocrystals deposited under ambient conditions without high temperature post-deposition processing, we have achieved reasonable power conversion efficiencies (PCE).[19] We find that devices made from MCC-capped CIS nanocrystals exhibit similar device performance as those made with oleylamine-capped CIS nanocrystals, but using significantly thinner nanocrystal layers.

3.2 EXPERIMENTAL METHODS

3.2.1 Chemicals

Copper (I) chloride (CuCl, 99.99%), elemental selenium (Se, 99.99%), copper (II) sulfide (CuS, 99.99%), indium (III) selenide (In2Se3, 99.99%), elemental sulfur (S, 99.98%), sodium sulfide nonahydrate (Na2S·9H2O, 99.99%), cadmium sulfate (CdSO4, 99.99%), thiourea (99%), anhydrous hydrazine (98%), anhydrous toluene (99.8%), anhydrous ethanol (99.5%), and anhydrous acetonitrile (99.8%) were obtained from Aldrich; indium (III) chloride (InCl3, 99.99%) was obtained from Strem Chemical; oleylamine (>40%) was obtained from TCI America; toluene, ethanol, hexanes, and ammonium hydroxide (18M NH4OH) were obtained from Fisher Scientific. Oleylamine was degassed by pulling vacuum overnight at ~200 mTorr at 110 °C and stored in an N_2 filled glovebox before use. Anhydrous hydrazine was distilled and stored inside an N_2 filled glovebox to prevent a possible explosion. Hydrazine is a highly toxic and explosive chemical, and all work with hydrazine was conducted inside of a N_2 filled glovebox. All other chemicals were used as received.

3.2.2 $CuInSe_2$ Nanocrystal Synthesis

CIS nanocrystals were synthesized as previously described.[9] In a typical reaction, 2 mmol of CuCl, 2 mmol of $InCl_3$, 4 mmol of Se, and 20 ml of degassed oleylamine are added to a 100 ml three neck flask inside an N_2 filled glovebox. The flask is attached to a standard Schlenk line and degassed at 110 °C under vacuum for 45 minutes. The flask is then filled with nitrogen and heated to 200 °C. After 30 min, the temperature is raised to 260 °C. After 10 min, the heating mantle is removed and the reaction is allowed to cool to room temperature. The nanocrystals are washed via

centrifugation using toluene and ethanol as the solvent and anti-solvent, respectively. Poorly-capped nanocrystals are then separated from the toluene solution via centrifugation. The final nanocrystals dispersion is then transferred to a glovebox for the ligand exchange.

3.2.3 Metal Chalcogenide Complex Preparation

MCCs of metal chalcogenide anions complexed with hydrazinium ($N_2H_5^+$)[25–29] were formed by dissolving metal and chalcogen in hydrazine following the procedures of Kovalenko et al.[22]. A 0.25 M solution of $N_4H_9Cu_7S_4$ (Cu_2S-MCC) was prepared by dissolving 2.5 mmol of Cu_2S powder in 7.5 ml of hydrazine and adding 3.5 ml of 1 M S solution in hydrazine. A 0.25 M solution of $(N_2H_4)_2(N_2H_5)_2In_2Se_4$ (In_2Se_3-MCC) was prepared by dissolving 2 mmol of In_2Se_3 powder in 4 ml of hydrazine and adding 4 ml of 1 M Se solution in hydrazine. A 0.25 M solution of $(N_2H_4)_x(N_2H_5)_3(Cu_2In_2S_3Se_4)$ (CIS-MCC ligand) was prepared by mixing equal volumes of the 0.25 M In_2Se_3-MCC and 0.25 M Cu_2S-MCC solutions.

3.2.4 Oleylamine/MCC Ligand Exchange

0.25 ml of 0.25 M MCC stock solution (in hydrazine), 10 ml of hydrazine and 5 mL of CIS nanocrystals dispersed in toluene at a concentration of 200 mg/mL were combined and stirred for two days. The nanocrystals transfer from the toluene phase to the hydrazine phase. The nanocrystals were isolated from the hydrazine phase by precipitation with ~4 ml acetonitrile and centrifugation (8000 rpm, 2 min). The nanocrystals were redispersed in 5 mL of hydrazine. 5 mL of toluene is added and the

vial is mixed to remove any residual oleylamine. The hydrazine phase was again decanted and the nanocrystals washed with the acetonitrile/hydrazine antisolvent/solvent combination.

Oleylamine ligands were exchanged with S^{2-}, HS^-, and OH^- ions as described by Nag et al.[20] 0.8 g of $Na_2S{\cdot}9H_2O$ was dissolved in 20 mL of DI water. 5 mL of a toluene dispersion of CIS nanocrystals (200 mg/mL) was added to the aqueous Na_2S solution and stirred overnight. The majority of the nanocrystals transfer from the toluene phase to the water phase. The nanocrystals were precipitated by adding 20 mL of acetone and centrifuging at 8000 rpm for 3 min. The S^{2-}, HS^-, and OH^- capped (collectively, Na_2S-capped) nanocrystals were redispersed in 5 mL of DI water. Residual organics are removed by adding hexanes and decanting the mixture three times.

3.2.5 Materials Characterization

Nanocrystals were characterized by transmission electron microscopy (TEM) using either a Phillips 208 TEM operated at 80 kV accelerating voltage or a JEOL 2010F TEM at 200 kV accelerating voltage. TEM samples were prepared by drop-casting dilute nanocrystal dispersions in chloroform or water onto a 200 mesh nickel grid with a continuous carbon film (Electron Microscopy Sciences). Scanning electron microscopy (SEM) was performed on a Zeiss Supra 40 VP SEM operated at 5 keV accelerating voltage through an In-lens detector with samples grounded using copper tape.

X-ray diffraction (XRD) was performed using a Rigaku R-Axis Spider diffractometer with an image-plate detector and Cu Kα (λ=1.54 Å) radiation operated at 40 kV and 40 mA. XRD samples were prepared by drying a drop of concentrated

nanoparticle dispersion onto a glass slide in a glovebox. The nanocrystal powder was then suspended on a 0.5 mm nylon loop using mineral oil for analysis. Samples were scanned for 15 min while rotating at 2 deg/s. The 2D diffraction patterns were integrated using the Rigaku 2DP powder processing suite with subtraction of the background scattering from the nylon loop and mineral oil.

3.2.6 CIS Nanocrystal PV Device Fabrication

CIS nanocrystal PVs were fabricated with a Au/CIS/CdS/i-ZnO/indium tin oxide (ITO) device structure. A 5 nm layer of Cr followed by 60 nm of Au were thermally deposited onto soda lime glass (Delta Technologies, 25 mm x 25 mm x 1.1 mm polished float glass). Films of CIS nanocrystals were then deposited. Oleylamine-capped nanocrystals were spray deposited from toluene at room temperature as described previously.[9] Na_2S-capped nanocrystals were spray deposited from water onto substrates heated to 100 °C. MCC-capped nanocrystals dispersed in hydrazine were deposited by a spin coating procedure. A layer of MCC-capped nanocrystals was deposited by dropping 70 μL of nanocrystal/hydrazine dispersion onto the substrate and rotating at 2000 rpm for 90 seconds to dry the film. The substrate was then heated to 150 °C for 5 min prior to depositing the next layer of nanocrystals. This spin coating procedure was repeated 1-4 times. A CdS buffer layer was deposited by dropping 0.7 mL of a CdS precursor solution (1.25 ml of 15 mM CdSO4, 2.2 ml of 1.5 M thiourea, and 2.8 ml of 18 M NH_4OH in water) onto the CIS nanocrystal film heated to 80 °C on a hot plate and covered with an inverted petri dish for 2 min.[30] The substrate was removed from the hot plate, rinsed with DI water, and dried with a stream of compressed air. Top layers of i-ZnO and ITO were deposited by RF sputtering from a ZnO target (Lesker, 99.9%) in a 0.5% O_2 in Ar

atmosphere (Praxair, 99.95%) and a ITO target (Lesker, 99.99% In2O3:SnO2 90:10) in Ar atmosphere (Praxair, research grade). ZnO and ITO are deposited selectively onto 8 rectangular regions with active device areas of 0.08 cm^2. Silver paint was applied for electrical contact to the devices. Prior to the device measurements, the completed devices were placed in a vacuum oven for 10 minutes at 200 °C to improve the conductivity of the ITO.

PV device response was measured using a Keithley 2400 General Purpose Sourcemeter under solar simulation using a Newport Xenon Lamp Solar Simulator with an AM 1.5 filter. Incident photon conversion efficiency (IPCE) was measured using a home-built device with lock-in amplifier (Stanford Research Systems, model SR830) and monochromator (Newport Cornerstone 260 1/4M), and calibrated with Si and Ge photodiodes (Hamamatsu).

3.3 RESULTS AND DISCUSSION

3.3.1 $CuInSe_2$ (CIS) Nanocrystals Before and After Inorganic Ligand Exchange

Figure 3.1 shows TEM images of CIS nanocrystals made with oleylamine capping ligands before and after Na_2S and CIS-MCC ligand exchange. TEM and XRD (Figure 3.2) confirmed that the particles are crystalline before and after ligand exchange. However, the inorganic ligand-capped nanocrystals are very prone to agglomeration and are not as easily deposited into thin films as the oleylamine-capped nanocrystals. Furthermore, the CIS-MCC capped nanocrystals disperse in hydrazine, which severely limits the way the nanocrystals can be deposited onto substrates.

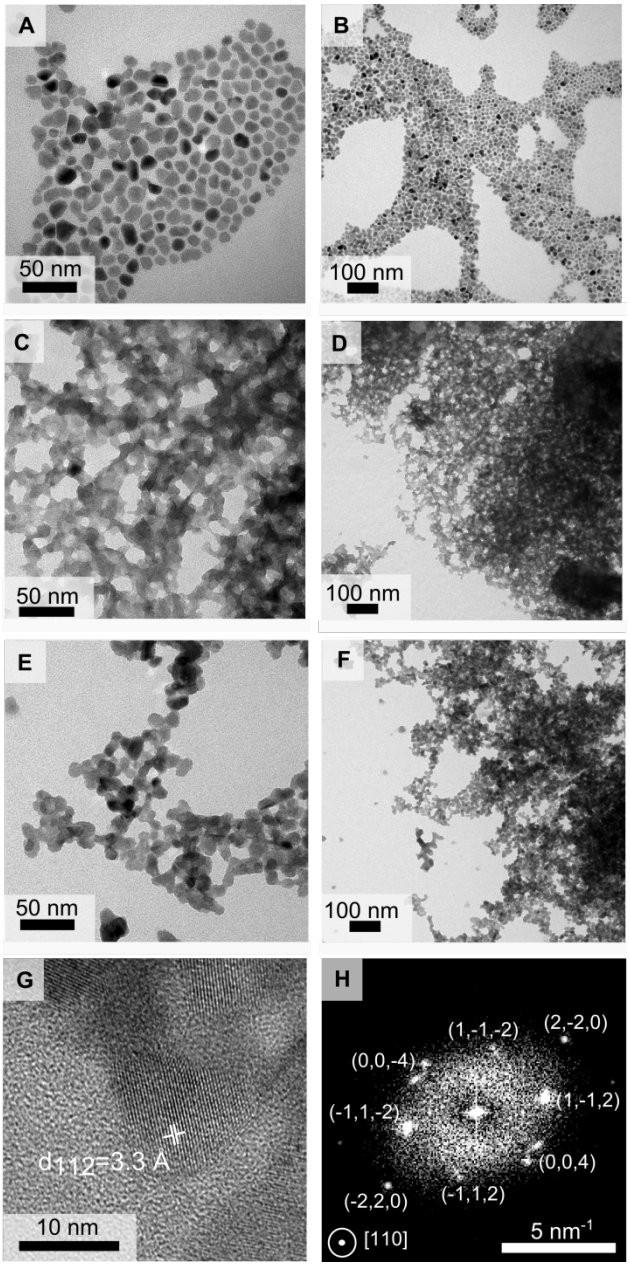

Figure 3.1 TEM images of CIS nanocrystals: (a,b) as-synthesized with oleylamine capping ligands and after ligand exchange with (c,d) Na_2S and (e,f) CIS-MCC. (g) High-resolution TEM image and (h) corresponding FFT of a CIS nanocrystal after oleylamine ligand exchange with CIS-MCC. The nanocrystal is imaged down the [110] crystallographic zone axis and the FFT is indexed to chalcopyrite CIS. The measured d-spacing is d_{112} = 3.3 Å.

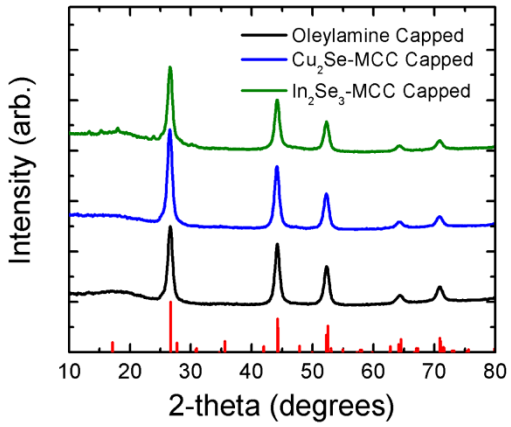

Figure 3.2 XRD patterns from CIS nanocrystals synthesized with oleylamine capping ligands before and after exchange with Cu_2S-MCC and In_2Se_4-MCC ligands. The red reference lines correspond to chalcopyrite CIS (PDF #97-006-892). The absence of the (112) peak indicates that there may be Cu and In positional disorder.

3.3.2 CIS Nanocrystal Film Deposition

For device fabrication, the oleylamine-capped CIS nanocrystals are dispersed in toluene (~20 mg/ml) and then spray-deposited into a uniform layer approximately 200 nm thick.[9] The Na_2S-capped CIS nanocrystals disperse in water and could also be spray-deposited, but the substrate needs to be heated to achieve uniform film thickness due to the low volatility of the solvent. The low solvent volatility made it difficult to deposit thicker films, and even with heating of the substrate it was not possible to increase the thickness of the Na_2S-capped CIS nanocrystal films above about 75 nm while retaining a uniform film thickness. The MCC-capped CIS nanocrystals are dispersible in hydrazine and other polar solvents, like dimethyl sulfoxide, and water. Films of MCC-capped CIS nanocrystals could be sprayed from dispersions in dimethyl sulfoxide and water, but devices using these layers performed extremely poorly. Only when the MCC-capped CIS

nanocrystals were deposited from hydrazine could PV devices with reasonable response be made. Unfortunately, nanocrystals dispersed in hydrazine cannot be spray-deposited due to the very high toxicity of hydrazine and its potential instability (i.e., explosiveness). Therefore, the MCC-capped CIS nanocrystals were spin-coated onto the device substrates, which ultimately limited the thickness of the nanocrystal films to about 75 nm.

Figure 3.3 shows SEM images of films of CIS nanocrystals capped with CIS-MCC ligands. The SEM images show that the nanocrystal film is relatively uniform in density with a nanocrystalline morphology—there is no particle sintering or grain growth due to film heating on the hot plate. The cross-sectional SEM image of a CIS-MCC-capped nanocrystal device shows the lateral uniformity of the nanocrystal film and the relative thicknesses of the device layers.

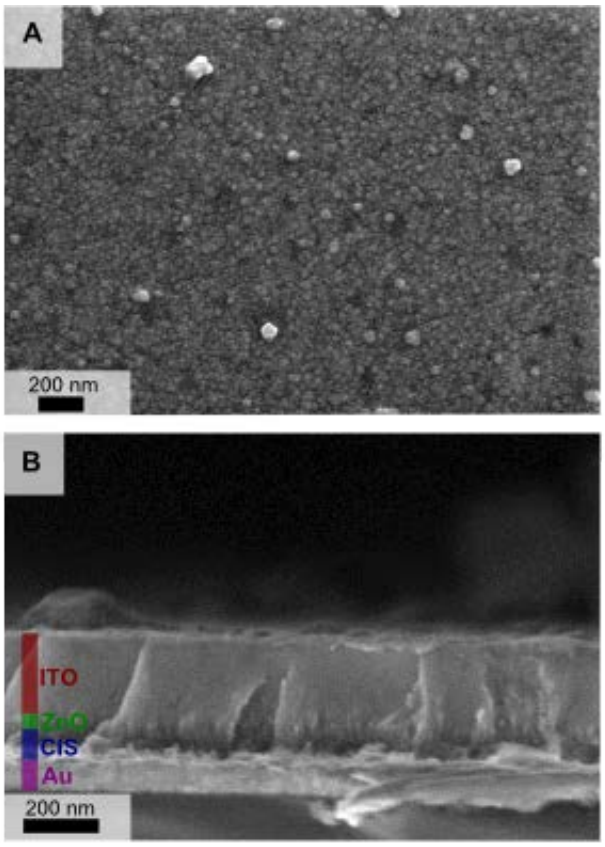

Figure 3.3 SEM images of (a) the surface of a spin-coated CIS nanocrystal film and (b) a cross-sectioned PV device with a layer of CIS-MCC ligand-capped CIS nanocrystals. The Au, CIS-MCC nanocrystal, ZnO and ITO layers are 70 nm, 75 nm, 40 nm and 200 nm thick, respectively.

3.3.3 PV Device Performance

The PV response and IPCE for devices made with oleylamine-capped, CIS-MCC ligand-capped, and Na_2S-capped CIS nanocrystals are shown in Figure 3.4. The efficiency of the best CIS-MCC ligand-capped CIS device is similar to the best oleylamine-capped CIS device. The best efficiency for a Na_2S-capped CIS device was significantly lower than the devices made with either oleylamine-capped or MCC-capped

CIS nanocrystals, but the devices worked, demonstrating that it may be possible to fabricate reasonable PV devices under ambient conditions using water as a solvent with further optimization.

The IPCE data confirm that the CIS nanocrystals are the active light-absorbing material in the device with the absorption edge extending into the near infrared towards the CIS band gap of 1.0 eV. On average, the devices made with the MCC-capped CIS nanocrystals exhibited more consistent performance with fewer shorted devices, and the series resistance R_s, of the devices was consistently lower for the devices with inorganic-capped CIS nanocrystals. Table 3.1 lists the values of R_s and the shunt resistances R_{sh}, of the best devices estimated by fitting the dark I-V curves to the diode equation,

$$I = J_0 A\left[\exp\left(\frac{V - IR_s}{nkT}\right) + \left(\frac{V - IR_s}{J_0 AR_{sh}}\right) - 1\right] \tag{3.1}$$

A is the device area, J_0 is the saturation current density under reverse bias, n is the ideality factor of the device, k is Boltzmann's constant, and T is the temperature.

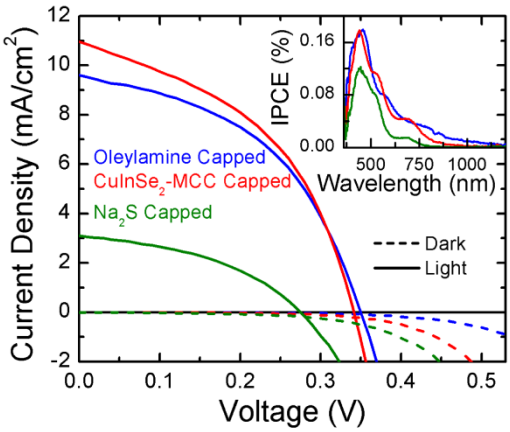

Figure 3.4 Dark and light I-V characteristics for the highest performance devices fabricated using oleylamine-capped CIS nanocrystals (blue), CIS-MCC ligand-capped CIS nanocrystals (red), and Na_2S-capped CIS nanocrystals (green). The dashed lines are the dark I-V characteristics and the solid lines are the light I-V characteristics. IPCE measurements for each device are shown in the inset.

Ligand	PCE (%)	Voc (V)	Jsc (mA/cm^2)	FF	R_s (Ω)	R_{sh} (MΩ)
Oleylamine	1.56	0.349	9.59	0.467	69.0	0.92
Cu_2S-MCC	1.42	0.396	7.76	0.461	7.65	1.00
CIS-MCC	1.68	0.340	10.96	0.450	6.46	0.36
Na_2S	0.35	0.274	3.10	0.416	11.6	0.09

Table 3.1 Characteristics of PV devices fabricated with CIS nanocrystals capped with various ligands.

Although the MCC-capped and oleylamine-capped CIS nanocrystal PVs exhibited comparable power conversion efficiency, the MCC-capped nanocrystal layers in the devices were much thinner than the oleylamine-capped nanocrystal layers, implying that

the internal quantum efficiency of the MCC-ligand capped nanocrystal devices may be higher. At the moment, we have not been able to increase the thickness of the MCC-ligand capped nanocrystals because they must be spin-coated under carefully controlled environmental conditions because of the hazardous nature of hydrazine. Additionally, these spin-coated layers are often streaky and non-uniform. The need for hydrazine represents one of the major bottlenecks to using these nanocrystals in PVs and new solvents and deposition techniques need to be explored in order to improve PV efficiency and deposit thicker, uniform films under ambient conditions.

3.4 CONCLUSIONS

The device results presented here prove that it is possible to use inorganic capping moieties for nanocrystal-based PVs. The device efficiencies are still relatively low, at about 2% PCE under AM1.5 illumination, so it is still unclear if the use of inorganic ligands will yield the needed boost in device efficiency without resorting to high temperature sintering, but undoubtedly MCC-capped nanocrystals can yield PV response. One of the biggest problems with the metal chalcogenide complexes is the need to use hydrazine as a solvent. With this limitation, it will never be possible to use these applications in commercial PVs. Therefore, the device results from the inorganic capped CIS nanocrystals using water as a solvent are encouraging, even though the performance was substantially less.

3.5 REFERENCES

1. Chuang, C.-H. M., Brown, P. R., Bulović, V. & Bawendi, M. G. Improved performance and stability in quantum dot solar cells through band alignment engineering. *Nat. Mater.* **13,** 796–801 (2014).

2. Choi, J. J. *et al.* PbSe Nanocrystal Excitonic Solar Cells. *Nano Lett.* **9,** 3749–3755 (2009).

3. Wu, Y., Wadia, C., Ma, W., Sadtler, B. & Alivisatos, A. P. Synthesis and Photovoltaic Application of Copper(I) Sulfide Nanocrystals. *Nano Lett.* **8,** 2551–2555 (2008).

4. Gur, I., Fromer, N. A., Geier, M. L. & Alivisatos, A. P. Air-Stable All-Inorganic Nanocrystal Solar Cells Processed from Solution. *Science* **310,** 462–465 (2005).

5. Olson, J. D., Rodriguez, Y. W., Yang, L. D., Alers, G. B. & Carter, S. A. CdTe Schottky diodes from colloidal nanocrystals. *Appl. Phys. Lett.* **96,** 242103 (2010).

6. Steinhagen, C. *et al.* Synthesis of Cu2ZnSnS4 Nanocrystals for Use in Low-Cost Photovoltaics. *J. Am. Chem. Soc.* **131,** 12554–12555 (2009).

7. Guo, Q., Hillhouse, H. W. & Agrawal, R. Synthesis of Cu2ZnSnS4 Nanocrystal Ink and Its Use for Solar Cells. *J. Am. Chem. Soc.* **131,** 11672–11673 (2009).

8. Panthani, M. G. *et al.* Synthesis of CuInS2, CuInSe2, and Cu(InxGa1-x)Se2 (CIGS) Nanocrystal 'Inks' for Printable Photovoltaics. *J. Am. Chem. Soc.* **130,** 16770–16777 (2008).

9. Akhavan, V. A. *et al.* Spray-deposited CuInSe2 nanocrystal photovoltaics. *Energy Environ. Sci.* **3,** 1600 (2010).

10. Jasieniak, J., MacDonald, B. I., Watkins, S. E. & Mulvaney, P. Solution-Processed Sintered Nanocrystal Solar Cells via Layer-by-Layer Assembly. *Nano Lett.* **11,** 2856–2864 (2011).

11. MacDonald, B. I. *et al.* Layer-by-Layer Assembly of Sintered CdSexTe1–x Nanocrystal Solar Cells. *ACS Nano* **6,** 5995–6004 (2012).

12. Guo, Q. *et al.* Development of CuInSe2 Nanocrystal and Nanoring Inks for Low-Cost Solar Cells. *Nano Lett.* **8,** 2982–2987 (2008).

13. Akhavan, V. A. *et al.* Influence of Composition on the Performance of Sintered Cu(In,Ga)Se2 Nanocrystal Thin-Film Photovoltaic Devices. *ChemSusChem* **6,** 481–486 (2013).

14. Harvey, T. B. *et al.* Copper Indium Gallium Selenide (CIGS) Photovoltaic Devices Made Using Multistep Selenization of Nanocrystal Films. *ACS Appl. Mater. Interfaces* **5,** 9134–9140 (2013).

15. Guo, Q., Ford, G. M., Hillhouse, H. W. & Agrawal, R. Sulfide Nanocrystal Inks for Dense Cu(In1−xGax)(S1−ySey)2 Absorber Films and Their Photovoltaic Performance. *Nano Lett.* **9,** 3060–3065 (2009).

16. Guo, Q., Ford, G. M., Agrawal, R. & Hillhouse, H. W. Ink formulation and low-temperature incorporation of sodium to yield 12% efficient Cu(In,Ga)(S,Se)2 solar cells from sulfide nanocrystal inks. *Prog. Photovolt. Res. Appl.* n/a–n/a (2012). doi:10.1002/pip.2200

17. Cao, Y. *et al.* High-Efficiency Solution-Processed Cu2ZnSn(S,Se)4 Thin-Film Solar Cells Prepared from Binary and Ternary Nanoparticles. *J. Am. Chem. Soc.* **134,** 15644–15647 (2012).

18. Talapin, D. V., Lee, J.-S., Kovalenko, M. V. & Shevchenko, E. V. Prospects of Colloidal Nanocrystals for Electronic and Optoelectronic Applications. *Chem. Rev.* **110,** 389–458 (2009).

19. Akhavan, V. A., Panthani, M. G., Goodfellow, B. W., Reid, D. K. & Korgel, B. A. Thickness-limited performance of CuInSe2 nanocrystal photovoltaic devices. *Opt. Express* **18,** A411–A420 (2010).

20. Nag, A. *et al.* Metal-free Inorganic Ligands for Colloidal Nanocrystals: S2–, HS–, Se2–, HSe–, Te2–, HTe–, TeS32–, OH–, and NH2– as Surface Ligands. *J. Am. Chem. Soc.* **133,** 10612–10620 (2011).

21. Tang, J. *et al.* Colloidal-quantum-dot photovoltaics using atomic-ligand passivation. *Nat. Mater.* **10,** 765–771 (2011).

22. Chuang, C.-H. M., Brown, P. R., Bulović, V. & Bawendi, M. G. Improved performance and stability in quantum dot solar cells through band alignment engineering. *Nat. Mater.* **advance online publication,** (2014).

23. Kovalenko, M. V., Scheele, M. & Talapin, D. V. Colloidal Nanocrystals with Molecular Metal Chalcogenide Surface Ligands. *Science* **324,** 1417–1420 (2009).

24. Kovalenko, M. V., Bodnarchuk, M. I. & Talapin, D. V. Nanocrystal Superlattices with Thermally Degradable Hybrid Inorganic−Organic Capping Ligands. *J. Am. Chem. Soc.* **132,** 15124–15126 (2010).

25. Kovalenko, M. V., Bodnarchuk, M. I., Zaumseil, J., Lee, J.-S. & Talapin, D. V. Expanding the Chemical Versatility of Colloidal Nanocrystals Capped with Molecular Metal Chalcogenide Ligands. *J. Am. Chem. Soc.* **132,** 10085–10092 (2010).

26. Mitzi, D. B., Kosbar, L. L., Murray, C. E., Copel, M. & Afzali, A. High-mobility ultrathin semiconducting films prepared by spin coating. *Nature* **428,** 299–303 (2004).

27. Mitzi, D. B. Synthesis, Structure, and Thermal Properties of Soluble Hydrazinium Germanium(IV) and Tin(IV) Selenide Salts. *Inorg. Chem.* **44,** 3755–3761 (2005).

28. Milliron, D. J., Mitzi, D. B., Copel, M. & Murray, C. E. Solution-Processed Metal Chalcogenide Films for p-Type Transistors. *Chem. Mater.* **18,** 587–590 (2006).

29. Mitzi, D. B. N4H9Cu7S4: A Hydrazinium-Based Salt with a Layered Cu7S4-Framework. *Inorg. Chem.* **46,** 926–931 (2007).

30. Yuan, M. *et al.* Controlled Assembly of Zero-, One-, Two-, and Three-Dimensional Metal Chalcogenide Structures. *Inorg. Chem.* **46,** 7238–7240 (2007).

31. McCandless, B. E. & Shafarman, W. N. Chemical surface deposition of ultra-thin semiconductors. (2003). at <http://www.google.com/patents/US6537845>

Chapter 4: $CuInSe_2$ Nanocrystal Sintering Using Photonic Curing[§]

4.1 INTRODUCTION

$Cu(In,Ga)Se_2$ (CIGS) is a promising semiconductor material for thin film photovoltaic (PV) devices, but has not made a commercial impact due to high fabrication cost compared to Si solar cells.[1,2] The fabrication cost is primarily driven by the need to process the films in vacuum conditions and at high temperature in a toxic selenium atmosphere, also known as selenization.[3] Selenization is used during CIGS film deposition during co-evaporation,[4] or as a subsequent step after physical vapor deposition (PVD) of Cu, In, and Ga metal layers.[5] To eliminate the high cost processing, $Cu(In,Ga)Se_2$ films have been fabricated using nanocrystal inks spray deposited in ambient conditions, but PV device efficiency has been limited (~3%).[6] Selenization of the nanocrystal films increases efficiency,[7] however reintroduces the high temperature selenization process. A rapid, non-toxic, roll-to-roll compatible process is needed to reduce CIGS processing cost and complexity. The use of microsecond length pulses of light, known as photonic curing, to sinter nanocrystal films at ambient pressure in a non-selenium environment is a promising route to low cost CIGS photovoltaics.

Photonic curing, also known as photonic sintering or intense pulsed light (IPL) annealing, uses short pulses of light to heat and sinter particulate films. For the treatment to be effective, the material must be a good light absorber in the wavelength range of the

[§] Parts of this chapter are adapted from: Harvey, Taylor B.; Stolle, C. Jackson; Akhavan, Vahid A.; Hibbert, Jarett I.; Pernik, Douglas R.; Du, Jiang; Korgel, Brian A., Photonic Curing of $CuInSe_2$ Nanocrystal Films for Photovoltaic Devices, *in preparation*. TBH and CJS both designed the experiments, fabricated and characterized devices, and collected and analyzed data. TBH wrote the manuscript. CJS assisted with writing the manuscript. VAA and JIH assisted with the photonic curing process. DRP and JD assisted with characterization and data analysis. BAK provided funding, guidance, and assistance with writing the manuscript.

light source. The technique has been used primarily to sinter metal nanoparticles, with both Ag[8–10] and Cu[8,11,12] nanoparticle inks demonstrating increased conductivity after treatment. Nanoparticle semiconductor films have also been treated, primarily CIGS. Sintering of CIGS nanoparticles,[13] CuInGa and Se nanoparticle mixtures,[14] and, recently, CIGS nanocrystals[15] has been carried out using photonic curing. While sintered films were reported in each of these cases, no working photovoltaics were demonstrated.

We recently reported $CuInSe_2$ nanocrystal PVs exhibiting multiple exciton generation (MEG) after being treated with photonic curing.[16] These devices were treated with mild energy pulses that did not sinter the nanocrystals, but reduced interparticle spacing allowing MEG extraction. In this work, the morphology of the nanocrystal layer and device characteristics after photonic curing with a wide range of pulse energies are investigated. Similar device performance is found using multiple back contact materials at mild pulse conditions. As the pulse energy increases, the nanocrystals begin to sinter into continuous films, and we find the pulsed film morphology is highly dependent on the back contact material. Nanocrystals on Mo back contacts exhibited dewetting and agglomeration, and the use of $MoSe_2$-coated Mo reduced this dewetting. Au back contacts also reduced dewetting, but the back contact was destroyed as pulse energy increased. At lower pulse energy, devices treated with photonic curing exhibit increased power conversion efficiency (PCE) compared to nontreated films. While efficiency decreases as pulse energy increases, working devices of sintered $CuInSe_2$ nanocrystal films are demonstrated on MoSe2-coated Mo.

4.2 EXPERIMENTAL METHODS

4.2.1 Chemicals

Copper (I) chloride (CuCl, 99.99%), elemental selenium (Se, 99.99%), diphenylphosphine (DPP, 98%) were purchased from Aldrich; oleylamine (>40%) from TCI America; indium (III) chloride ($InCl_3$, 99.99%) from Strem Chemical; toluene and ethanol from Fisher Scientific. Oleylamine (OLA) was degassed at 110°C overnight. CuCl, $InCl_3$, DPP and OLA were stored in an N_2 filled glovebox.

4.2.2 Nanocrystal Synthesis

$CuInSe_2$ nanocrystals were synthesized using reported methods.[17,16] In a N2 filled glove box, 0.198 g CuCl, 0.442 g $InCl_3$, and 20 mL degassed OLA are combined in a three neck flask, removed from the glovebox and attached to a standard Schlenk line. Concurrently, 4 mmol of Se and DPP are mixed and diluted in 2 mL of OLA to form a DPP:Se solution. The 3 neck flask is degassed by heating to 100°C while pulling vaccum for 30 min. The flask is then filled with N_2 and the temperature is raised to 180^{o}C where the DPP:Se solution is injected. The reaction mixture is then heated to 240 ^{o}C for 30 min, after which the heating mantle is removed and the reaction is allowed to cool to room temperature.

Purification of the nanocrystals is conducted by centrifugation using toluene/ethanol as solvent and antisolvent. The nanocrystals are precipitated by centrifuging at 4000 rpm for 2 min after adding 20 ml of ethanol, then redispersed in 5 ml of toluene and centrifuged to separate the poorly-capped particles. The nanocrystals are precipitated again by adding 5 ml of ethanol and centrifuging. The final solution is prepared by redispersing the nanocrystals in 5 mL of toluene

4.2.3 Nanocrystal Film Preparation

Bare glass substrates (Delta Technologies) were sonicated in 1:1 IPA/acetone for 10 minutes followed by sonication in DI water for 10 minutes. A two step rf-sputtering process was used to deposit Mo (99.95% Lesker). 400 nm of Mo was sputtered at 5 mtorr as an adhesive layer followed by 600 nm at 1.5 mtorr of highly conductive Mo. Au substrates were fabricated by thermally depositing 5 nm of Cr followed by 60 nm of Au (Kurt J. Lesker Co). Ag substrates were fabricated by thermally depositing 5 nm of Cr followed by 60 nm of Ag (Kurt J. Lesker Co). Ni substrates were fabricated by thermally depositing 100 nm of Ni (Kurt J. Lesker Co). ITO substrates (Thin Film Devices) were cleaned in the same manner as the bare glass substrates and used without further treatment. $MoSe_2$ coated Mo was prepared by converting the top 50 nm of a Mo substrate to $MoSe_2$ by annealing in an Se-rich atmosphere at 450°C for 10 minutes as previously described.[7]

$CuInSe_2$ nanocrystal films with thickness between 0.5-1 μm were deposited by spray-coating from toluene dispersions (~50 mg/mL).

4.2.4 Photonic Curing

Photonic curing was performed with a Novacentrix PulseForge 3300 using pulse energies ranging from 1 J/cm^2 to 7 J/cm^2, controlled by varying the pulse voltage with a 300 μs pulse length. The reported energy inputs were measured with a bolometer (Novacentrix BX-100). For photonic curing, substrates were loaded into a stainless steel chamber with 2” thickness and 7” diameter and a 6” diameter circular quartz window. The chamber was purged with nitrogen for one minute and sealed, then positioned under

the center of the xenon lamps and pulsed. A single light pulse with duration of 300 μs was used. After photonic curing, the chamber was opened in a fume hood.

4.2.5 Materials Characterization

A Rigaku R-Axis diffractometer was used to collect X-ray diffraction (XRD) data. A 10° glancing angle was used between graphite monochromatized Cu Kα (λ = 1.5418 Å) radiation operated at 40 kV and 40 mA was and the samples, which were rotated at 1° per second. Spectra were collected on an image-plate detector and two-dimensional diffraction patterns were radially integrated after background subtraction using 2DP V. 1.0 Data Processing Software (Rigaku). High resolution XRD over a short wavelength ranges was collected at 0.01 2 θ increments on a Bruker-Nonius D8 powder diffractometer equipped and 1.54 Å radiation (Cu Kα).

Scanning electron microscopy (SEM) was conducted using an In-lens detector and a 5 keV accelerating voltage on a Zeiss Supra VP SEM. A Quanta 650 FEG SEM equipped with a Bruker XFlash EDS Detector 5010 was used to collect Energy-dispersive X-ray spectroscopy (EDS), and maps were generated at 20 kV accelerating voltage and a working distance of 10 mm with a spot size of 5.

4.2.6 PV Device Fabrication

A CdS layer (50 nm thick) was deposited on cured $CuInSe_2$ nanocrystal films by chemical bath deposition (CBD). DI water (160 mL) was heated to 70 °C and 15 mM $Cd(SO_4)_2$ (25 mL), 1.5 M thiourea (12.5 mL), and 28 wt% ammonia hydroxide (32 mL) were added. The films were then immersed for 15 minutes. ZnO (50 nm) and ITO (600

nm) was then deposited by rf-sputter coating at 2 mtorr. Physical shadow masks were used during window layer deposition, providing an active device area of 0.08 cm^2.

Current-Voltage characteristics were measured using a Keithley 2400 general purpose source meter. The devices were illumination using a Xenon lamp solar simulator (Newport) equipped with an AM1.5G optical filter and calibrated to 100 mW/cm^2 light intensity with a NIST-calibrated Si photodiode (Hamamatsu, S1787-08).

4.3 RESULTS AND DISCUSSION

4.3.1 Photonic Curing of Nanocrystal Films on Mo Back Contacts

Photonic curing was carried out by exposing a $CuInSe_2$ nanocrystal film to a single 300 μs pulse of high-intensity light from a Xe lamp. Short pulse duration was utilized to limit total energy input and achieve the relatively low-energy, non-equilibrium, heating conditions needed to ensure the integrity of the back contact while exceeding the power threshold required to sinter the films.[18] The nanocrystal film heats to its peak temperature in approximately the same amount of time as the pulse length (300 μs). The peak temperature and cooling rate is determined by the amount of light absorbed and the rate of heat transfer to the metal contact, underlying substrate, and surrounding N_2 environment. Thus, the thickness of the nanocrystal film and the type of metal contact and substrate chosen greatly impact the heating profile of the film during photonic curing. Figure 4.1 shows a schematic illustration of the photonic curing process, wherein the light pulse heats up the nanocrystal film, vaporizes the organic ligands surrounding each nanocrystal, and induces grain growth in the film.

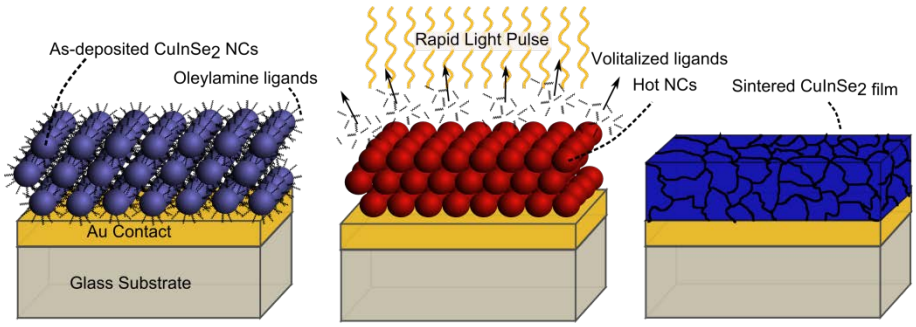

Figure 4.1 A schematic illustration of the photonic curing process.

Figure 4.2 shows SEM of 600 nm thick $CuInSe_2$ nanocrystal films deposited on Mo back contacts before and after photonic curing with a 300 µs pulse at increasing energy inputs. A 1.0 J/cm^2 pulse (Fig 4.2B) leaves the majority of the film relatively unchanged from the untreated nanocrystal film (Fig 4.2A); however, some regions of sintered $CuInSe_2$ are observed. Increasing the pulse intensity to 1.3 J/cm^2 (Fig 4.2C) continues conversion of the nanocrystal film to isolated sintered $CuInSe_2$ regions. As observed in Figure 4.2D and 4.2E, further increases of pulse energy lead to almost complete dewetting and agglomeration of the film into sintered $CuInSe_2$ melt balls, leaving the Mo back contact almost completely exposed.

Figure 4.3 shows XRD data for the films corresponding to the SEM in Figure 4.2. No new diffraction peaks appear after photonic curing and all peaks correspond to $CuInSe_2$ and Mo (reference patterns at bottom of graph). The primary change is the narrowing of the (112) diffraction peak for $CuInSe_2$ at $2\Theta=26.65^o$, indicating that sintering and crystal growth occur. Slight (112) peak narrowing is observed after a 1.0 J/cm^2 pulse, which most likely corresponds to the formation of melted $CuInSe_2$ in some regions of the film. The peak continues to narrow with higher intensity photonic curing treatment. Peak narrowing reaches the machine broadening limit with a 1.8 J/cm^2 pulse.

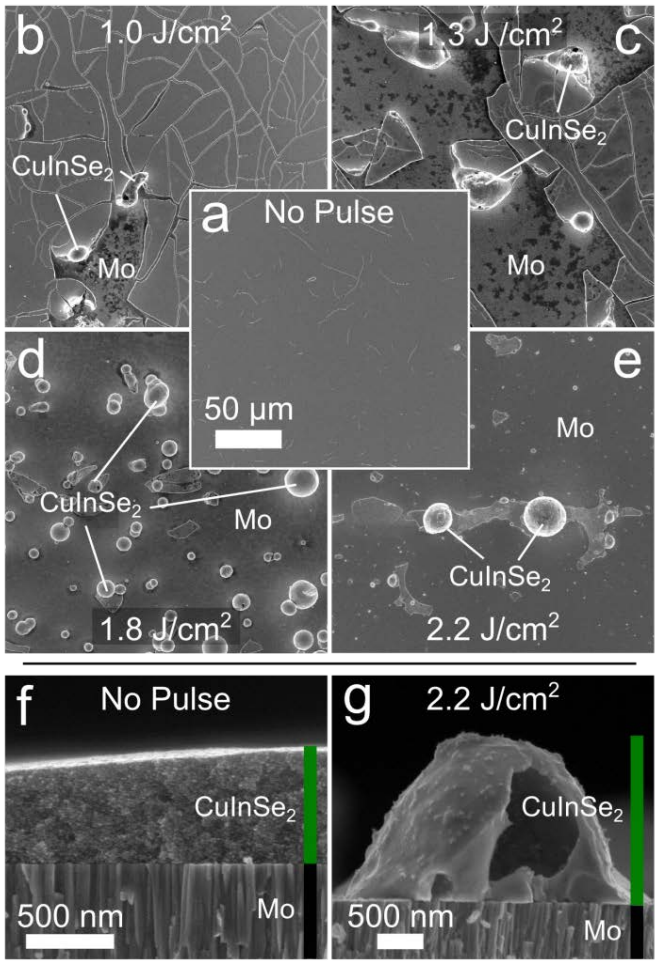

Figure 4.2 SEM images of $CuInSe_2$ nanocrystal films on Mo-coated soda lime glass a) before and after photonic curing with a 300 µs pulse with b) 1.0 J/cm^2, c) 1.3 J/cm^2, d) 1.8 J/cm^2, and e) 2.2 J/cm^2 energy. Cross sectional SEM images f) before and g) after a 2.2 J/cm^2 pulse are also shown.

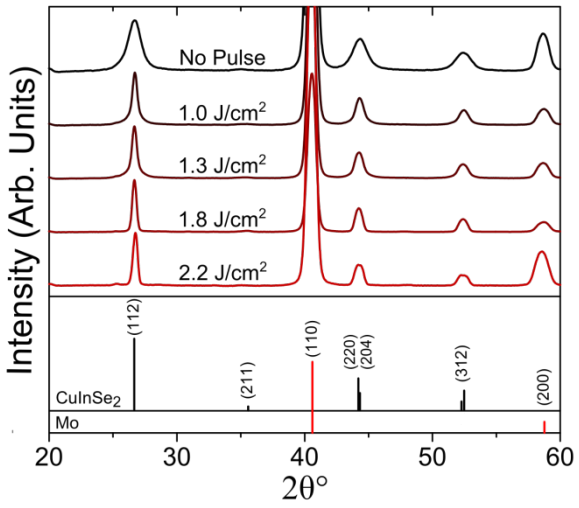

Figure 4.3 XRD of CIS deposited on Mo. XRD is shown for $CuInSe_2$ nanocrystals on Mo-coated soda-lime glass (solid lines) before and after photonic curing. Reference patterns are for chalcopyrite $CuInSe_2$ (PDF # 97-006-8928) and Mo (PDF# 97-064-3959).

4.3.2 Photonic Curing on $MoSe_2$/Mo Bilayer Contacts

Melt ball formation is significantly reduced in photonically cured $CuInSe_2$ nanocrystal films deposited on $MoSe_2$-coated Mo back contacts. $MoSe_2$-coated Mo back contacts were chosen based on the traditional CIGS photovoltaic structure. A small layer of $MoSe_2$ between the $CuInSe_2$ and Mo is formed during the selenization process, and optimization of this layer is important for high efficiency sintered nanocrystal devices.[7] In contrast to a selenization process, no $MoSe_2$ is formed during the photonic curing process due to the rapid nature of the treatment. To add a $MoSe_2$ layer, a 50 nm layer of $MoSe_2$ on the Mo back contact was created prior to depositing the $CuInSe_2$ nanocrystals. Figure 4.4 shows SEM and Figure 4.5 shows XRD from pulsed one micron nanocrystal films on $MoSe_2$-coated Mo back contacts at different pulse energies. A 2 J/cm^2 pulse has little effect on the nanocrystal film (Fig 4.4B) and there is minimal peak narrowing of the

(112) peak. Some small areas of sintered $CuInSe_2$ are formed with 2.2 J/cm^2 (Fig 4.4C) and 2.5 J/cm^2 (Fig 4.4D) pulses, but the majority of the film continues to be small grained although the (112) peak narrows in XRD. At pulse energies of 3 J/cm^2 and 3.5 J/cm^2, significant sintering is observed and the (112) peak reaches the narrowing limit due to instrument broadening. A marked change in sintering threshold between nanocrystal films on Mo and $MoSe_2$-coated Mo is observed in both the SEM and XRD. A 2.2 J/cm^2 pulse on Mo leads to strong melt ball formation and fully narrowed XRD peak, where on $MoSe_2$-coated Mo very little sintering or peak narrowing is observed. There is still coalescence of nanocrystals that leads to some exposed back contact; however, the majority of the film is covered with absorber layer unlike films treated on Mo.

The increased grain size at higher energy pulses can also be observed in cross sectional SEM shown in Figure 4.6. Some necking of the nanoparticles can be observed after a 3 J/cm^2 pulse (Fig. 4.6D); however the grain size in the majority of the film is still small. With a larger 3.5 J/cm^2 pulse, large grains are seen through the entire film (Fig. 4.6F).

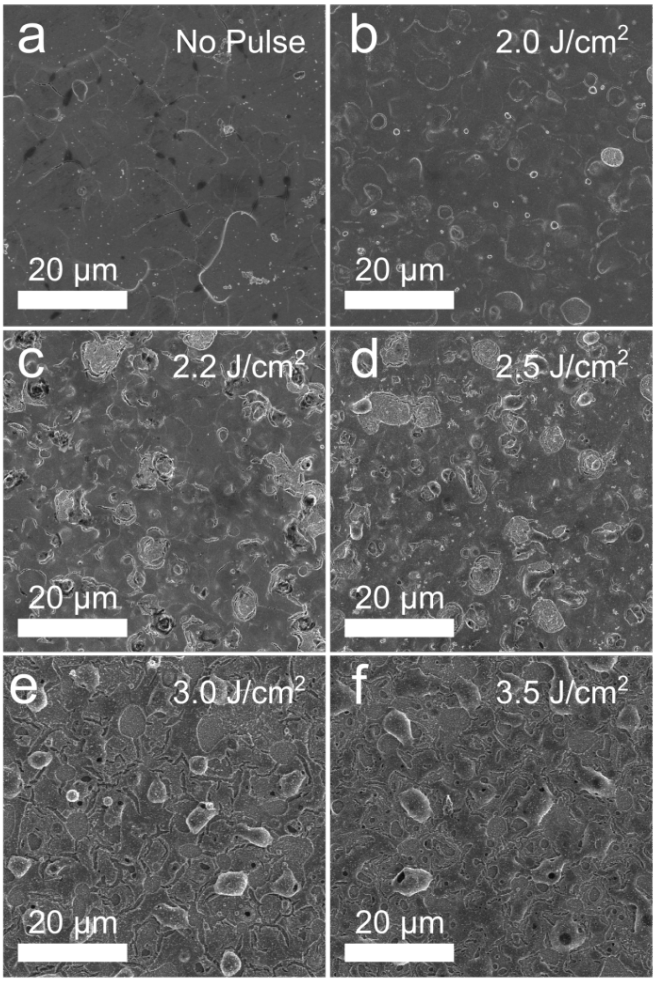

Figure 4.4 SEM images of $CuInSe_2$ nanocrystals films a) before and after b) 2 J/cm^2, c) 2.2 J/cm^2, d) 2.5 J/cm^2, e) 3 J/cm^2 and f) 3.5 J/cm^2 on $MoSe_2$-coated Mo back contacts. Minimal change is observed with lower energy pulses from the as-deposited nanocrystal film. With increasing pulse energy, more sintering is observed. Some localized $CuInSe_2$ sintering is observed; however, the formation of large melt balls is significantly reduced compared to the treatment of nanocrystal films on Mo back contacts.

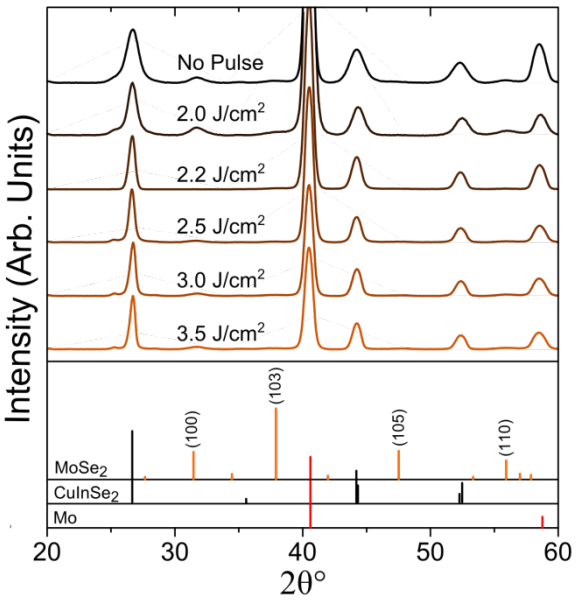

Figure 4.5 XRD data of nanocrystal films before and after 2, 2.2, 2.5, 3 and 3.5 J/cm^2 pulses on $MoSe_2$/Mo bilayer back contacts (from top to bottom). Indexed XRD references for chalcopyrite $CuInSe_2$, Mo, and $MoSe_2$ (pdf# 97-004-9800) are also shown. As is typical of $MoSe_2$ synthesized via selenization of Mo, the (103) peak intensity is significantly reduced due to the preferential orientation of the $MoSe_2$ to the underlying Mo.[19,20]

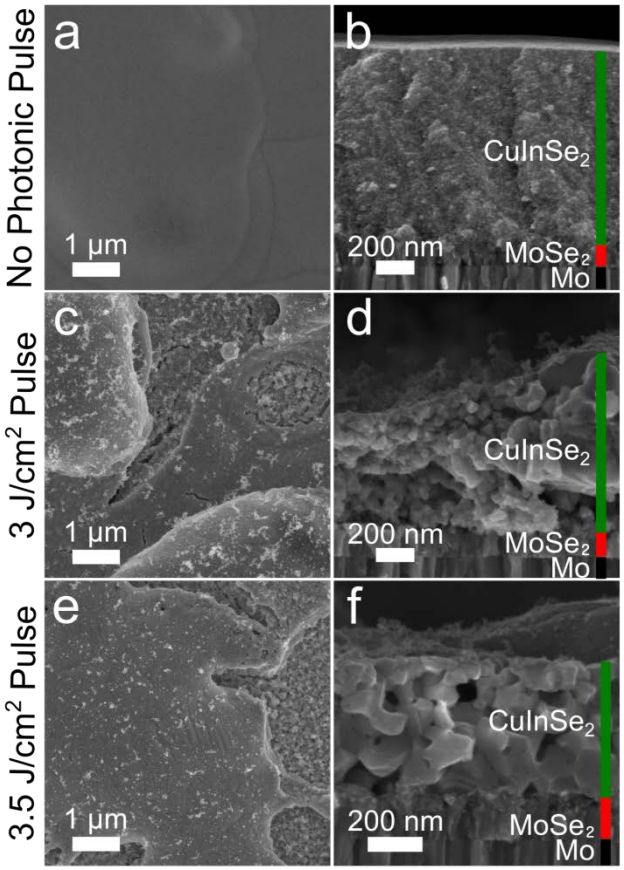

Figure 4.6 Higher magnification SEM images of $CuInSe_2$ on $MoSe_2$. (a) Spatial and (b) cross sectional SEM of films with no photonic treatment. (c) Spatial SEM of film after 3 J/cm^2 treatment showing some agglomeration of sintered CIS layer as well as areas of local sintering seen in more detail in (d)cross sectional SEM image. (e) SEM of film after 3.5 J/cm^2 pulse showing increased sintering leading to large grain CIS seen in (F)cross sectional SEM image.

The change in photonically treated film morphology from Mo to $MoSe_2$-coated glass may have several explanations. Ghosh et al.[21] show that the difference in thermal expansion between Mo and $CuInSe_2$ can lead to poor adhesion during the high temperature treatments used in $Cu(In,Ga)Se_2$ co-evaporation deposition. This thermal expansion mismatch is exacerbated due to large thermal gradients in the film due to the

brevity of the pulse, allowing the nanocrystal film to reach high temperatures while the underlying substrate remains at a lower temperature.[18] Both the thermal expansion difference and the temperature mismatch likely destabilize the $CuInSe_2$ film, leading to dewetting and agglomeration. Partial conversion of Mo to $MoSe_2$ during the standard high temperature selenization process increases adhesion between $CuInSe_2$ and Mo.[22] The increased adhesion between $MoSe_2$ and $CuInSe_2$ may prevent much of the dewetting after film destabilization during pulse treatment. Changes in surface roughness, film wetting, and potential interfacial reactions between the back contact and $CuInSe_2$ layer may also contribute to the differences in observed film morphology on Mo and $MoSe_2$.

4.3.3 Optimization of Photonic Curing Pulse Length

The PulseForge 3300 tool used for photonic curing was originally developed for making solution-deposited metal connects. For example, a slurry of CuO nanoparticles, a reducing agent, and binder material are dispersed in solvent and cast onto a substrate such as paper. The slurry is then treated with photonic curing, where the CuO is reduced into conductive copper. Figure 4.7 shows a patterned CuO slurry before and after photonic curing with a 380 V, 2000 μs pulse. Longer pulse durations are used for curing of CuO nanoparticles because the slurry must remain at a high temperature for a longer period of time in order for the nanocparticles to react with the reducing agent. Figure 4.8 shows SEM images of a CuO nanoparticle slurry spray cast onto a $MoSe_2$/Mo bilayer substrate before and after photonic curing with varying pulse lengths. After a photonic curing pulse of 300 μs duration (Fig. 4.8B), the Cu tends to form large agglomerates, similar to what is observed for CuInSe2 nanocrystals at these pulse lengths. Using longer duration pulses of 1200 μs (Fig. 4.8C) or 2000 μs (Fig. 4.8D) yields much better film morphology and

allows for the successful conversion of CuO into conductive copper. Even at the longer pulse durations, the films still show some holes present, which can be attributed to the volatilization of the binder material from the slurry.

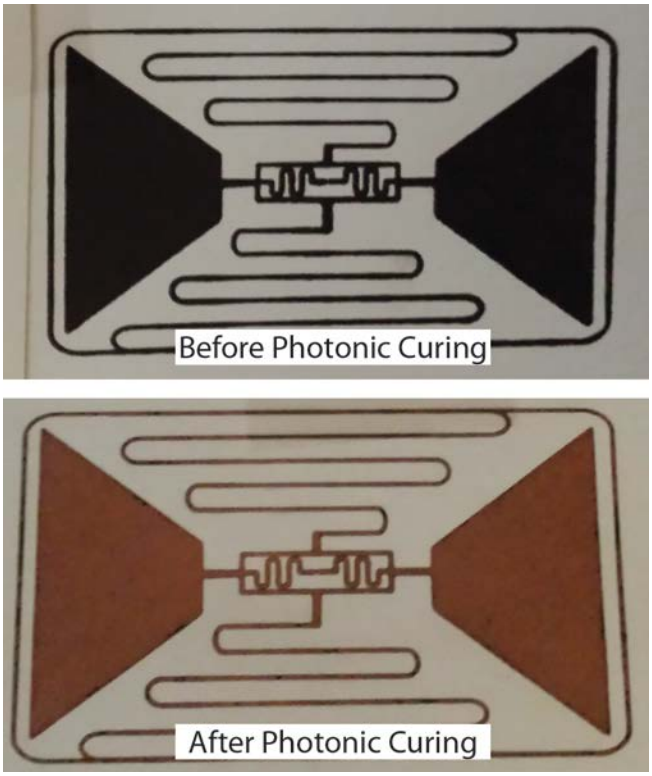

Figure 4.7 A patterned CuO nanoparticle slurry before and after photonic curing with a 380 V, 2000 μs pulse. During photonic curing, the CuO reacts with a reducing agent to form conductive copper.

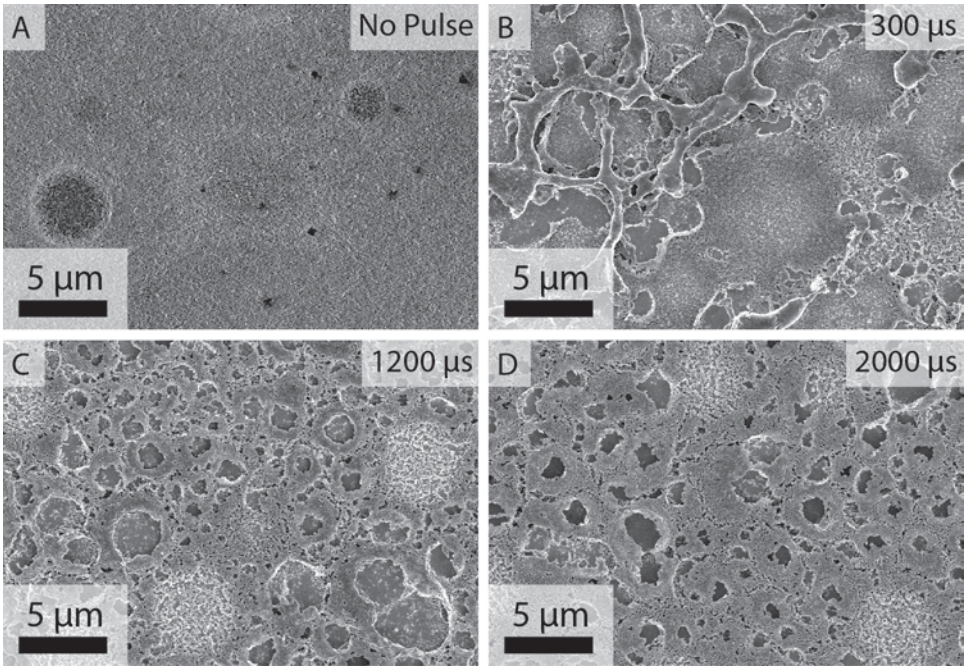

Figure 4.8 SEM images of a spray-cast CuO nanoparticle slurry (A) before photonic curing and after photonic curing pulses with durations of (B) 300 µs, (C) 1200 µs, and (D) 2000 µs.

Figure 4.9 shows SEM images for $CuInSe_2$ nanocrystals spray cast onto a $MoSe_2$/Mo bilayer substrate and treated with various photonic curing pulse durations. Unlike the CuO nanoparticle slurry film, the CuInSe2 nanocrystal film uniformity actually decreases with longer pulse durations. At 300 µs (Fig. 4.9A), the film sinters into some large melt structures while the rest of the film remains unsintered. As the pulse duration increases, these melt structures get larger and larger, leaving greater area of exposed back contact. Longer pulse durations allow for the melted nanocrystals at film hot spots to wick up into even large melt structures while having little impact on the rest of the unsintered nanocrystals.

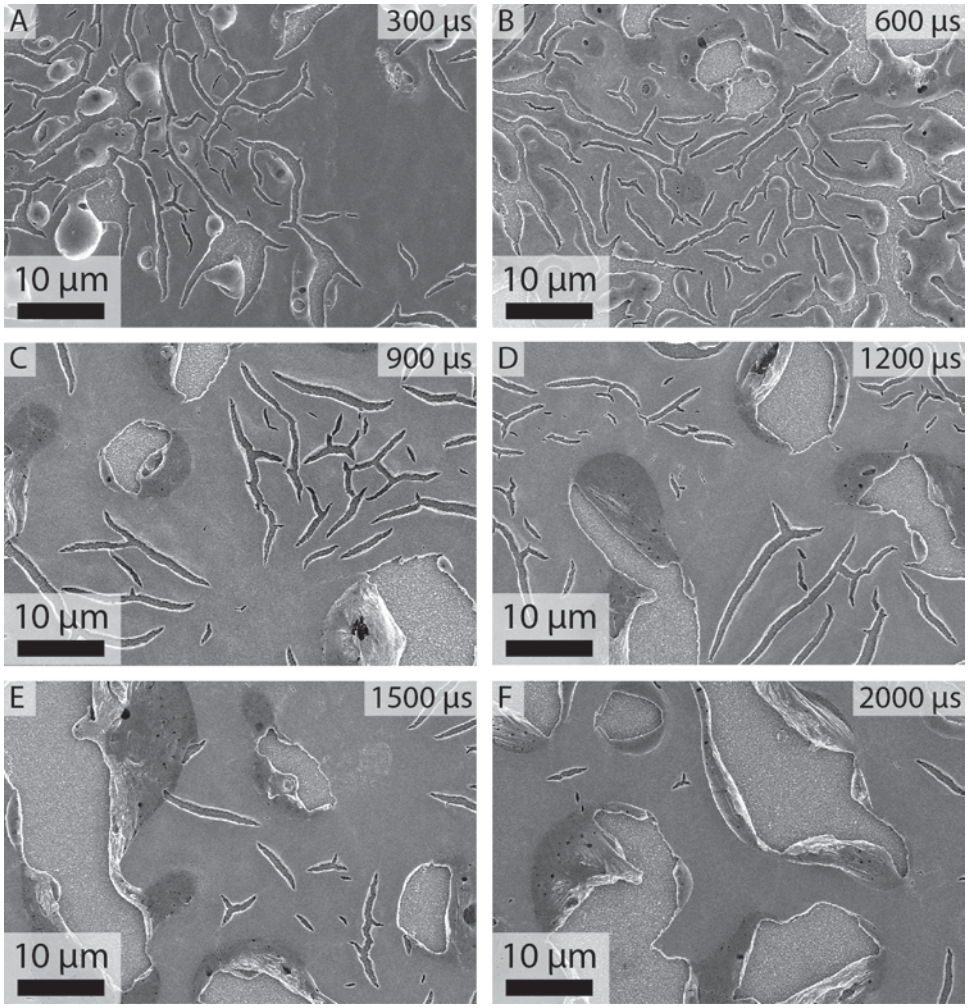

Figure 4.9 SEM images of a $CuInSe_2$ nanocrystal film spray cast on a $MoSe_2$/Mo bilayer substrate after photonic curing with varying pulse conditions of (A) 600 V, 300 µs, (B) 550 V, 600 µs, (C) 520 V, 900 µs, (D) 500 V, 1200 µs, (E) 470 V, 1500 µs, and (F) 450 V, 2000 µs. The pulse voltage was varied inversely to the pulse duration in order to maintain a similar lamp output power (based on the NovaCentrix pulse modeling software).

4.3.4 Photonic Curing on Au and Other Metal Contacts

We have recently reported in depth about low energy photonic curing treatments on Au back contacts.[16] Here we focus on higher pulse intensities that lead to necking and

sintering of the nanocrystals. Figure 4.10 shows XRD and SEM images of the a nanocrystal film deposited on a Au back contact after photonic curing at 3 and 3.5 J/cm^2. At both energy inputs, the (112) diffraction peaks are significantly narrowed after curing (Fig. 4.10A). Cross sectional SEM images of films cured at 3 J/cm^2 show nanocrystal necking (Fig. 4.10B) with no loss in integrity of the the 40 nm Au back contact. Similar to nanocrystal films on $MoSe_2$-coated Mo, a higher pulse energy of 3.5 J/cm^2 pulse was required to fully sinter the $CuInSe_2$ nanocrystal layer, but these conditions destroyed the Au back contact (Fig. 4.10D). Figure 4.10E-4.10G shows an EDS map of the nanocrystal film after 3.5 J/cm^2 curing with agglomerates of Au scattered throughout the $CuInSe_2$ film.

Additional back contact materials besides Au and $MoSe_2$/Mo were also investigated. Figure 4.11 shows a comparison of the nanocrystal film morphology on various metal back contact materials (Mo, $MoSe_2$/Mo, Au, ITO, and Ni) after photonic curing. Ag metal back contacts were also used, but the adhesion was so poor between $CuInSe_2$ and Ag that no film remained following photonic curing. Films on Mo substrates show significant delamination due to the poor $CuInSe_2$-Mo adhesion. Unfortunately, we were unable to find a substrate material from our standard library of materials with sufficient adhesion to prevent melt ball formation. Films deposited on MoSe2/Mo bilayer substrates, Gold , Indium Tin Oxide, and Nickel substrates all show a similar film morphology after photonic curing. Ideally, the metal contact should be chosen such that liquid $CuInSe_2$ would preferentially wet the substrate surface rather than agglomerate into large structures.

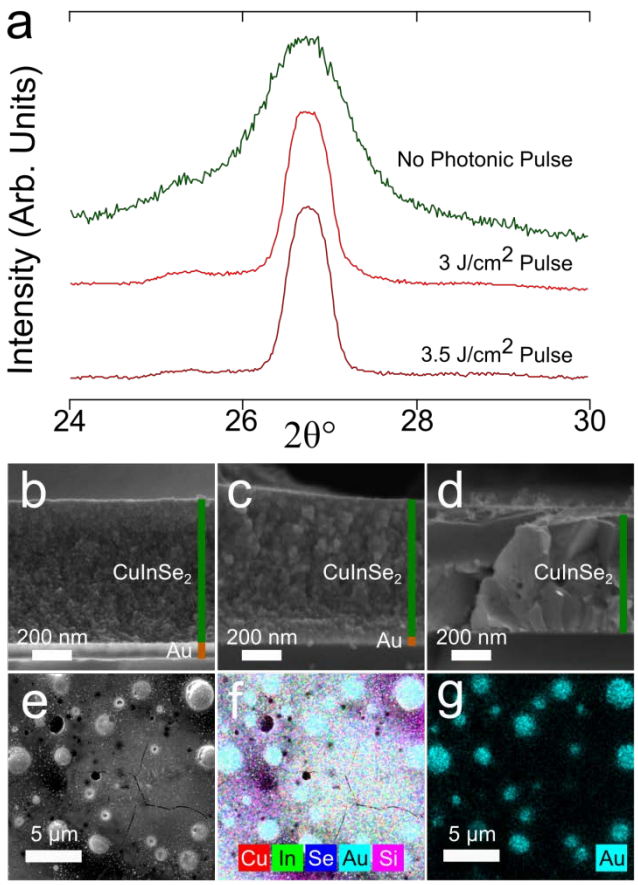

Figure 4.10 (a) XRD of CIS (112) peak before and after photonic curing with 3 and 3.5 J/cm^2 pulses of nanocrystal films deposited on Au back contacts. Cross sectional SEM images (b)before, (c) after 3 J/cm2 and (d) 3.5 J/cm^2 treatment. (e) Spatial SEM and (f-g) Spatial EDS maps of film after 3.5 J/cm^2 pulse. (f) Composite EDS response for Cu (red), In (green), Se (dark blue), Au (light blue) and Si(violet). (g) Au EDS response showing Au agglomeration scattered across the substrate.

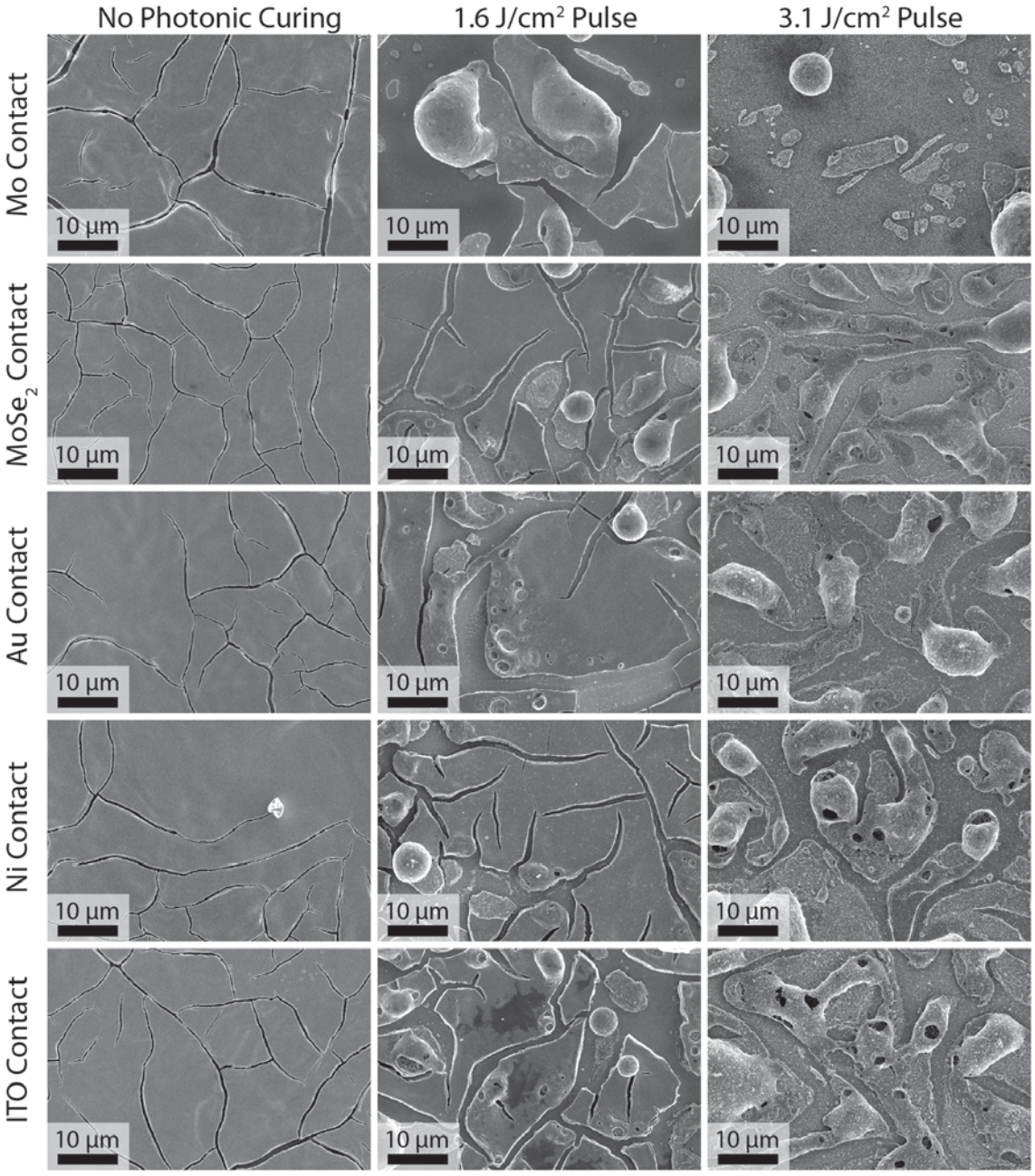

Figure 4.11 SEM images of $CuInSe_2$ nanocrystal films deposited on Mo, $MoSe_2$/Mo, Au, Ni, and ITO back contacts before photonic curing and after photonic curing at 1.6 J/cm^2 and 3.1 J/cm^2.

4.3.5 Photovoltaic Device Performance

	Energy Input (J/cm^2)	Back Contact	Voc (V)	Jsc (mA/cm^2)	FF	PCE (%)
No Sintering	No Pulse	$MoSe_2$/Mo	0.37	3.19	0.46	0.55
	2.2	$MoSe_2$/Mo	0.30	10.6	0.34	1.05
Sintering	2.5	$MoSe_2$/Mo	0.16	1.78	0.29	0.08
	3	$MoSe_2$/Mo	0.20	2.85	0.28	0.16
	3.5	$MoSe_2$/Mo	0.11	3.96	0.26	0.11
No Sintering	No Pulse	Au	0.41	5.65	0.49	1.19
	2.2	Au	0.21	18.25	0.32	1.25
	2.5	Au	0.21	12.87	0.31	0.85
Sintering	3	Au	0.05	4.82	0.24	0.06
	3.5	Au	-	-	-	-

Table 4.1 Device Characteristics of Pulsed Films deposited on $MoSe_2$-coated Mo and Au back contacts.

Table 4.1 summarizes the performance of devices made with nanocrystal films before and after photonic curing. Photovoltaic devices fabricated using the pulsed $CuInSe_2$ nanocrystals on Mo-coated soda-lime glass as the absorber layer exhibited ohmic IV response without any measureable photocurrent due to the exposed Mo back contact. Use of the $MoSe_2$-coated Mo back contact reduced the amount of exposed back contact, and working devices were fabricated at all pulse conditions. In addition to reducing exposed back contact, the $MoSe_2$ layer is also important for device performance as it eliminates the Schottky barrier between CIGS and the Mo back contact in PV devices.[18] Au also is a better back contact than Mo for spray-deposited $CuInSe_2$ nanocrystal films since it has a higher work function than Mo, making it more suitable to form contact with the p-type $CuInSe_2$ layer.[6] Figure 4.12 shows the current/voltage characteristics of the devices shown in Table 4.1. Power conversion efficiency (PCE) of

devices on $MoSe_2$-coated Mo and Au back contacts improve after a 2.2 J/cm_2 pulse, with both exhibiting decreases in V_{oc} and FF and increases in J_{sc}. This arises from the fact that, under these pulse conditions, the film exhibits little sintering. This pulse energy regime is discussed further in Chapter 6. As pulse intensity increases and the nanocrystals begin to sinter, the PCE decreases; however the device still exhibit PCE even after sintering thresholds have been reached. Films treated with 3.5 J/cm^2 pulses on Au did not have any measureable device current due to Au back contact destruction.

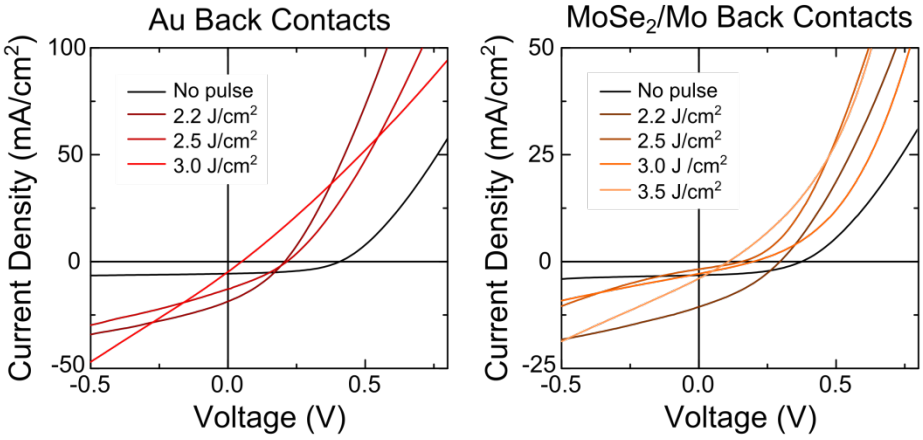

Figure 4.12 Current/Voltage characteristics of photonic cured nanocrystal films on Au (left) and $MoSe_2$-coated Mo (right) back contacts.

In comparison with untreated nanocrystal films, J_{sc} values are slightly lower for both $MoSe_2$/Mo and Au for a 3 J/cm^2 pulse. J_{sc} improves on $MoSe_2$/Mo from 3.2 to 4.0 mA/cm^2 when a nanocrystal film is pulsed with 3.5 J/cm^2. Additionally, due to exposed back contact, active $CuInSe_2$ area is smaller in the photonically cured films than as-deposited nanocrystal films. Figure 4.13 shows EDS maps from the 3 J/cm^2 pulse of films on $MoSe_2$/Mo back contacts. Sintered absorber layer is shown in the green [In] EDS Maps (Fig 4.13B), while dark areas in the In maps and bright areas in the Mo EDS

maps (Fig 4.13D) have no sintered $CuInSe_2$ absorber layer and would not contribute to the short circuit current. Correcting J_{sc} values for the reduced active area of the device in pulsed films would increase short circuit current values, highlighting the potential of this technique for increased device performance with improved sintered layers. Additional improvement is expected as back contact exposure from film dewetting is improved.

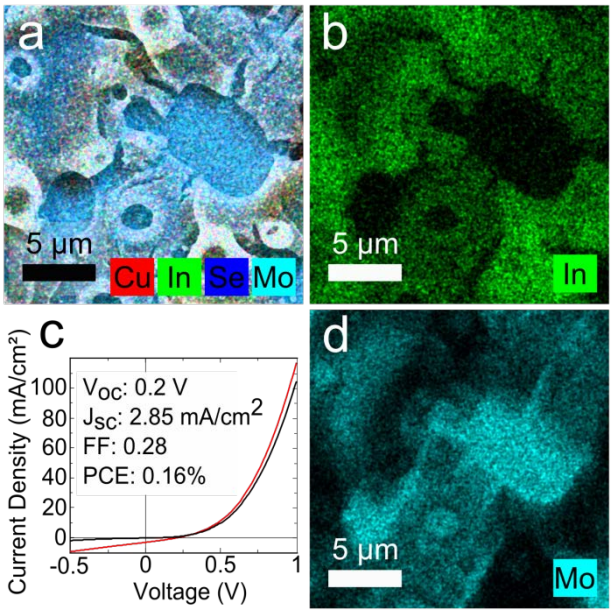

Figure 4.13 EDS maps and IV curves of sintered CIS film on $MoSe_2$/Mo back contacts with pulse energies of 3 J/cm^2. a) Cu (red), In (green), Se (dark blue), and Mo (light blue) composite response, b) green In EDS response showing absorber layer location, and d) light blue Mo EDS response showing exposed back contact. d) IV response for device after 3 J/cm^2 pulse.

4.4 CONCLUSIONS

Photonic curing is used to treat $CuInSe_2$ nanocrystal films on Mo, $MoSe_2$-coated Mo, and Au back contacts. During pulsing, large thermal gradients are generated, allowing the nanocrystal film to reach high temperatures while the underlying back

contact remains at a lower temperature. Films on Mo back contacts dewett and agglomerated into large sintered $CuInSe_2$ melt balls, exposing the back contact and making the films unsuitable for photovoltaics. Nanocrystal dewetting is reduced by using a $MoSe_2$-coated Mo or Au back contact, and working devices are fabricated. Increase power conversion efficiency is demonstrated at low pulse intensities. As pulse intensity increases, PCE decreases, but working photovoltaics are manufactured with sintered $CuInSe_2$ nanocrystal films.

4.5 REFERENCES

1. Fraunhofer ISE. Fraunhofer Institiute For Solar Energy Systems ISE: Photovoltaics Report. (2014). at <http://www.ise.fraunhofer.de/de/downloads/pdf-files/aktuelles/photovoltaics-report-in-englischer-sprache.pdf>
2. Stevens, G. Thin film CIGS report card - Progress in CIGS achieving scale. in *2012 38th IEEE Photovoltaic Specialists Conference (PVSC)* 002487–002489 (2012). doi:10.1109/PVSC.2012.6318099
3. Jackson, P. *et al.* New world record efficiency for Cu(In,Ga)Se2 thin-film solar cells beyond 20%. *Prog. Photovolt. Res. Appl.* **19,** 894–897 (2011).
4. Repins, I. *et al.* 19·9%-efficient ZnO/CdS/CuInGaSe2 solar cell with 81·2% fill factor. *Prog. Photovolt. Res. Appl.* **16,** 235–239 (2008).
5. Goushi, Y., Hakuma, H., Tabuchi, K., Kijima, S. & Kushiya, K. Fabrication of pentanary Cu(InGa)(SeS)2 absorbers by selenization and sulfurization. *Sol. Energy Mater. Sol. Cells* **93,** 1318–1320 (2009).
6. Akhavan, V. A., Panthani, M. G., Goodfellow, B. W., Reid, D. K. & Korgel, B. A. Thickness-limited performance of CuInSe2 nanocrystal photovoltaic devices. *Opt. Express* **18,** A411–A420 (2010).
7. Harvey, T. B. *et al.* Copper Indium Gallium Selenide (CIGS) Photovoltaic Devices Made Using Multistep Selenization of Nanocrystal Films. *ACS Appl. Mater. Interfaces* **5,** 9134–9140 (2013).
8. Schroder, K. A., McCool, S. C. & Furlan, W. F. Broadcast photonic curing of metallic nanoparticle films. in (2006). at <http://www.novacentrix.com/images/downloads/NSTI%202006%20Boston.pdf>

9. Jang, S., Lee, D. J., Lee, D. & Oh, J. H. Electrical sintering characteristics of inkjet-printed conductive Ag lines on a paper substrate. *Thin Solid Films* **546,** 157–161 (2013).

10. Lee, D. J. *et al.* Pulsed light sintering characteristics of inkjet-printed nanosilver films on a polymer substrate. *J. Micromechanics Microengineering* **21,** 125023 (2011).

11. Ryu, J., Kim, H.-S. & Hahn, H. T. Reactive Sintering of Copper Nanoparticles Using Intense Pulsed Light for Printed Electronics. *J. Electron. Mater.* **40,** 42–50 (2011).

12. Joo, S.-J., Hwang, H.-J. & Kim, H.-S. Highly conductive copper nano/microparticles ink via flash light sintering for printed electronics. *Nanotechnology* **25,** 265601 (2014).

13. Dhage, S. R. & Thomas Hahn, H. Rapid treatment of CIGS particles by intense pulsed light. *J. Phys. Chem. Solids* **71,** 1480–1483 (2010).

14. Dhage, S. R., Kim, H.-S. & Hahn, H. T. Cu(In,Ga)Se2 Thin Film Preparation from a Cu(In,Ga) Metallic Alloy and Se Nanoparticles by an Intense Pulsed Light Technique. *J. Electron. Mater.* **40,** 122–126 (2011).

15. Singh, M., Jiu, J., Sugahara, T. & Suganuma, K. Photonic Sintering of Thin Film Prepared by Dodecylamine Capped CuInxGa1 -xSe2 Nanoparticles for Printed Photovoltaics. *Thin Solid Films* doi:10.1016/j.tsf.2014.06.036

16. Stolle, C. J. *et al.* Multiexciton Solar Cells of CuInSe2 Nanocrystals. *J. Phys. Chem. Lett.* **5,** 304–309 (2014).

17. Panthani, M. G. *et al.* CuInSe2 Quantum Dot Solar Cells with High Open-Circuit Voltage. *J. Phys. Chem. Lett.* **4,** 2030–2034 (2013).

18. Guillot, M. J., McCool, S. C. & Schroder, K. A. Simulating the Thermal Response of Thin Films During Photonic Curing. 19–27 (2012). doi:10.1115/IMECE2012-87674

19. Zhu, X. *et al.* Determining factor of MoSe2 formation in Cu(In,Ga)Se2 solar Cells. *Sol. Energy Mater. Sol. Cells* **101,** 57–61 (2012).

20. Abou-Ras, D. *et al.* Formation and characterisation of MoSe2 for Cu(In,Ga)Se2 based solar cells. *Thin Solid Films* **480–481,** 433–438 (2005).

21. Ghosh, B., Chakraborty, D. P. & Carter, M. J. A novel back-contacting technology for thin films. *Semicond. Sci. Technol.* **11,** 1358 (1996).

22. Kohara, N., Nishiwaki, S., Hashimoto, Y., Negami, T. & Wada, T. Electrical properties of the Cu(In,Ga)Se2/ MoSe2/Mo structure. *Sol. Energy Mater. Sol. Cells* **67,** 209–215 (2001).

Chapter 5: Photonic Curing of Nanocrystals Capped with Inorganic ChaM Ligands**

5.1 INTRODUCTION

Colloidal semiconductor nanocrystals are being investigated to create low-cost, high efficiency photovoltaic (PV) devices.[1] Nanocrystals can be synthesized in large quantities, dispersed in solvents, and deposited under ambient conditions on virtually any type of substrate. The highest efficiency reported for a nanocrystal PV without high-temperature processing is 7% for PbS nanocrystals.[2] High temperature sintering has been used to achieve higher efficiencies, of up to 12% for nanocrystals of CdTe[3], Cu(In,Ga)Se_2 (CIGS)[4], Cu(In,Ga)S_2[5], and Cu_2ZnSnS_4.[6] High-temperature processing, however, adds significant manufacturing cost—especially for $CuInSe_2$ and CIGS nanocrystals, which require heating under a selenium-rich atmosphere to induce sintering (known as selenization). To eliminate the need for high temperature selenization and still achieve reasonably high device efficiency from ink-processed $CuInSe_2$ and CIGS nanocrystal devices, we have been exploring photonic curing as a way to sinter nanocrystal layers, which utilizes a high-intensity pulsed broad-band light source and is capable of high-throughput roll-to-roll manufacturing.

$CuInSe_2$ nanocrystals were synthesized with either oleylamine capping ligands or chalcogenidometallate cluster (ChaM) ligands. Oleylamine is a common capping ligand for $CuInSe_2$ that enables good dispersibility in organic solvents and easy processing, but

** Reproduced in part with permission from: Stolle, C. Jackson; Harvey, Taylor B.; Korgel, Brian A., Photonic Curing of Ligand-Capped $CuInSe_2$ Nanocrystal Films, *Proc. IEEE Photovoltaic Specialists Conference 40* (2014). Copyright 2014 Institute of Electrical and Electronics Engineers. CJS designed the experiments, fabricated and characterized the films and devices, analyzed the data, and wrote the manuscript. TBH assisted with characterization and data analysis. BAK provided funding, guidance, and assisted with writing the manuscript.

also hinders charge transport in devices and limits efficiency.[7] ChaM ligands, also referred to as metal chalcogenide complexes (MCCs) in the recent literature, can improve nanocrystal film electrical properties,[8] and have been shown to aid sintering of $CuInSe_2$ and CIGS nanocrystals.[9]

Oleylamine-capped or ChaM-capped $CuInSe_2$ nanocrystals were deposited into films and then processed by photonic curing using a NovaCentrix PulseForge 3300 tool equipped with a broadband xenon flash lamp. Nanocrystal films can reach over 1000°C in less than a millisecond and then rapidly return to room temperature.[10] Recently, mild photonic curing of $CuInSe_2$ nanocrystals to remove capping ligands without sintering enabled enhanced charge extraction from the PV devices with peak external quantum efficiencies exceeding 100%, indicative of the generation and extraction of multiexcitons in the device.[11] Higher energy photonic curing leads to nanocrystal sintering. We have found that higher energy photonic curing of oleylamine-capped nanocrystals leads to non-uniform sintered layers with extensive regions of exposed back contact; whereas, the ChaM-capped nanocrystals could be sintered into relatively uniform layers.

5.2 EXPERIMENTAL METHODS

5.2.1 Nanocrystal Synthesis

$CuInSe_2$ nanocrystals were synthesized by arrested precipitation following reported methods.[11] Briefly, 2 mmol of CuCl and 2 mmol of $InCl_3$ are added to a three neck flask under an inert atmosphere. 4 mmol of Se powder is dissolved in 1.5 mL diphenylphosphine and 2 mL oleylamine. The flask is attached to a standard Schlenk line and degassed at 110°C for 30 minutes under vacuum. The flask is then purged with nitrogen and heated to 180°C. Once the flask reaches 180°C, the Se solution is injected

and the flask is rapidly ramped to 240°C and held for 30 minutes. The heating mantle is then removed and the flask is allowed to cool to room temperature. The nanocrystals are precipitated by adding excess ethanol and centrifugation at 4000 rpm. The nanocrystals are washed by precipitation using toluene/ethanol solvent/antisolvent pair.

5.2.2 Ligand Exchange

CIS-ChaM $[(N_2H_4)_x(N_2H_5)_3(In_2Cu_2Se_4S_3)]$ was synthesized in hydrazine by established methods.[12] CIS-ChaM is formed by mixing equal amounts of Cu_2S-ChaMs $[N_4H_9Cu_7S_4]$ and In_2Se_3-ChaMs $[(N_2H_4)_2(N_2H_5)_2In_2Se_4]$. Cu_2S-ChaM was synthesized by dissolving 1 mmol of Cu_2S and 1 mmol S powder in 4 mL of hydrazine. In_2Se_3-ChaM was synthesized by mixing 2.5 mmol In_2Se_3, 2.5 mL of 1M Se:N_2H_4 solution and 7.5 mL of additional hydrazine. CIS-ChaM is dried under nitrogen and redispersed in ~10 mL of N-methylformamide (all subsequent processing can be completed without the need for hydrazine). Oleylamine ligand exchange was carried out in N-methylformamide.[8,9,12] Typically, 2 mL of oleylamine-capped nanocrystals dispersed in toluene (~100 mg/mL) are mixed with 5 mL N-methylformamide and 0.3 mL of CIS-ChaMs dispersed in N-methylformamide and stirred overnight in an inert atmosphere. Nanocrystals are precipitated by adding 20 mL of acetonitrile and centrifuging at 4000 rpm and then redispersed in 5 mL N-methylformamide.

5.2.3 Film Deposition and Treatment

Oleylamine-capped $CuInSe_2$ nanocrystals dispersed in toluene were spray cast onto Au-coated glass substrates heated to 80°C and ChaM-capped nanocrystals dispersed in N-methylformamide were doctor-bladed onto Au-coated glass substrates heated to

250°C. Photonic curing was performed using a PulseForge 3300 (NovaCentrix). Samples were loaded into a stainless steel chamber with a quartz window and purged with nitrogen for 30 seconds. Samples were then cured with a single, 300 μs pulse with energies ranging from 1.0-3.5 J/cm^2, as measured by bolometer (NovaCentrix). SimPulse software (NovaCentrix) was used to calculate the temperature of the film during photonic curing.

5.2.4 Characterization Techniques

Scanning electron microscopy (SEM) was performed using a Zeiss Supra 40 VP operated at 5 keV accelerating voltage. X-ray diffraction (XRD) was performed using a Rigaku R-Axis Spider diffractometer using Cu Kα radiation (λ = 1.5418 Å) operated at 40 kV and 40 mA and an image-plate detector. 2D diffraction patterns were radially integrated using Rigaku 2DP software.

5.3 Results and Discussion

5.3.1 Film Morphology and Photonic Curing Temperature

Figure 5.1 shows SEM images of a 1 μm thick film of oleylamine-capped $CuInSe_2$ nanocrystals before and after photonic curing. The as-deposited film (Fig. 5.1A) is relatively uniform with some small cracks and thickness variations. After pulsing at 1.6 J/cm^2 (Fig. 5.1B), the film remains largely unsintered, although some regions of the nanocrystal film begin to peel off the substrate. The nanocrystal films cured with pulse energies ranging from 2.1 to 3.5 J/cm^2 shown in Figures 5.1C-5.1F are all highly non-uniform, regardless of pulse energy used, with a significant amount of exposed back contact. The temperatures of the films were calculated using SimPulse (Fig. 5.1G). Local

variations in thickness can lead to hot spots in the film due to the absorption of more light in those regions. These hot spots can nucleate the formation of melt balls in particular regions of the substrate that lead to exposed back contact. As the pulse energy was increased, the extent of nanocrystal sintering also increased (Fig. 5.1C-5.1F). Once the pulse conditions pushed the temperature of the film over the $CuInSe_2$ melting point of ~990°C, most of the film exhibited globular melt structures, as in Figure 5.1F especially.

ChaM-capped $CuInSe_2$ nanocrystals were found to respond much differently to photonic curing than the oleylamine-capped nanocrystals. Figure 5.2 shows SEM images of 1 μm thick films of CIS-ChaM-capped $CuInSe_2$ nanocrystals before and after photonic curing with pulse energies ranging from 1.0 to 2.8 J/cm^2. The film temperatures calculated with SimPulse for each pulse condition shown in Figure 5.2G. The as-deposited film is relatively smooth (Fig. 5.2A) and the lowest energy, 1.0 J/cm^2 pulse has little effect on the film (peak temperature ~400 ^{o}C, Fig. 5.2B). Higher pulse energies of 1.4 and 1.8 J/cm^2 (peak temperatures of ~600°C and ~800°C, respectively, Fig. 5.2C, 5.2D) led to slight amount of sintering that was uniform across the substrate without any exposed back contact or melting structures. The film temperatures are too low to induce melting; however, curing temperature of 500°C is hot enough to induce crystal growth of ChaM-capped nanocrystals heated in argon.[9] The crystal grains formed during photonic curing are much smaller than those formed during high-temperature annealing. The smaller grain size is likely due to the short heating times during photonic curing. At higher pulse energies of 2.3 and 2.8 J/cm^2 (peak temperatures of ~1000°C and ~1200°C, respectively, Fig. 5.2E, 5.2F), the nanocrystal films exhibit significant melting. Unlike the oleylamine-capped nanocrystals, however, there is little exposed back contact and the film adhesion appears to be much better.

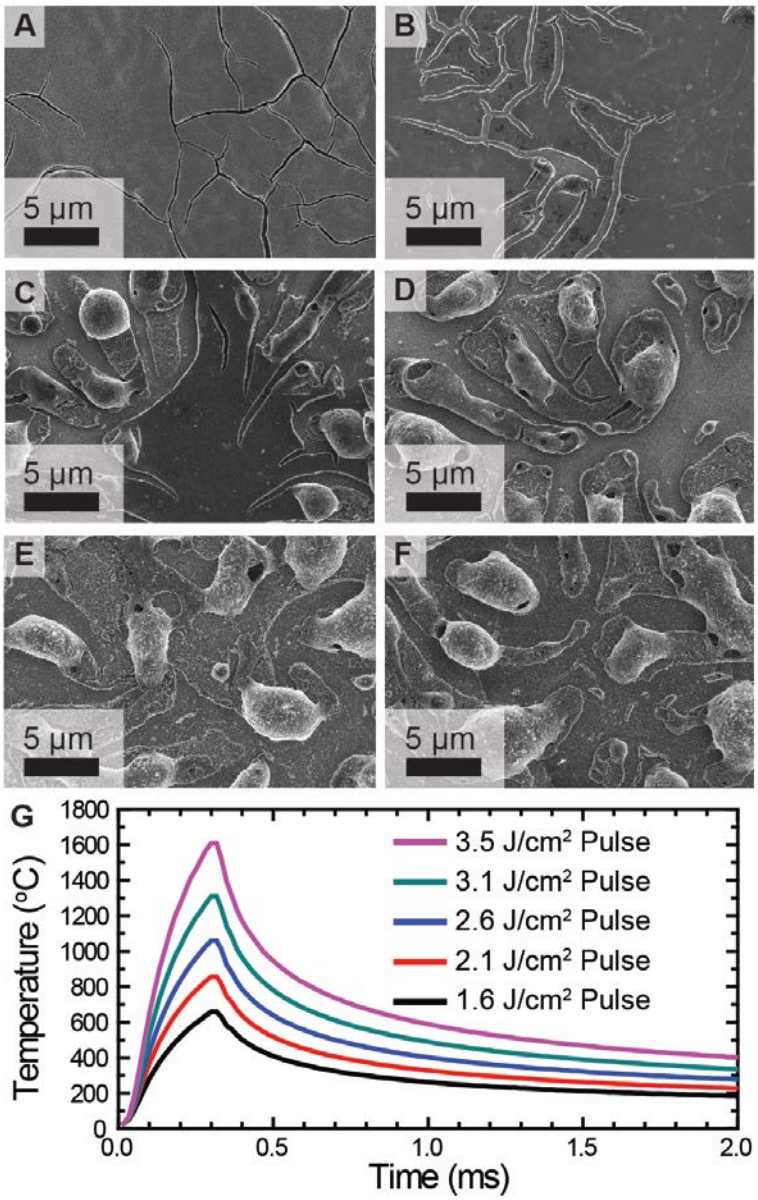

Figure 5.1 SEM images of a 1 µm thick oleylamine-capped $CuInSe_2$ nanocrystal film (A) before photonic curing and after photonic curing pulses of (B) 1.6 J/cm^2, (C) 2.1 J/cm^2, (D) 2.6 J/cm^2, (E) 3.1 J/cm^2, and (F) 3.5 J/cm^2. (G) SimPulse modeling of the nanocrystal film temperature during photonic curing pulses of 1.6, 2.1, 2.6, 3.1, and 3.5 J/cm^2, each 300 µs in duration. For the model a layered structure was used with a 1 µm thick $CuInSe_2$ film on a 60 nm thick Au metal film deposited on a 1.1 mm thick soda-lime glass substrate.

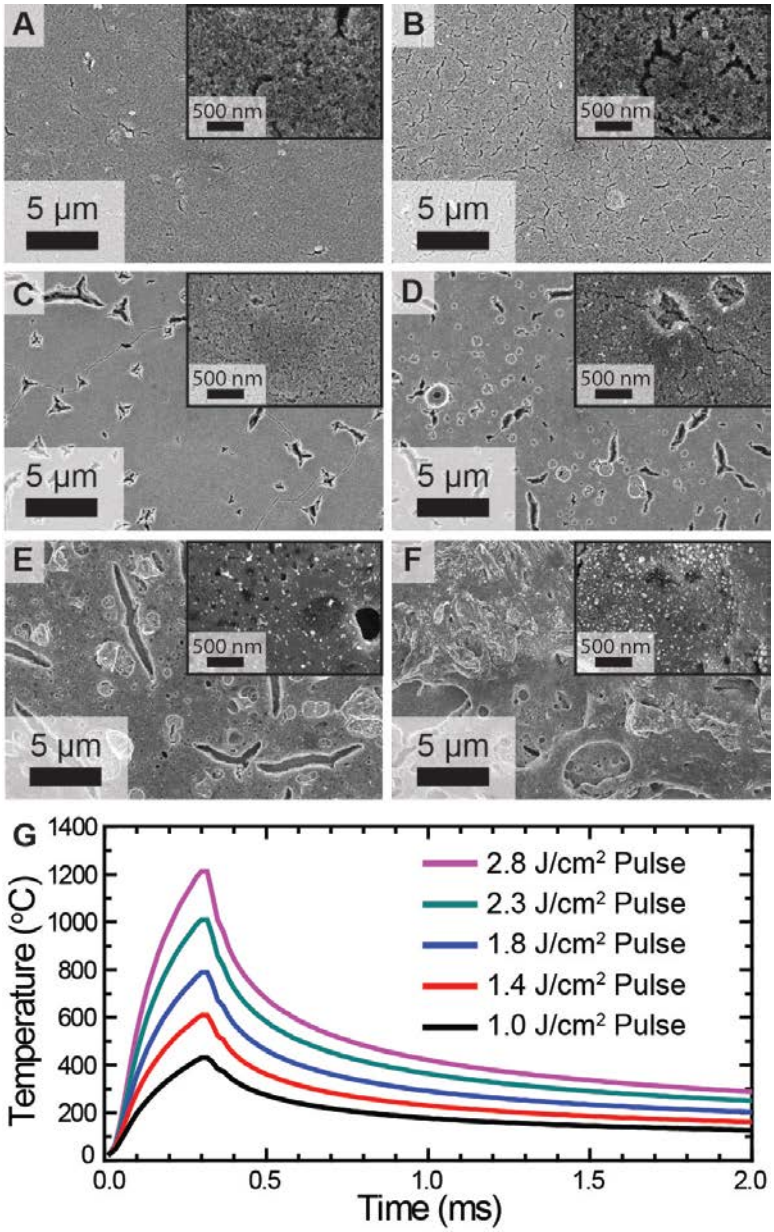

Figure 5.2 SEM images of a 1 µm thick ChaM-capped $CuInSe_2$ nanocrystal film (A) before photonic curing and after photonic curing pulses of (B) 1.0 J/cm^2, (C) 1.4 J/cm^2, (D) 1.8 J/cm^2, (E) 2.3 J/cm^2, and (F) 2.8 J/cm^2. Higher magnification is shown for each image in the insets, with the scale bars 500 nm long. (G) SimPulse modeling of the nanocrystal film temperature during photonic curing pulses of 1.0, 1.4, 1.8, 2.3, and 2.8 J/cm^2, each 300 µs in duration. For the model a layered structure was used with a 1 µm thick $CuInSe_2$ film on a 60 nm thick Au metal film deposited on a 1.1 mm thick soda-lime glass substrate.

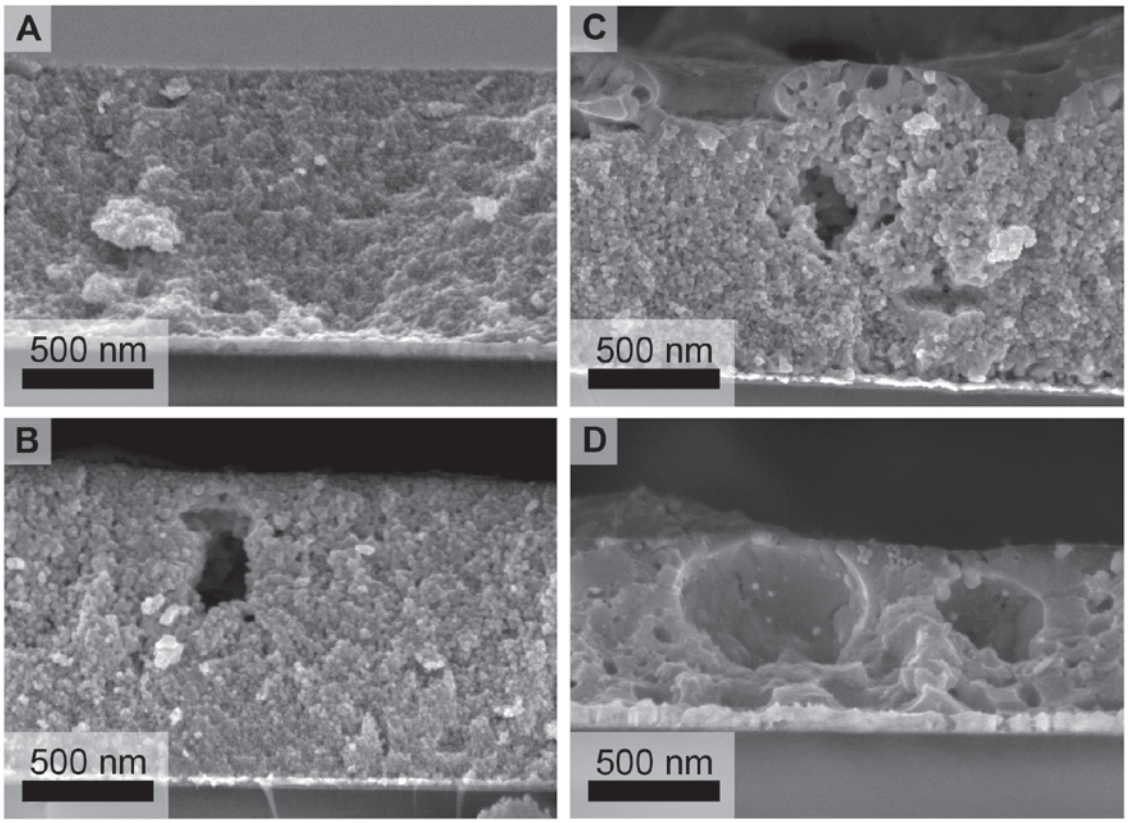

Figure 5.3 Cross-sectional SEM of ChaM-capped nanocrystals (A) before photonic curing and after photonic curing pulses of (B) 1.8 J/cm^2, (C) 2.3 J/cm^2, and (D) 2.8 J/cm^2.

Figure 5.3 shows SEM images of cross-sectioned ChaM-capped nanocrystal films. Prior to photonic curing, the nanocrystals are too small to be easily resolved by SEM (Fig. 5.3A). Curing the nanocrystal film at 1.8 J/cm^2 (Fig. 5.3B) leads to noticeable crystal grain growth; however, the crystal grain size is still nanometers in scale. The grain size is slightly larger near the surface of the film. Apparently, the nanocrystals near the surface of the film reach slightly higher temperature during the curing process. Higher pulse energies of 2.3 J/cm^2 (Fig. 5.3C) appear to increase the film temperature above the $CuInSe_2$ melting point and a layer of large $CuInSe_2$ crystal domains appear on the top of the film. Most of the film exhibits similar structure as the film cured at 1.8 J/cm^2. The

film treated with 2.8 J/cm2 pulse energy (Fig. 5.3D), forms even larger crystal grains, indicating that significant melting of the nanocrystals occurred. Unlike the oleylamine-capped nanocrystals, the melted $CuInSe_2$ layer remained adhered to the substrate in a relatively uniform layer. The film did also shrink considerably, due to the loss of void volume in the film.

5.3.2 XRD Peak Narrowing and Phase Transformations

Figure 5.4 shows X-ray diffraction (XRD) of oleylamine-capped and ChaM-capped nanocrystals before and after photonic curing. Both oleylamine-capped and ChaM-capped $CuInSe_2$ nanocrystals exhibit narrowing of the diffraction peaks with increased photonic curing pulse energy, indicating that crystal grain growth has occurred. For oleylamine-capped nanocrystals, the (112) $CuInSe_2$ diffraction peak (Fig. 5.4B) is broad for films with no photonic curing and films treated with a 1.6 J/cm^2 pulse, which indicates that the grains are still primarily nanocrystalline for the low 1.6 J/cm^2 pulse energy. When the pulse energy is increased, the (112) peak narrows considerably, which corresponds to the presence of large melt balls as seen in SEM (Fig. 5.1C-5.1F). For ChaM-capped nanocrystals, the crystal grains grow more gradually with increasing pulse energy (Fig. 5.4C). At 1.0 J/cm^2, there is only a small amount of peak narrowing. At 1.4 J/cm^2 and 1.8 J/cm^2, the peaks begin to narrow significantly, which corresponds to the sintering of the nanocrystals into larger grains without melting (Fig. 5.2C, 5.2D). At the highest pulse energies of 2.3 J/cm^2 and 2.8 J/cm^2, the primary (112) peak continues to narrow towards the instrument resolution. At these pulse energies, the nanocrystals reach temperatures where nanocrystal melting is possible, leading to very large grains. The emergence of secondary peaks at 25.1° and 28.5° is also observed, which likely

corresponds to the formation of wurtzite-phase $CuInSe_2$. Wurtzite is an unstable phase in bulk $CuInSe_2$, but can be stabilized in nanostructures.[13–15] In this case, the wurtzite phase may be kinetically trapped after nanocrystal melting due to the very rapid cooling of the film. It is not clear why the wurtzite phase only emerges for ChaM-capped nanocrystals.

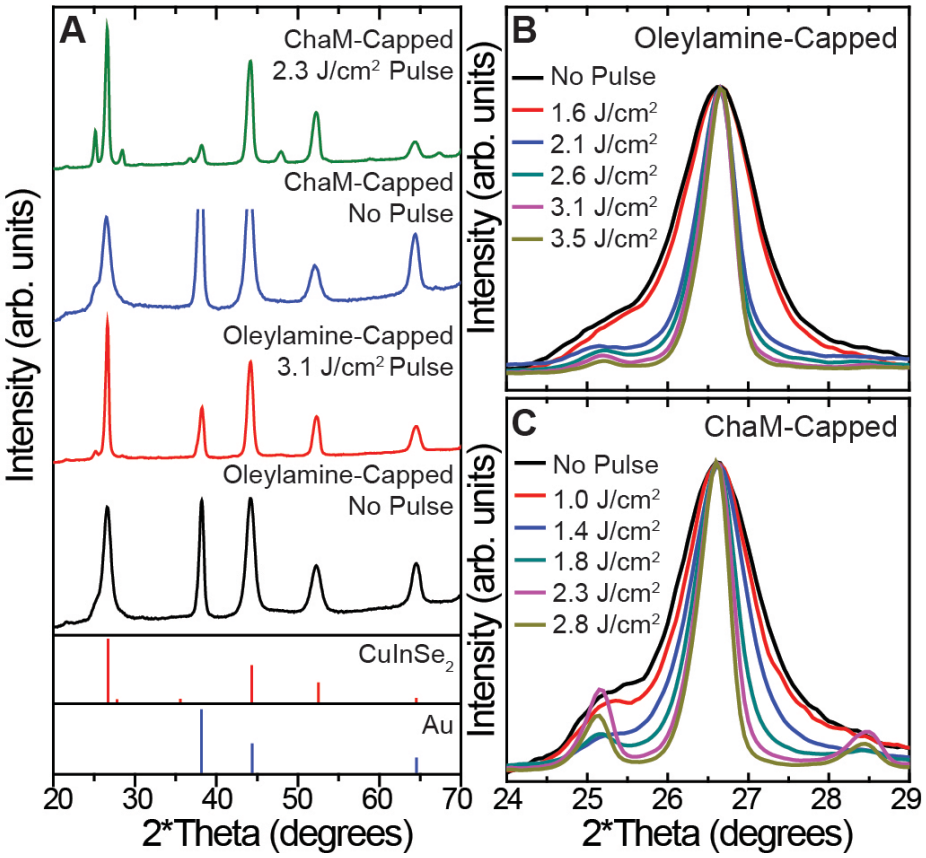

Figure 5.4 (A) XRD of both oleylamine-capped and ChaM-capped nanocrystals with and without photonic curing. The diffraction peaks for chalcopyrite $CuInSe_2$ (red lines, PDF #01-073-6321) and Au (blue lines, PDF #01-075-6560) are shown for reference. (B) XRD highlighting the (112) diffraction peak of $CuInSe_2$ for oleylamine-capped nanocrystals before photonic curing (black), and after photonic curing pulses of 1.6 J/cm^2 (red), 2.1 J/cm^2 (blue), 2.6 J/cm^2 (green), 3.1 J/cm^2 (purple), and 3.5 J/cm^2 (gold). (C) XRD highlighting the (112) diffraction peak of $CuInSe_2$ for ChaM-capped nanocrystals before photonic curing (black) and after photonic curing pulses of 1.0 J/cm^2 (red), 1.4 J/cm^2 (blue), 1.8 J/cm^2 (green), 2.3 J/cm^2 (purple), and 2.8 J/cm^2 (gold).

5.3.3 Device Performance

Thus far, photovoltaic devices fabricated from $CuInSe_2$ nanocrystal films sintered by photonic curing have not exhibited significant improvements in device performance. Figure 5.5 shows the photovoltaic device performance of ChaM-capped $CuInSe_2$ nanocrystal films treated with photonic curing. At the lowest pulse energy (Fig. 5.5B), there is no significant sintering or grain growth and the device performs similarly to the device with no photonic curing. At slightly higher pulse energies (Fig. 5.5C), the nanocrystals begin to neck together and sinter (see Figs. 5.2 and 5.4), which give the device improved short circuit current. However, this increased current also comes with a loss of open circuit voltage which could be caused by the formation of small cracks in the film. As the pulse energy increases, the nanocrystals further sinter together. At 1.8 J/cm^2 pulse energy, the enhanced electronic transport in the film is overwhelmed by the formation of cracks in the film and a dramatically lower voltage and fill factor (Fig. 5.5D). Finally, at very high pulse energies where the film begins to melt, all photovoltaic device performance is lost (Figs. 5.5E and 5.5F). Interestingly, these films are highly resistive, which is not typical for a film with large areas of exposed back contact or even highly sintered $CuInSe_2$. The high resistance could be due to the wurtize phase formation which occurs at these high photonic curing temperatures (See Figs. 5.3 and 5.4).

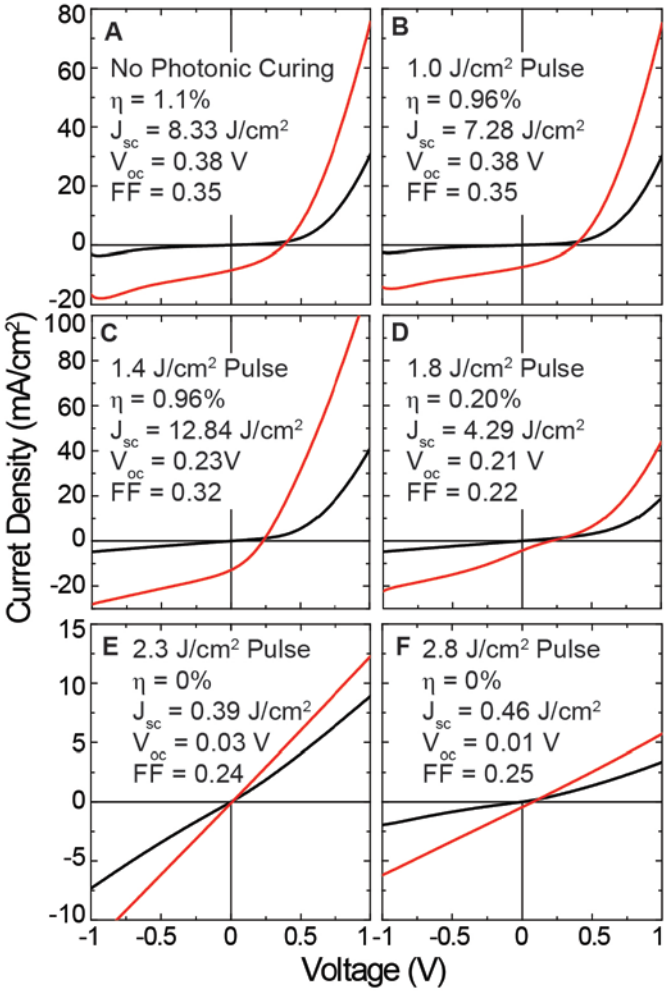

Figure 5.5 Current-voltage plots showing the dark (black curves) and light (red curves) photovoltaic response of ChaM-capped nanocrystals (A) before photonic curing and after photonic curing with pulse energies of (B) 1.0 J/cm^2, (C) 1.4 J/cm^2, (D) 1.8 J/cm^2, (E) 2.3 J/cm^2, and (F) 2.8 J/cm^2.

5.4 CONCLUSIONS

This work shows that $CuInSe_2$ nanocrystals can be sintered into uniform films without the use of high-temperature annealing or a selenium-rich atmosphere. Photonic curing did not sinter films made with oleylamine-capped nanocrystals until temperatures

exceeding the $CuInSe_2$ melting point are reached, which led to melt-ball formation and back contact exposure. Replacing oleylamine with inorganic ChaM ligand led to nanocrystal sintering without melting using the photonic curing process. This resulted in increased device currents for intermediate pulse energies. At high pulse energy, the nanocrystals exhibited wurtzite/chalcopyrite polytypism and devices had no device efficiency and very high series resistance as well. Utilizing ChaM ligands mostly eliminated back contact exposure after photonic curing, which is an important step towards achieving high device efficiency from nanocrystal films sintered by photonic curing.

5.5 REFERENCES

1. Stolle, C. J., Harvey, T. B. & Korgel, B. A. Nanocrystal photovoltaics: a review of recent progress. *Curr. Opin. Chem. Eng.* **2,** 160–167 (2013).
2. Ip, A. H. *et al.* Hybrid passivated colloidal quantum dot solids. *Nat. Nanotechnol.* **7,** 577–582 (2012).
3. Panthani, M. G. *et al.* High Efficiency Solution Processed Sintered CdTe Nanocrystal Solar Cells: The Role of Interfaces. *Nano Lett.* (2013). doi:10.1021/nl403912w
4. Harvey, T. B. *et al.* Copper Indium Gallium Selenide (CIGS) Photovoltaic Devices Made Using Multistep Selenization of Nanocrystal Films. *ACS Appl. Mater. Interfaces* **5,** 9134–9140 (2013).
5. Guo, Q., Ford, G. M., Agrawal, R. & Hillhouse, H. W. Ink formulation and low-temperature incorporation of sodium to yield 12% efficient Cu(In,Ga)(S,Se)2 solar cells from sulfide nanocrystal inks. *Prog. Photovolt. Res. Appl.* n/a–n/a (2012). doi:10.1002/pip.2200
6. Guo, Q. *et al.* Fabrication of 7.2% Efficient CZTSSe Solar Cells Using CZTS Nanocrystals. *J. Am. Chem. Soc.* **132,** 17384–17386 (2010).
7. Akhavan, V. A., Panthani, M. G., Goodfellow, B. W., Reid, D. K. & Korgel, B. A. Thickness-limited performance of CuInSe2 nanocrystal photovoltaic devices. *Opt. Express* **18,** A411–A420 (2010).

8. Stolle, C. J., Panthani, M. G., Harvey, T. B., Akhavan, V. A. & Korgel, B. A. Comparison of the Photovoltaic Response of Oleylamine and Inorganic Ligand-Capped CuInSe2 Nanocrystals. *ACS Appl. Mater. Interfaces* **4,** 2757–2761 (2012).

9. Jiang, C., Lee, J.-S. & Talapin, D. V. Soluble Precursors for CuInSe2, CuIn1–xGaxSe2, and Cu2ZnSn(S,Se)4 Based on Colloidal Nanocrystals and Molecular Metal Chalcogenide Surface Ligands. *J. Am. Chem. Soc.* **134,** 5010–5013 (2012).

10. Schroder, K., A. Mechanisms of photonic curing: processing high temperatures on low temperature substrates. *Nanotech Conf. Expo 2011 Interdiscip. Integr. Forum Nanotechnol. Biotechnol. Microtechnology* **2,**

11. Stolle, C. J. *et al.* Multiexciton Solar Cells of CuInSe2 Nanocrystals. *J. Phys. Chem. Lett.* **5,** 304–309 (2014).

12. Kovalenko, M. V., Scheele, M. & Talapin, D. V. Colloidal Nanocrystals with Molecular Metal Chalcogenide Surface Ligands. *Science* **324,** 1417–1420 (2009).

13. Steinhagen, C. *et al.* Solution−Liquid−Solid Synthesis of CuInSe2 Nanowires and Their Implementation in Photovoltaic Devices. *ACS Appl. Mater. Interfaces* **3,** 1781–1785 (2011).

14. Norako, M. E. & Brutchey, R. L. Synthesis of Metastable Wurtzite CuInSe2 Nanocrystals. *Chem. Mater.* **22,** 1613–1615 (2010).

15. Wang, J.-J., Wang, Y.-Q., Cao, F.-F., Guo, Y.-G. & Wan, L.-J. Synthesis of Monodispersed Wurtzite Structure CuInSe2 Nanocrystals and Their Application in High-Performance Organic−Inorganic Hybrid Photodetectors. *J. Am. Chem. Soc.* **132,** 12218–12221 (2010).

Chapter 6: Ligand Removal with Photonic Curing: Enhanced Nanocrystal Coupling and Multiexciton Extraction††

6.1 INTRODUCTION

A maximum of 34% of the energy available in sunlight can be converted to electricity by a single junction solar cell, known as the Shockley-Queisser limit.[1] The semiconductor in the device does not absorb photons with energy less than its band gap energy and photon energy greater than the band gap is lost as heat due to the rapid relaxation of the photoexcited electron and hole to their band minima before they can be extracted as electrical current. One way to surpass the Shockley-Queisser limit is to use quantum dots that convert high-energy photons into multiple electron-hole pairs that can be extracted as photocurrent by the device.[2,3] Colloidal nanocrystals provide a convenient source of quantum dots in which multiexciton generation (MEG) has been observed optically from a host of materials, including PbS, PbSe, PbTe, CdSe, InAs, and Si.[4–8] Extraction of more than one electron per absorbed photon as electrical current in devices has also been reported,[9–12] with a few instances of device quantum efficiencies (QE) exceeding 100%—PbS (internal QE only),[13] PbSe (external QE)[14] nanocrystal solar cells and an organic device exhibiting a related process of singlet fission.[15] Here, we

†† Reproduced in part with permission from: Stolle, C. Jackson; Harvey, Taylor B.; Pernik, Douglas R.; Hibbert, Jarett I.; Du, Jiang; Rhee, DongJoon; Akhavan, Vahid A.; Schaller, Richard D.; Korgel, Brian A., Multiexciton Solar Cells of $CuInSe_2$ Nanocrystals, *J. Phys. Chem. Lett.* (2013) **5**, 304-309. Copyright 2013 American Chemical Society. CJS designed the experiments, fabricated and characterized the films and devices, collected and analyzed the data, and wrote the manuscript. TBH assisted with experimental design, device and film fabrication and characterization, and data analysis related to photonic curing. DRP assisted with experimental design, film characterization, and data analysis related to transient absorption spectroscopy. JIH, JD, DR, and VAA assisted with device and film fabrication and characterization related to photonic curing. RDS assisted with experimental design, data collection, and data analysis for transient absorption spectroscopy. BAK provided funding, guidance, and assisted with writing the manuscript.

report PV devices of $CuInSe_2$ nanocrystals with multiexciton generation and extraction and peak external quantum efficiencies of just over 125%.

$CuInSe_2$ is an important model semiconductor for PV devices that is closely related to $Cu(In_xGa_{1-x})Se_2$ (CIGS), which holds the record for highest device efficiency of all thin film semiconductors at just over 20%.[16] PV devices made from ink-deposited $CuInSe_2$ nanocrystals have reached power conversion efficiencies of 3%, limited by poor charge transport.[17–19] Ink-deposited $Cu(In_xGa_{1-x})S_2$ nanocrystals can be sintered into polycrystalline films by heating (>500 °C) under selenium vapor (i.e., selenization) to achieve much higher efficiencies of just over 12%.[20,21] To try to avoid the need for high temperature selenization, an alternative nanocrystal film processing technique called photonic curing was explored here to improve charge transport in the nanocrystal film. Photonic curing was carried out using a PulseForge 3300 (NovaCentrix) tool that uses pulsed light from a flash lamp with Xenon fill gas with spectrally broad blackbody radiation that can produce very rapid heating to high temperature. Photonic curing can provide enough energy to sinter nanocrystals,[22] but in this study relatively mild pulse conditions were used to remove organic ligands and bring nanocrystals into better electrical contact without destroying their nanoscale dimensions. Nanocrystal films processed in this way were found to yield PVs with peak external quantum efficiencies (EQE) exceeding 100%, indicating the occurrence of multiple exciton generation (MEG) and extraction from the devices. Transient absorption spectroscopy was employed to verify that MEG does indeed occur in the nanocrystal films.

6.2 EXPERIMENTAL METHODS

6.2.1 Materials

Oleylamine (OLA) was purchased from TCI America; copper (I) chloride (CuCl; 99.99+%), gallium (III) chloride ($GaCl_3$; 99.999+%), selenium powder (Se; 99.99%), diphenylphosphine (DPP, 98%), thiourea (< 99.0%), and cadmium sulfate ($CdSO_4$; 99.999%) from Aldrich Chemical Co.; indium (III) chloride ($InCl_3$; 99.999%) from Strem Chemicals; ammonium hydroxide (18M NH_3; ACS certified), toluene (99.99%), ethanol (absolute) from Fischer Scientific. Prior to use, oleylamine was degassed overnight under vacuum at 110 °C. All other chemicals were used as received without further purification. Copper (I) chloride, indium (III) chloride, diphenylphosphine, and degassed oleylamine were stored in a N_2-filled glovebox.

6.2.2 $CuInSe_2$ nanocrystal synthesis

$CuInSe_2$ nanocrystals were synthesized according to previously reported methods.[19] Briefly, 2 mmol of CuCl, 2 mmol of $InCl_3$, and 20 mL degassed OLA were loaded into a 3-neck flask inside an N_2-filled glovebox. DPP:Se solution was made by mixing 4 mmol each of Se powder and DPP and diluting with 2mL OLA. The flask was sealed, removed from the glovebox, and attached to a Schlenk line. The reaction mixture was stirred and heated to 110 °C under vacuum for a 30 minute period. It was then blanketed with nitrogen and heated to 180°C at which point the DPP:Se solution was injected. The flask was heated to 240 °C and held for 30 minutes before the heating mantle was removed, allowing it to cool to room temperature. The nanocrystals were precipitated with excess ethanol and centrifuged at 4000 rpm for 2 min. The supernatant was discarded and the precipitate was redispersed in 5 mL of toluene. The dispersion

was centrifuged at 4000 rpm for 1 min to precipitate poorly-capped nanocrystals. The supernatant was transferred to a centrifuge tube. Ethanol was added dropwise until the mixture became slightly turbid. After centrifugation at 4000 rpm for 1 min the supernatant was discarded, and the precipitate was dispersed in toluene. The nanocrystal dispersion was stored in a N_2-filled glovebox.

6.2.3 Film Deposition

Soda lime glass substrates (Delta Technologies) were cleaned by sonication for 10 minutes in 1:1 IPA/acetone followed by sonication in DI water for 10 minutes. 5 nm of Cr followed by 60 nm of Au (Kurt J. Lesker Co.) was then deposited by thermal evaporation. $CuInSe_2$ nanocrystals were spray-deposited on the Au-coated substrates in approximately 500 nm thick layers from toluene dispersions (~20 mg/ml).

6.2.4 PV Device Fabrication

Photonic curing was carried out using a PulseForge 3300 (NovaCentrix). Films were loaded into a 2 inch thick cylindrical stainless steel chamber with a 7 inch diameter and a 6 inch diameter circular quartz window on the top surface. The chamber was purged with nitrogen for one minute, sealed, positioned in the center of the xenon lamp illumination area, and then pulsed. A single 160 μs light pulse was used on each film, and the pulse voltages varied from 500 V to 640 V. The energy of each pulse was 2 J/cm^2 to 3 J/cm^2 as determined by bolometer (NovaCentrix) readings at the same position and distance from the xenon lamps. 10 pulses were measured at each pulse condition and averaged to determine energy input.

Nanocrystal surface repassivations were carried out after photonic curing by soaking the films for 60 seconds in either hexanethiol, pyridine, oleylamine, CTAB dissolved in methanol (1:9 by weight), or 5 mM InSe-ChaM ligands dispersed in DMSO. The films are then rinsed with methanol and dried under a stream of dry air.

Devices were completed by depositing layers of CdS, ZnO, and ITO after the photonic curing process. A CdS layer (~20 nm thick) was deposited on the nanocrystal layer by drop casting 700 µL of CdS precursor solution (1.25 mL of 15 mM $CdSO_4$, 2.2 mL of 1.5 M thiourea, and 2.8 mL of 18 M NH_4OH in water) onto the $CuInSe_2$ film heated to 95 °C on a hot plate. The $CuInSe_2$ film was covered with an inverted Petri dish for two minutes while the reaction progressed. The substrate was then removed from the hot plate, rinsed with DI water, and dried under a compressed air stream. A 40 nm thick layer of ZnO followed by a 600 nm thick layer of ITO are deposited by RF-sputtering under a 2 mtorr Ar atmosphere.

6.2.5 Characterization

X-ray diffraction (XRD) was performed on a Rigaku R-Axis Spider diffractometer with an image-plate detector and using graphite monochromatized Cu Kα (λ = 1.5418 Å) radiation operated at 40 kV and 40 mA. Data were collected on nanocrystal films with and without pulse treatment on Au-coated soda-lime glass substrates. Samples were placed at a 10° glancing angle and rotated at 1° per second for 10 min. 2D diffraction patterns were radially integrated using 2DP V.1.0 Data Processing Software (Rigaku) for 2-Dimensional detectors with subtraction of background scattering. XRD was also performed on a Bruker-Nonius D8 advance θ−2θ powder diffractometer equipped with a Bruker Sol-X Si(Li) solid state detector and 1.54 Å

radiation (Cu Kα). Data were collected at 0.01 increments of 2θ at a scan rate of 6 °/min. Scanning electron microscopy (SEM) was performed on a Zeiss Supra 40 VP SEM operated at 5 keV accelerating voltage through an In-lens detector. Transmission electron microscopy (TEM) was performed on an FEI Tecnai G2 Spirit BioTwin microscopy operated at 80 kV. Thermogravimetric analysis (TGA) was collected using a Mettler-Toledo DCS/TGA instrument with a temperature ramp of 20 °C /min under a N_2 flow. Fourier transform infrared spectroscopy (FTIR) was acquired using a Thermo Mattson Infinity Gold FTIR with a Harrick VariGART crystal. UV-Vis-NIR absorbance spectra were acquired using a Cary 500 spectrophotometer equipped with an integrating sphere to collect diffuse reflection and transmission. Transient absorption (TA) measurements were performed using an 800 nm, 35 fs pulse width, 2 kHz amplified Ti:sapphire laser. Pump pulses at 800 or 400 nm were spatially overlapped with a mechanically delayed white light probe that was produced by focusing 5% of the amplifier output into a 2-mm thick sapphire plate.

6.2.6 PV Device Testing

A Keithley 2400 general purpose source meter was used to collect current-voltage characteristics with and without exposure to a Xenon lamp solar simulator (Newport) equipped with an AM1.5G optical filter. The light source was calibrated with a NIST-calibrated Si photodiode (Hamamatsu, S1787-08). Neutral density filters with optical densities of 0.1, 0.3, 0.6, and 1.0 where used to measure PV characteristics at lower intensity light. External quantum efficiency (EQE) was measured using monochromatic light generated using a commercial monochromator (Newport Cornerstone 260 1/4M) chopped at 213 Hz and focused to a spot size of 1 mm diameter on the active region.

EQE measurements were made with the device at zero bias at wavelengths ranging from 350 and 1200 nm in 10 nm increments using a lock-in-amplifier (Stanford Research Systems, model SR830) with and without a 50 mW/cm2 white light bias. Monochromated light intensity was calibrated using calibrated photodiodes of silicon (Hamamatsu) and germanium (Judson) and white light bias intensity was measured with a thermopile (Newport 818P-020-12). Neutral density filters were used to reduce the monochromated and light bias intensity. For additional confirmation, external quantum efficiency measurements were also taken using a QEX10 Solar Cell Spectral Response Measurement System purchased commercially from PV Measurements, Inc. The system uses monochromatic light chopped at 100 Hz and is calibrated using Si and Ge diodes and shows repeatability of better than 0.6% for the 300-400 nm range and better than 0.3% for the 400-1000 nm range.

6.3 RESULTS AND DISCUSSION

6.3.1 Ligand Removal

PV devices were made by spray-depositing $CuInSe_2$ nanocrystals from toluene dispersions on Au-coated soda lime glass substrates similar to Akhavan, et al.,[17] but the nanocrystal films were cured (Figure 6.1) in a closed chamber with a quartz window with a single 160 μs light pulse with flux ranging from 2-3 J/cm^2 before adding the CdS buffer layer and top contact. Nanocrystal films pulsed with 2.2 J/cm^2 light reach about 600 °C within 1 ms, which removes oleylamine ligand but does not induce grain growth.

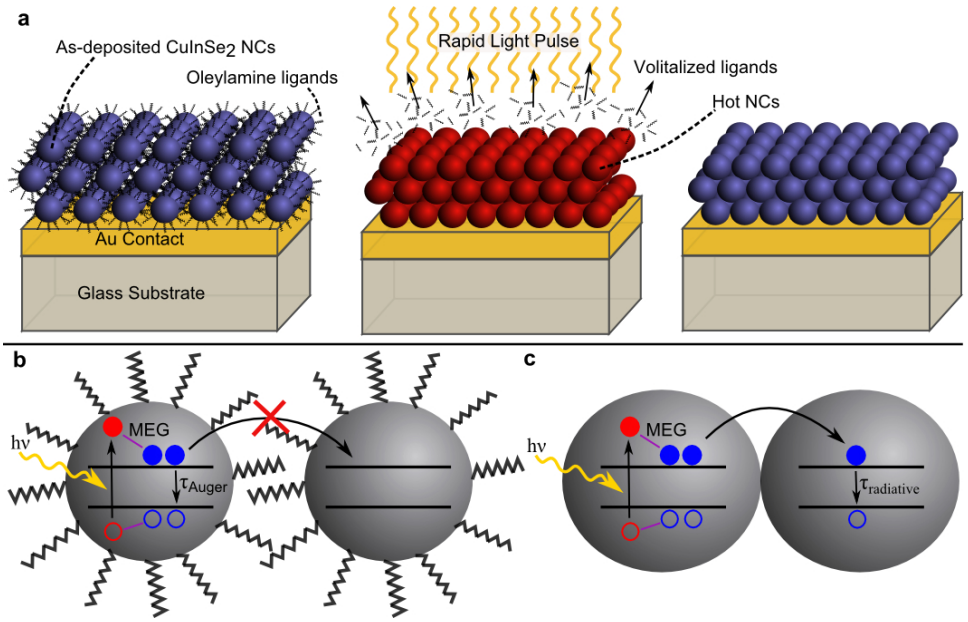

Figure 6.1 Photonic curing of nanocrystal films on Au-coated glass substrates. (a) Photonic curing can be used to remove oleylamine capping ligands from the CuInSe2 nanocrystal film without inducing grain growth. (b) When the capping ligands are present, they inhibit the collection of multiexcitons from the film, leading to electron-hole recombination by Auger recombination. (c) Without the ligand barrier between nanocrystals, multiexciton transport becomes much more probable.

Loss of oleylamine capping ligands during photonic curing was confirmed by TGA and FTIR of the nanocrystal film. Oleylamine vaporizes from the nanocrystal film between about 150 °C and 400 °C. The TGA data in Figure 6.2 shows less mass loss in this temperature range from films that had been cured and there is systematically decreasing amount of mass loss from nanocrystal films treated with increasing pulse power. The FTIR data in Figure 6.3 shows loss of the C-H stretch absorption feature after photonic curing which is representative of the oleylamine capping ligands.

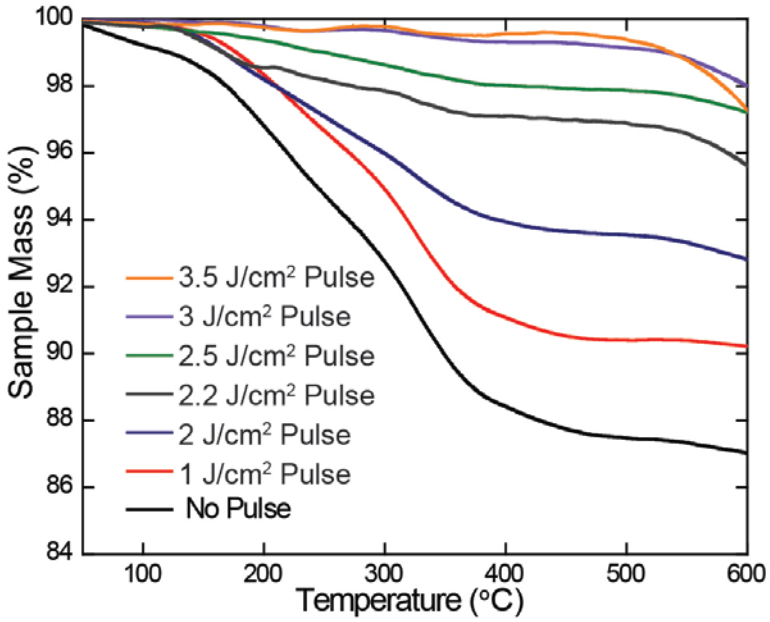

Figure 6.2 Thermogravimetric analysis (TGA) of $CuInSe_2$ nanocrystals processed by photonic curing using various pulse conditions.

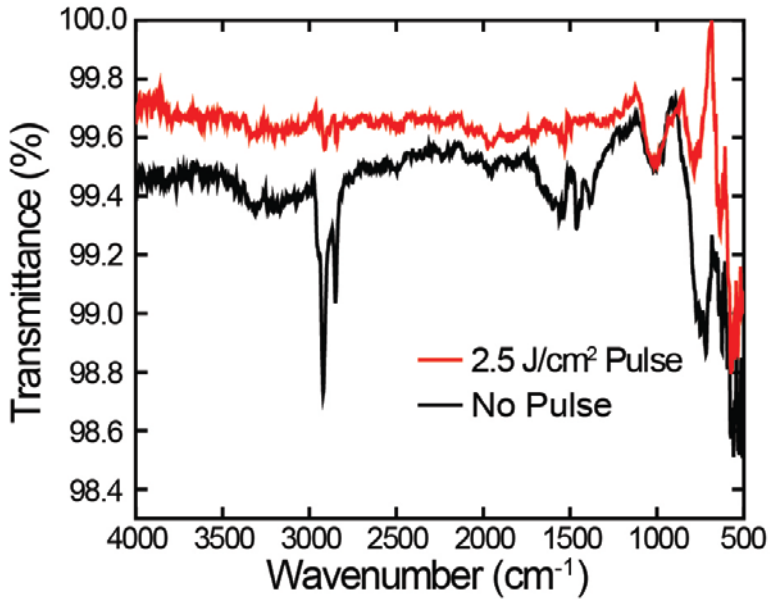

Figure 6.3 FTIR analysis of $CuInSe_2$ nanocrystals without photonic curing (black) and treated with a 2.5 J/cm^2 pulse.

Figure 6.4 shows the calculated average temperature of a 500 nm thick $CuInSe_2$ nanocrystal layer on 60 nm thick Au on soda lime glass (1.1 mm thick) after a single (160 µs) pulse. The temperature was calculated using SimPulse software from NovaCentrix. The extent of nanocrystal sintering as a result of photonic curing was determined by examining X-ray diffraction peak widths. Figure 6.5 shows the (112) diffraction peak for chalcopyrite $CuInSe_2$. Decreasing peak width indicates an increase in crystal domain size. Using a Scherrer analysis, the as-deposited nanocrystals are 8.3 nm in diameter, which matches well with the size measured in TEM (Figure 6.6). After curing at 2.2 J/cm^2 and 2.5 J/cm^2, the nanocrystal size is 9.2 and 23.1 nm respectively. After curing at 3 J/cm^2 and 3.5 J/cm^2, the nanocrystals have sintered and the size is too large to calculate using Scherrer analysis.

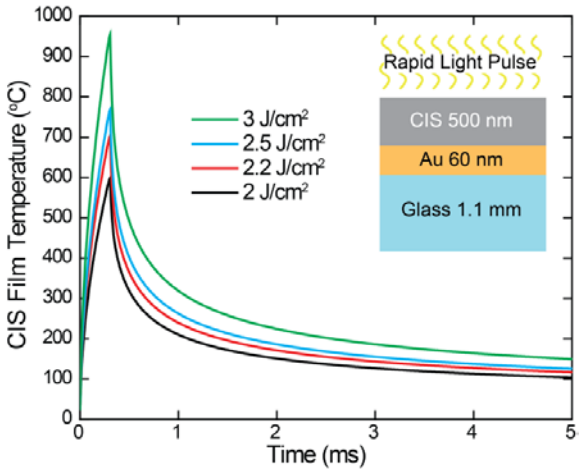

Figure 6.4 Temperature of a 500 nm thick $CuInSe_2$ (CIS) nanocrystal layer on 60 nm thick Au on soda lime glass (1.1 mm thick) induced by a single (160 µs) photonic curing pulse (calculated using SimPulse software from NovaCentrix).

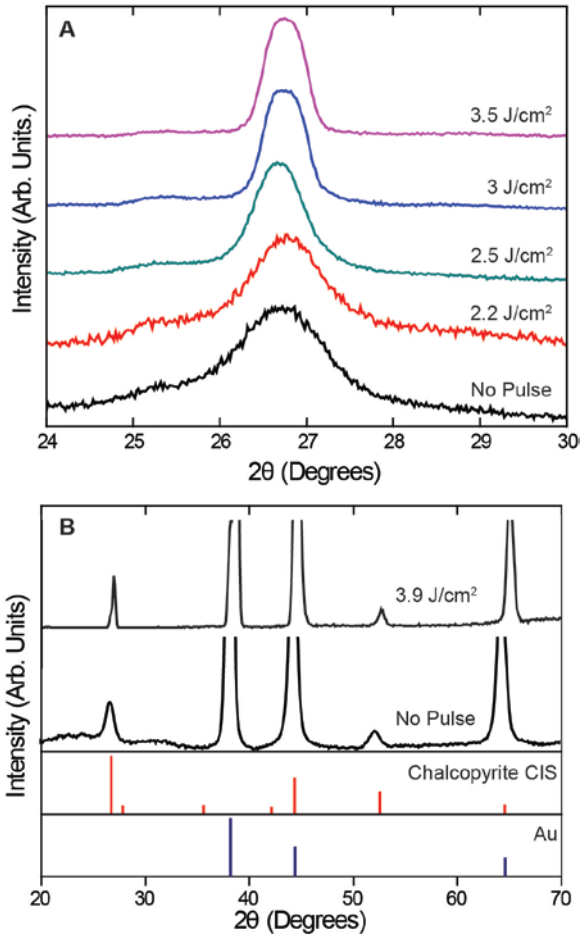

Figure 6.5 (A) X-ray diffraction (XRD) data highlighting the (112) diffraction peak of chalcopyrite $CuInSe_2$. The crystal sizes for each pulse condition were calculated using Scherrer analysis. Prior to photonic curing, the nanocrystals are 8.3 nm in diameter, which matches well with the size measured in TEM. After curing at 2.2 J/cm^2 and 2.5 J/cm^2, the nanocrystal size is 9.2 and 23.1 nm respectively. After curing at 3 J/cm^2 and 3.5 J/cm^2, the nanocrystals have sintered and the size is too large to calculate using Scherrer analysis. (B) XRD data showing a nanocrystal film before and after curing at 3.9 J/cm^2. The red reference lines are for chalcopyrite $CuInSe_2$ (PDF #01-073-6321) and the blue lines are for Au (the back contact material) (PDF #01-075-6560).

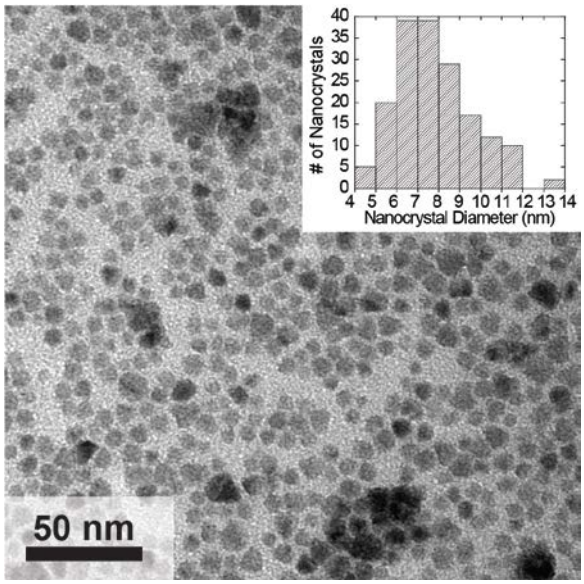

Figure 6.6 TEM image of $CuInSe_2$ nanocrystals with average particle diameter of 8.1±2.1 nm based on the histogram shown in the inset generated from the TEM image.

6.3.2 Film Morphology and Device Results

Figure 6.7 shows scanning electron microscope (SEM) images of $CuInSe_2$ nanocrystal films before and after curing with 2.2 J/cm^2 and >3 J/cm^2 exposure. The nanocrystals remain small grains after 2.2 J/cm^2 exposure, but clearly grow into larger grains after >3 J/cm^2 exposure.

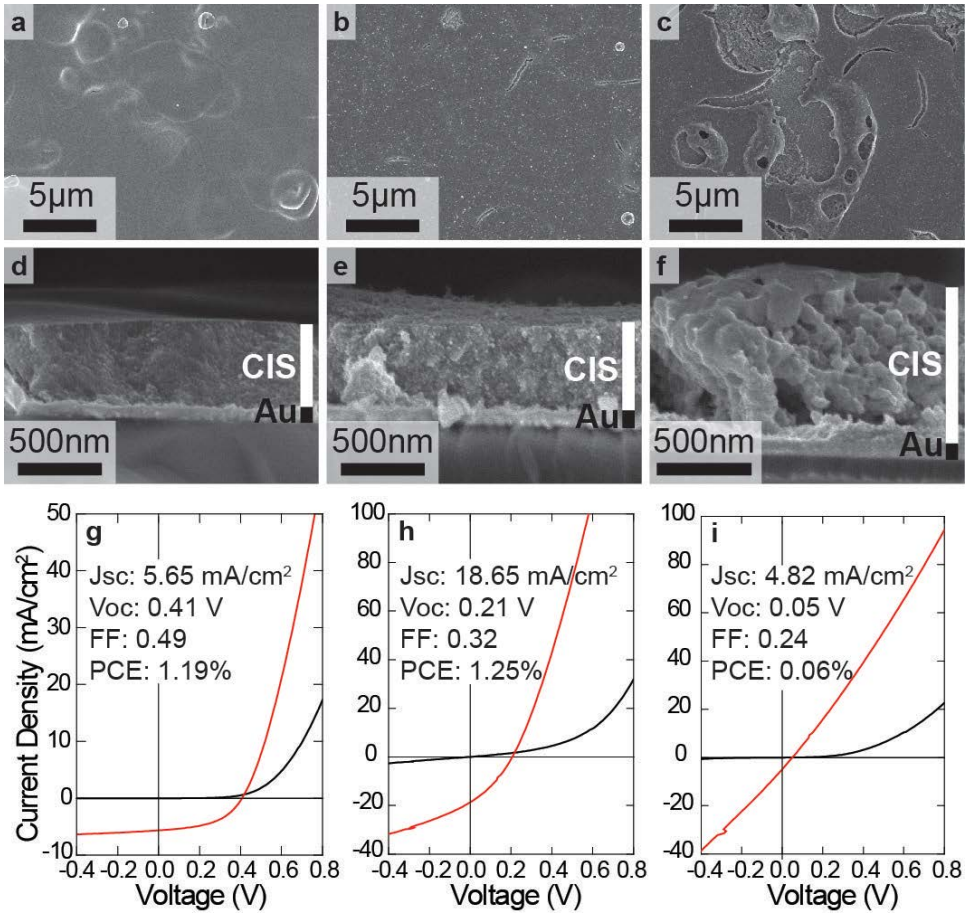

Figure 6.7 $CuInSe_2$ nanocrystal layers before and after photonic curing and their PV device performance. Top-down and cross-section SEM images of oleylamine-capped $CuInSe_2$ (CIS) nanocrystal film on Au-coated glass (a, d) before and after photonic curing with (b, e) 2.2 J/cm^2 and (c, f) and 3 J/cm^2 pulse fluence. (g, h, i) Corresponding current-voltage measurements (black curve is dark current; red curve is measured under AM1.5G illumination (100 mW/cm^2)) of devices made with the nanocrystal films are provided below the SEM images.

Although the nanocrystals could be grown into large grains by photonic curing, devices made from these sintered nanocrystals performed very poorly, as shown in Figure 6.6. Exposure of 3 J/cm^2 sintered the nanocrystals, but also led to dewetting by the formation of melt balls, leaving significant back contact exposed and devices with almost

no short circuit current. In contrast, devices made with nanocrystals cured using 2.2 J/cm^2 exposure gave reasonable device response with power conversion efficiency (PCE) of 1.25%, similar to the devices made with as-deposited nanocrystals (PCE=1.19%). The biggest change in device response after photonic curing is a large increase in short circuit current (Jsc) and drop in open circuit voltage (Voc), for example in Figures 2g the Jsc and Voc changed from 5.65 mA/cm^2 to 18.65 mA/cm^2 and 0.41 V to 0.21 V, respectively.

6.3.3 Quantum Efficiency Analysis

EQE (also known as IPCE) measurements showed that most of the increased short circuit current in the devices made with cured nanocrystals occurred in the short wavelength (<600 nm) range. Figure 6.8A shows a comparison of EQE spectra from PVs made with as-deposited $CuInSe_2$ nanocrystals and nanocrystals that had been processed by photonic curing at 2.2 J/cm^2. The as-deposited $CuInSe_2$ nanocrystal device has a peak EQE of about 25%, whereas the peak EQE of the cured nanocrystal device is 123%. It was also found that the application of a white light bias had a significant influence on the EQE spectra of the cured nanocrystal devices, which is usually not the case for the as-deposited nanocrystal devices (Figure 6.8B).

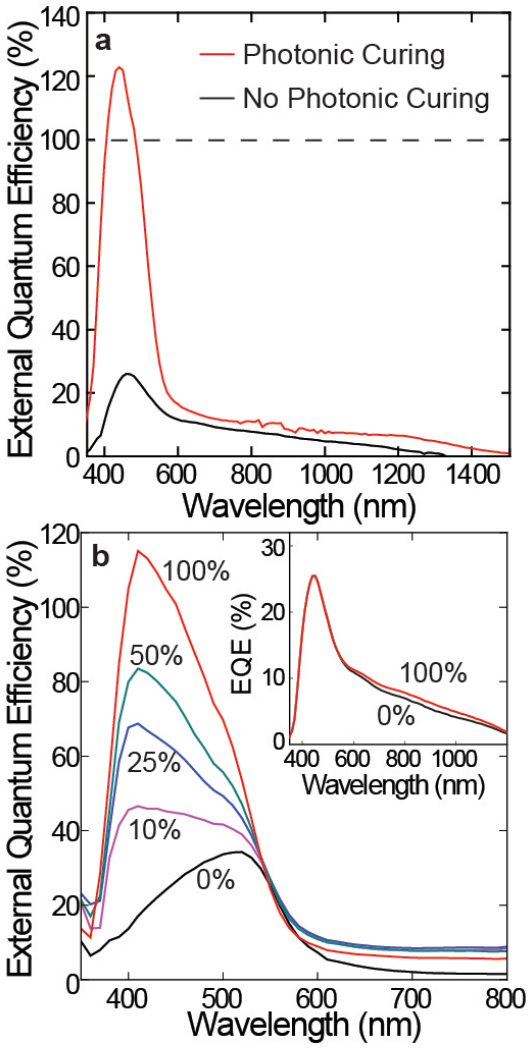

Figure 6.8 External quantum efficiency (EQE) enhancements resulting from photonic curing of the $CuInSe_2$ nanocrystal layer used in PV devices. (a) EQE measurements taken under white light bias for $CuInSe_2$ nanocrystal devices without photonic curing (black curve) compared to the device made with cured (2.2 J/cm^2 pulse fluence) nanocrystals (red curve). The short circuit currents determined from these data, of 4.95 mA/cm^2 and 14.29 mA/cm^2, are consistent with the short circuit currents measured under AM1.5 illumination (100 mW/cm^2). (b) EQE measured under varying white light bias intensity (100%, 50%, 25%, 10%, and 0% of the 50 mW/cm^2 bias light) with the same intensity of monochromated probe light. There is no change in EQE for the device made with as-deposited nanocrystals (inset), but the EQE decreases significantly for the cured device when the white light bias intensity was reduced to the amounts indicated.

Figure 6.9 shows the external quantum efficiency (EQE), internal quantum efficiency (IQE), and absorptance for a PV device made with CuInSe2 nanocrystals cured with a 2.2 J/cm2 pulse. The device absorptance is measured by UV-Vis with an integrating sphere to collect direct and diffuse reflectance and is given as 1-R, where R is the total device reflectance. IQE is calculated by dividing the device EQE by the absorptance. The peak EQE for this device is 123% and the peak IQE is 143%.

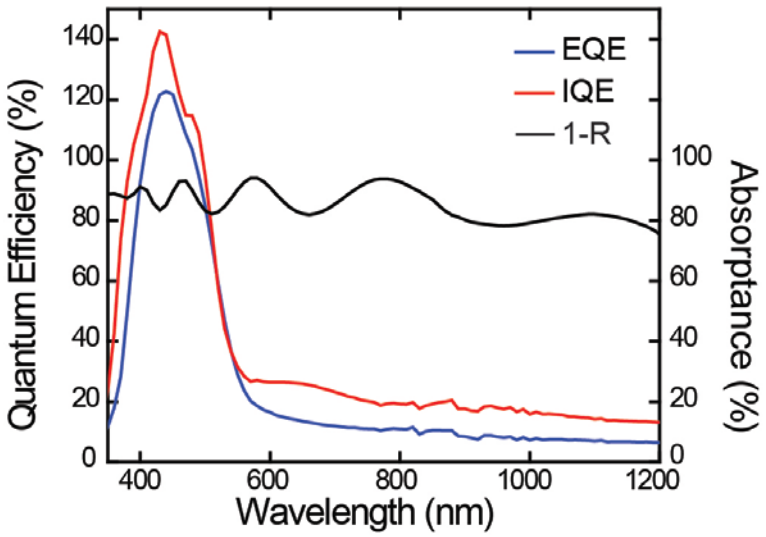

Figure 6.9 External quantum efficiency (blue), internal quantum efficiency (red), and absorptance (black) for a PV device made with $CuInSe_2$ nanocrystals and cured with a 2.2 J/cm^2 pulse.

The substantial effect of white light bias on the EQE of cured nanocrystal devices indicates that the curing process introduces traps into the nanocrystal layer that hinder charge extraction under low light conditions.[23,24] EQE measurements typically use a low-intensity monochromated probe beam to generate carriers in the device, which often does

not represent true device performance under full sunlight. EQE measurements should be acquired under realistic illumination conditions (i.e., under full sunlight), and a white light bias with intensity near 100 mW/cm^2 is usually applied.[25] The probe beam is passed through a chopper, and a lock-in amplifier is used to measure the current generated only by the probe beam and not by the unchopped bias light. EQE measurements taken without white light bias can give anomalous results.[23–26] For example, traps in the CdS layer in CdTe/CdS devices usually filled under AM 1.5 illumination remain empty under low light conditions, significantly reducing device currents and leading to artificially low EQE values if white light bias is not used.[23–26] CdTe and CIGS PV devices can also exhibit EQE variations with light bias intensity due to photoconductive CdS.[23,24,26,27] In our case, the CdS layer is the same for all devices and the EQE of the as-deposited nanocrystal device is not affected by the white light bias intensity (Figure 6.8 (B inset)).

6.3.4 Possible Anomalous Effects

There have been numerous discussions about anomalous EQE measurements.[23–27] One common anomalous result related to light biasing comes from photoconductive gain, as in vapor-deposited CdTe devices with photoconductive CdS layers.[23,27] Photoconductive gain can lead to an erroneously large EQE when a red light bias is applied (bias light with high energy photons removed by a filter) and the photocurrent is measured using blue probe light. In this case, the red bias light is not absorbed by the CdS layer and only generates charges in the CdTe film. The blue probe light is absorbed by the CdS layer and can modulate its conductivity. Photons generated by the red light bias can be more easily extracted when the CdS conductivity is increased by illumination with blue light. Thus, photoconductive gain in EQE occurs as the modulation of the CdS

conductivity at the probe frequency causes charges not generated by the probe to be extracted and measured by the lock-in amplifier.[23] This effect has also been reported for a white light bias in CdTe/CdS solar cells with the increase in EQE also attributed to modulation of the CdS layer.[27] Therefore, experiments were carried out to rule out the occurrence of photoconductive gain in the $CuInSe_2$ nanocrystal devices. Anomalous effects can also be observed if the charge carrier kinetics are slow compared to the chopping frequency, since such carriers may not be able to be extracted at the chopper frequency. We conducted EQE measurements on two different systems with two different frequencies (100 Hz and 213 Hz). The EQE is very similar, demonstrating that the measurements are not limited by charge carrier kinetics (Fig. 6.10).

The white light bias lamp in the EQE testing setup has an intensity of ~50 mW/cm^2 (about half the intensity AM 1.5 solar radiation) and the monochromated light intensity is only ~50 $\mu W/cm^2$, which is three orders of magnitude less than the bias light, making the modulation of the CdS conductivity very small compared to the conductivity increase from the bias lamp under standard white light bias. To confirm that photoconductive gain does not influence the measured EQE under white light bias, the EQE was measured under different probe beam intensity. Neutral density filters were used to cut the light intensity of the monochromated probe beam. In the absence of photoconductive gain, the reduction in the probe beam should yield a proportional reduction in peak EQE and J_{sc}. Photoconductive gain on the other hand results in a less significant decrease in peak EQE and J_{sc}, as charges generated by the bias light would still be measured. Figure 6.11 shows EQE measurements of a cured nanocrystal sample with peak EQE >100% under white light bias. The monochromated probe is cut to 80%, 50%, 25%, and 10% of its original intensity using neutral density filters. The EQE and

J_{sc} match the expected values and the sample shows no photoconductive gain (See Table 6.1).

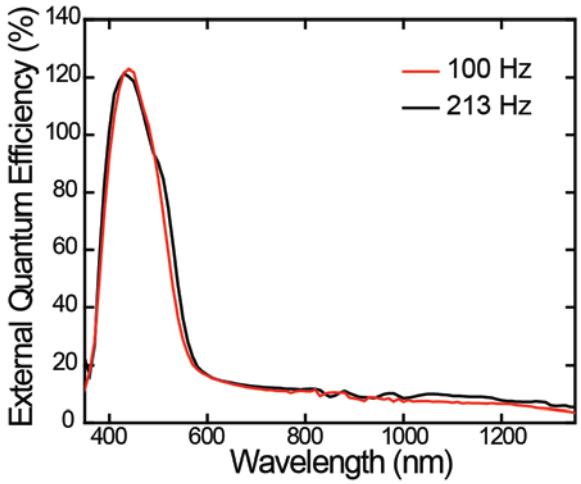

Figure 6.10 External quantum efficiency of a PV device made with $CuInSe_2$ nanocrystals cured at 2.2 J/cm^2 taken with two separate testing setups. The setup using the Newport monochrometer had a probe beam chopped at 213 Hz and the commercial setup from PV Measurements, Inc. had a probe beam chopped at 100 Hz.

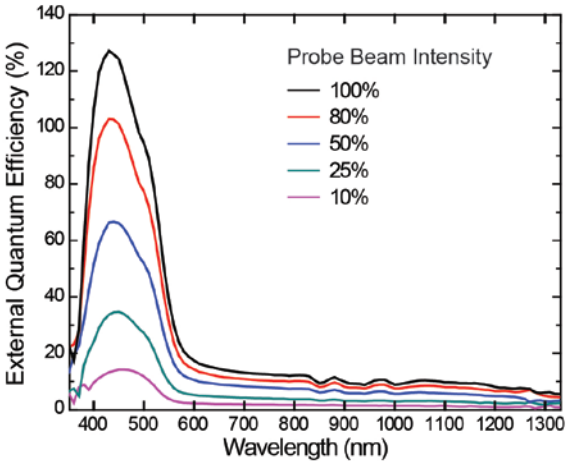

Figure 6.11 External quantum efficiency of a PV device made with $CuInSe_2$ nanocrystals cured at 2.2 J/cm2. Neutral density filters are used to cut the monochromated probe beam to 100% (no filter, black), 80% (red), 50% (blue), 25% (green), and 10% (pink) of its original intensity. The white light bias intensity (~50 mW/cm2) was the same for all measurements.

Probe Beam Intensity (compared to maximum)	Peak EQE (%)	% Change in EQE	Calculated J_{sc} (mA/cm^2)	% Change in Calculated J_{sc}
100%	127		14.3	
80%	103	81%	11.4	80%
50%	66	52%	7.5	52%
25%	34	27%	3.8	27%
10%	14	11%	1.6	11%

Table 6.1 Table showing peak EQE and calculated Jsc for each probe beam intensity from Figure 6.11.

Lastly, the measured J_{sc} values of the $CuInSe_2$ nanocrystal devices in Figure 6.7 agree pretty well with those calculated from the EQE measurements in Figure 6.8. The measured J_{sc} from the as-deposited nanocrystal device was 5.65 mA/cm^2 compared to 4.95 mA/cm^2 calculated from EQE data. The cured nanocrystal device J_{sc} is 18.65 mA/cm^2 (Fig. 8.7h) compared to 14.29 mA/cm^2 calculated from the EQE data. The lower calculated J_{sc} value for the cured nanocrystal device results from the fact that the white

light bias intensity in our IPCE setup was limited to ~50 mW/cm^2 and since the EQE of these devices was sensitive to the bias intensity the measured EQE under white light bias was still slightly lower than under true AM1.5 illumination at 100 mW/cm^2.

6.3.5 Transient Absorption Spectroscopy

To confirm that MEG does occur in the nanocrystal films with peak EQE>100%, the recombination dynamics of photoexcited excitons were determined by transient absorption (TA) spectroscopy with 400 nm and 800 nm pump light. Figure 6.12 shows transient absorption spectra for $CuInSe_2$ nanocrystal films before and after photonic curing. The peak minimum corresponds to the optical gap and shifts to slightly lower energy after photonic curing. Figures 6.13 (A, B) show the decay in bleach signal near the absorption edge for the nanocrystal film after photonic curing with a 2.2 J/cm^2 pulse.[28,29] Multiexcitons undergo Auger recombination (the inverse process to MEG) on very short time scales (typically ~100 ps) compared to much longer lived single excitons.[28] With 800 nm pump light (Fig. 6.13A), an individual photon does not have enough energy to induce MEG and only one exciton per nanocrystal is generated at low pump fluence. Under these conditions, the normalized TA kinetics curves overlap. When the 800-nm pump fluence is increased so that some nanocrystals absorb more than one photon per excitation pulse, multiexcitons can be created and Auger recombination dynamics can be observed. The 400 nm pump photons carry about three times the band gap energy, so multiexciton generation from a single photon is possible and Auger recombination dynamics can be observed even at low fluences. Figure 6.13B shows the bleach signal for two low-fluence TA kinetics with 400 nm pump wavelength as well as an average of the 3, 6, and 15 μJ/cm^2 TA curves at 800 nm pump wavelength for

comparison. The low fluence TA kinetics at 400 nm show increased signal at short times compared to the low fluence 800 nm pump TA kinetics, indicating the presence of Auger recombination and therefore multiexciton generation. The possibility of anomalous results due to photocharging was eliminated by rapidly translating the sample through the measurement area.[30] Figure 6.14 shows negligible differences between measurements of static and translating sample, which indicates that there is no influence of sample charging on the TA spectra.

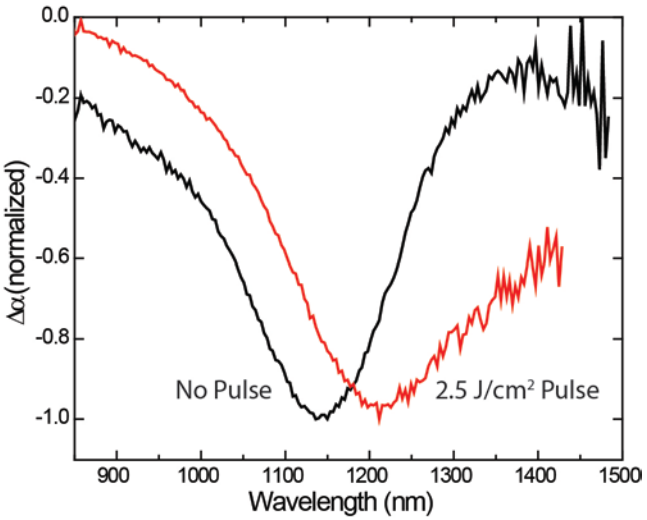

Figure 6.12 Transient absorption (TA) spectra showing the spectral peak in the bleach signal for a nanocrystal film without photonic curing (black) and a film cured with a 2.5 J/cm^2 pulse (red).

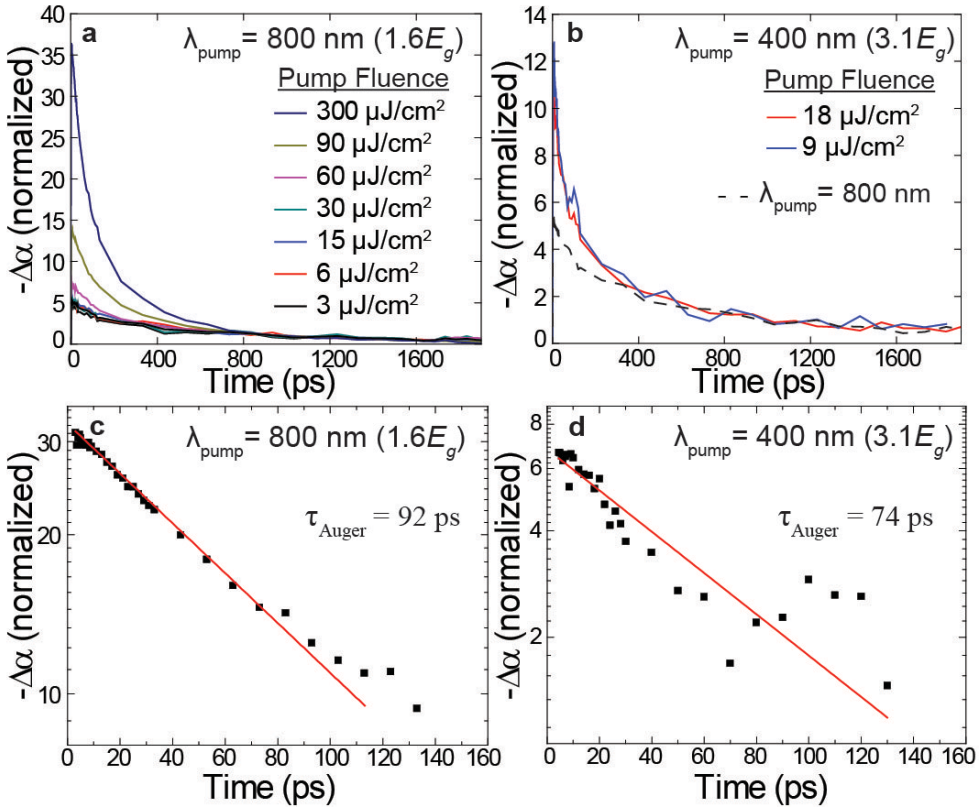

Figure 6.13 Transient absorption (TA) spectroscopy of $CuInSe_2$ nanocrystal films after photonic curing. (a) TA kinetics normalized to $-\Delta\alpha=1$ at 1000 ps with an 800 nm pump wavelength and pump fluences of 300 $\mu J/cm^2$ (dark blue), 90 $\mu J/cm^2$ (green), 60 $\mu J/cm^2$ (pink), 30 $\mu J/cm^2$ (teal), 15 $\mu J/cm^2$ (blue), 6 $\mu J/cm^2$ (red) and 3 $\mu J/cm^2$ (black). (b) TA kinetics normalized to $-\Delta\alpha=1$ at 1000 ps with a 400 nm pump wavelength and pump fluences of 18 $\mu J/cm^2$ (red) and 9 $\mu J/cm^2$ (blue). The average low fluence background (average of 3, 6, 15 and 30 $\mu J/cm^2$ signals) at 800 nm pump wavelength is also shown for comparison (black). (c) TA kinetics showing the Auger recombination rate. The single exciton TA kinetics background (average 800 nm wavelength low fluence pump) is subtracted from the high fluence TA kinetics at 800 nm, 300 $\mu J/cm^2$ pump, which shows the creation of multiexcitons due to the absorption of multiple photons per nanocrystal. The kinetics are plotted on a log scale and can be fitted to a single exponential with a time constant of 92 ps. (d) TA kinetics showing Auger recombination at 400 nm pump and low fluence. The single exciton TA kinetics background (average 800 nm wavelength low fluence pump) is subtracted from the TA kinetics at 400 nm, 9 $\mu J/cm^2$ pump, which should only show Auger recombination if MEG is present. The kinetics are plotted on a log scale and can be fitted to a single exponential with a time constant of 74 ps.

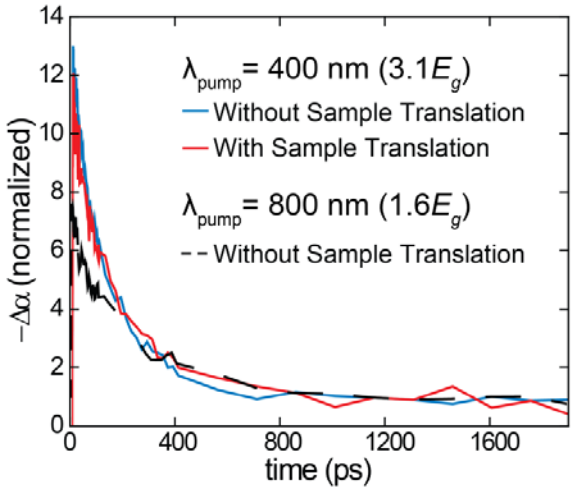

Figure 6.14 Transient absorption kinetics measured with and without sample translation and normalized to $-\Delta\alpha=1$ at 1 ns for a film photonically cured at 2.5 J/cm^2. Sample translation helps ensure that sample charging does not affect the TA signal.

The average single exciton recombination kinetics at 800 nm pump and low fluence was used as a baseline to determine the Auger recombination rate. In Figures 6.13A and 6.13B, the single exciton recombination background kinetics were subtracted (time constant ~600 ps) from the TA kinetics at 800 nm pump wavelength and 300 μJ/cm^2 fluence (a high-power regime where multiple photons are present per absorbing nanocrystal) and at 400 nm pump wavelength and 9 μJ/cm^2 fluence (in the regime of less than one photon per nanocrystal). The curves in Figures 6.13C and 6.13D both fit single exponentials with similar time constants of 93 ps and 74 ps, respectively. The presence of Auger recombination at low fluences of 400 nm pump light supports the presence of MEG in the cured $CuInSe_2$ nanocrystal films.

Figure 6.15 shows the ratio of the TA signal at short time compared to long time at a range of pump fluences. The ratio, R_{pop}, is measured at low pump energy ($1.6E_g$) where only single excitons can be generated and at high pump energy ($3.1E_g$) where

multiexcitons can possible be generated. The curves can be fitted with a Poisson distribution which follows the form,

$$R_{pop} = QY\sigma J[1 - \exp(-\sigma J)]^{-1}.$$

QY is the quantum yield of the sample and can be determined by R_{pop} in the limit of low pump fluence (J). The absorption cross section, σ, can be determined by fitting the data to the equation and can then be used to calculate the exciton occupancy, $\langle N_0 \rangle = \sigma J$. R_{pop} is normalized to one in the limit of low pump fluence for the low energy pump, since only a single exciton can be generated per incident photon. The quantum yield at 3.1Eg is estimated to be ~125%.

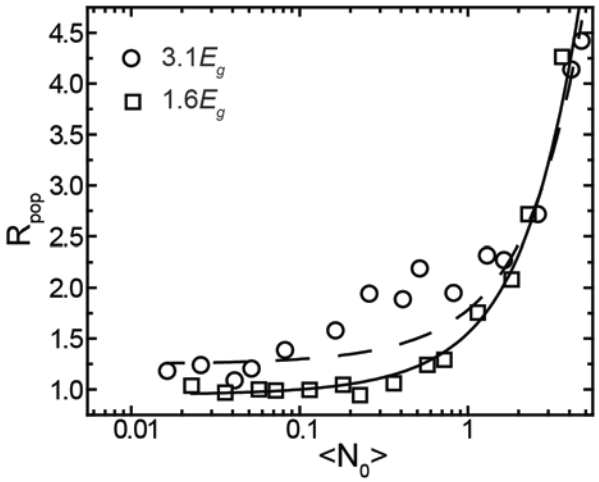

Figure 6.15 The ratio of exciton population (R_{pop}) at early-time compared to late-time TA signal for high energy (circles, $3.1E_g$) and low energy (squares, $1.6E_g$) pump energy with varying exciton occupancy ($<N_0>$). The exciton population is normalized so that the exciton population at low energy pump is one in the limit of low pump fluence, since only a single exciton can be generated per nanocrystal. The data is fitted to the expected Poisson statistics for high energy (dashed line) and low energy (solid line) pump energy.

6.3.6 Surface Trap States

The influence of the trap states limiting multiexciton extraction under low light conditions on the exciton decay dynamics was tested by applying an intense white light bias during TAS measurements. Figure 6.16 shows that white light biasing has little effect on the TA kinetics, which implies that the traps only have a detrimental effect on charge extraction and do not effect charge generation. Perhaps these traps are related to unpassivated surface defects.[31–33] TEM shows that prior to photonic curing the nanocrystals have a diameter of 8.1 ± 2.1 nm, which is smaller than the Bohr exciton radius for $CuInSe_2$ (Figure 6.6).[34] The red-shift of 60 meV in the peak wavelength of the absorption bleach in the TA spectrum (Figure 6.12) after curing probably results from a loss of quantum confinement. However, the fact that the reduction in optical gap is larger than this (0.12 eV, Figure 6.17) and that the TA spectrum exhibits an asymmetric broadening into the red part of the spectrum (Figure 6.12) indicate that trap-related defects are present after photonic curing. In order to extract multiexcitons from a device, the photogenerated multiple electron-hole pairs must separate before Auger recombination can occur. CdTe and PbS nanocrystals both show charge transfer rates between nanocrystals of ~100 ps and biexcitons can be extracted from separate nanocrystals without Auger recombination.[9,35–37] Charge transfer rates as fast as 50 fs have been observed in PbSe nanocrystals and reported for hot carrier extraction.[38] Our calculated biexciton decay time is similar to coupled PbSe quantum dot films (~100 ps), which have also demonstrated MEG in devices.[14,28] Enhanced coupling in films of PbSe nanocrystals allows for efficient conversion of multiexcitons into free charge carriers compared to the competing Auger recombination process.[39] In CIS nanocrystal films with organic ligands attached, charge carriers cannot rapidly dissociate by transferring to neighboring nanocrystals and multiexcitons are lost to Auger recombination (See Fig.

6.1B). However, attaining peak quantum efficiencies over 100% after photonic curing indicates that nanocrystal coupling is sufficient for multiexcitons to dissociate and be extracted prior to recombination (See Fig. 6.1C).

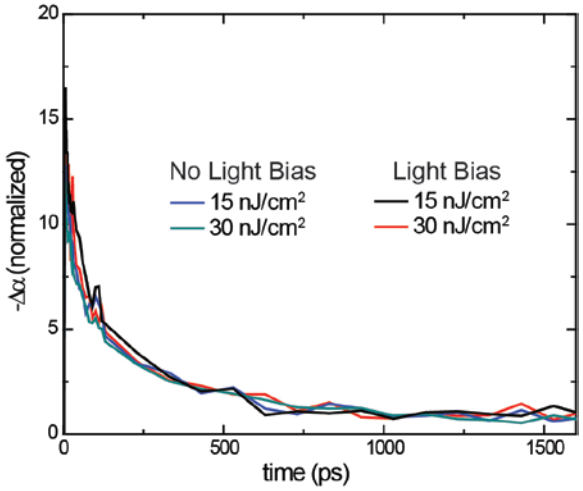

Figure 6.16 Transient absorption kinetics normalized to $-\Delta\alpha=1$ at 1 ns for a nanocrystal film cured at 2.5 J/cm^2. The kinetics were taken using 9 and 18 µJ /cm^2 pump fluences at 400 nm pump wavelength.

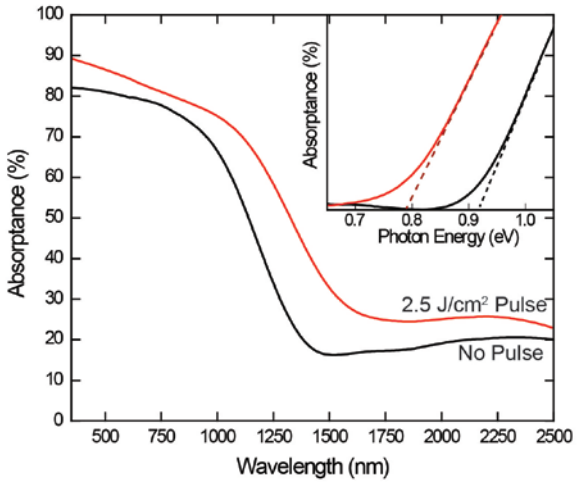

Figure 6.17 Absorptance measurements of a $CuInSe_2$ nanocrystal film before (black) and after photonic curing (red, 2.5 J/cm^2). Inset: Absorptance measured near the band edge; the dashed lines indicate the optical gap of each film: 0.91 and 0.79 eV for the nanocrystals before and after curing.

6.3.7 Photonic Curing of Multi-Layer Films

Although nanocrystal films electronically coupled with photonic curing exhibit significantly increased device current, the loss of voltage and fill factor prevent these devices from achieving high efficiencies. One possible reason for the loss in voltage and fill factor relates to the formation of small regions of exposed back contact in the film after photonic curing. The pulse energies used for electronic coupling are not high enough to cause significant nanocrystal sintering; however, there may still be small local regions of sintering. This is most likely caused by non-uniformities in the film prior to photonic curing. Slightly thicker regions of the film will absorb more of the pulse light and heat to a higher temperature, allowing for small melt structures to form along with small areas of exposed back contact. One possible way to improve the device performance is to fill the areas of exposed contact with a new layer of nanocrystals. This new layer could possibly be treated with photonic curing to remove the organic ligands and further enhance nanocrystal coupling.

Figure 6.18 shows SEM images for a series of nanocrystal films with additional spray deposition and photonic curing steps. Figure 6.18A shows a film treated with a 2.5 J/cm2 pulse. The film is largely unsintered, but does show some small regions of exposed back contact. After the initial photonic curing treatment, an additional layer of nanocrystals is spray cast on the film (Fig. 6.18B), which fills in all of the exposed contact. Ideally, a non-conformal coating of nanocrystals would be achieved; however, this proved difficult even using a wide variety of deposition techniques (spray coating, spin coating, drop casting, blade coating) and the new nanocrystal film conformally coats the underlying film. Next, the film is again treated with photonic curing at 2.5 J/cm2 to remove the organic ligands (Fig. 6.18C). In this case, much larger areas of exposed contact are formed and more significant sintering is observed. Because the second spray

deposition step coats conformally, the overall film thickness is increased, which causes the film to reach higher temperatures than before. Furthermore, the film is more susceptible to melt structures forming at hot spots since the overall film uniformity is worse after the second coat compared to the first coat. A third nanocrystal layer is then deposited (Fig. 6.18D), which fills in the exposed contact, but leaves the film much less uniform.

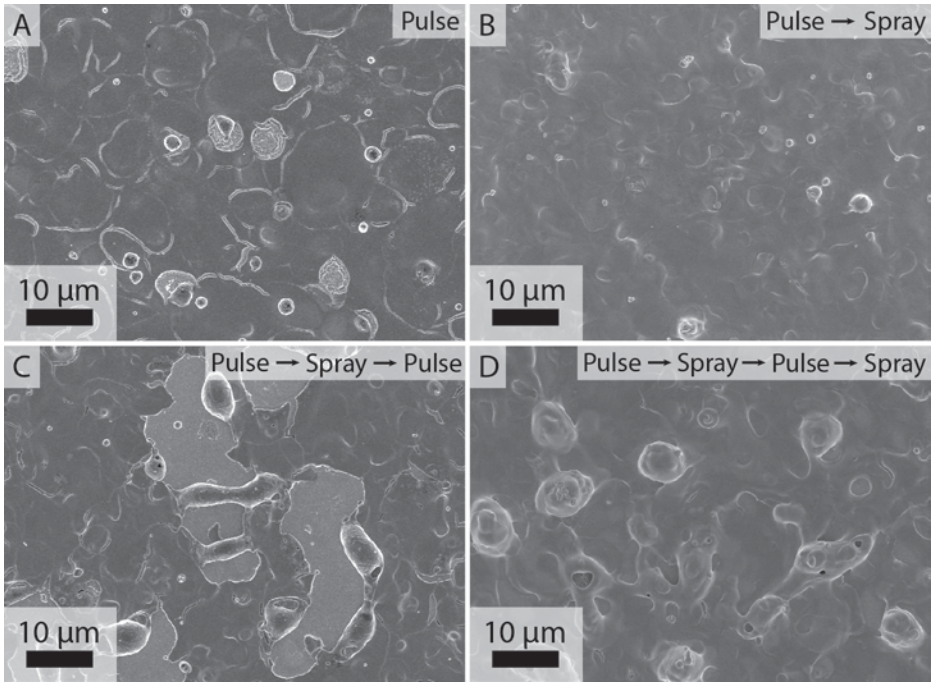

Figure 6.18 SEM images of nanocrystal films pulsed at 2.5 J/cm^2 and with some additional spray deposition steps. (A) A nanocrystal film pulsed one time. (B) After the photonic curing pulse, a new layer of nanocrystals is spray deposited. (C) The second nanocrystal layer is treated with a photonic curing pulse. (D) Finally, a third nanocrystal layer is deposited on top of the twice-pulsed film.

Table 6.2 shows the photovoltaic device results for the films discussed above. Although non-conformal coatings of nanocrystals was not possible, ideally a thin layer of nanocrystals deposited on the surface of an electronically coupled film remove any possible voltage loss due to exposed back contact while still allowing high device currents. However, we instead observe a tradeoff between device voltage and current, with the most recent treatment step (either photonic curing or spray casting) dominating the device performance. When the top layer of the film is treated with photonic curing, ligands are removed from the entire film and some exposed contact is revealed, yielding low voltage and high current. When the top layer of the film is left untreated, the exposed contact is removed, but the excellent charge transport from the underlying layer is masked by the poorly conducting top layer, yielding high voltage and low current. Although this approach proved unsuccessful, high efficiencies may yet be achieved if non-conformal nanocrystal coatings can be developed which preferentially fill gaps in the underlying film.

Film Treatment	PCE (%)	V_{oc} (V)	J_{sc} (mA/cm^2)	FF
No Pulse	0.30	0.34	-2.36	0.37
Pulse	1.13	0.27	-9.61	0.43
Pulse → Spray	0.48	0.33	-4.26	0.34
Pulse, Spray → Pulse	1.10	0.28	-13.54	0.29
Pulse, Spray, Pulse → Spray	0.57	0.37	-4.07	0.38

Table 6.2 Table showing the PV device PCE, V_{oc}, J_{sc}, and fill factor for devices corresponding to the films shown in Figure 6.18.

6.3.8 Surface Repassivation

Another possible reason for the low device open circuit voltage after nanocrystal coupling is the formation of a large number of surface trap states. These surface trap states likely arise from unpassivated bonds on the surface of the nanocrystals after ligand removal and such states have been shown to lie within the band gap.[31] Because the voltage extracted from the device is proportional to the band gap of the constituent semiconductors, the presence of a large number of mid-gap trap states would effectively reduce the band gap and lead to substantially reduced device voltage. High device efficiencies could be achieved if these surface trap states could be passivated while still retaining excellent electronic contact between nanocrystals.

Chemical surface passivation via solid-state ligands exchanges have been extensively explore in the literature.[20,31,32,40–45] The procedure involves simply soaking the nanocrystal film in a solution containing the desired ligand, which will replace the original ligand so long as the new ligand binds preferentially to the nanocrystal surface. For films with ligands removed with photonic curing, the passivating ligand should passivate as many of the surface traps as possible without increasing the spacing between nanocrystals.

Post photonic curing ligand exchanges using hexanethiol, oleylamine, pyridine, Br- ions, and inorganic ChaM ligands were conducted and the device results are shown in Figure 6.19 and Table 6.3. Device results are not shown for hexanethiol repassivation, since treating the nanocrystal film caused the film to disperse in the hexanethiol. It appears as though hexanethiol is such a strong passivant that it separated the coupled nanocrystals completely. Treating the nanocrystal film with oleylamine or pyridine led to an increase in device current compared to the pulsed film with no surface repassivation, however there was no increase in open circuit voltage or fill factor. It is possible that

pyridine and oleylamine are too large to penetrate deep into the film. After photonic curing, the nanocrystal film becomes denser with the removal of the organic ligands, which could make it difficult for large molecules to penetrate. A partial passivation, particularly of the nanocrystal film should give a small increase in device current, but without passivating through the entire nanocrystal layer, the voltage may not increase. Passivation through the entire thickness of the film could be achieved by using much smaller ligands such as Br- ions or ChaM ligands; however, these ligands appear to be poor passivants for these films, as the device current substantially decreased without giving any increase in voltage as well. Although none of these ligands were successful in repassivating the nanocrystal film to achieve higher device efficiency, the ligands studied do not make an exhaustive list and it is possible that different small ligands could sufficiently passivate the nanocrystal surface trap states.

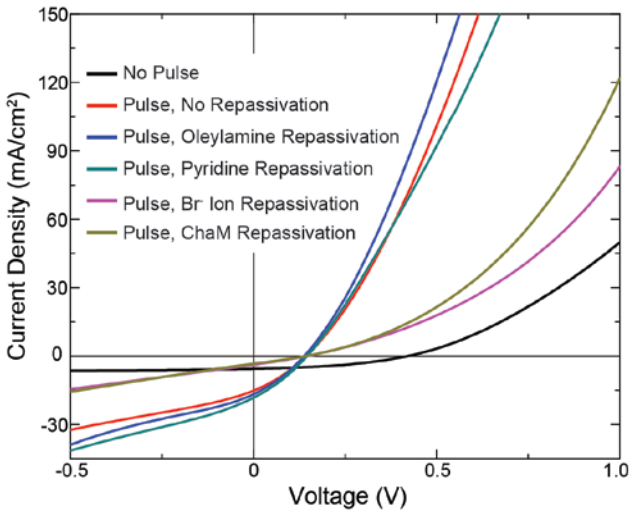

Figure 6.19 Current-voltage measurements for photovoltaic devices fabricated from nanocrystal films before photonic curing (black), after photonic curing with no further repassivation treatments (red), and after photonic curing with repassivation treatments using oleylamine (blue), pyridine (green), Br- ions (magenta), and InSe-ChaM ligands (gold).

Film Treatment	PCE (%)	V_{oc} (V)	J_{sc} (mA/cm^2)	FF
No Pulse	0.95	0.42	-5.57	0.41
Pulse → No Repassivation	0.68	0.14	-15.14	0.31
Pulse → Oleylamine Repassivation	0.70	0.14	-16.67	0.31
Pulse → Pyridine Repassivation	0.81	0.15	-18.22	0.30
Pulse → Br- Ion Repassivation	0.15	0.15	-3.83	0.27
Pulse → ChaM Repassivation	0.13	0.14	-3.36	0.27

Table 6.3 Table showing the PV device PCE, V_{oc}, J_{sc}, fill factor, and peak quantum efficiency for the devices shown in Figure 6.19.

6.4 CONCLUSIONS

Ink-deposited $CuInSe_2$ nanocrystal PVs treated by photonic curing exhibited high short circuit currents and peak external quantum efficiencies of over 120% due to the extraction of multiexcitons in the high energy wavelength region of the solar spectrum. TAS measurements substantiate the claim of MEG in cured nanocrystal films. It appears that photonic curing brings the nanocrystals into better electrical contact to enable multiexciton extraction. Ligand removal, however, still appears to induce a significant amount of traps in the nanocrystal film, which reduces device performance, especially under low light conditions. Still, the coupled nanocrystals can more readily transfer charge and allow for rapid separation and extraction of multiexcitons. TAS measurements show little difference in multiexciton generation with and without light biasing, which indicates that surface traps only affect multiexciton extraction and not generation. Passivation of these surface traps could perhaps provide a route to high efficiency devices that utilize multiexciton generation and extraction along with reasonably efficient charge extraction for electrons and holes photoexcited closer to the band gap energy.

6.5 REFERENCES

1. Henry, C. H. Limiting efficiencies of ideal single and multiple energy gap terrestrial solar cells. *J. Appl. Phys.* **51,** 4494–4500 (1980).
2. Hanna, M. C. & Nozik, A. J. Solar conversion efficiency of photovoltaic and photoelectrolysis cells with carrier multiplication absorbers. *J. Appl. Phys.* **100,** 074510 (2006).
3. Beard, M. C. Multiple Exciton Generation in Semiconductor Quantum Dots. *J. Phys. Chem. Lett.* **2,** 1282–1288 (2011).
4. Schaller, R. D. & Klimov, V. I. High Efficiency Carrier Multiplication in PbSe Nanocrystals: Implications for Solar Energy Conversion. *Phys. Rev. Lett.* **92,** 186601 (2004).
5. Beard, M. C. *et al.* Multiple Exciton Generation in Colloidal Silicon Nanocrystals. *Nano Lett.* **7,** 2506–2512 (2007).
6. Murphy, J. E. *et al.* PbTe Colloidal Nanocrystals: Synthesis, Characterization, and Multiple Exciton Generation. *J. Am. Chem. Soc.* **128,** 3241–3247 (2006).
7. Lin, Z., Franceschetti, A. & Lusk, M. T. Size Dependence of the Multiple Exciton Generation Rate in CdSe Quantum Dots. *ACS Nano* **5,** 2503–2511 (2011).
8. Califano, M. Direct and Inverse Auger Processes in InAs Nanocrystals: Can the Decay Signature of a Trion Be Mistaken for Carrier Multiplication? *ACS Nano* **3,** 2706–2714 (2009).
9. Sukhovatkin, V., Hinds, S., Brzozowski, L. & Sargent, E. H. Colloidal Quantum-Dot Photodetectors Exploiting Multiexciton Generation. *Science* **324,** 1542–1544 (2009).
10. Kim, S. J., Kim, W. J., Sahoo, Y., Cartwright, A. N. & Prasad, P. N. Multiple exciton generation and electrical extraction from a PbSe quantum dot photoconductor. *Appl. Phys. Lett.* **92,** 031107–031107–3 (2008).
11. Kim, S. J., Kim, W. J., Cartwright, A. N. & Prasad, P. N. Carrier multiplication in a PbSe nanocrystal and P3HT/PCBM tandem cell. *Appl. Phys. Lett.* **92,** 191107–191107–3 (2008).
12. Gabor, N. M., Zhong, Z., Bosnick, K., Park, J. & McEuen, P. L. Extremely Efficient Multiple Electron-Hole Pair Generation in Carbon Nanotube Photodiodes. *Science* **325,** 1367–1371 (2009).
13. Sambur, J. B., Novet, T. & Parkinson, B. A. Multiple Exciton Collection in a Sensitized Photovoltaic System. *Science* **330,** 63–66 (2010).
14. Semonin, O. E. *et al.* Peak External Photocurrent Quantum Efficiency Exceeding 100% via MEG in a Quantum Dot Solar Cell. *Science* **334,** 1530–1533 (2011).

15. Congreve, D. N. *et al.* External Quantum Efficiency Above 100% in a Singlet-Exciton-Fission–Based Organic Photovoltaic Cell. *Science* **340,** 334–337 (2013).

16. Jackson, P. *et al.* New world record efficiency for Cu(In,Ga)Se2 thin-film solar cells beyond 20%. *Prog. Photovolt. Res. Appl.* **19,** 894–897 (2011).

17. Akhavan, V. A., Panthani, M. G., Goodfellow, B. W., Reid, D. K. & Korgel, B. A. Thickness-limited performance of CuInSe2 nanocrystal photovoltaic devices. *Opt. Express* **18,** A411–A420 (2010).

18. Stolle, C. J., Panthani, M. G., Harvey, T. B., Akhavan, V. A. & Korgel, B. A. Comparison of the Photovoltaic Response of Oleylamine and Inorganic Ligand-Capped CuInSe2 Nanocrystals. *ACS Appl. Mater. Interfaces* **4,** 2757–2761 (2012).

19. Panthani, M. G. *et al.* CuInSe2 Quantum Dot Solar Cells with High Open-Circuit Voltage. *J. Phys. Chem. Lett.* **4,** 2030–2034 (2013).

20. Guo, Q., Ford, G. M., Agrawal, R. & Hillhouse, H. W. Ink formulation and low-temperature incorporation of sodium to yield 12% efficient Cu(In,Ga)(S,Se)2 solar cells from sulfide nanocrystal inks. *Prog. Photovolt. Res. Appl.* **21,** 64–71 (2013).

21. Harvey, T. B. *et al.* Copper Indium Gallium Selenide (CIGS) Photovoltaic Devices Made Using Multistep Selenization of Nanocrystal Films. *ACS Appl. Mater. Interfaces* **5,** 9134–9140 (2013).

22. Schroder, K., A. Mechanisms of photonic curing: processing high temperatures on low temperature substrates. *Nanotech Conf. Expo 2011 Interdiscip. Integr. Forum Nanotechnol. Biotechnol. Microtechnology* **2,**

23. Hegedus, S., Ryan, D., Dobson, K., McCandless, B. & Desai, D. Photoconductive CdS: how does it Affect CdTe/CdS Solar Cell Performance? *MRS Online Proc. Libr.* **763,** B9.5.1–B9.5.6 (2003).

24. Gloeckler, M. & Sites, J. R. Apparent quantum efficiency effects in CdTe solar cells. *J. Appl. Phys.* **95,** 4438–4445 (2004).

25. Sites, J. R., Tavakolian, H. & Sasala, R. A. Analysis of apparent quantum efficiency. *Sol. Cells* **29,** 39–48 (1990).

26. Hegedus, S. S. The photoresponse of CdS/CuInSe2thin-film heterojunction solar cells. *IEEE Trans. Electron Devices* **31,** 629–633 (1984).

27. Demtsu, S., Albin, D. & Sites, J. Role of Copper in the Performance of CdS/CdTe Solar Cells. in *Conference Record of the 2006 IEEE 4th World Conference on Photovoltaic Energy Conversion* **1,** 523–526 (2006).

28. Luther, J. M. *et al.* Multiple Exciton Generation in Films of Electronically Coupled PbSe Quantum Dots. *Nano Lett.* **7,** 1779–1784 (2007).

29. Stewart, J. T. *et al.* Comparison of Carrier Multiplication Yields in PbS and PbSe Nanocrystals: The Role of Competing Energy-Loss Processes. *Nano Lett.* **12,** 622–628 (2012).

30. McGuire, J. A., Sykora, M., Joo, J., Pietryga, J. M. & Klimov, V. I. Apparent Versus True Carrier Multiplication Yields in Semiconductor Nanocrystals. *Nano Lett.* **10,** 2049–2057 (2010).

31. Ip, A. H. *et al.* Hybrid passivated colloidal quantum dot solids. *Nat. Nanotechnol.* **7,** 577–582 (2012).

32. Barkhouse, D. A. R., Pattantyus-Abraham, A. G., Levina, L. & Sargent, E. H. Thiols Passivate Recombination Centers in Colloidal Quantum Dots Leading to Enhanced Photovoltaic Device Efficiency. *ACS Nano* **2,** 2356–2362 (2008).

33. Konstantatos, G., Levina, L., Fischer, A. & Sargent, E. H. Engineering the Temporal Response of Photoconductive Photodetectors via Selective Introduction of Surface Trap States. *Nano Lett.* **8,** 1446–1450 (2008).

34. Castro, S. L., Bailey, S. G., Raffaelle, R. P., Banger, K. K. & Hepp, A. F. Nanocrystalline Chalcopyrite Materials (CuInS2 and CuInSe2) via Low-Temperature Pyrolysis of Molecular Single-Source Precursors. *Chem. Mater.* **15,** 3142–3147 (2003).

35. Franzl, T. *et al.* Fast energy transfer in layer-by-layer assembled CdTe nanocrystal bilayers. *Appl. Phys. Lett.* **84,** 2904–2906 (2004).

36. Lazarenkova, O. L. & Balandin, A. A. Miniband formation in a quantum dot crystal. *J. Appl. Phys.* **89,** 5509–5515 (2001).

37. Trinh, M. T. *et al.* Direct generation of multiple excitons in adjacent silicon nanocrystals revealed by induced absorption. *Nat. Photonics* **6,** 316–321 (2012).

38. Tisdale, W. A. *et al.* Hot-Electron Transfer from Semiconductor Nanocrystals. *Science* **328,** 1543–1547 (2010).

39. Sandeep, C. S. S. *et al.* High charge-carrier mobility enables exploitation of carrier multiplication in quantum-dot films. *Nat. Commun.* **4,** (2013).

40. Tang, J. *et al.* Colloidal-quantum-dot photovoltaics using atomic-ligand passivation. *Nat. Mater.* **10,** 765–771 (2011).

41. Jasieniak, J., MacDonald, B. I., Watkins, S. E. & Mulvaney, P. Solution-Processed Sintered Nanocrystal Solar Cells via Layer-by-Layer Assembly. *Nano Lett.* **11,** 2856–2864 (2011).

42. Brown, P. R. *et al.* Energy Level Modification in Lead Sulfide Quantum Dot Thin Films through Ligand Exchange. *ACS Nano* **8,** 5863–5872 (2014).

43. Chuang, C.-H. M., Brown, P. R., Bulović, V. & Bawendi, M. G. Improved performance and stability in quantum dot solar cells through band alignment engineering. *Nat. Mater.* **13,** 796–801 (2014).

44. Kovalenko, M. V., Scheele, M. & Talapin, D. V. Colloidal Nanocrystals with Molecular Metal Chalcogenide Surface Ligands. *Science* **324,** 1417–1420 (2009).

45. Lee, J.-S., Kovalenko, M. V., Huang, J., Chung, D. S. & Talapin, D. V. Band-like transport, high electron mobility and high photoconductivity in all-inorganic nanocrystal arrays. *Nat. Nanotechnol.* **6,** 348–352 (2011).

Chapter 7: Multiexciton Generation in Colloidal $CuInSe_2$ Nanocrystals[‡‡]

7.1 INTRODUCTION

The absorption of a photon by a semiconductor typically leads to the formation of a single electron-hole pair and the photon energy exceeding the band gap is lost as heat. However, an absorbed photon can also create more than one electron-hole pair, or exciton, if the photon provides enough energy. In bulk semiconductors, multiexciton generation (MEG)—or carrier multiplication (CM)—typically requires photons with at least more than four times the band gap energy.[1] Quantum dots on the other hand, can exhibit especially efficient MEG and the MEG efficiency tends to increase with decreasing quantum dot size.[1–3] The mechanism of multiexciton formation has been the subject of several experimental and theoretical studies.[1,4–7] MEG has been observed spectroscopically in a variety of nanocrystals, including Si, PbS, PbSe, PbTe, CdSe, Ag_2S, InP, InAs and $CuInSe_2$ with photon energies nearing two times the optical gap.[8–16] Photovoltaic devices of PbSe[17] and $CuInSe_2$[16] nanocrystals have also been made showing peak external quantum efficiencies exceeding 100% in the wavelength range where MEG occurs, indicating that photogenerated multiexcitons can also be extracted. In the case of the $CuInSe_2$ nanocrystal films used to make PV devices with >100% EQE, transient absorption spectroscopy (TAS) measurements confirmed spectroscopically that MEG indeed occurred in those $CuInSe_2$ nanocrystal films.[16] Here we report a more extensive set of size-dependent TAS measurements of $CuInSe_2$ nanocrystal dispersions to

[‡‡] Reproduced in part with permission from: Stolle, C. Jackson; Schaller, Richard D.; Korgel, Brian A., Efficient Carrier Multiplication in Colloidal $CuInSe_2$ Nanocrystals, *J. Phys. Chem. Lett.* (2014), **5**, 3169-3174. Copyright 2014 American Chemical Society. CJS designed the experiments, synthesized and characterized the samples, collected and analyzed the data, and wrote the manuscript. RDS assisted with experimental design, data collection and analysis, and manuscript preparation. BAK provided funding, guidance, and assistance writing the manuscript.

determine the MEG efficiency, the energy threshold for MEG, the carrier cooling rates, absorption cross-sections and Auger lifetimes of $CuInSe_2$ nanocrystals. The $CuInSe_2$ nanocrystals had slightly lower MEG threshold energy, longer Auger lifetimes, and similar MEG efficiency as compared to PbSe nanocrystal quantum dots.

7.2 EXPERIMENTAL METHODS

7.2.1 Nanocrystal Synthesis

$CuInSe_2$ nanocrystals were synthesized using the methods described by Panthani, et al.[18] Briefly, 2 mmol CuCl (anhydrous beads, Aldrich), 2 mmol $InCl_3$ (anhydrous, Strem), and 20 ml of degassed oleylamine (OLA, TCI America) were added to a 100 ml three neck flask inside an N_2 filled glovebox. The flask is then sealed, removed from the glovebox, and attached to a standard Schlenk line setup. The flask is degassed for 30 minutes at 110^{o}C under vacuum. In a separate vial, 4 mmol Se powder (Aldrich) is dissolved in 1.5 ml diphenylphosphine (DPP, Aldrich) and 2 ml degassed oleylamine inside the glovebox. The OLA:DPP:Se solution is drawn into a syringe and removed from the glovebox.

The size of the nanocrystals was controlled by manipulating the injection and reaction temperature. Following degassing, the reaction flask is heated under nitrogen to between 100^{o}C and 180^{o}C, depending on the desired nanocrystal size before injecting the OLA:DPP:Se solution. For reactions carried out at temperature higher than 180^{o}C, the OLA:DPP:Se solution is injected at 180^{o}C and then the reaction is rapidly heated to the final reaction temperature of either 200^{o}C or 240^{o}C. After one hour, the reaction flask is allowed to cool to room temperature. The nanocrystals are washed twice using an ethanol/toluene antisolvent/solvent pair and then centrifuged in toluene to precipitate

poorly-capped nanocrystals. The nanocrystals are then stored in the glovebox. Nanocrystals with average diameters of 4.5 ± 0.8 nm, 6.2 ± 1.5 nm and 9.2 ± 3.2 nm were synthesized using reaction temperatures of 180^{o}C, 200^{o}C, and 240^{o}C.

7.2.2 Characterization Techniques

UV-Vis-NIR absorbance data was taken using a Cary 500 spectrophotometer. X-ray diffraction was taken using a Rigaku R-Axis Spider diffractometer using Cu Kα radiation operated at 40 kV and 40 mA. Transmission electron microscopy images were collected using an FEI Tecnai G2 Spirit BioTwin microscope operated at 80 kV. Transient absorption spectroscopy measurements were carried out at the Center for Nanoscale Materials using an 800 nm, 35 fs pulse width, 2 kHz amplified Ti:sapphire laser and white-light seeded optical parametric amplifier. Pump pulses of 800, 400, 340, or 320 nm were spatially overlapped with a mechanically delayed white light probe beam formed by focusing 5% of the amplifier output into a 2 mm thick sapphire plate.

7.3 RESULTS AND DISCUSSION

7.3.1 Materials Characterization

TAS measurements were performed on $CuInSe_2$ nanocrystals of three different sizes synthesized using the methods of Panthani, et al.[18] Figure 7.1 shows transmission electron microscopy (TEM) and UV-Vis Absorbance spectra of the nanocrystals, which have average diameters of 4.5 ± 0.8 nm, 6.2 ± 1.5 nm and 9.2 ± 3.2 nm. The optical absorption edge shifts to higher energy with decreasing size due to quantum confinement. There are no exciton peaks in the spectra for these relatively large sizes. Absorbance spectra of smaller nanocrystals with exciton peaks are shown in Figure 7.2. These

smaller sizes were not studied by TAS because of the relatively high photon energies required to produce multiple excitons. X-ray diffraction (XRD) showed that the nanocrystals are composed of the compositionally-ordered chalcopyrite $CuInSe_2$ crystal phase (Figure 7.3).

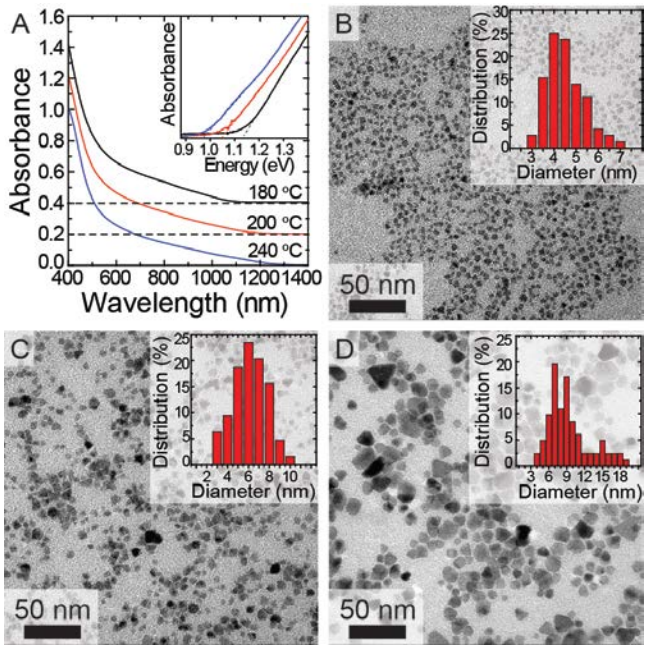

Figure 7.1 $CuInSe_2$ nanocrystals studied by TAS. (A) optical absorbance spectra and (B-D) TEM images**.** (A) Absorbance spectra were measured at room temperature for nanocrystals dispersed in toluene. Spectra are offset by 0.2 O.D. for clarity. The temperatures noted in (A) correspond to the synthesis temperatures used to make the samples with corresponding TEM images in (B) 180°C, (C) 200°C, and (D) 240°C. The insets of (B-D) are size histograms obtained from the TEM images average diameters of (B) 4.5 ± 0.8 nm, (C) 6.2 ± 1.5 nm and (D) 9.2 ± 3.2 nm. The absorption edges determined in the inset of (A) are 0.98 eV (240 °C), 1.05 eV (200 °C), and 1.14 eV (180 °C).[§§]

[§§] The band gap energy values estimated from optical absorption spectroscopy are different from those measured from TAS. For the purpose of these calculations, we used the band gap values measured from TAS.

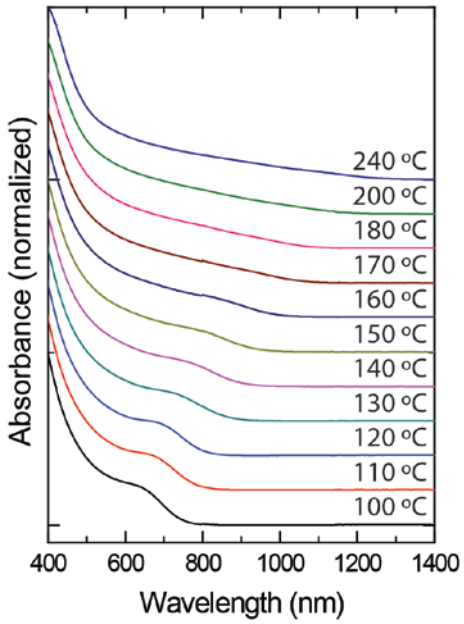

Figure 7.2 Optical absorbance spectra of $CuInSe_2$ nanocrystals dispersed in toluene synthesized at the reaction temperatures indicated. Higher reaction temperatures yielded larger nanocrystals, consistent with the observed shift of the exciton peak and absorption edge to longer wavelength. Absorbance spectra are normalized to 1 at 400 nm and offset for clarity.

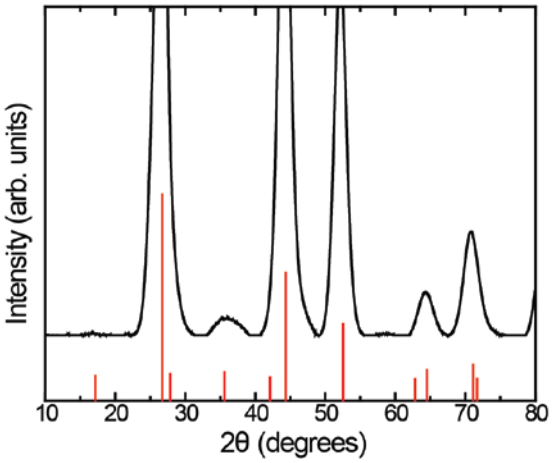

Figure 7.3 X-ray diffraction data for $CuInSe_2$ nanocrystals synthesized at 200°C. The reference pattern corresponds to chalcopyrite $CuInSe_2$ (PDF #01-073-6321). The ordered chalcopyrite phase is distinguished from the disordered sphalerite phase by the presence of the (211) diffraction peak at 35.6°.

7.3.2 TA Spectra, Carrier Cooling, and Absorption Cross Sections

Figure 7.4 shows TA bleach spectra of three different sizes of $CuInSe_2$ nanocrystals dispersed in toluene obtained using an 800 nm pump laser and a white light probe beam. All TAS measurements were carried out with magnetic stirring to ensure that photocharging did not influence the detected signal.[19] The peaks in the TA bleach spectra appear at 1170 nm (1.06 eV), 1050 nm (1.18 eV), and 910 nm (1.36 eV) for nanocrystals with average diameters of 9.2 nm, 6.2 nm, and 4.5 nm, respectively, corresponding to the 1S absorption edge. In the very early time regime (<2 ps), the TA peak appears initially at slightly shorter wavelength than the 1S feature because of the presence of hot carriers. As the hot carriers relax to the conduction and valence band minima, the bleach peak shifts to slightly longer wavelength.[20] After 2.5 ps of delay, the wavelength of the 1S-related peaks in the TA spectra are largely unaffected by delay time or pump fluence, as shown in Figures 7.4 (B,D,F).

The carrier cooling rates were calculated from the intraband cooling times determined from the evolution of the TA peak absorption at relatively short delay times (<5 ps) in Figure 7.5A.[21] Figure 7.5B shows the carrier cooling rates plotted as a function of nanocrystal size. The carrier cooling rate increases as the nanocrystals become smaller, and there is a linear relationship between particle volume and carrier cooling rate, which is consistent with experimental results and theory for other semiconductor nanocrystals.[20–22]

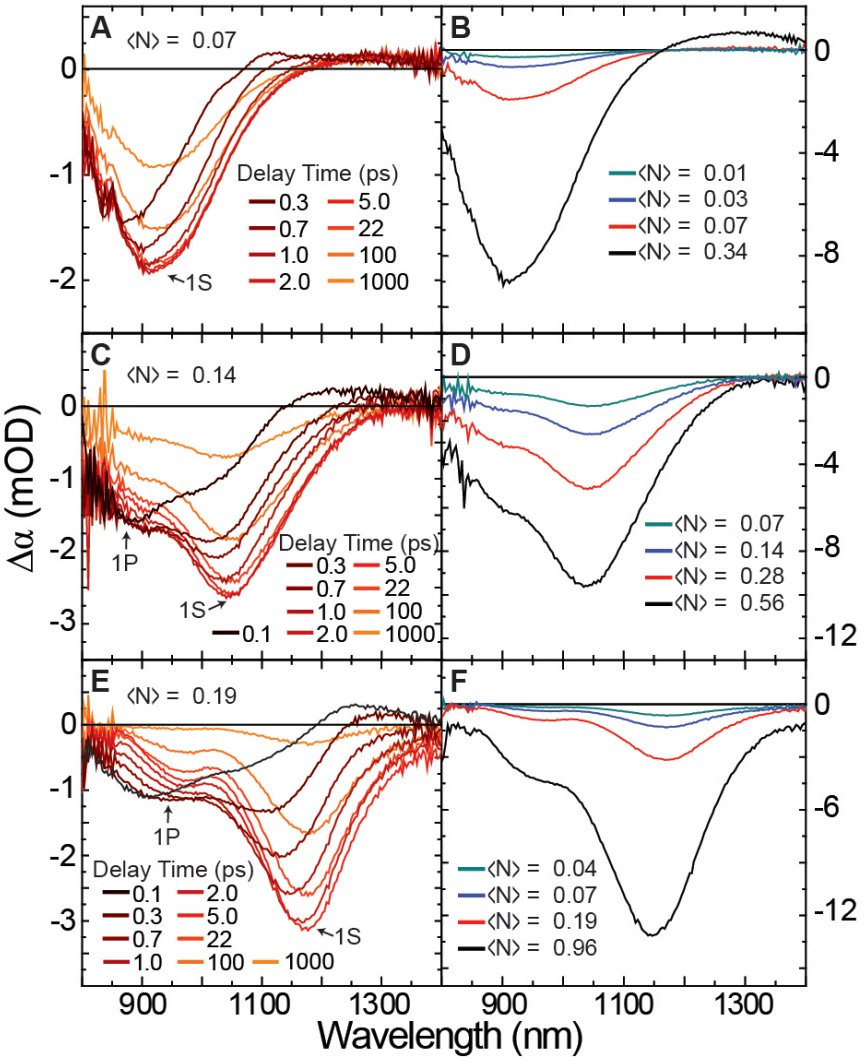

Figure 7.4 $CuInSe_2$ nanocrystal transient absorption spectra (TAS) acquired with 800 nm pump wavelength. Samples with three different average diameters were measured: (A,B) 4.5 ± 0.8 nm, (C,D) 6.2 ± 1.5 nm, and (E,F) 9.2 ± 3.2 nm. (A,C,E) show the evolution of the TA bleach spectra as function of delay time (spectra with 0.1 ps delay time are shown in black) and (B,D,F) show TA spectra of each sample after 2.5 ps delay time with varying average number of photons absorbed per nanocrystal, $\langle N \rangle$. $\langle N \rangle$ was varied by changing the pump fluence, j_p (# of photons/cm^2): $\langle N \rangle = \sigma \cdot j_p$, where σ is the absorption cross section of each nanocrystal sample (cm^2).

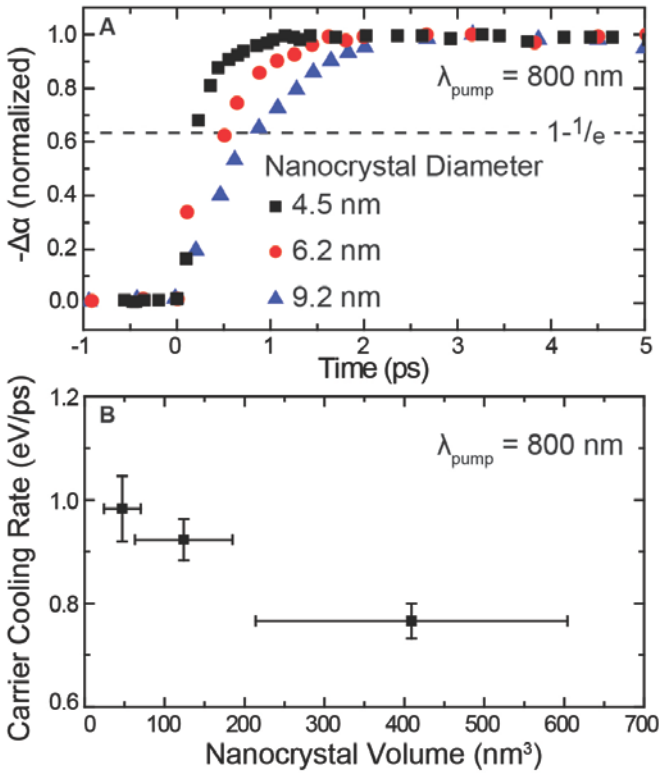

Figure 7.5 Carrier cooling rates. A) Early–time (<5 ps) TA kinetics for each nanocrystal sample at 800 nm pump wavelength (black squares, 4.5 nm nanocrystals; red circles, 6.2 nm nanocrystals; blue triangles, 9.2 nm nanocrystals). The TA kinetics are examined at the location of the absorption bleach maximum for each sample (910 nm for the 4.5 nm diameter nanocrystals, 1050 nm for the 6.2 nm nanocrystals, and 1170 nm for the 9.2 nm nanocrystals). The maximum bleach signals are normalized to one. To calculate the carrier cooling rate, the characteristic cooling times were taken as the delay time when the normalized TA bleach reached $1 - \frac{1}{e}$ (dashed line).[23] B) Carrier cooling rates versus nanocrystal volume measured using 800 nm pump wavelength. Carrier cooling rates were calculated from the difference in energy between the 800 nm pump energy and the nanocrystal optical gap (taken as the peak of the TA bleach) divided by the carrier cooling time. The nanocrystal volume was determined from the average diameter assuming spherical shape. The error bars shown for the carrier cooling rate represent the standard deviation obtained from four measurements using different pump fluence. The error bars for nanocrystal volume correspond to the standard deviation of particle size distribution.

Figure 7.6 shows the absorption cross-sections calculated from TAS. In Figure 7.6A and 7.6B, the bleached absorption signals measured after 1 ns delay time using different pump fluences of 400 nm and 800 nm light are shown. After 1 ns, only single excitons are present in the nanocrystals (i.e., the biexciton lifetime is much shorter than 1 ns). The increase in the absorption bleach signal with increasing pump fluence (or photon flux j_p) depends on the absorption cross section σ:[23]

$$-\Delta\alpha \propto \left(1 - e^{-\sigma * j_p}\right) \qquad 7.1$$

As shown in Figure 7.6C, the bleached absorption signal increases linearly with increasing pump fluence and then saturates. The ratios of the (400 nm and 800 nm) absorption cross sections in Figure 7.6C are consistent with the absorbance spectra in Figure 7.1 (8:1 for all three nanocrystal sizes by TAS compared to 7:1 from the absorbance spectra). The absorption cross-sections are also comparable to those of PbSe nanocrystals with similar size.[15]

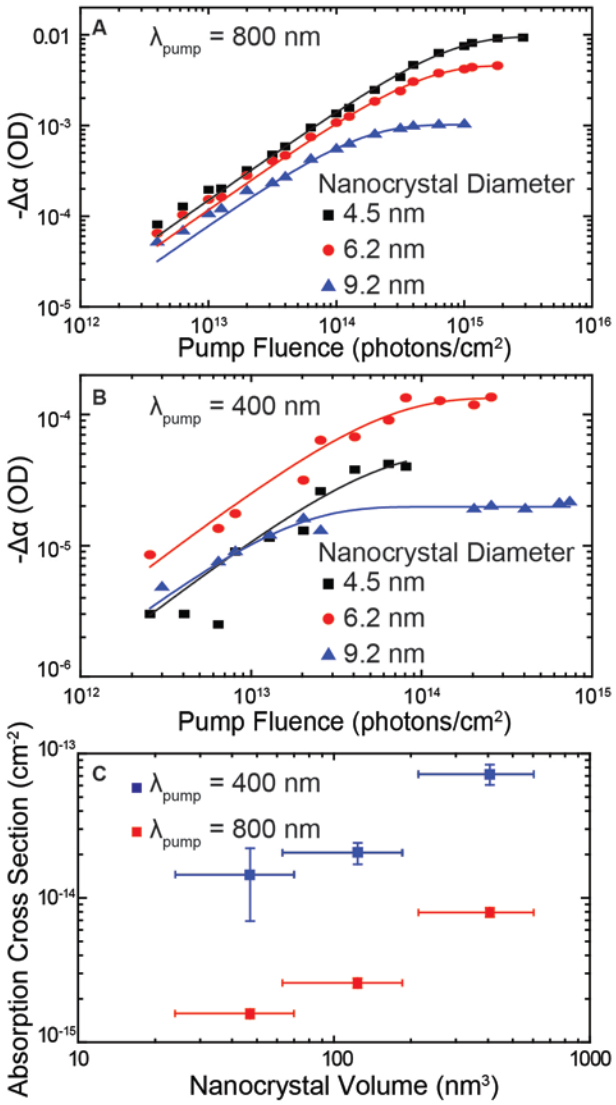

Figure 7.6 Absorption Cross Section. Transient absorption signal at long delay time (1000 ps) for each nanocrystal sample (4.5 nm, black squares; 6.2 nm, red circles; 9.2 nm, blue triangles) as a function of pump fluence for (A) 800 nm pump wavelength and (B) 400 nm pump wavelength. C) Absorption cross section plotted against particle volume for both (blue) 400 nm pump wavelength and (red) 800 nm pump wavelength. The absorption cross section is calculated by fitting the data in A and B to Eq. (7.1). The error bars for absorption cross section correspond to error in the fit of the data.

7.3.3 TA Kinetics, Auger Lifetimes, and Multiexciton generation

Figure 7.7 shows the TA kinetics of three different sizes of $CuInSe_2$ nanocrystals using two pump wavelengths (400 nm and 800 nm). A single absorbed 800 nm photon cannot generate more than one exciton, so the TA kinetics at low fluence (normalized at 1 ns) represent the single exciton decay. Multiple excitons are photoexcited with 800 nm light by increasing the pump fluence to induce multiphoton absorption.[9] When multiphoton absorption occurs, the normalized TA kinetics show a higher intensity early time signal with a biexponential decay and two carrier relaxation processes come into play: (1) a fast Auger recombination process (the process inverse to MEG) and (2) a much longer lived single exciton signal. The biexciton (Auger) lifetimes were determined by subtracting the single exciton baseline TA kinetics (low fluence, 800 nm pump wavelength) and fitting the signal to a single exponential function (Figure 7.8). The Auger lifetimes are plotted in Figure 7.9A as a function of particle volume. The biexciton lifetime scales linearly with particle volume, consistent with literature reports.[26]

The TA kinetics measured using 800 nm pump light provide the single exciton TA kinetics baseline (using low fluence pump) and the biexciton Auger recombination kinetics (using high fluence pump) for comparison to the TA kinetics using 400 nm pump light. Figure 7.7B shows the TA kinetics of the 4.5 nm diameter nanocrystals measured using 400 nm and 800 nm pump light. The signals overlap, indicating that the TA decay does not result from hot carrier cooling and that the energy of the 400 nm photons (equal to $2.28E_g$) lies below the energy threshold for MEG. The TA kinetics for the larger nanocrystals (6.2 nm and 9.2 nm) obtained using 400 nm pump light (Fig. 7.7D, 7.7F), show much faster kinetics at early times, indicative of Auger recombination. The average number of photons absorbed per nanocrystal is low under these conditions and therefore the observed Auger recombination is attributed to multiexciton generation.[9]

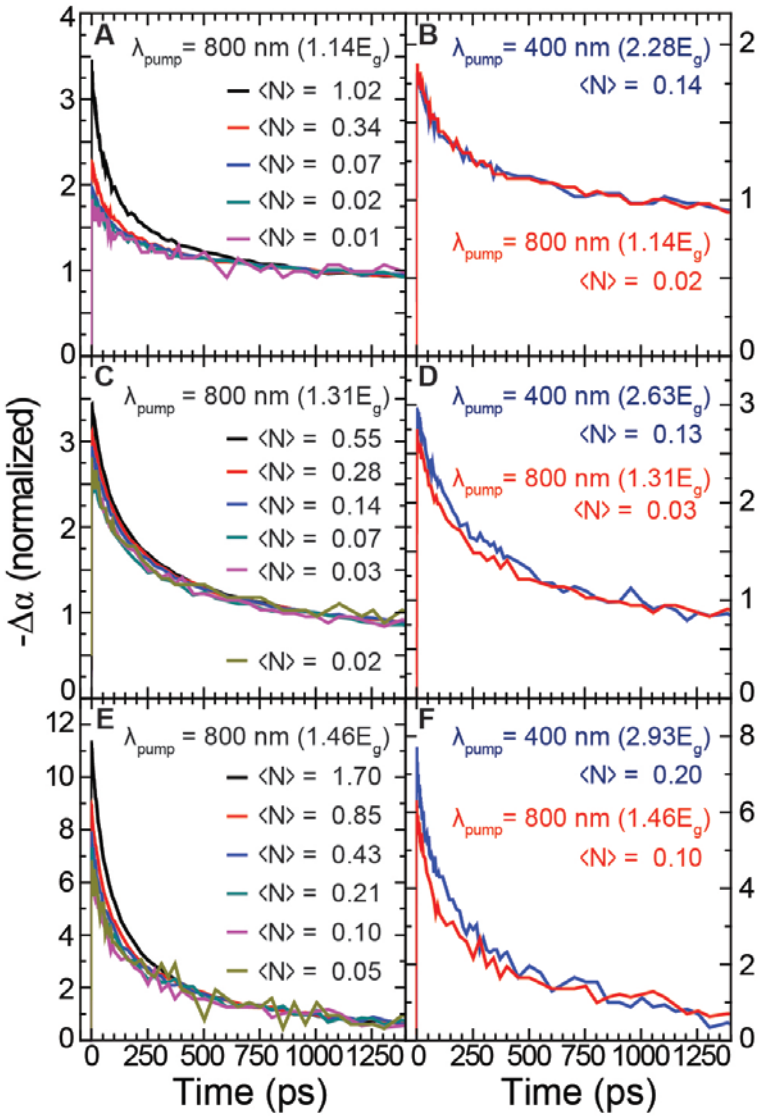

Figure 7.7 Transient absorption kinetics of (A,B) 4.5 ± 0.8 nm nanocrystals, (C,D) 6.2 ± 1.5 nm nanocrystals, and (E,F) 9.2 ± 3.2 nm diameter $CuInSe_2$ nanocrystals measured using two different pump wavelengths of 400 nm and 800 nm. All curves are normalized at long delay times (1 ns) where only single excitons are present in the nanocrystals. TA kinetics taken with a low pump fluence at 400 nm and 800 nm pump wavelength for (B) 4.5 nm nanocrystals, (D) 6.2 nm nanocrystals, and (F) 9.2 nm nanocrystals, where the kinetics measured at 400 nm are shown in blue and kinetic measured at 800 nm are shown in red. The kinetics are taken at the peak in the absorption bleach for each sample (910 nm for the 4.5 nm particles, 1050 nm for the 6.2 nm particles, and 1170 nm for the 9.2 nm particles).

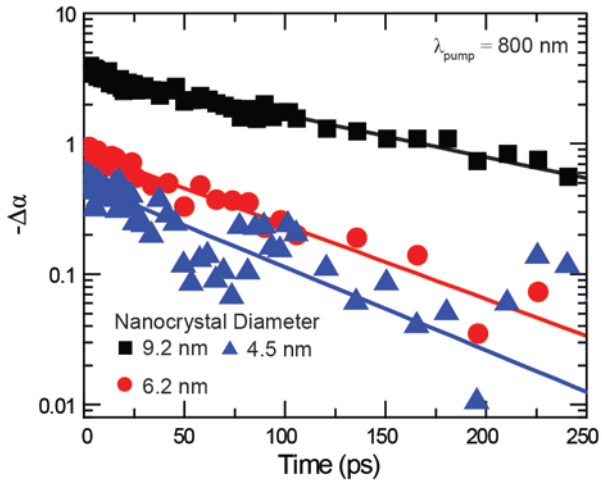

Figure 7.8 Transient absorption kinetics at 800 nm pump wavelength used to determine the biexciton lifetime for $CuInSe_2$ nanocrystals with varying diameter (9.2 nm nanocrystals, black squares; 6.2 nm nanocrystals, red circles; 4.5 nm nanocrystals, blue triangles). The low-fluence (single photon per nanocrystal) background is subtracted from high-fluence (multiple photons per nanocrystal) and fitted to a single exponential. The error in the calculated Auger lifetimes comes from error in the exponential fit of the data (See Fig. 7.9A).

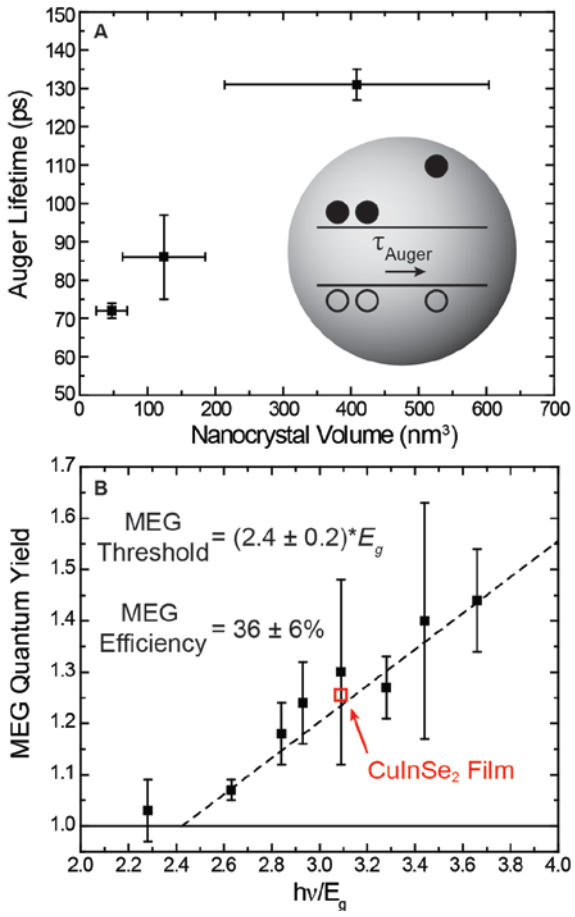

Figure 7.9 Auger lifetimes and MEG quantum yield. A) Biexciton lifetimes plotted against particle volume for the 4.5 ± 0.8 nm, 6.2 ± 1.5 nm, and 9.2 ± 3.2 nm diameter $CuInSe_2$ nanocrystals. The error bars for nanocrystal volume correspond to the standard deviation of nanocrystal sizes within each sample. The error bars for biexciton lifetime correspond to error in the single exponential fit in Fig. S3. B) MEG quantum yield plotted as a function of pump energy (relative to the nanocrystal band gap energy). Data were collected for 4.5 nm, 6.2 nm, and 9.2 nm diameter nanocrystals using pump wavelengths of 400 nm, 340 nm, and 320 nm. The data are fit to a straight line, excluding the data point at $2.28E_g$, which is below the MEG threshold. The intersection of the lines QY=0 and the fit line is defined as the MEG threshold ($(2.4 \pm 0.2)E_g$) and the slope of the fit line times 100% is defined as the MEG efficiency (36 ± 6%). The open red box corresponds to the MEG quantum yield measured for the $CuInSe_2$ nanocrystal film from Chapter 6. Error bars for the measured MEG quantum yield correspond to the standard deviation of quantum yields measured for a range of pump fluences (See Fig. S4).

To determine the MEG quantum yield, TAS was performed using a range of low pump fluences where the TA signal is independent of the pump-fluence (Figure 7.10). The MEG quantum yield was measured using a range of pump wavelengths of 800 nm, 400 nm, 340 nm, and 320 nm by taking the ratio of the average TA signal at high energy pump (either 400 nm, 340 nm, or 320 nm) to the average single exciton TA signal (800 nm pump wavelength). Figure 7.9B shows the MEG quantum yield measured as a function of photon energy relative to the nanocrystal optical gap. A weighted fit of the data gives a straight line with a slope corresponding to the MEG efficiency (36 ± 6%). The energy where the line intersects QY=1 is the MEG threshold (2.4 ± 0.2)E_g.[1] This means that an extra 0.36 excitons are generated per absorbed photon (on average) for each band gap multiple of energy that the incident photon energy is increased above the MEG threshold. These data fit well with our previous transient absorption measurements on $CuInSe_2$ nanocrystal thin films, which showed a MEG QY of ~1.25 at photon energies of 3.1E_g.[16]

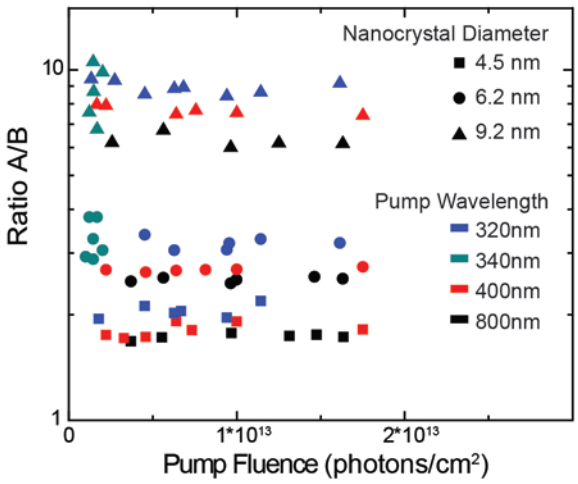

Figure 7.10 The ratio of the transient absorption signal at short time delay (5 ps) and long time delay (1000 ps) as a function of pump fluence for low pump fluences. The ratio is shown for (black) 800 nm, (red) 400nm, (teal) 340 nm, and (blue) 320 nm pump wavelengths. The ratio for each nanocrystal samples is represented by squares (4.5 nm), circles (6.2 nm), and triangles (9.2 nm). The MEG quantum yield is calculated by dividing the average ratio at each high-energy pump wavelength by the average ratio at 800 nm pump wavelength (See Fig. 7). The error in the MEG quantum yield is derived from the standard deviations of the measured ratios.

7.3.4 Comparison of MEG Efficiency, MEG Threshold, and Auger Lifetimes

Multiexciton solar cells require a light-absorbing layer with a combination of high MEG efficiency, low MEG threshold, long Auger lifetimes, and an optimal band gap. A table listing the MEG efficiency and threshold for a variety of semiconductor nanocrystals is given in Table 7.1.[8,12,19,24,25] The MEG efficiency of the $CuInSe_2$ nanocrystals is comparable to PbSe (36% vs 40%), which is the only other material to demonstrate EQE values exceeding 100% in PV devices.[17,26] The MEG threshold for PbSe is $3E_g$.[26] The lower MEG threshold for $CuInSe_2$ nanocrystals of $2.4E_g$ provides for the possibility of slight gains in the device efficiency. For example, the maximum

efficiency of a multiexciton device, assuming 100% MEG QY, could be slightly enhanced from 33.7% to 37.2% with a reduction in MEG threshold from $3E_g$ to $2E_g$.[27] It might be possible for the MEG threshold of $CuInSe_2$ to be further reduced. The minimum MEG threshold of $CuInSe_2$ can be estimated based on the relationship[28]

$$E_{th} = \left(2 + \frac{m_e}{m_h}\right) E_g \tag{7.2}$$

where E_{th} is the MEG threshold energy, m_e and m_h are the electron and hole effective masses. Using bulk values for $CuInSe_2$ of m_e=0.1m_0 and m_h=0.7m_0, Equation (7.2) give E_{th} = 2.14E_g, which is slightly lower than the measured value of 2.4E_g.

Nanocrystal	Threshold (hv/E_g)	Efficiency (%)	Bulk Eg (eV)	Ref
$CuInSe_2$	2.4	36	1	
PbSe	3	40	0.37	[19]
PbS	3	40	0.50	[24]
InAs*	2	35	0.36	[25]
Ag_2S	2.28	73	0.90	[12]
Si*	2.5	~100	1.1	[8]

Table 7.1 A table showing the MEG threshold, MEG efficiency, and Bulk band gap values for a variety of semiconductor nanocrystals. Nanocrystals marked with an * were measured without sample stirring to eliminate effects from photocharging and may not be accurate.

$CuInSe_2$ nanocrystals can be made with band gaps near the optimal band gap range of 0.75-1.15 eV while simultaneously achieving long biexciton lifetimes, both of which depend on nanocrystal size.[27,29] The Auger lifetime is important for multiexciton extraction in solar cells, as the biexciton lifetime relates to the ability to extract the generated multiexcitons.[30] From the perspective of carrier extraction in a multiexciton

solar cell, large nanocrystals with long Auger lifetimes would be used to minimize biexciton annihilation. At the same time, the benefit of slow Auger decay must be balanced with the need for increased band gap through quantum confinement. Detailed energy balances have shown that for an MEG efficiency of 100% and a MEG threshold of $2E_g$, the peak optimal nanocrystal band gap is near ~0.9 eV.[9,27,31] Figure 7.11 shows the Auger lifetimes for several semiconductor nanocrystals.[8,12,19,24,25] To achieve this near-optimum band gap from small band gap materials like PbS (0.5 eV) and PbSe (0.37 eV), relatively small nanocrystals are needed. Larger band gap semiconductors like $CuInSe_2$ (~1 eV) do not require significant quantum confinement and therefore can make use of nanocrystals with slower Auger decay that still exhibit relatively high MEG efficiency. For $CuInSe_2$, the largest nanocrystals measured (9.2 nm diameter) have a near optimal band gap of 1.06 eV and a biexciton lifetime of 130 ps. PbSe has a bulk band gap of 0.37 eV, and particles must be confined to a diameter of 5-6 nm to achieve a band gap near 0.75 eV.[32,33] At these sizes, PbSe has a biexciton lifetime of ~30 ps.[34] The relevant biexciton lifetime for $CuInSe_2$ is therefore much longer than for PbSe.

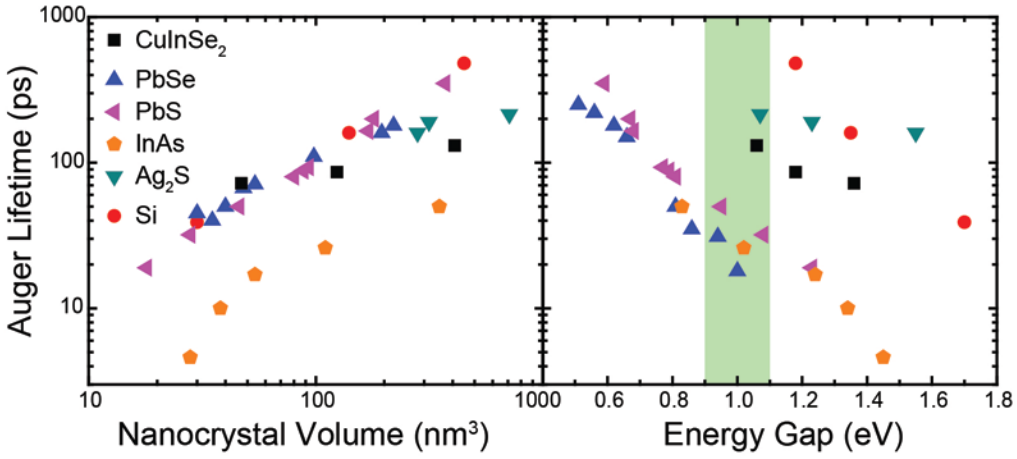

Figure 7.11 Auger lifetimes as a function of nanocrytstal volume and band gap energy for $CuInSe_2$, PbSe[19], PbS[24], InAs[25], Ag_2S[12], and Si[8] nanocrystals. The green box shows the optimal band gap range for an MEG solar cell.

7.4 CONCLUSIONS

In summary, TAS measurements showed that the MEG efficiency of $CuInSe_2$ nanocrystals is comparable to other types of nanocrystals. The MEG threshold of the nanocrystals was slightly higher ($2.4E_g$) than the value predicted by the carrier effective mass (of $2.14E_g$). A lower MEG threshold closer to $2E_g$ and higher MEG efficiency would improve the efficiency of multexciton solar cells. Nonetheless, the biexciton lifetimes are relatively long in the $CuInSe_2$ nanocrystals in this size range, which could aid in extracting multiexcitons from a solar cell. For these reasons, $CuInSe_2$ looks to be an interesting, and perhaps reasonably unique, material for the study and fabrication of multiexciton solar cells.

7.5 REFERENCES

1. Beard, M. C. *et al.* Comparing Multiple Exciton Generation in Quantum Dots To Impact Ionization in Bulk Semiconductors: Implications for Enhancement of Solar Energy Conversion. *Nano Lett.* **10,** 3019–3027 (2010).
2. Midgett, A. G. *et al.* Size and Composition Dependent Multiple Exciton Generation Efficiency in PbS, PbSe, and PbSxSe1–x Alloyed Quantum Dots. *Nano Lett.* **13,** 3078–3085 (2013).
3. Nootz, G. *et al.* Size dependence of carrier dynamics and carrier multiplication in PbS quantum dots. *Phys. Rev. B* **83,** 155302 (2011).
4. Schaller, R. D., Agranovich, V. M. & Klimov, V. I. High-efficiency carrier multiplication through direct photogeneration of multi-excitons via virtual single-exciton states. *Nat. Phys.* **1,** 189–194 (2005).
5. Franceschetti, A., An, J. M. & Zunger, A. Impact Ionization Can Explain Carrier Multiplication in PbSe Quantum Dots. *Nano Lett.* **6,** 2191–2195 (2006).
6. Allan, G. & Delerue, C. Influence of electronic structure and multiexciton spectral density on multiple-exciton generation in semiconductor nanocrystals: Tight-binding calculations. *Phys. Rev. B* **77,** 125340 (2008).
7. Velizhanin, K. A. & Piryatinski, A. Numerical Study of Carrier Multiplication Pathways in Photoexcited Nanocrystal and Bulk Forms of PbSe. *Phys. Rev. Lett.* **106,** 207401 (2011).
8. Beard, M. C. *et al.* Multiple Exciton Generation in Colloidal Silicon Nanocrystals. *Nano Lett.* **7,** 2506–2512 (2007).
9. Schaller, R. D. & Klimov, V. I. High Efficiency Carrier Multiplication in PbSe Nanocrystals: Implications for Solar Energy Conversion. *Phys. Rev. Lett.* **92,** 186601 (2004).
10. Ellingson, R. J. *et al.* Highly Efficient Multiple Exciton Generation in Colloidal PbSe and PbS Quantum Dots. *Nano Lett.* **5,** 865–871 (2005).
11. Lin, Z., Franceschetti, A. & Lusk, M. T. Size Dependence of the Multiple Exciton Generation Rate in CdSe Quantum Dots. *ACS Nano* **5,** 2503–2511 (2011).
12. Sun, J. *et al.* Generation of Multiple Excitons in Ag2S Quantum Dots: Single High-Energy versus Multiple-Photon Excitation. *J. Phys. Chem. Lett.* **5,** 659–665 (2014).
13. Stubbs, S. K. *et al.* Efficient carrier multiplication in InP nanoparticles. *Phys. Rev. B* **81,** 081303 (2010).
14. Califano, M. Direct and Inverse Auger Processes in InAs Nanocrystals: Can the Decay Signature of a Trion Be Mistaken for Carrier Multiplication? *ACS Nano* **3,** 2706–2714 (2009).

15. Luther, J. M. *et al.* Multiple Exciton Generation in Films of Electronically Coupled PbSe Quantum Dots. *Nano Lett.* **7,** 1779–1784 (2007).

16. Stolle, C. J. *et al.* Multiexciton Solar Cells of CuInSe2 Nanocrystals. *J. Phys. Chem. Lett.* **5,** 304–309 (2014).

17. Semonin, O. E. *et al.* Peak External Photocurrent Quantum Efficiency Exceeding 100% via MEG in a Quantum Dot Solar Cell. *Science* **334,** 1530–1533 (2011).

18. Panthani, M. G. *et al.* CuInSe2 Quantum Dot Solar Cells with High Open-Circuit Voltage. *J. Phys. Chem. Lett.* **4,** 2030–2034 (2013).

19. McGuire, J. A., Sykora, M., Joo, J., Pietryga, J. M. & Klimov, V. I. Apparent Versus True Carrier Multiplication Yields in Semiconductor Nanocrystals. *Nano Lett.* **10,** 2049–2057 (2010).

20. Blackburn, J. L., Ellingson, R. J., Mićić, O. I. & Nozik, A. J. Electron Relaxation in Colloidal InP Quantum Dots with Photogenerated Excitons or Chemically Injected Electrons. *J. Phys. Chem. B* **107,** 102–109 (2003).

21. Yu, P., Nedeljkovic, J. M., Ahrenkiel, P. A., Ellingson, R. J. & Nozik, A. J. Size Dependent Femtosecond Electron Cooling Dynamics in CdSe Quantum Rods. *Nano Lett.* **4,** 1089–1092 (2004).

22. Shabaev, A., Efros, A. L. & Nozik, A. J. Multiexciton Generation by a Single Photon in Nanocrystals. *Nano Lett.* **6,** 2856–2863 (2006).

23. García-Santamaría, F. *et al.* Suppressed Auger Recombination in 'Giant' Nanocrystals Boosts Optical Gain Performance. *Nano Lett.* **9,** 3482–3488 (2009).

24. Binks, D. J. Multiple exciton generation in nanocrystal quantum dots – controversy, current status and future prospects. *Phys. Chem. Chem. Phys.* **13,** 12693–12704 (2011).

25. Schaller, R. D., Pietryga, J. M. & Klimov, V. I. Carrier Multiplication in InAs Nanocrystal Quantum Dots with an Onset Defined by the Energy Conservation Limit. *Nano Lett.* **7,** 3469–3476 (2007).

26. Midgett, A. G., Hillhouse, H. W., Hughes, B. K., Nozik, A. J. & Beard, M. C. Flowing versus Static Conditions for Measuring Multiple Exciton Generation in PbSe Quantum Dots. *J. Phys. Chem. C* **114,** 17486–17500 (2010).

27. Hanna, M. C. & Nozik, A. J. Solar conversion efficiency of photovoltaic and photoelectrolysis cells with carrier multiplication absorbers. *J. Appl. Phys.* **100,** 074510 (2006).

28. Schaller, R. D., Petruska, M. A. & Klimov, V. I. Effect of electronic structure on carrier multiplication efficiency: Comparative study of PbSe and CdSe nanocrystals. *Appl. Phys. Lett.* **87,** 253102 (2005).

29. Beard, M. c. & Ellingson, R. j. Multiple exciton generation in semiconductor nanocrystals: Toward efficient solar energy conversion. *Laser Photonics Rev.* **2,** 377–399 (2008).

30. Trinh, M. T. *et al.* Direct generation of multiple excitons in adjacent silicon nanocrystals revealed by induced absorption. *Nat. Photonics* **6,** 316–321 (2012).

31. Klimov, V. I. Detailed-balance power conversion limits of nanocrystal-quantum-dot solar cells in the presence of carrier multiplication. *Appl. Phys. Lett.* **89,** 123118 (2006).

32. Moreels, I. *et al.* Size-Dependent Optical Properties of Colloidal PbS Quantum Dots. *ACS Nano* **3,** 3023–3030 (2009).

33. Moreels, I. *et al.* Composition and Size-Dependent Extinction Coefficient of Colloidal PbSe Quantum Dots. *Chem. Mater.* **19,** 6101–6106 (2007).

34. Stewart, J. T. *et al.* Comparison of Carrier Multiplication Yields in PbS and PbSe Nanocrystals: The Role of Competing Energy-Loss Processes. *Nano Lett.* **12,** 622–628 (2012).

Chapter 8: Conclusions and Future Directions

8.1 CONCLUSIONS

Semiconductor nanocrystal photovoltaics have the potential to make a big impact on the solar cell market, particularly in the area of light-weight flexible solar power. Nanocrystal absorber layers can be processed under ambient conditions at low cost using high-throughput manufacturing techniques, which offers a substantial cost benefit compared to traditional bulk thin film photovoltaics.[1] However, despite this cost benefit, the device efficiencies are too low to be commercially viable without resorting to expensive high-temperature processing techniques. This research has explored a variety of ways by which nanocrystal device performance might be improved, both from a fundamental and applied perspective. The effects of nanocrystal size and surface chemistry on device performance were investigated, which involved the development of new nanocrystal synthesis techniques and ligand exchange procedures.[2,3] A new processing technique called photonic curing was explored with the goal of achieving high-temperature sintering and device improvements at very low cost and on flexible, temperature-sensitive substrates.[4,5] Finally, the fundamental aspects of charge carrier generation in nanocrystals and charge extraction in nanocrystal devices were studied, particularly as it relates to multiexciton generation.[6]

8.1.1 Nanocrystal Synthesis and Ligand Exchanges

$CuInSe_2$ nanocrystals are typically synthesized with sizes typically in the range of 12-20 nm in diameter with a large polydispersity. Nanocrystals in this size range are larger than the Bohr exciton radius (~10nm) and therefore do not show any quantum

confinement effects. The synthesis of smaller nanocrystals with more tightly controlled size distribution could allow for the tuning of optical properties of $CuInSe_2$. Nanocrystals with tunable size from 2 to 9 nm diameter were made using a secondary phosphine selenide as the Se source. Compared to tertiary phosphine selenide precursors, secondary phosphide selenides were found to provide higher product yields and smaller nanocrystals that elicit quantum confinement with size-dependent optical gap. Photovoltaic devices fabricated from spray-cast nanocrystal films demonstrated large, size-dependent open circuit voltages—up to 849 mV for absorber films with a 1.46 eV optical gap—a record for any colloidal nanocrystal-based solar cell. However, the device currents were much lower than for larger nanocrystal films due to the larger optical gap and the larger organic content associated with smaller nanocrystals.[2]

In order to improve charge transport between nanocrystals in photovoltaic devices, short inorganic chalcogenidometallate cluster (ChaM) ligands and S^{2-} ionic ligands were investigated as a replacement for oleylamine. Nanocrystals were capped with ChaM ligands or S^{2-} ionic ligands using a solution-based ligand exchange procedure in hydrazine or water, respectively. Nanocrystal films were deposited from these new nanocrystal solutions to make photovoltaic devices. The ChaM ligand-capped nanocrystal devices exhibited power conversion efficiencies (1.7%) comparable to the oleylamine-capped nanocrystals (1.6%), but with significantly thinner absorber layers. This is due to the enhanced interparticle charge transport between ChaM-capped nanocrystals. $S^{2—}$ capped nanocrystal devices exhibited lower device performance, but allow for device fabrication from aqueous solutions.[3]

8.1.2 Photonic Curing

Photonic curing is a promising new technique which could allow for the fabrication of very high efficiency devices on flexible, temperature-sensitive substrates. Photonic curing uses Xe flash lamps to generate ~300 μs long, high-intensity, broad band light pulses. The light is absorbed by the nanocrystal film, which causes it to rapidly heat. The temperature reached in the film is dependent on how much light is absorbed (the film thickness) and the thermal conductivity of the film and substrate. When using thermally insulating substrates such as glass or plastic, the film dissipates most of its heat radiatively and the substrate remains cool. There are two pulse energy regimes of interest. High intensity photonic curing pulses cause the nanocrystal film to sinter into large grains whereas lower intensity photonic curing pulses cause the organic ligands to vaporize from the film, but the nanocrystal grain sizes remain intact.

High-intensity photonic curing was examined as a way to convert $CuInSe_2$ nanocrystals into large grains without the need for selenization. Nanocrystal films were deposited on a variety of metal back contact materials and treated with photonic curing. In all cases, the nanocrystals grew into large grains without the presence of a selenium-rich atmosphere. However, the curing process was found to dewet $CuInSe_2$ nanocrystal from Mo back contacts and form large agglomerations. These agglomerations left large regions of exposed back contact which destroyed device performance. Nanocrystals cured on Au, Ni, ITO, and $MoSe_2$/Mo bilayer substrates demonstrated much better adhesion, making it possible to form sintered films with relatively uniform thickness that could be used to make working photovoltaic devices. Device performance was still low, due largely to regions of exposed back contact, but this work still provides the first report of a working $CuInSe_2$ nanocrystal device sintered with broad-band light.

Thermal modeling of the photonic curing process showed that oleylamine-capped $CuInSe_2$ nanocrystals grow into larger grains via melting and resolidification rather than traditional sintering mechanisms, resulting in somewhat non-uniform films and significant regions of exposed back contact. When the nanocrystals are capped with ChaM ligands, however, the films can be sintered at significantly lower pulse energies to avoid melting and thereby retain layer integrity. At higher pulse energies, ChaM-capped nanocrystals melt, but adhere more uniformly to substrate. Device performance is poor, however, most likely due to the formation of wurtzite phase $CuInSe_2$ after photonic curing.[4]

Treating nanocrystal films with lower-intensity photonic curing removes organic ligands from the film, but the nanocrystals retain their small size. This leads to greatly enhanced electronic coupling between nanocrystals and therefore very high device short circuit current. Peak external quantum efficiencies of just over 125% were observed in devices, which is indicative of multiexciton generation and extraction from the nanocrystal film under typical solar illumination conditions. Under low light conditions, however, the quantum efficiency drops significantly, indicating that photonic curing-induced ligand desorption creates a significant amount of traps in the film that limits the device open circuit voltage and overall power conversion efficiency.[5]

8.1.3 Transient Absorption Spectroscopy

Transient absorption spectroscopy (TAS) was used to confirm the presence of multiexciton generation (MEG) in films of $CuInSe_2$ nanocrystals with desorbed ligands treated with photonic curing. TAS was also used to study MEG in solvent-dispersed colloidal $CuInSe_2$ nanocrystals. Size-dependent carrier cooling rates, absorption cross

sections, and Auger lifetimes were also determined. The energy threshold for MEG in the $CuInSe_2$ nanocrystals was found to be 2.4 ± 0.2 times the nanocrystal optical gap and the MEG efficiency was 36 ± 6%. These parameters are similar to other types of nanocrystal quantum dot materials. However, $CuInSe_2$ has much longer Auger lifetimes for nanocrystals near the optimum band gap energy compared to any other quantum dot materials, making $CuInSe_2$ an attractive material for harnessing MEG in a working solar cell.[6]

8.2 FUTURE DIRECTIONS

Despite the advances in $CuInSe_2$ nanocrystal photovoltaics reported here, there are many unsolved technical and fundamental challenges that need to be solved before this technology has an impact on the photovoltaics market. One possible area for improvement is the synthesis of luminescent $CuInSe_2$ nanocrystals. Current synthesis techniques for $CuInSe_2$ nanocrystals used in photovoltaic devices produce very weakly luminescent nanocrystals.[2,7] This weak luminescence results from fast charge trapping on the nanocrystal surfaces due to poor surface passivation. Removing these surface traps could greatly improve device performance, so long as the passivation scheme doesn't greatly hinder interparticle charge transport.

Another interesting path forward involves using solid-state ligand exchange procedures to replace the long insultating organic ligands used during synthesis with much shorter ligands once the nanocrystal film has already been deposited. These procedures take advantage of the excellent solution stability and easy film deposition that long ligands provide as well as the superior electronic properties of shorter ligands. Solid-state ligand exchanges have been used to greatly improve the efficiency of PbS quantum

dot solar cells from 5%[8] up to 8.6%[9] without adding any significant cost or processing steps. However, these techniques have not been thoroughly explored for $CuInSe_2$ nanocrystal solar cells.

Photonic curing perhaps has the greatest potential to make very high efficiency devices at low cost. For high-intensity photonic curing, performing some type of ligand exchange procedure prior to curing appears to be important to obtaining uniform films without exposed back contact. Some more fundamental understanding is required, though, to prevent the formation of wurtzite $CuInSe_2$ and achieve high-efficiency devices. For lower-intensity photonic curing, the device open circuit voltage and fill factor need to be improved while maintaining the very high short circuit current. This may be possible through an optimal solid-state repassivation technique, but new creative solutions may be required.

Apart from solving these challenges with $CuInSe_2$, photonic curing of other semiconductor nanocrystals could be interesting. Successful sintering of $Cu_2(Zn,Sn)S_4$ could be important for attaining high efficiency devices, particularly if the phase can be controlled during the process. Photonic curing of CdTe nanocrystals could be highly successful since CdTe nanocrystals are known to sinter under less harsh conditions than $CuInSe_2$ (350 °C in air is sufficient). Finally, studying MEG in PbS or PbSe nanocrystals treated with low-intensity photonic curing could be interesting, since PbS and PbSe have overall higher device efficiencies compared with $CuInSe_2$.

Understanding MEG in a variety of nanocrystal materials is important for achieving the highest possible device currents in nanocrystal solar cells. In order for MEG to have a large impact on the overall device performance, materials must have an MEG threshold close to $2*E_g$ and an MEG efficiency close to 100%. Thus far, $CuInSe_2$ nanocrystals show promise for use in multiexciton solar cells, but their MEG properties

could possibly be improved by altering their size, shape, or surface passivation. Furthermore, alternative materials not yet studied may have superior MEG properties and should be investigated.

8.3 REFERENCES

1. Akhavan, V. A. *et al.* Colloidal CIGS and CZTS nanocrystals: A precursor route to printed photovoltaics. *J. Solid State Chem.* **189**, 2–12 (2012).
2. Panthani, M. G. *et al.* CuInSe2 Quantum Dot Solar Cells with High Open-Circuit Voltage. *J. Phys. Chem. Lett.* **4**, 2030–2034 (2013).
3. Stolle, C. J., Panthani, M. G., Harvey, T. B., Akhavan, V. A. & Korgel, B. A. Comparison of the Photovoltaic Response of Oleylamine and Inorganic Ligand-Capped CuInSe2 Nanocrystals. *ACS Appl. Mater. Interfaces* **4**, 2757–2761 (2012).
4. Stolle, C. J., Harvey, T. B. & Korgel, B. A. Photonic curing of ligand-capped CuInSe2 nanocrystal films. in *Photovoltaic Specialist Conference (PVSC)*, 2014 IEEE 40th 0270–0274 (2014). doi:10.1109/PVSC.2014.6924897
5. Stolle, C. J. *et al.* Multiexciton Solar Cells of CuInSe2 Nanocrystals. *J. Phys. Chem. Lett*. **5**, 304–309 (2014).
6. Stolle, C. J., Schaller, R. D. & Korgel, B. A. Efficient Carrier Multiplication in Colloidal CuInSe2 Nanocrystals. *J. Phys. Chem. Lett.* 3169–3174 (2014). doi:10.1021/jz501640f
7. Panthani, M. G. *et al.* Synthesis of CuInS2, CuInSe2, and Cu(InxGa1-x)Se2 (CIGS) Nanocrystal 'Inks' for Printable Photovoltaics. *J. Am. Chem. Soc.* **130**, 16770–16777 (2008).
8. Pattantyus-Abraham, A. G. *et al.* Depleted-Heterojunction Colloidal Quantum Dot Solar Cells. *ACS Nano* **4**, 3374–3380 (2010).
9. Chuang, C.-H. M., Brown, P. R., Bulović, V. & Bawendi, M. G. Improved performance and stability in quantum dot solar cells through band alignment engineering. *Nat. Mater.* **13**, 796–801 (2014).

Appendix A: Nanocrystal Synthesis Recipes

A.1 CU(IN,GA)SE_2 AND RELATED NANOCRYSTAL SYNTHESIS RECIPES

A.1.1 Elemental:Se Reaction

This reaction was the most common reaction used for Vahid and Taylor's selenization work.

1. Determine the desired nanocrystal composition based on: $CuIn1\text{-}_xGa_xSe_2$
2. Clean one 100 ml three neck round bottom flask, stir bar, and thermocouple three times with DI water. Rinse with acetone and dry over heat gun.
3. Seal two necks with rubber septa and wire shut. Pierce one septa with a needle and insert the thermocouple. Place stir bar in the flask. Leave the third neck uncapped.
4. Measure 8 mmol of selenium powder and place in the flask (for a 4 mmol reaction). Place a septa over the final neck. Close septa, but do not wire shut. Pierce a needle through the septa and leave in place. This will allow air to exchange between the flask and glovebox antechamber without letting the selenium escape the flask.
5. Cycle flask, three pieces of weight paper, a 10 ml syringe, and a needle into the glovebox.
6. Measure 4 mmol of anhydrous CuCl beads, 4*(1-x) mmol of anhydrous $InCl_3$ powder, and 4x mmol of anhydrous $GaCl_3$ powder and place into the flask.
7. Add 20 ml of oleylamine to the flask (previously degassed at 110 °C overnight and stored in the glovebox). Seal the flask with a septa and remove from glovebox.

8. Wire down the last septa and attach to the Schlenk line.
9. Degas reaction at 110 °C for 30 minutes under vacuum.
10. Close vacuum line and open flask to nitrogen. Ramp reaction temperature to 200 °C.
11. Hold reaction at 200 °C for 30 minutes, then ramp temperature to 260 °C and hold for 10 minutes.
12. Turn off the heat and remove the heating mantle. Allow the flask to reach 50-100 °C before removing from Schlenk line.
13. Poor the reaction mixture equally between two glass 50 ml centrifuge tubes. Precipitate by adding excess ethanol (~20 ml to each tube). Centrifuge at 4000 rpm for 2 minutes. Note that the amount of ethanol added during this step has an impact on the overall organic content of the film. For films sprayed using the automatic sprayer, less ethanol should be added.
14. Discard the clear supernatant and redisperse the precipitated nanocrystals in toluene. Centrifuge the nanocrystals without adding any antisolvent at 4000 rpm for 2 min. Keep the supernatant and discard any precipitated particles (called the separation step).
15. Slowly add ethanol to the nanocrystal solution until the solution becomes turbid. Centrifuge at 4000 rpm for 2 min. Discard the supernatant (which may still be somewhat dark, but not completely opaque) and redisperse the precipitated nanocrystals in toluene.
16. Transfer the nanocrystals to a vial and cycle the nanocrystals into the glovebox for storage.

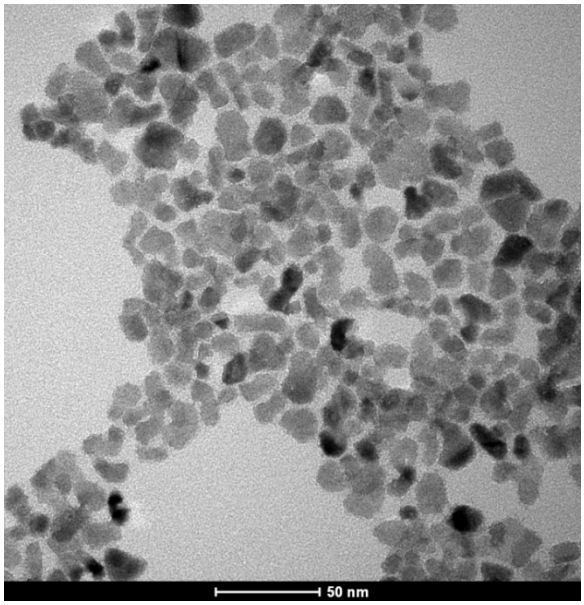

Figure A.1 TEM image of $CuInSe_2$ nanocrystals synthesized using recipe A.1.1.

A.1.2 TBP:Se and DPP:Se Reactions

The TBP:Se reaction has been shown to give the best results for nanocrystal devices with no further treatment step. The DPP:Se reaction give the best reaction yields and is used to make size-controlled nanocrystals (by varying the injection and reaction temperature). It is also the reaction used for all of the MEG experiments (photonic curing and TAS).

1. Determine the desired nanocrystal composition based on: $CuIn1\text{-}_xGa_xSe_2$
2. Clean one 100 ml three neck round bottom flask, two stir bars, and one thermocouple three times with DI water. Rinse with acetone and dry over heat gun.

3. Seal two necks with rubber septa and wire shut. Pierce one septa with a needle and insert the thermocouple. Place stir bar in the flask. Leave the third neck uncapped.
4. Measure 8 mmol of selenium powder and place into a clean vial (for a 4 mmol reaction) along with a stir bar. Loosely cap the vial.
5. Cycle flask, vial, three pieces of weight paper, two 10 ml syringes, and two needles into the glovebox.
6. Dissolve the Se in either 8 ml of tributylphosphine (TBP reaction) or 3 ml of diphenylphosphine and 4 ml of oleylamine (DPP reaction). Draw the dissolved TBP:Se or DPP:Se solutions into a syringe and cap the needle.
7. Measure 4 mmol of anhydrous CuCl beads, 4*(1-x) mmol of anhydrous $InCl_3$ powder, and 4x mmol of anhydrous $GaCl_3$ powder and place into the flask.
8. Add 20 ml of oleylamine to the flask (previously degassed at 110 °C overnight and stored in the glovebox). Seal the flask with a septa and remove the flask and Se precursor syringe from glovebox.
9. Wire down the last septa and attach to the Schlenk line.
10. Degas reaction at 110 °C for 30 minutes under vacuum.
11. Close vacuum line and open flask to nitrogen. Ramp reaction temperature to 240 °C.
12. When the reaction temperature reaches 180 °C, inject the TBP:Se or DPP:Se precursor into the flask and continue ramping to 240°C. Hold the reaction at 240 °C for 30 minutes.
13. DPP:Se Synthesis only: The size of the nanocrystals can be varying by changing the injection and reaction temperature. For smaller nanocrystals, inject and hold the reaction at any temperature between 100 °C and 180°C.

14. Turn off the heat and remove the heating mantle. Allow the flask to reach 50-100 °C before removing from Schlenk line.
15. Wash the nanocrystals according to steps 13-16 of the Elem:Se reaction recipe in A.1.1.

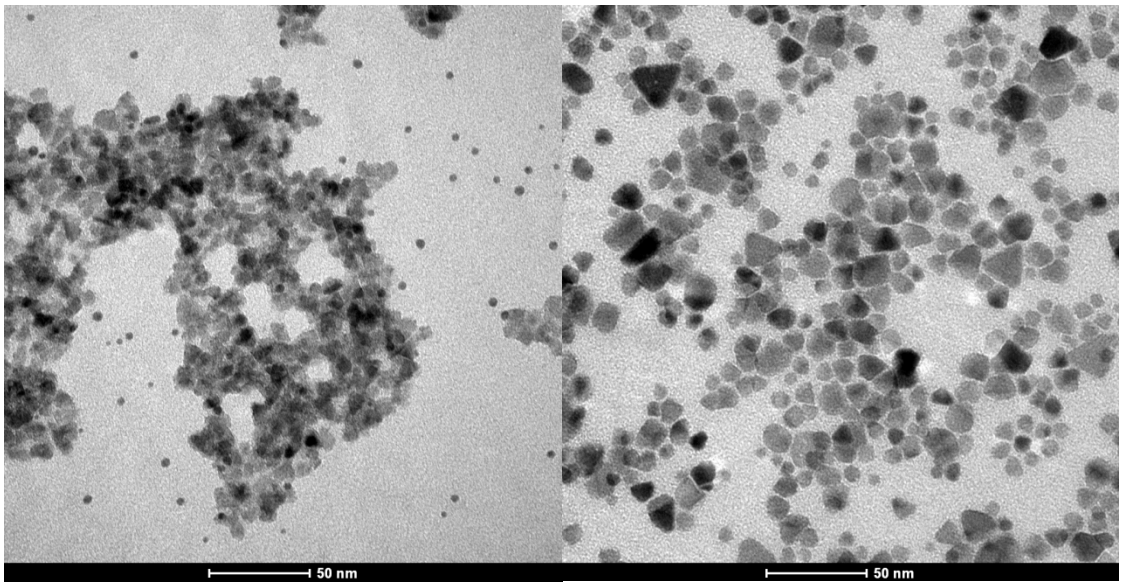

Figure A.2 (left) TEM image of $CuInSe_2$ nanocrystals synthesized using recipe A.1.2 (TBP method). (right) TEM image of $CuInSe_2$ nanocrystals synthesized using recipe A.1.2 (DPP method).

A.1.3 Hydrated Precursors Recipe

This reaction has the advantage of not needing a glovebox; however, this is only true for making $CuInSe_2$, since $GaCl_3$ is not sold in hydrated form.

1. Clean one 100 ml three neck round bottom flask, one stir bar, and one thermocouple three times with DI water. Rinse with acetone and dry over heat gun.

2. Seal two necks with rubber septa and wire shut. Pierce one septa with a needle and insert the thermocouple. Place stir bar in the flask. Leave the third neck uncapped.
3. Measure 8 mmol of selenium powder, 4 mmol of $CuCl_2 \cdot 2H_2O$, and 4 mmol of $InCl_3 \cdot 4H_2O$ and place in the flask (for a 4 mmol reaction). Add 20 ml of non-degassed oleylamine. Place a septa over the final neck, wire shut, and attach to the Schlenk line.
4. Degas reaction at 110 °C for 2 hours under vacuum.
5. Follow steps 10-16 for the Elemental:Se reaction in A.1.1.

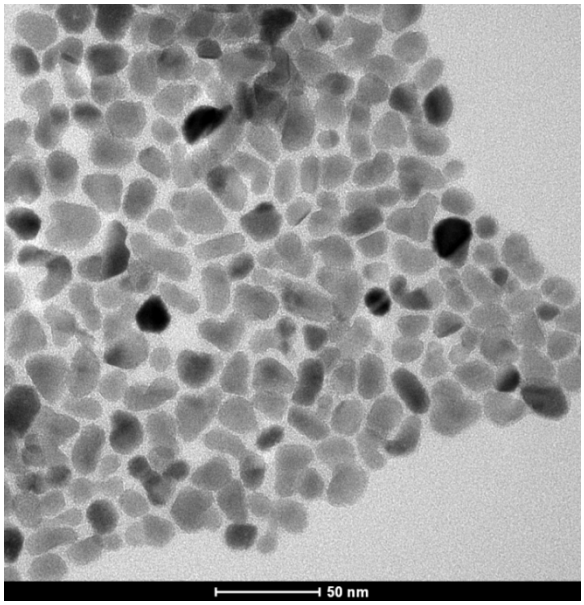

Figure A.3 TEM image of $CuInSe_2$ nanocrystals synthesized using recipe A.1.3.

A.1.4 Cu(In,Ga)S_2 Recipe

1. Determine the desired nanocrystal composition based on: $CuIn1-_xGa_xS_2$

2. Clean one 100 ml three neck round bottom flask, one 50 ml three neck round bottom flask, two stir bars, and one thermocouple three times with DI water. Rinse with acetone and dry over heat gun.
3. Seal two necks of each flask with rubber septa and wire shut. Pierce one septa for the 100 ml flask with a needle and insert the thermocouple. Leave the third neck uncapped for each flask.
4. For a 5 mmol reaction: In the 100 ml flask, add 5 mmol of Cu(II)ACAC (Copper II acetylacetonate), 5*(1-x) mmol of In(III)ACAC, 5x mmol of Ga(III)ACAC, and 35 ml of dichlorobenzene.
5. In the 50 ml flask, add 10 mmol of sulfur powder and 15 ml of dichlorobenzene.
6. Seal both flasks with wired septa and attach to the Schlenk line.
7. Degas flasks while stirring by pulling vacuum at room temperature for 15 minutes followed by 15 minutes of nitrogen purging. Repeat this step three times.
8. During the degas step, cycle a 10 ml syringe and needle into the glovebox. Take out 10 ml of already-degassed oleylamine.
9. After degas step, inject oleylamine into the 100 ml flask.
10. Take 50 ml flask off the Schlenk line, but leave sealed under nitrogen. Withdraw DCB:Se solution into a syringe.
11. Heat the 100 ml flask to 180 °C. When the reaction reaches 110 °C, inject the DCB:Se solution.
12. React at 180 °C for 1 hour.
13. Turn off the heat and remove the heating mantle. Allow the flask to reach 50-100 °C before removing from Schlenk line.

14. To wash the nanocrystals, follow steps 13-16 for Elemental:Se reaction in A.1.1.

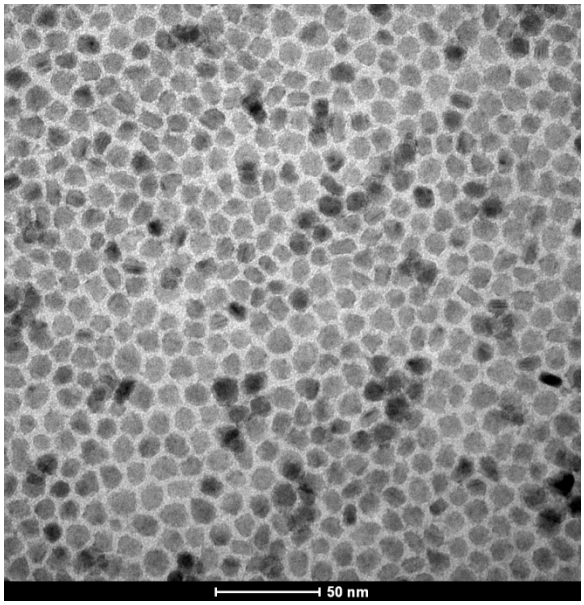

Figure A.4 TEM image of $CuInS_2$ nanocrystals synthesized using recipe A.1.4.

A.1.5 In_2Se_3 recipe

This recipe is adapted from Son, *et al.*[1]

1. Clean one 100 ml three neck round bottom flask, stir bar, and thermocouple three times with DI water. Rinse with acetone and dry over heat gun.
2. Seal two necks with rubber septa and wire shut. Pierce one septa with a needle and insert the thermocouple. Place stir bar in the flask. Leave the third neck uncapped.
3. Measure 0.11 g of selenium powder and place in the flask. Place a septa over the final neck. Close septa, but do not wire shut. Pierce a needle through the

septa and leave in place. This will allow air to exchange between the flask and glovebox antechamber without letting the selenium escape the flask.

4. Cycle flask, one piece of weight paper, a 10 ml syringe, and a needle into the glovebox.
5. Measure 0.2 g of anhydrous $InCl_3$ powder and place into the flask.
6. Add 18 ml of oleylamine to the flask (previously degassed at 110 °C overnight and stored in the glovebox). Seal the flask with a septa and remove from glovebox.
7. Wire down the last septa and attach to the Schlenk line.
8. Degas reaction at 110 °C for 30 minutes under vacuum.
9. Close vacuum line and open flask to nitrogen. Ramp reaction temperature to 215 °C and hold for 2 hours.
10. Turn off the heat and remove the heating mantle. Allow the flask to reach 50-100 °C before removing from Schlenk line.
11. Follow steps 13-16 from Elemental:Se reaction in section A.1.1 for nanocrystal washing.

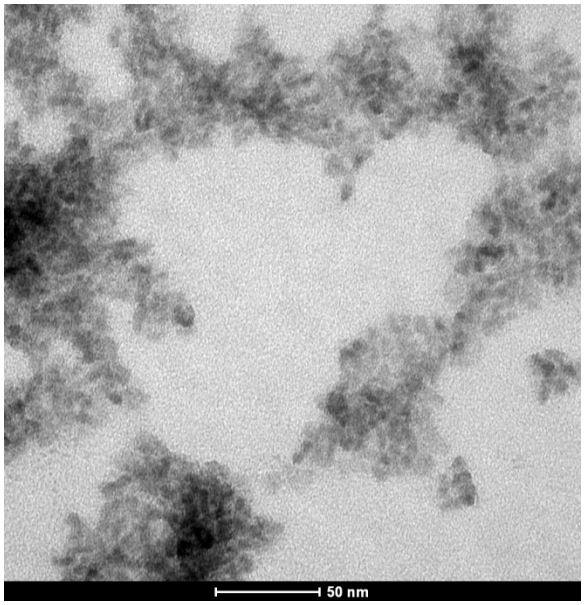

Figure A.5 TEM image of In_2Se_3 nanocrystals synthesized using recipe A.1.5.

A.1.6 $Cu_{2-x}Se$ /Recipe

This recipe is adapted from Deka *et al.*[2]

1. Clean one 100 ml three neck round bottom flask, one 50 ml three neck round bottom flask, two stir bars, and two thermocouples three times with DI water. Rinse with acetone and dry over heat gun.
2. Seal two necks of each flask with rubber septa and wire shut. Pierce one septa for each flask with a needle and insert a thermocouple. Leave the third neck uncapped for each flask.
3. In the 50 ml flask, add 0.079 g of selenium powder. Seal the neck and pierce with a needle for air-exchange in the glovebox.
4. Cycle both flasks into the glovebox along with 1 piece of weight paper, two 10 ml syringes, and two needles.

5. In the 50 ml flask, add 4 ml octadecene.
6. In the 100 ml flask, add 0.2 g anhydrous CuCl beads, 10 ml degassed oleylamine, and 10 ml octadecene.
7. Seal both flasks with wired septa, remove from glovebox, and attach to the Schlenk line.
8. Degas the 100 ml flask under vacuum while stirring for 1 hour at 80 °C.
9. For the 50 ml flask, pull vacuum briefly at room temperature, then purge with nitrogen and heat to 200 °C while stirring. Hold at 200 °C until the selenium is dissolved, then cool flask to room temperature.
10. Draw the Se:ODE solution into a syringe.
11. Heat the 100 ml flask to 310 °C under nitrogen. At 310 °C, inject the cold Se:ODE solution. React at 310 °C for 15 minutes (starting immediately after the injection).
12. Turn off the variac and remove the heating mantle. Let cool to 50-100 °C before removing from the Schlenk line.
13. To wash the nanocrystals, follow steps 13-16 for Elemental:Se reaction in A.1.1.

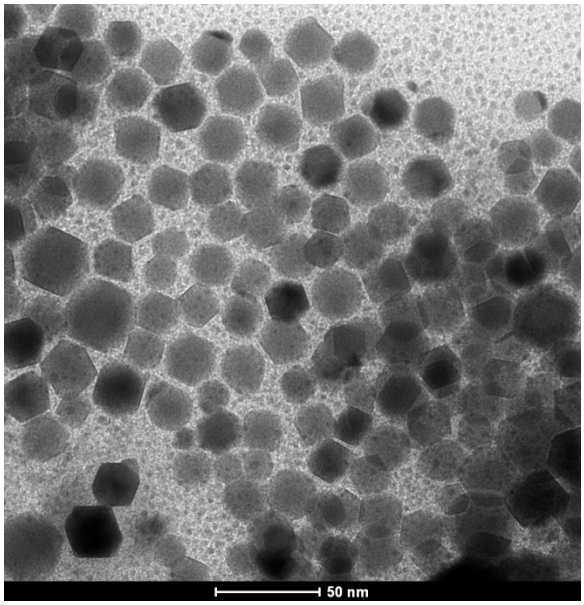

Figure A.6 TEM image of In_2Se_3 nanocrystals synthesized using recipe A.1.6.

A.2 OTHER NANOCRYSTAL SYNTHESIS RECIPES

A.2.1 PbS Recipe

This recipe is adapted from Tang, *et al.*[3]

1. Before starting the reaction, make a stock solution of bis(trimethylsilyl)sulfide (TMS) diluted to 0.28M in octadecene. Make and store the stock solution in the glovebox.
2. Clean one 100 ml three neck round bottom flask, stir bar, and thermocouple three times with DI water. Rinse with acetone and dry over heat gun.
3. Seal two necks with rubber septa and wire shut. Pierce one septa with a needle and insert the thermocouple. Place stir bar in the flask. Leave the third neck uncapped.

4. Add 4 mmol PbO, 3 ml oleic acid, and 36 ml octadecene to the flask. Seal the flask with the third septa, wire down, and attach to the Schlenk line.
5. To degas, heat flask to 100 °C under vacuum while stirring for until the solution turns clear (~2 hours).
6. During the degas step, Cycle a 10 ml syringe and needle into the glovebox and retrieve 7.2 ml of (0.28 M) TMS solution.
7. Heat the flask to 120 °C under nitrogen and then inject the TMS solution.
8. Immediately turn off the variac, but do not lower the heating mantle. Instead, allow the reaction to cool slowly down to 40 °C before removing.
9. Wash the nanocrystals following steps 13-16 of the Elemental:Se reaction in A.1.1; however, use acetone instead of ethanol as the antisolvent.

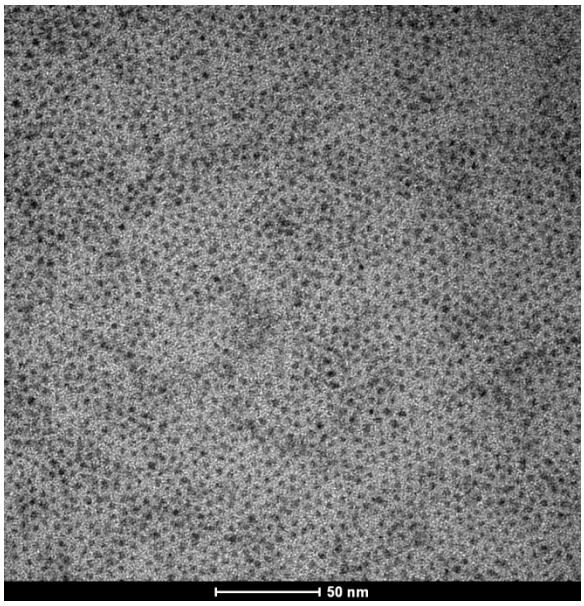

Figure A.7 TEM image of PbS nanocrystals synthesized using recipe A.2.1.

A.2.2 CdTe Recipe

This recipe is adapted from Jasieniak, *et al.*[4]

1. Clean one 100 ml three neck round bottom flask, stir bar, and thermocouple three times with DI water. Rinse with acetone and dry over heat gun.
2. Seal two necks with rubber septa and wire shut. Pierce one septa with a needle and insert the thermocouple. Place stir bar in the flask. Leave the third neck uncapped.
3. Add 0.96 g CdO, 0.48 g Te powder, 9 ml oleic acid, and 40 ml octadecene to the flask. Seal the flask with the third septa, wire down, and attach to the Schlenk line.
4. Cycle a 10 ml syringe and needle into the glovebox and retrieve 10 ml of trioctylphosphine (TOP).
5. Stir the reaction flask under vacuum and heat to 80 °C to degas.
6. Once the flask reaches 80 °C, close the vacuum and open the nitrogen. Inject the 10 ml of TOP.
7. Heat to 260 °C and react for 30 minutes.
8. Turn off the heat and remove the heating mantle. Allow the flask to reach 50-100 °C before removing from Schlenk line.
9. Follow steps 13-16 for the Elemental:Se reaction in A.1.1 for nanocrystal washing.

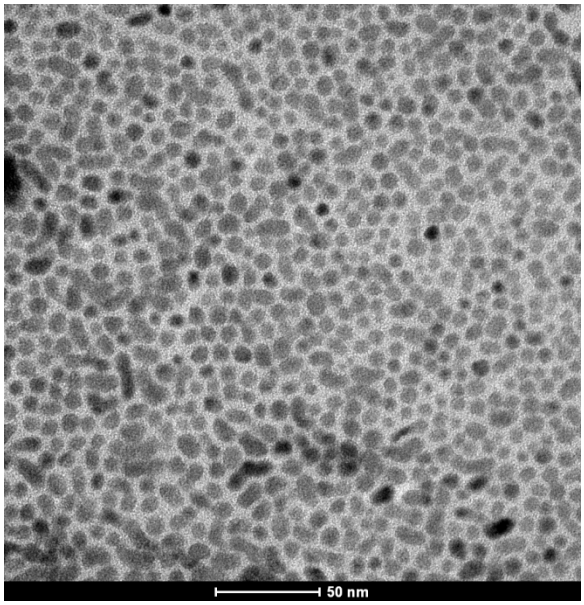

Figure A.8 TEM image of CdTe nanocrystals synthesized using recipe A.2.2.

A.3 REFERENCES

1. Park, K. H., Jang, K., Kim, S., Kim, H. J. & Son, S. U. Phase-Controlled One-Dimensional Shape Evolution of InSe Nanocrystals. *J. Am. Chem. Soc.* **128,** 14780–14781 (2006).

2. Deka, S. *et al.* Phosphine-Free Synthesis of p-Type Copper(I) Selenide Nanocrystals in Hot Coordinating Solvents. *J. Am. Chem. Soc.* **132,** 8912–8914 (2010).

3. Tang, J. *et al.* Quantum Dot Photovoltaics in the Extreme Quantum Confinement Regime: The Surface-Chemical Origins of Exceptional Air- and Light-Stability. *ACS Nano* **4,** 869–878 (2010).

4. Jasieniak, J., MacDonald, B. I., Watkins, S. E. & Mulvaney, P. Solution-Processed Sintered Nanocrystal Solar Cells via Layer-by-Layer Assembly. *Nano Lett.* **11,** 2856–2864 (2011).

References

Abou-Ras, D. *et al.* Formation and characterisation of MoSe2 for Cu(In,Ga)Se2 based solar cells. *Thin Solid Films* **480–481,** 433–438 (2005).

Akhavan, V. A. *et al.* Colloidal CIGS and CZTS nanocrystals: A precursor route to printed photovoltaics. *J. Solid State Chem.* **189,** 2–12 (2012).

Akhavan, V. A. *et al.* Influence of Composition on the Performance of Sintered Cu(In,Ga)Se2 Nanocrystal Thin-Film Photovoltaic Devices. *ChemSusChem* **6**, 481–486 (2013).

Akhavan, V. A. *et al.* Spray-deposited CuInSe2 nanocrystal photovoltaics. *Energy Environ. Sci.* **3**, 1600 (2010).

Akhavan, V. A., Panthani, M. G., Goodfellow, B. W., Reid, D. K. & Korgel, B. A. Thickness-limited performance of CuInSe2 nanocrystal photovoltaic devices. *Opt. Express* **18,** A411–A420 (2010).

Allan, G. & Delerue, C. Influence of electronic structure and multiexciton spectral density on multiple-exciton generation in semiconductor nanocrystals: Tight-binding calculations. *Phys. Rev. B* **77,** 125340 (2008).

Allen, P. M. & Bawendi, M. G. Ternary I−III−VI Quantum Dots Luminescent in the Red to Near-Infrared. *J. Am. Chem. Soc.* **130**, 9240–9241 (2008).

An, J. M., Franceschetti, A. & Zunger, A. The Excitonic Exchange Splitting and Radiative Lifetime in PbSe Quantum Dots. *Nano Lett.* **7,** 2129–2135 (2007).

Arango, A. C., Oertel, D. C., Xu, Y., Bawendi, M. G. & Bulović, V. Heterojunction Photovoltaics Using Printed Colloidal Quantum Dots as a Photosensitive Layer. *Nano Lett.* **9**, 860–863 (2009).

Barkhouse, D. A. R., Pattantyus-Abraham, A. G., Levina, L. & Sargent, E. H. Thiols Passivate Recombination Centers in Colloidal Quantum Dots Leading to Enhanced Photovoltaic Device Efficiency. *ACS Nano* **2,** 2356–2362 (2008).

Baumgardner, W. J., Whitham, K. & Hanrath, T. Confined-but-Connected Quantum Solids via Controlled Ligand Displacement. *Nano Lett.* **13,** 3225–3231 (2013).

Beard, M. C. & Ellingson, R. j. Multiple exciton generation in semiconductor nanocrystals: Toward efficient solar energy conversion. *Laser Photonics Rev.* **2,** 377–399 (2008).

Beard, M. C. *et al.* Comparing Multiple Exciton Generation in Quantum Dots To Impact Ionization in Bulk Semiconductors: Implications for Enhancement of Solar Energy Conversion. *Nano Lett.* **10,** 3019–3027 (2010).

Beard, M. C. *et al.* Multiple Exciton Generation in Colloidal Silicon Nanocrystals. *Nano Lett.* **7**, 2506–2512 (2007).

Beard, M. C. Multiple Exciton Generation in Semiconductor Quantum Dots. *J. Phys. Chem. Lett.* **2,** 1282–1288 (2011).

Binks, D. J. Multiple exciton generation in nanocrystal quantum dots – controversy, current status and future prospects. *Phys. Chem. Chem. Phys.* **13,** 12693–12704 (2011).

Blackburn, J. L., Ellingson, R. J., Mićić, O. I. & Nozik, A. J. Electron Relaxation in Colloidal InP Quantum Dots with Photogenerated Excitons or Chemically Injected Electrons. *J. Phys. Chem. B* **107,** 102–109 (2003).

Brown, P. R. *et al.* Energy Level Modification in Lead Sulfide Quantum Dot Thin Films through Ligand Exchange. *ACS Nano* **8,** 5863–5872 (2014).

Califano, M. Direct and Inverse Auger Processes in InAs Nanocrystals: Can the Decay Signature of a Trion Be Mistaken for Carrier Multiplication? *ACS Nano* **3,** 2706–2714 (2009).

Castro, S. L., Bailey, S. G., Raffaelle, R. P., Banger, K. K. & Hepp, A. F. Nanocrystalline Chalcopyrite Materials (CuInS2 and CuInSe2) via Low-Temperature Pyrolysis of Molecular Single-Source Precursors. *Chem. Mater.* **15,** 3142–3147 (2003).

Cao, Y. *et al.* High-Efficiency Solution-Processed Cu2ZnSn(S,Se)4 Thin-Film Solar Cells Prepared from Binary and Ternary Nanoparticles. *J. Am. Chem. Soc.* **134,** 15644–15647 (2012).

Cassette, E. *et al.* Synthesis and Characterization of Near-Infrared Cu−In−Se/ZnS Core/Shell Quantum Dots for In vivo Imaging. *Chem. Mater.* **22**, 6117–6124 (2010).

Chapin, D. M., Fuller, C. S. & Pearson, G. L. A New Silicon p-n Junction Photocell for Converting Solar Radiation into Electrical Power. *J. Appl. Phys.* **25,** 676–677 (1954).

Chirilă, A. *et al.* Highly efficient Cu(In,Ga)Se2 solar cells grown on flexible polymer films. *Nat. Mater.* **10,** 857–861 (2011).

Choi, J.-H. *et al.* Bandlike Transport in Strongly Coupled and Doped Quantum Dot Solids: A Route to High-Performance Thin-Film Electronics. *Nano Lett.* **12**, 2631–2638 (2012).

Choi, J. J. *et al.* PbSe Nanocrystal Excitonic Solar Cells. *Nano Lett.* **9,** 3749–3755 (2009).

Choi, J. J. *et al.* Solution-Processed Nanocrystal Quantum Dot Tandem Solar Cells. *Adv. Mater.* **23,** 3144–3148 (2011).

Chuang, C.-H. M., Brown, P. R., Bulović, V. & Bawendi, M. G. Improved performance and stability in quantum dot solar cells through band alignment engineering. *Nat. Mater.* **13**, 796–801 (2014).

Congreve, D. N. *et al.* External Quantum Efficiency Above 100% in a Singlet-Exciton-Fission–Based Organic Photovoltaic Cell. *Science* **340,** 334–337 (2013)

Demtsu, S., Albin, D. & Sites, J. Role of Copper in the Performance of CdS/CdTe Solar Cells. in *Conference Record of the 2006 IEEE 4th World Conference on Photovoltaic Energy Conversion* **1,** 523–526 (2006).

Deka, S. *et al.* Phosphine-Free Synthesis of p-Type Copper(I) Selenide Nanocrystals in Hot Coordinating Solvents. *J. Am. Chem. Soc.* **132,** 8912–8914 (2010).

Dhage, S. R. & Thomas Hahn, H. Rapid treatment of CIGS particles by intense pulsed light. *J. Phys. Chem. Solids* **71,** 1480–1483 (2010).

Dhage, S. R., Kim, H.-S. & Hahn, H. T. Cu(In,Ga)Se2 Thin Film Preparation from a Cu(In,Ga) Metallic Alloy and Se Nanoparticles by an Intense Pulsed Light Technique. *J. Electron. Mater.* **40,** 122–126 (2011).

Dovrat, M., Goshen, Y., Jedrzejewski, J., Balberg, I. & Sa'ar, A. Radiative versus nonradiative decay processes in silicon nanocrystals probed by time-resolved photoluminescence spectroscopy. *Phys. Rev. B* **69,** 155311 (2004).

Ellingson, R. J. *et al.* Highly Efficient Multiple Exciton Generation in Colloidal PbSe and PbS Quantum Dots. *Nano Lett.* **5**, 865–871 (2005).

Evans, C. M., Evans, M. E. & Krauss, T. D. Mysteries of TOPSe Revealed: Insights into Quantum Dot Nucleation. *J. Am. Chem. Soc.* **132**, 10973–10975 (2010).

First Solar Sets World Record for CdTe Solar PV Efficiency. (First Solar, Inc., 2011). at <http://investor.firstsolar.com/releasedetail.cfm?ReleaseID=593,994>

Franceschetti, A., An, J. M. & Zunger, A. Impact Ionization Can Explain Carrier Multiplication in PbSe Quantum Dots. *Nano Lett.* **6,** 2191–2195 (2006).

Franzl, T. *et al.* Fast energy transfer in layer-by-layer assembled CdTe nanocrystal bilayers. *Appl. Phys. Lett.* **84,** 2904–2906 (2004).

Fraunhofer Institute for Solar Energy Systems. *Photovoltaics Report*. (2014). at <http://www.ise.fraunhofer.de/en/downloads-englisch/pdf-files-englisch/photovoltaics-report-slides.pdf>

Fraunhofer ISE. Fraunhofer Instituite For Solar Energy Systems ISE: Photovoltaics Report. (2014). at <http://www.ise.fraunhofer.de/de/downloads/pdf-files/aktuelles/photovoltaics-report-in-englischer-sprache.pdf>

Gabor, N. M., Zhong, Z., Bosnick, K., Park, J. & McEuen, P. L. Extremely Efficient Multiple Electron-Hole Pair Generation in Carbon Nanotube Photodiodes. *Science* **325,** 1367–1371 (2009).

García-Santamaría, F. *et al.* Suppressed Auger Recombination in 'Giant' Nanocrystals Boosts Optical Gain Performance. *Nano Lett.* **9,** 3482–3488 (2009).

Ghosh, B., Chakraborty, D. P. & Carter, M. J. A novel back-contacting technology for thin films. *Semicond. Sci. Technol.* **11,** 1358 (1996).

Gloeckler, M. & Sites, J. R. Apparent quantum efficiency effects in CdTe solar cells. *J. Appl. Phys.* **95,** 4438–4445 (2004).

Goushi, Y., Hakuma, H., Tabuchi, K., Kijima, S. & Kushiya, K. Fabrication of pentanary Cu(InGa)(SeS)2 absorbers by selenization and sulfurization. *Sol. Energy Mater. Sol. Cells* **93,** 1318–1320 (2009).

Green, M. The nature of quantum dot capping ligands. *J. Mater. Chem.* **20,** 5797–5809 (2010).

Green, M. A., Emery, K., Hishikawa, Y., Warta, W. & Dunlop, E. D. Solar cell efficiency tables (version 44). *Prog. Photovolt. Res. Appl.* **22,** 701–710 (2014).

Guillot, M. J., McCool, S. C. & Schroder, K. A. Simulating the Thermal Response of Thin Films During Photonic Curing. 19–27 (2012). doi:10.1115/IMECE2012-87674

Guo, Q. *et al.* Development of CuInSe2 Nanocrystal and Nanoring Inks for Low-Cost Solar Cells. *Nano Lett.* **8**, 2982–2987 (2008).

Guo, Q. *et al.* Fabrication of 7.2% Efficient CZTSSe Solar Cells Using CZTS Nanocrystals. *J. Am. Chem. Soc.* **132**, 17384–17386 (2010).

Guo, Q., Ford, G. M., Agrawal, R. & Hillhouse, H. W. Ink formulation and low-temperature incorporation of sodium to yield 12% efficient Cu(In,Ga)(S,Se)2 solar cells from sulfide nanocrystal inks. *Prog. Photovolt. Res. Appl.* **21,** 64–71 (2013).

Guo, Q., Ford, G. M., Hillhouse, H. W. & Agrawal, R. Sulfide Nanocrystal Inks for Dense Cu(In1−xGax)(S1−ySey)2 Absorber Films and Their Photovoltaic Performance. *Nano Lett.* **9**, 3060–3065 (2009).

Guo, Q., Hillhouse, H. W. & Agrawal, R. Synthesis of Cu2ZnSnS4 Nanocrystal Ink and Its Use for Solar Cells. *J. Am. Chem. Soc.* **131**, 11672–11673 (2009).

Gur, I., Fromer, N. A., Geier, M. L. & Alivisatos, A. P. Air-Stable All-Inorganic Nanocrystal Solar Cells Processed from Solution. *Science* **310,** 462–465 (2005).

Hagfeldt, A., Boschloo, G., Sun, L., Kloo, L. & Pettersson, H. Dye-Sensitized Solar Cells. *Chem. Rev.* **110,** 6595–6663 (2010).

Hanna, M. C. & Nozik, A. J. Solar conversion efficiency of photovoltaic and photoelectrolysis cells with carrier multiplication absorbers. *J. Appl. Phys.* **100,** 074510 (2006).

Harvey, T. B. *et al.* Copper Indium Gallium Selenide (CIGS) Photovoltaic Devices Made Using Multistep Selenization of Nanocrystal Films. *ACS Appl. Mater. Interfaces* **5,** 9134–9140 (2013).

Hegedus, S., Ryan, D., Dobson, K., McCandless, B. & Desai, D. Photoconductive CdS: how does it Affect CdTe/CdS Solar Cell Performance? *MRS Online Proc. Libr.* **763,** B9.5.1–B9.5.6 (2003).

Hegedus, S. S. The photoresponse of CdS/CuInSe2thin-film heterojunction solar cells. *IEEE Trans. Electron Devices* **31,** 629–633 (1984).

Henry, C. H. Limiting efficiencies of ideal single and multiple energy gap terrestrial solar cells. *J. Appl. Phys.* **51**, 4494–4500 (1980).

Hillhouse, H. W. & Beard, M. C. Solar cells from colloidal nanocrystals: Fundamentals, materials, devices, and economics. *Curr. Opin. Colloid Interface Sci.* **14,** 245–259 (2009).

Ip, A. H. *et al.* Hybrid passivated colloidal quantum dot solids. *Nat. Nanotechnol.* **7**, 577–582 (2012).

Jackson, P. *et al.* New world record efficiency for Cu(In,Ga)Se2 thin-film solar cells beyond 20%. *Prog. Photovolt. Res. Appl.* **19,** 894–897 (2011).

Jang, S., Lee, D. J., Lee, D. & Oh, J. H. Electrical sintering characteristics of inkjet-printed conductive Ag lines on a paper substrate. *Thin Solid Films* **546,** 157–161 (2013).

Janssen, R. A. J. & Nelson, J. Factors Limiting Device Efficiency in Organic Photovoltaics. *Adv. Mater.* **25,** 1847–1858 (2013).

Jasieniak, J., MacDonald, B. I., Watkins, S. E. & Mulvaney, P. Solution-Processed Sintered Nanocrystal Solar Cells via Layer-by-Layer Assembly. *Nano Lett.* **11**, 2856–2864 (2011).

Jiang, C., Lee, J.-S. & Talapin, D. V. Soluble Precursors for CuInSe2, CuIn1–xGaxSe2, and Cu2ZnSn(S,Se)4 Based on Colloidal Nanocrystals and Molecular Metal Chalcogenide Surface Ligands. *J. Am. Chem. Soc.* **134,** 5010–5013 (2012).

Joo, S.-J., Hwang, H.-J. & Kim, H.-S. Highly conductive copper nano/microparticles ink via flash light sintering for printed electronics. *Nanotechnology* **25,** 265601 (2014).

Kamat, P. V. Emergence of New Materials for Light–Energy Conversion: Perovskites, Metal Clusters, and 2-D Hybrids. *J. Phys. Chem. Lett.* **5,** 4167–4168 (2014).

Kessler, F., Herrmann, D. & Powalla, M. Approaches to flexible CIGS thin-film solar cells. *Thin Solid Films* **480–481,** 491–498 (2005).

Khare, A., Wills, A. W., Ammerman, L. M., Norris, D. J. & Aydil, E. S. Size control and quantum confinement in Cu2ZnSnS4 nanocrystals. *Chem. Commun.* **47**, 11721–11723 (2011).

Kim, S. J., Kim, W. J., Cartwright, A. N. & Prasad, P. N. Carrier multiplication in a PbSe nanocrystal and P3HT/PCBM tandem cell. *Appl. Phys. Lett.* **92,** 191107–191107–3 (2008).

Kim, S. J., Kim, W. J., Sahoo, Y., Cartwright, A. N. & Prasad, P. N. Multiple exciton generation and electrical extraction from a PbSe quantum dot photoconductor. *Appl. Phys. Lett.* **92,** 031107–031107–3 (2008).

Kippelen, B. & Brédas, J.-L. Organic photovoltaics. *Energy Environ. Sci.* **2,** 251–261 (2009).

Klimov, V. I. Detailed-balance power conversion limits of nanocrystal-quantum-dot solar cells in the presence of carrier multiplication. *Appl. Phys. Lett.* **89,** 123118 (2006).

Kobayashi, Y., Nishimura, T., Yamaguchi, H. & Tamai, N. Effect of Surface Defects on Auger Recombination in Colloidal CdS Quantum Dots. *J. Phys. Chem. Lett.* **2,** 1051–1055 (2011).

Kohara, N., Nishiwaki, S., Hashimoto, Y., Negami, T. & Wada, T. Electrical properties of the Cu(In,Ga)Se2/ MoSe2/Mo structure. *Sol. Energy Mater. Sol. Cells* **67,** 209–215 (2001).

Kojima, A., Teshima, K., Shirai, Y. & Miyasaka, T. Organometal Halide Perovskites as Visible-Light Sensitizers for Photovoltaic Cells. *J. Am. Chem. Soc.* **131,** 6050–6051 (2009).

Koleilat, G. I., Wang, X. & Sargent, E. H. Graded Recombination Layers for Multijunction Photovoltaics. *Nano Lett.* **12,** 3043–3049 (2012).

Konstantatos, G., Levina, L., Fischer, A. & Sargent, E. H. Engineering the Temporal Response of Photoconductive Photodetectors via Selective Introduction of Surface Trap States. *Nano Lett.* **8,** 1446–1450 (2008).

Koo, B., Patel, R. N. & Korgel, B. A. Synthesis of CuInSe2 Nanocrystals with Trigonal Pyramidal Shape. *J. Am. Chem. Soc*. **131**, 3134–3135 (2009).

Koo, B., Patel, R. N. & Korgel, B. A. Wurtzite−Chalcopyrite Polytypism in CuInS2 Nanodisks. *Chem. Mater*. **21**, 1962–1966 (2009).

Kovalenko, M. V., Bodnarchuk, M. I. & Talapin, D. V. Nanocrystal Superlattices with Thermally Degradable Hybrid Inorganic−Organic Capping Ligands. *J. Am. Chem. Soc.* **132,** 15124–15126 (2010).

Kovalenko, M. V., Bodnarchuk, M. I., Zaumseil, J., Lee, J.-S. & Talapin, D. V. Expanding the Chemical Versatility of Colloidal Nanocrystals Capped with Molecular Metal Chalcogenide Ligands. *J. Am. Chem. Soc.* **132,** 10085–10092 (2010).

Kovalenko, M. V., Scheele, M. & Talapin, D. V. Colloidal Nanocrystals with Molecular Metal Chalcogenide Surface Ligands. *Science* **324,** 1417–1420 (2009).

Kramer, I. J. *et al.* Efficient Spray-Coated Colloidal Quantum Dot Solar Cells. *Adv. Mater.* **27,** 116–121 (2015).

Kramer, I. J. & Sargent, E. H. Colloidal Quantum Dot Photovoltaics: A Path Forward. *ACS Nano* **5,** 8506–8514 (2011).

Lazarenkova, O. L. & Balandin, A. A. Miniband formation in a quantum dot crystal. *J. Appl. Phys.* **89,** 5509–5515 (2001).

Law, M. *et al.* Determining the Internal Quantum Efficiency of PbSe Nanocrystal Solar Cells with the Aid of an Optical Model. *Nano Lett.* **8**, 3904–3910 (2008).

Lee, D. J. *et al.* Pulsed light sintering characteristics of inkjet-printed nanosilver films on a polymer substrate. *J. Micromechanics Microengineering* **21,** 125023 (2011).

Lee, J.-S., Kovalenko, M. V., Huang, J., Chung, D. S. & Talapin, D. V. Band-like transport, high electron mobility and high photoconductivity in all-inorganic nanocrystal arrays. *Nat. Nanotechnol.* **6,** 348–352 (2011).

Li, L., Coates, N. & Moses, D. Solution-Processed Inorganic Solar Cell Based on in Situ Synthesis and Film Deposition of CuInS2 Nanocrystals. *J. Am. Chem. Soc.* **132,** 22–23 (2010).

Li, L. *et al.* Efficient Synthesis of Highly Luminescent Copper Indium Sulfide-Based Core/Shell Nanocrystals with Surprisingly Long-Lived Emission. *J. Am. Chem. Soc.* **133**, 1176–1179 (2011).

Lin, Z., Franceschetti, A. & Lusk, M. T. Size Dependence of the Multiple Exciton Generation Rate in CdSe Quantum Dots. *ACS Nano* **5,** 2503–2511 (2011).

Luther, J. M. *et al.* Multiple Exciton Generation in Films of Electronically Coupled PbSe Quantum Dots. *Nano Lett.* **7**, 1779–1784 (2007).

Luther, J. M. *et al.* Schottky Solar Cells Based on Colloidal Nanocrystal Films. *Nano Lett.* **8**, 3488–3492 (2008).

MacDonald, B. I. *et al.* Layer-by-Layer Assembly of Sintered CdSexTe1–x Nanocrystal Solar Cells. *ACS Nano* **6,** 5995–6004 (2012).

McCandless, B. E. & Shafarman, W. N. Chemical surface deposition of ultra-thin semiconductors. (2003). at <http://www.google.com/patents/US6537845>

McDaniel, H., Fuke, N., Makarov, N. S., Pietryga, J. M. & Klimov, V. I. An integrated approach to realizing high-performance liquid-junction quantum dot sensitized solar cells. *Nat. Commun.* **4,** (2013).

McDaniel, H., Fuke, N., Pietryga, J. M. & Klimov, V. I. Engineered CuInSexS2–x Quantum Dots for Sensitized Solar Cells. *J. Phys. Chem. Lett.* 355–361 (2013). doi:10.1021/jz302067r

McGuire, J. A., Sykora, M., Joo, J., Pietryga, J. M. & Klimov, V. I. Apparent Versus True Carrier Multiplication Yields in Semiconductor Nanocrystals. *Nano Lett.* **10,** 2049–2057 (2010).

Midgett, A. G. *et al.* Size and Composition Dependent Multiple Exciton Generation Efficiency in PbS, PbSe, and PbSxSe1−x Alloyed Quantum Dots. *Nano Lett.* **13,** 3078–3085 (2013).

Midgett, A. G., Hillhouse, H. W., Hughes, B. K., Nozik, A. J. & Beard, M. C. Flowing versus Static Conditions for Measuring Multiple Exciton Generation in PbSe Quantum Dots. *J. Phys. Chem. C* **114,** 17486–17500 (2010).

Milliron, D. J., Mitzi, D. B., Copel, M. & Murray, C. E. Solution-Processed Metal Chalcogenide Films for p-Type Transistors. *Chem. Mater.* **18,** 587–590 (2006).

Miskin, C. K. *et al.* 9.0% efficient Cu2ZnSn(S,Se)4 solar cells from selenized nanoparticle inks. *Prog. Photovolt. Res. Appl.* n/a–n/a (2014). doi:10.1002/pip.2472

Mitzi, D. B., Gunawan, O., Todorov, T. K., Wang, K. & Guha, S. The path towards a high-performance solution-processed kesterite solar cell. *Sol. Energy Mater. Sol. Cells* **95,** 1421–1436 (2011).

Mitzi, D. B., Kosbar, L. L., Murray, C. E., Copel, M. & Afzali, A. High-mobility ultrathin semiconducting films prepared by spin coating. *Nature* **428,** 299–303 (2004).

Mitzi, D. B. N4H9Cu7S4: A Hydrazinium-Based Salt with a Layered Cu7S4-Framework. *Inorg. Chem.* **46,** 926–931 (2007).

Mitzi, D. B. Synthesis, Structure, and Thermal Properties of Soluble Hydrazinium Germanium(IV) and Tin(IV) Selenide Salts. *Inorg. Chem.* **44,** 3755–3761 (2005).

Moreels, I. *et al.* Composition and Size-Dependent Extinction Coefficient of Colloidal PbSe Quantum Dots. *Chem. Mater.* **19,** 6101–6106 (2007).

Moreels, I. *et al.* Size-Dependent Optical Properties of Colloidal PbS Quantum Dots. *ACS Nano* **3,** 3023–3030 (2009).

Murphy, J. E. *et al.* PbTe Colloidal Nanocrystals: Synthesis, Characterization, and Multiple Exciton Generation. *J. Am. Chem. Soc.* **128**, 3241–3247 (2006).

Murray, C. B., Norris, D. J. & Bawendi, M. G. Synthesis and characterization of nearly monodisperse CdE (E = sulfur, selenium, tellurium) semiconductor nanocrystallites. *J. Am. Chem. Soc.* **115**, 8706–8715 (1993).

Nag, A. *et al.* Metal-free Inorganic Ligands for Colloidal Nanocrystals: S2–, HS–, Se2–, HSe–, Te2–, HTe–, TeS32–, OH–, and NH2– as Surface Ligands. *J. Am. Chem. Soc.* **133,** 10612–10620 (2011).

Nagpal, P. & Klimov, V. I. Role of mid-gap states in charge transport and photoconductivity in semiconductor nanocrystal films. *Nat. Commun.* **2**, 486 (2011).

Nelson, J. *The Physics of Solar Cells: Photons In, Electrons Out*. (Imperial College Press, 2003).

Nootz, G. *et al.* Size dependence of carrier dynamics and carrier multiplication in PbS quantum dots. *Phys. Rev. B* **83,** 155302 (2011).

Norako, M. E. & Brutchey, R. L. Synthesis of Metastable Wurtzite CuInSe2 Nanocrystals. *Chem. Mater.* **22,** 1613–1615 (2010).

Olson, J. D., Rodriguez, Y. W., Yang, L. D., Alers, G. B. & Carter, S. A. CdTe Schottky diodes from colloidal nanocrystals. *Appl. Phys. Lett.* **96,** 242103 (2010).

Padilha, L. A. *et al.* Aspect Ratio Dependence of Auger Recombination and Carrier Multiplication in PbSe Nanorods. *Nano Lett.* **13,** 1092–1099 (2013).

Panthani, M. G. *et al.* CuInSe2 Quantum Dot Solar Cells with High Open-Circuit Voltage. *J. Phys. Chem. Lett.* **4,** 2030–2034 (2013).

Panthani, M. G. *et al.* High Efficiency Solution Processed Sintered CdTe Nanocrystal Solar Cells: The Role of Interfaces. *Nano Lett.* (2013). doi:10.1021/nl403912w

Panthani, M. G. *et al.* Synthesis of CuInS2, CuInSe2, and Cu(InxGa1-x)Se2 (CIGS) Nanocrystal 'Inks' for Printable Photovoltaics. *J. Am. Chem. Soc.* **130**, 16770–16777 (2008).

Panthani, M. G. & Korgel, B. A. Nanocrystals for Electronics. *Annu. Rev. Chem. Biomol. Eng.* **3**, 287–311 (2012).

Park, K. H., Jang, K., Kim, S., Kim, H. J. & Son, S. U. Phase-Controlled One-Dimensional Shape Evolution of InSe Nanocrystals. *J. Am. Chem. Soc.* **128,** 14780–14781 (2006).

Pattantyus-Abraham, A. G. *et al.* Depleted-Heterojunction Colloidal Quantum Dot Solar Cells. *ACS Nano* **4,** 3374–3380 (2010).

Pons, T. et al. Cadmium-Free CuInS2/ZnS Quantum Dots for Sentinel Lymph Node Imaging with Reduced Toxicity. *ACS Nano* **4**, 2531–2538 (2010).

Ren, S. *et al.* Inorganic–Organic Hybrid Solar Cell: Bridging Quantum Dots to Conjugated Polymer Nanowires. *Nano Lett.* **11,** 3998–4002 (2011).

Repins, I. *et al.* 19·9%-efficient ZnO/CdS/CuInGaSe2 solar cell with 81·2% fill factor. *Prog. Photovolt. Res. Appl.* **16,** 235–239 (2008).

Romeo, A. *et al.* High-efficiency flexible CdTe solar cells on polymer substrates. *Sol. Energy Mater. Sol. Cells* **90,** 3407–3415 (2006).

Ryu, J., Kim, H.-S. & Hahn, H. T. Reactive Sintering of Copper Nanoparticles Using Intense Pulsed Light for Printed Electronics. *J. Electron. Mater.* **40,** 42–50 (2011).

Sambur, J. B., Novet, T. & Parkinson, B. A. Multiple Exciton Collection in a Sensitized Photovoltaic System. *Science* **330,** 63–66 (2010).

Sandeep, C. S. S. *et al.* High charge-carrier mobility enables exploitation of carrier multiplication in quantum-dot films. *Nat. Commun.* **4,** (2013).

Schaller, R. D., Agranovich, V. M. & Klimov, V. I. High-efficiency carrier multiplication through direct photogeneration of multi-excitons via virtual single-exciton states. *Nat. Phys.* **1,** 189–194 (2005).

Schaller, R. D. & Klimov, V. I. High Efficiency Carrier Multiplication in PbSe Nanocrystals: Implications for Solar Energy Conversion. *Phys. Rev. Lett.* **92,** 186601 (2004).

Schaller, R. D., Petruska, M. A. & Klimov, V. I. Effect of electronic structure on carrier multiplication efficiency: Comparative study of PbSe and CdSe nanocrystals. *Appl. Phys. Lett.* **87,** 253102 (2005).

Schroder, K. A., McCool, S. C. & Furlan, W. F. Broadcast photonic curing of metallic nanoparticle films. in (2006). <http://www.novacentrix.com/images/downloads/NSTI%202006%20Boston.pdf>

Schroder, K., A. Mechanisms of photonic curing: processing high temperatures on low temperature substrates. *Nanotech Conf. Expo 2011 Interdiscip. Integr. Forum Nanotechnol. Biotechnol. Microtechnology* **2,**

Semonin, O. E. *et al.* Peak External Photocurrent Quantum Efficiency Exceeding 100% via MEG in a Quantum Dot Solar Cell. *Science* **334**, 1530–1533 (2011).

Shabaev, A., Efros, A. L. & Nozik, A. J. Multiexciton Generation by a Single Photon in Nanocrystals. *Nano Lett.* **6,** 2856–2863 (2006).

Sharp Develops Concentrator Solar Cell with World's Highest Conversion Efficiency of 43.5% | Press Releases | Sharp Global. at <http://sharp-world.com/corporate/news/120531.html>

Singh, M., Jiu, J., Sugahara, T. & Suganuma, K. Photonic Sintering of Thin Film Prepared by Dodecylamine Capped CuInxGa1 -xSe2 Nanoparticles for Printed Photovoltaics. *Thin Solid Films* doi:10.1016/j.tsf.2014.06.036

Sites, J. R., Tavakolian, H. & Sasala, R. A. Analysis of apparent quantum efficiency. *Sol. Cells* **29,** 39–48 (1990).

Stolle, C. J. *et al.* Multiexciton Solar Cells of CuInSe2 Nanocrystals. *J. Phys. Chem. Lett.* **5,** 304–309 (2014).

Steinhagen, C. *et al.* Solution−Liquid−Solid Synthesis of CuInSe2 Nanowires and Their Implementation in Photovoltaic Devices. *ACS Appl. Mater. Interfaces* **3,** 1781–1785 (2011).

Steinhagen, C. *et al*. Synthesis of Cu2ZnSnS4 Nanocrystals for Use in Low-Cost Photovoltaics. J. Am. Chem. Soc. 131, 12554–12555 (2009).

Stevens, G. Thin film CIGS report card - Progress in CIGS achieving scale. in *2012 38th IEEE Photovoltaic Specialists Conference (PVSC)* 002487–002489 (2012). doi:10.1109/PVSC.2012.6318099

Stewart, J. T. *et al.* Comparison of Carrier Multiplication Yields in PbS and PbSe Nanocrystals: The Role of Competing Energy-Loss Processes. *Nano Lett.* **12,** 622–628 (2012).

Stolle, C. J. *et al.* Multiexciton Solar Cells of CuInSe2 Nanocrystals. *J. Phys. Chem. Lett.* **5**, 304–309 (2014).

Stolle, C. J., Harvey, T. B. & Korgel, B. A. Nanocrystal photovoltaics: a review of recent progress. *Curr. Opin. Chem. Eng.* **2**, 160–167 (2013).

Stolle, C. J., Panthani, M. G., Harvey, T. B., Akhavan, V. A. & Korgel, B. A. Comparison of the Photovoltaic Response of Oleylamine and Inorganic Ligand-Capped CuInSe2 Nanocrystals. *ACS Appl. Mater. Interfaces* **4,** 2757–2761 (2012).

Stolle, C. J., Schaller, R. D. & Korgel, B. A. Efficient Carrier Multiplication in Colloidal CuInSe2 Nanocrystals. *J. Phys. Chem. Lett.* 3169–3174 (2014). doi:10.1021/jz501640f

Stubbs, S. K. *et al.* Efficient carrier multiplication in InP nanoparticles. *Phys. Rev. B* **81,** 081303 (2010).

Sukhovatkin, V., Hinds, S., Brzozowski, L. & Sargent, E. H. Colloidal Quantum-Dot Photodetectors Exploiting Multiexciton Generation. *Science* **324,** 1542–1544 (2009).

Sun, J. *et al.* Generation of Multiple Excitons in Ag2S Quantum Dots: Single High-Energy versus Multiple-Photon Excitation. *J. Phys. Chem. Lett.* **5,** 659–665 (2014).

Talapin, D. V., Lee, J.-S., Kovalenko, M. V. & Shevchenko, E. V. Prospects of Colloidal Nanocrystals for Electronic and Optoelectronic Applications. *Chem. Rev.* **110,** 389–458 (2009).

Tang, J. *et al.* Colloidal-quantum-dot photovoltaics using atomic-ligand passivation. *Nat. Mater*. **10,** 765–771 (2011).

Tang, J. *et al.* Quantum Dot Photovoltaics in the Extreme Quantum Confinement Regime: The Surface-Chemical Origins of Exceptional Air- and Light-Stability. *ACS Nano* **4**, 869–878 (2010).

Tang, J. *et al.* Quantum Junction Solar Cells. *Nano Lett.* **12**, 4889–4894 (2012).

Tisdale, W. A. *et al.* Hot-Electron Transfer from Semiconductor Nanocrystals. *Science* **328,** 1543–1547 (2010).

Trinh, M. T. *et al.* Direct generation of multiple excitons in adjacent silicon nanocrystals revealed by induced absorption. *Nat. Photonics* **6,** 316–321 (2012).

U.S.Department of Energy. SunShot Vision Study. (2012).

Velizhanin, K. A. & Piryatinski, A. Numerical Study of Carrier Multiplication Pathways in Photoexcited Nanocrystal and Bulk Forms of PbSe. *Phys. Rev. Lett.* **106,** 207401 (2011).

Wang, F., Wu, Y., Hybertsen, M. S. & Heinz, T. F. Auger recombination of excitons in one-dimensional systems. *Phys. Rev. B* **73,** 245424 (2006).

Wang, J.-J., Wang, Y.-Q., Cao, F.-F., Guo, Y.-G. & Wan, L.-J. Synthesis of Monodispersed Wurtzite Structure CuInSe2 Nanocrystals and Their Application in High-Performance Organic−Inorganic Hybrid Photodetectors. *J. Am. Chem. Soc.* **132,** 12218–12221 (2010).

Wang, L.-W., Califano, M., Zunger, A. & Franceschetti, A. Pseudopotential Theory of Auger Processes in CdSe Quantum Dots. *Phys. Rev. Lett.* **91,** 056404 (2003).

Wang, X. *et al.* Tandem colloidal quantum dot solar cells employing a graded recombination layer. *Nat. Photonics* **5,** 480–484 (2011).

Wu, Y., Wadia, C., Ma, W., Sadtler, B. & Alivisatos, A. P. Synthesis and Photovoltaic Application of Copper(I) Sulfide Nanocrystals. *Nano Lett.* **8,** 2551–2555 (2008).

Yu, P., Nedeljkovic, J. M., Ahrenkiel, P. A., Ellingson, R. J. & Nozik, A. J. Size Dependent Femtosecond Electron Cooling Dynamics in CdSe Quantum Rods. *Nano Lett.* **4,** 1089–1092 (2004).

Yuan, M. *et al.* Controlled Assembly of Zero-, One-, Two-, and Three-Dimensional Metal Chalcogenide Structures. *Inorg. Chem.* **46,** 7238–7240 (2007).

Zhang, J. *et al.* PbSe Quantum Dot Solar Cells with More than 6% Efficiency Fabricated in Ambient Atmosphere. *Nano Lett.* **14,** 6010–6015 (2014).

Zhao, J. *et al.* 20 000 PERL silicon cells for the '1996 World Solar Challenge' solar car race. *Prog. Photovolt. Res. Appl.* **5,** 269–276 (1997).

Zhong, H. *et al.* Colloidal CuInSe2 Nanocrystals in the Quantum Confinement Regime: Synthesis, Optical Properties, and Electroluminescence. *J. Phys. Chem. C* **115**, 12396–12402 (2011).

Zhu, J. *et al*. Optical Absorption Enhancement in Amorphous Silicon Nanowire and Nanocone Arrays. *Nano Lett.* **9,** 279–282 (2008).

Vita

Carl Jackson Stolle was born in Sunnyvale, California and has lived in Austin, Texas since 1997. He graduated from Westlake High School in 2007. He went on to attend The University of Texas at Austin, where he graduated in 2010 with high honors with a Bachelor of Science in Physics. In the fall of 2010, he began his graduate studies in chemical engineering under the supervision of Dr. Brian Korgel. He earned a Master of Science in Engineering in 2014 and completed his Ph.D. in the spring of 2015.

The author can be reached at cjstolle@utexas.edu

This dissertation was typed by the author